

Electromagnetic Scattering on Spherical Polydispersions

D. Deirmendjian

April 1969

R-456-PR

A REPORT PREPARED FOR
UNITED STATES AIR FORCE PROJECT RAND

The **RAND** *Corporation*

1700 MAIN ST. • SANTA MONICA • CALIFORNIA • 90406

This research is supported by the United States Air Force under Project RAND—Contract No. F44620-67-C-0045—monitored by the Directorate of Operational Requirements and Development Plans, Deputy Chief of Staff, Research and Development, Hq USAF. Views or conclusions contained in this study should not be interpreted as representing the official opinion or policy of the United States Air Force.

Electromagnetic Scattering on Spherical Polydispersions

Electromagnetic Scattering on Spherical Polydispersions

D. DEIRMENDJIAN

The RAND Corporation, Santa Monica, California



AMERICAN ELSEVIER PUBLISHING COMPANY, INC.
NEW YORK

1969

AMERICAN ELSEVIER PUBLISHING COMPANY, INC.

52 Vanderbilt Avenue, New York, N.Y. 10017

ELSEVIER PUBLISHING CO. LTD.

Barking, Essex, England

ELSEVIER PUBLISHING COMPANY

335 Jan Van Galenstraat, P.O. Box 211, Amsterdam, The Netherlands

Standard Book Number 444-00038-0

Library of Congress Card Number 68-28759

Copyright © 1969 by The RAND Corporation

All rights reserved. This book or any part thereof must not be reproduced in any form without the written permission of the publisher, American Elsevier Publishing Company, Inc., 52 Vanderbilt Avenue, New York, N.Y. 10017.

PRINTED IN THE UNITED STATES OF AMERICA

Foreword

It is a long way from the old saying that every cloud has a silver lining to the new plans, say, for a global satellite weather prediction system. This book by Dr. Diran Deirmendjian is a useful guide to a difficult part of this route. In future no scientist analyzing the heat budget of the atmosphere can afford to be sloppy about errors of 5 or 10 percent. And no study of the planets, whether from our own distant earth or from a nearby spacecraft, carried out with photometric, polarimetric, or spectroscopic instruments, will be complete without a quantitative study of the subtle interplay of radiation with the haze and clouds floating above the planet's surface.

The magic word for these studies is radiative transfer, a subject known to lead to complicated mathematics even if very crude simplifying assumptions are made. The understandable consequence is that, until recently, the great majority of papers on the subject have dealt with the assumption of isotropic scattering in any single volume element. Other papers have dealt at length with mild anisotropy assumptions, easy on the mathematics, but contradicting our knowledge about aerosol scattering since nearly a century. This book replaces these assumptions with reliable and complete data for many representative examples. The formalism, involving Mie theory and Stokes parameters, is well explained and is brought to the point where computer programs for specific transfer problems must take over. We trust that this book will find many attentive readers and grateful users who will discover that one limited but essential part of their problem has already been solved.

H. C. VAN DE HULST

PREFACE

The present monograph is an outgrowth of the author's more or less continuous interest in atmospheric light-scattering phenomena, inspired by the rich color of the Grecian skies and seas of his youth. The bulk of the work was performed while working as a member of the scientific staff of The RAND Corporation and generously supported under the provisions of its Air Force Project RAND contract allowing for fundamental research in the geophysical and planetary sciences.

Under the increasing pressures of the space age, the urge to change our physical environment, and the massive government support of related fields of research, the traditional scientific attitudes are rapidly changing. It appears that the times when scientists *qua* scholars were free to pursue their bent for painstaking but leisurely observation, cogitation, digestion, analysis, and synthesis of information on the diverse aspects of our environment are forever gone. Spectacular and often unverified pieces of research are summarily published and uncritically used by others, merely on the strength of their promise to modify natural processes, purportedly to man's immediate advantage. As it often happens, however, what appears to be a shortcut turns out to be the longest and costliest route toward the desired end. This is particularly true of the terrestrial atmosphere, still incompletely understood, and specifically, of the local and global interactions of sunlight with the surface-atmosphere system in influencing climate and weather.

In such times it is important to emphasize the value of critically selected

and edited compilations of data based on well-verified observation or theory, so that they can be used in several related fields of research. This we have attempted to do here, encouraged by a recent article by the eminent physicist Samuel A. Goudsmit ("Is the literature worth retrieving?", *Physics Today*, **19**, No. 9, 1966), who says, with reference to experimental results, that "tables and graphs of numerical data . . . play an important role in the progress of physics" (p. 52). The tables in Part II of this book are, in fact, experimental results in a certain context and should be used as such. To our knowledge there are no existing compilations similar to ours in scope, uniformity, and completeness of relevant parameters. The only exception is that of A. F. Stevenson and W. Heller (*Tables of Scattering Functions for Heterodisperse Systems*, Wayne State University Press, 1961). This book is restricted to 90° scattering angles only, to nonabsorbing dielectrics, and to a single size-distribution function, which is equivalent to a special case of the generalized form used here.

The significant portion of the present work is in the form of numerical tables, which make up Part II, designed to be used by those interested primarily in terrestrial and other planetary atmospheric problems as well as in astrophysical problems related to interplanetary and interstellar dust. The introductory text, arranged in four chapters, became somewhat longer in the process of writing than initially planned, for reasons that will appear and despite efforts to keep it within minimum bounds. Nevertheless, we have resisted, so far as possible, the current temptation to redefine well-known concepts and quantities or to introduce novel but otherwise superfluous terminology, units, and symbols. Rather we have made maximum use of the established ones where these are readily available in other publications.

Because of various circumstances, the author has been unable to familiarize himself fully with all the pertinent literature published in Russian or in certain other languages, except through translation, references, or abstracts. A priori apologies are offered to the authors of such original papers which, though related to subjects discussed here, have not been specifically cited. The list of references appearing at the end of Part I should not, therefore, be regarded as an exhaustive bibliography.

Undoubtedly there will be found in the following pages errors of fact and judgment as well as occasional statements written in a facetious vein. For these the author assumes entire responsibility, as indeed he must. Any expressed views, scientific or otherwise, in no way reflect those of The RAND Corporation and its sponsors, nor of the author's close associates.

The contents of the introductory text in Part I, particularly Chapter 4, are based on the situation during the completion of the manuscript (July, 1967). Subsequent developments and publications are not discussed or cited.

The author acknowledges the assistance, encouragement, and moral support freely proffered by his associates and colleagues while preparing this work, especially during times of personal distress. He owes particular debts of gratitude in the first place to Prof. Zdenek Sekera of the University of California in his capacity as personal friend, advisor, and consultant, and for his careful reading of the manuscript and helpful suggestions; to Drs. W. W. Kellogg and S. M. Greenfield, past and present heads of the Department of Environmental Sciences of The RAND Corporation for the invaluable freedom afforded to the author in the choice of a problem area, for their faith in his ability, and for their patience, encouragement, and personal friendship; to colleagues such as Drs. M. H. Davis, E. H. Vestine, A. G. Wilson, and M. Warshaw for occasional assistance and suggestions whenever requested; to Anne B. Kahle, another colleague, for her active and valuable assistance in the final "debugging" and refinement of the computer program, which was initially developed to the author's satisfaction by R. J. Clasen, staff member of another department in RAND; and last but not least, to Mrs. Alice V. Jeffs for undertaking with patience and enthusiasm the tedious task of extraction, roundoff, typing, and checking of the numerous tables comprising Part II of the book, under the author's guidance; and to the editorial and secretarial staff for the performance of the many tasks involved in the preparation of the final manuscript.

The author further expresses his special gratitude to Prof. H. C. van de Hulst of the Leiden Observatory, the Netherlands, for urging the publication of this monograph and for agreeing to contribute a Foreword; and to J. W. Hovenier, of the same Observatory, for advising him of a sign inconsistency in the definition of the ellipticity parameter ($q.v.$) in time for its correction before publication.

D. DEIRMENDJIAN

Santa Monica, California
May, 1968

Contents

Foreword by H. C. van de Hulst	v
Preface	vii
Glossary of Symbols	xvii

PART I POLYDISPERSE SCATTERING AND ITS APPLICATIONS

1 INTRODUCTION	3
1.1 Motivation	3
1.2 Brief History	5
1.3 General Organization of the Monograph	6
2 SCATTERING ON SINGLE PARTICLES	9
2.1 Various Approximations	9
2.11 Rayleigh Approximation	9
2.12 Rayleigh–Gans Approximation	10
2.13 Van de Hulst’s Approximation	10
2.14 Other Approximations	10
2.15 The Mie Solution	11
2.2 The Basic Mie Functions	12
2.21 Adaptation of Mie Expressions to Machine Computation	14
2.22 Behavior of the Function $A_n(y)$	19
2.3 Examples of Single-Particle Scattering Parameters	24
2.31 The Mie Coefficients a_n and b_n	24
2.32 The Extinction, Scattering, and Absorption Efficiencies	28
2.33 The Backscattering or “Radar” Cross Section and Efficiency	37

2.34	The Amplitude Components S_1 and S_2	41
2.35	The Dimensionless Intensity Parameters $i_1(\theta)$ and $i_2(\theta)$	46
3	SINGLE SCATTERING ON MANY PARTICLES	56
3.1	Choice of Characteristic Parameters	56
3.2	The Stokes Parameters for a Single Particle	57
3.21	Derivation and Properties of the Stokes Parameters	60
3.22	The Stokes Matrix for Mie Scattering	68
3.3	The Stokes Matrix Elements for a Polydispersion	72
3.31	Normalization and Separation in Monodisperse Systems	72
3.32	Extension to Polydisperse Systems	74
3.4	Form and Properties of the Distribution Function	75
3.41	Actual Distribution Functions Used	77
3.5	Choice of Refractive Indices (Optical Constants)	83
3.6	Preparation of the Tables	88
4	DISCUSSION AND APPLICATION OF THE RESULTS	94
4.1	General Remarks	94
4.2	Equation of Radiative Transfer	94
4.3	Applications to the Terrestrial Atmosphere	97
4.31	Aerosol, Haze, and Dust Layers	98
4.32	Natural Water Clouds	108
4.33	Microwave Scattering Properties of Natural Precipitation	119
4.34	Laser Applications	124
4.4	Other Planetary Atmospheres	127
4.41	Venus	128
4.42	Mars	132
4.43	Saturn's Rings	134
4.5	Interplanetary and Interstellar Dust	136
4.51	Zodiacal Light	137
4.52	Interstellar Particles	139
	References	143

PART II NUMERICAL TABLES

Water Haze M	Table T.1 ($\lambda 0.45 \mu$)	151
	Table T.2 ($\lambda 0.70 \mu$)	152
	Table T.3 ($\lambda 1.19 \mu$)	153
	Table T.4 ($\lambda 1.45 \mu$)	154
	Table T.5 ($\lambda 1.61 \mu$)	155
	Table T.6 ($\lambda 1.94 \mu$)	156
	Table T.7 ($\lambda 2.25 \mu$)	157
	Table T.8 ($\lambda 3.00 \mu$)	158
	Table T.9 ($\lambda 3.9 \mu$)	159
	Table T.10 ($\lambda 5.30 \mu$)	160
	Table T.11 ($\lambda 6.05 \mu$)	161
	Table T.12 ($\lambda 8.15 \mu$)	162
	Table T.13 ($\lambda 10.0 \mu$)	163
	Table T.14 ($\lambda 11.5 \mu$)	164
	Table T.15 ($\lambda 16.6 \mu$)	165
Water Haze L	Table T.16 ($\lambda 0.45 \mu$)	166
	Table T.17 ($\lambda 0.70 \mu$)	167
	Table T.18 ($\lambda 1.19 \mu$)	168
	Table T.19 ($\lambda 1.94 \mu$)	169
	Table T.20 ($\lambda 3.00 \mu$)	170
	Table T.21 ($\lambda 3.90 \mu$)	171
	Table T.22 ($\lambda 5.30 \mu$)	172
	Table T.23 ($\lambda 6.05 \mu$)	173
	Table T.24 ($\lambda 8.15 \mu$)	174
	Table T.25 ($\lambda 8.15 \mu$)	175
	Table T.26 ($\lambda 16.6 \mu$)	176
Water Haze H	Table T.27 ($\lambda 0.45 \mu$)	177
	Table T.28 ($\lambda 0.70 \mu$)	178
	Table T.29 ($\lambda 1.19 \mu$)	179
	Table T.30 ($\lambda 1.94 \mu$)	180
	Table T.31 ($\lambda 3.00 \mu$)	181
	Table T.32 ($\lambda 3.90 \mu$)	182
	Table T.33 ($\lambda 5.30 \mu$)	183
	Table T.34 ($\lambda 6.05 \mu$)	183
Water Cloud C.1	Table T.35 ($\lambda 0.45 \mu$)	184
	Table T.36 ($\lambda 0.70 \mu$)	186

	Table T.37 ($\lambda 1.19 \mu$)	188
	Table T.38 ($\lambda 1.45 \mu$)	190
	Table T.39 ($\lambda 1.61 \mu$)	192
	Table T.40 ($\lambda 1.94 \mu$)	194
	Table T.41 ($\lambda 2.25 \mu$)	196
	Table T.42 ($\lambda 3.00 \mu$)	197
	Table T.43 ($\lambda 3.90 \mu$)	198
	Table T.44 ($\lambda 5.30 \mu$)	199
	Table T.45 ($\lambda 6.05 \mu$)	200
	Table T.46 ($\lambda 8.15 \mu$)	201
	Table T.47 ($\lambda 8.15 \mu$)	202
	Table T.48 ($\lambda 10.0 \mu$)	203
	Table T.49 ($\lambda 11.5 \mu$)	204
	Table T.50 ($\lambda 16.6 \mu$)	205
Water Cloud C.2	Table T.51 ($\lambda 0.45 \mu$)	206
	Table T.52 ($\lambda 0.70 \mu$)	208
	Table T.53 ($\lambda 1.61 \mu$)	210
	Table T.54 ($\lambda 3.00 \mu$)	212
	Table T.55 ($\lambda 3.90 \mu$)	213
	Table T.56 ($\lambda 6.05 \mu$)	214
	Table T.57 ($\lambda 10.0 \mu$)	215
	Table T.58 ($\lambda 16.60 \mu$)	216
Water Cloud C.3	Table T.59 ($\lambda 0.45 \mu$)	217
	Table T.60 ($\lambda 0.70 \mu$)	219
	Table T.61 ($\lambda 1.61 \mu$)	221
	Table T.62 ($\lambda 2.25 \mu$)	222
	Table T.63 ($\lambda 3.00 \mu$)	223
	Table T.64 ($\lambda 3.90 \mu$)	224
	Table T.65 ($\lambda 5.30 \mu$)	225
	Table T.66 ($\lambda 6.05 \mu$)	226
	Table T.67 ($\lambda 8.15 \mu$)	227
	Table T.68 ($\lambda 10.0 \mu$)	228
	Table T.69 ($\lambda 16.6 \mu$)	228
Water Cloud C.4	Table T.70 ($\lambda 0.45 \mu$)	229
	Table T.71 ($\lambda 0.70 \mu$)	231
Rain L (0°C Water)	Table T.72 ($\lambda 0.1 \text{ cm}$)	233
	Table T.73 ($\lambda 0.2 \text{ cm}$)	234
	Table T.74 ($\lambda 0.3 \text{ cm}$)	235

	Table T.75 ($\lambda 0.5$ cm)	236
	Table T.76 ($\lambda 1.0$ cm)	237
	Table T.77 ($\lambda 2.0$ cm)	238
	Table T.78 ($\lambda 3.3$ cm)	239
	Table T.79 ($\lambda 5.0$ cm)	240
	Table T.80 ($\lambda 8.0$ cm)	240
Rain L (10°C Water)	Table T.81 ($\lambda 0.1$ cm)	241
	Table T.82 ($\lambda 0.3$ cm)	242
	Table T.83 ($\lambda 1.0$ cm)	243
	Table T.84 ($\lambda 3.3$ cm)	244
	Table T.85 ($\lambda 8.0$ cm)	245
Rain L (Ice)	Table T.86 ($\lambda 0.2$ cm)	246
	Table T.87 ($\lambda 1.0$ cm)	247
	Table T.88 ($\lambda 3.3$ cm)	248
Hail H (Ice)	Table T.89 ($\lambda 0.2$ cm)	249
	Table T.90 ($\lambda 0.5$ cm)	250
	Table T.91 ($\lambda 1.0$ cm)	251
	Table T.92 ($\lambda 2.0$ cm)	252
	Table T.93 ($\lambda 3.3$ cm)	253
	Table T.94 ($\lambda 8.0$ cm)	253
Hail H (0°C Water)	Table T.95 ($\lambda 1.0$ cm)	254
	Table T.96 ($\lambda 3.3$ cm)	255
	Table T.97 ($\lambda 8.0$ cm)	255
Silicate Haze M	Table T.98 ($\lambda 0.589 \mu$)	256
	Table T.99 ($\lambda 0.589 \mu$)	257
	Table T.100 ($\lambda 0.589 \mu$)	258
Silicate Haze L	Table T.101 ($\lambda 0.589 \mu$)	259
Silicate Haze H	Table T.102 ($\lambda 0.45 \mu$)	260
	Table T.103 ($\lambda 0.70 \mu$)	261
Silicate Cloud C.3	Table T.104 ($\lambda 0.45 \mu$)	262
	Table T.105 ($\lambda 0.70 \mu$)	264
Limonite Haze M	Table T.106 ($\lambda 0.589 \mu$)	266
	Table T. 107 ($\lambda 0.589 \mu$)	267
	Table T.108 ($\lambda 0.589 \mu$)	268
Limonite Haze L	Table T.109 ($\lambda 0.589 \mu$)	269

Limonite Cloud C.3	Table T.110 ($\lambda 0.45 \mu$)	270
	Table T.111 ($\lambda 0.70 \mu$)	271
Iron Haze M	Table T.112 ($\lambda 0.441 \mu$)	272
	Table T.113 ($\lambda 0.589 \mu$)	273
	Table T.114 ($\lambda 0.668 \mu$)	274
Iron Haze L	Table T.115 ($\lambda 0.441 \mu$)	275
	Table T.116 ($\lambda 0.668 \mu$)	276
	Table T.117 ($\lambda 0.441 \mu$)	277
	Table T.118 ($\lambda 0.589 \mu$)	278
	Table T.119 ($\lambda 0.668 \mu$)	279
Iron Haze H	Table T.120 ($\lambda 0.441 \mu$)	280
	Table T.121 ($\lambda 0.668 \mu$)	281
	Table T.122 ($\lambda 0.441 \mu$)	282
	Table T.123 ($\lambda 0.668 \mu$)	283
Iron Cloud C.3	Table T.124 ($\lambda 0.441 \mu$)	284
	Table T.125 ($\lambda 0.668 \mu$)	285
Subject Index	287

Glossary of Symbols

For convenience and economy the principal symbols appearing in the text are listed below alphabetically. Some of these may play a dual role, in which case the meaning should be obvious from the context. The numbers in parentheses refer to typical equations in which the symbols appear or are defined. Symbols whose usage is well established in the literature are omitted.

- a constant in the size-distribution function (82,83)
- a_n, b_n Mie series coefficients independent of angle (10,11)
- A_1, A_2 dimensionless scattering amplitudes (1,2)
- $A_n(y)$ factor in Mie series coefficients containing functions of complex argument (10,11,20,21)
- b constant in the size-distribution function (82,85)
- $D_{1,2,3,4}$ correction factors extending the validity of $K(\rho, m)$ (26)
- $D(P)$ depolarization factor (110)
- E_1, E_2 components of electric field vector amplitude \mathbf{E} (42)
- F magnitude of incident flux in arbitrary units (70)
- \mathbf{F}_0 dimensionless normalized Stokes vector for the incident flux (71)
- g van de Hulst absorption parameter (25)
- G factor used in radiation pressure efficiency (32)
- h geometric height above the lower boundary of a scattering atmosphere (93)
- \mathbf{H} magnetic field vector amplitude

- $i_j(m, x, \theta)$ dimensionless intensity parameters for Mie scattering (39,72)
 $\mathbf{I}(h; \mu, \varphi)$ Stokes vector for diffuse component in a scattering medium (77,93,99)
 $I^{(\Lambda)}$ unpolarized component of intensity vector of a partially polarized stream (60)
 $I^{(\Pi)}$ polarized component of the foregoing (60)
 I_1, I_2, U, V modified set of Stokes parameters (65)
 j subscript ($j = 1, 2, 3, 4$) denoting the elements in the Stokes scattering matrix (75,76)
 \mathbf{J} Stokes vector for the source function (93)
 k free-space propagation constant $2\pi/\lambda$ (1,2)
 $K(x, m)$ normalized Mie cross section or efficiency factor per particle for extinction, scattering, or absorption, as denoted by subscripts (5,6)
 $K_{\text{ex}}(\rho, m)$ van de Hulst extinction efficiency factor for an almost transparent sphere (25)
 $K_b(m, x)$ normalized backscattering cross section or efficiency per particle (35)
 m complex index of refraction with respect to free space (10,11)
 $n(r), n(x)$ differential size-distribution function (79,82)
 N number concentration of all particles per unit volume (79)
 \mathbf{N} Poynting vector for electromagnetic radiation
 p real part of mx (21)
 $P_j(\theta)$ elements of normalized phase function for a polydispersion (75,76)
 $\mathbf{P}(\theta)$ normalized phase matrix for a polydispersion (76)
 q imaginary part of mx (21)
 Q primitive Stokes parameter for the difference $I_1 - I_2$ (58b)
 r geometrical radius of a scattering sphere
 r_c mode radius of size distribution (85)
 r_1, r_2 complex amplitudes for Fresnel reflection (30)
 R, M subscripts denoting Rayleigh and Mie components, respectively, in a mixed atmosphere (101)
 S_1, S_2 dimensionless components of Mie scattering complex amplitudes (1,2)
 V_p volume occupied by particles per unit volume of space (87), (Table 5)
 $w_n(x)$ recurring function used in generation of Mie coefficients (15,16)
 W integrated Fresnel reflection on a sphere (31)
 x dimensionless Mie size parameter kr

- y dimensionless complex argument mx of function A_n (10,11)
 z arbitrary argument, real or complex, of a function (12)
 α constant in the size-distribution function (82,85)
 β angle determining the ratio of minor to major axis of the polarization ellipse (51,58)
 $\beta[\lambda, n(x)]$ volume cross section for extinction, scattering, or absorption (indicated by subscripts) for a polydispersion (78,80)
 γ constant in the size-distribution function (82,85)
 γ_b bulk absorption coefficient per unit mass of substance (Table 6, Table 8)
 γ_{sc} scattering absorption coefficient per unit mass of particles (Table 8)
 Γ gamma function of mathematical analysis (83)
 δ phase difference between two harmonic oscillators (42,43)
 Δ small finite element of a quantity (40)
 θ scattering angle between the incident and scattered streams (Fig. 19)
 κ imaginary part of the complex index of refraction m (23)
 λ free-space wavelength of electromagnetic radiation
 μ cosine of the scattering angle (7); also, length unit equivalent to 10^{-6} m
 μ_0, μ cosines of the local zenith angle for incident and diffuse radiation in a planetary atmosphere (97)
 ν real part of the complex index of refraction m (23)
 ξ, η orthogonal coordinates along the major and minor axes of the polarization ellipse (44), (Fig. 19)
 $\pi_n(\theta)$ angle-dependent coefficient in Mie series (7,8)
 Π degree of partial polarization of a stream (61)
 ρ van de Hulst's normalized size parameter $2x(\nu - 1)$ (25)
 $\sigma(m, x)$ true cross section per particle for extinction, scattering, or absorption, as denoted by subscripts (4)
 $\sigma_b(m, x)$ true backscattering or radar cross section per particle (33,111)
 $\sigma(\theta)$ scattering matrix for a single particle (41)
 $\sigma_j(\theta)$ elements of the scattering matrix for a single particle (41,63,72)
 $\tau(h)$ local optical thickness in a scattering atmosphere (96)
 τ_1 total optical thickness of a scattering atmosphere (99)
 $\tau_n(\theta)$ angle-dependent coefficient in Mie series (7,8)
 φ, φ' angles of incidence and refraction in Fresnel reflection (30); also azimuths in a plane-parallel planetary atmosphere (93,97)

- χ angle formed by the axes of the polarization ellipse with a reference system of coordinates (41), (Fig. 19)
- ψ phase angle of harmonic oscillator (42)
- ω angular frequency of electromagnetic oscillation (42)
- $d\omega$ elementary solid angle for scattering on a volume element at a point in space (97)
- Ω solid angle 4π of all space around a point (97)
- ϖ albedo of single scattering for a single particle or for a polydispersion (95)

PART I
POLYDISPERSE SCATTERING
AND ITS APPLICATIONS

Chapter I Introduction

1.1 MOTIVATION

With the appearance in 1957 of H. C. van de Hulst's authoritative treatise *Light Scattering by Small Particles* [1], the subject of electromagnetic scattering on homogeneous particles was put in proper perspective in relation to many current problems in astrophysics, geophysics, and radio propagation. Indeed, if one considers the properties of *single particles or aggregates of identical particles*, there is very little one can add to van de Hulst's comprehensive and well-knit discussion of the subject, except to check numerically some of the elegant analytical approximations derived by that author and others before him.

Now any interested observer who has followed Minnaert's delightful book *Light and Colour in the Open Air* [2] and become aware of the diverse and wondrous optical phenomena offered by nature to the naked eye, will find that most of these phenomena are seldom, if ever, caused by the presence of identical particles in the atmosphere. If they were, the daylight sky would be replete with colored rings around the sun and the antisolar point, of varying hues, brightness, and polarizations. Instead, one observes gradual changes of these things over the sky, depending on its optical condition. Only under special conditions, when, for example, the beautiful coronas around the moon and sun make their appearance, can one state that the responsible particles are almost identical.

When neither the shape, size, nor constitution of the scattering particles in a medium is uniform, we speak of a *polydispersed suspension* as distinguished from a *monodispersed* one. Both these terms are accepted usage

in colloid chemistry, although etymologically they derive from the classical concept of light dispersion by a prism. In what follows the terms *polydispersed* and *polydispersion* will be adopted in a slightly stricter sense, that is, to mean a suspension of scattering particles uniform in physical constitution and shape but *varying in number concentration depending on the size*.

Our motivation in compiling this monograph then is a rather modest one: On the basis of the so-called Mie theory [3], and armed with a modern digital computer, we shall produce a set of tables listing the scattering parameters characteristic of polydispersions likely to be found in the terrestrial and planetary atmospheres and perhaps also in interplanetary and interstellar space. We shall restrict ourselves to spherical particles only, and to continuous size distributions. Even with these restrictions our aim is by no means that of a complete catalogue of models. We wish rather to provide a few well-chosen examples as guides to the researcher in identifying the types of scattering media likely to serve his needs. In this we are guided by aesthetic considerations as well as by the principles of consistency and economy. The usefulness of the tables will, we hope, become apparent in the description and commentary on the tables in the following chapters.

A word about the uses of the Mie theory is in order. It was initially developed on the basis of Maxwell's electromagnetic theory as a natural continuation of Tyndal's well-known investigations on chemical suspensions. Its results have been amply used in *colloid research*, where the suspensions are composed of almost identical particles with a *narrow* size distribution. In atmospheric suspensions, however, the distributions are wide, and they can seldom be reproduced in the laboratory both as to the type of distribution function and the shape and physical and chemical characteristics of the individual particles. As to the shape factor, so far only the spherical and homogeneous case can be described completely by the theory, with some limited extensions into the theory of concentric spheres and prolate and oblate spheroids. The finite cylinder and regular prism cases are nowhere near a complete solution.

Nevertheless, we believe that a thorough investigation into the properties of spherical particle polydispersions is well worthwhile, not only because of the aesthetic appeal and reliability of the theory, but also because an important class of atmospheric suspensions, namely, water-droplet fogs and clouds, does consist of homogeneous spherical particles. Another important class, that of ice-crystal clouds, cannot be exactly modeled, but the spherical case may still be used as a standard, and observed deviations

may be interpreted by comparison to and in terms of the standard case. As for fine particles, such as upper atmospheric dusts, the shape factor is not of great importance. After all, the analytical student of nature by inclination has always preferred an idealized—but well understood—model to one that reproduces every detail. Lord Rayleigh's first insights in his elegant interpretation of the blue color of the sky [4] did not involve the shape of the particles but only their volume. His later refinement in terms of spherical particles [5,6] gave the same results with more work, but somehow it is not as appealing as the first, very simple, theory.

Today, with the availability of high-speed computers, the Mie theory, which is *the* analytical solution of a classical field problem, becomes in a certain sense an idealized experimental tool. That is, it may be used to simulate scattering aggregates with characteristics often impossible to reproduce in the laboratory but likely to exist, say, in space particles or those to be found on the Moon's surface. We are almost tempted to say "forbidden" characteristics, in imitation of the upper-atmospheric physicist's use of "forbidden lines" to describe transitions that cannot be induced in the laboratory.

1.2 BRIEF HISTORY

Since our aim is to make available a source book rather than a treatise on the subject, no comprehensive review of the literature or state of the art will be given. Van de Hulst [1] in his introduction has succinctly reviewed the development of the theory of light scattering on single particles. An excellent review of unsolved scattering problems from the point of view of electromagnetic theory alone, including scattering on nonspherical and inhomogeneous particles, was given by Twersky [7].

The author, acting on a suggestion by Z. Sekera, first became interested in problems of scattering in polydispersed media in connection with the theory of the skylight aureole around the Sun [8,9,10]. The white, featureless aureole cannot be explained by monodisperse scattering, as was already recognized by other investigators. Upon attempting further work in the scattering properties of polydispersions such as clouds and hazes [11,12], the author found that analytical approximations and interpolations of even the extinction cross sections for spheres gave insufficient accuracy for a good estimate of the volume extinction coefficient and albedo of single scattering of the aggregate. This led to the development of a computer program based on the complete Mie solution for spheres of

arbitrary size and a complex index of refraction, incorporating an integrating technique with respect to prescribed, continuous size-distribution functions. Initial and encouraging results, as applied to distributions containing particles as large as actual cloud droplets, demonstrated the capabilities of the technique and were first presented at a 1961 international conference on atmospheric radiation [13]. Similar work related to the zodiacal particles was published the same year by Giese [14]. Some of our results were first published in the proceedings of a conference [15, p. 171], and some tables of angular scattering functions appeared only recently [16].

In the meantime we have been accumulating numerical data connected with various scattering problems as these arose in the course of our current research interests at The RAND Corporation. The real object, of course, was to have a set of models ready for use if and when a complete solution of the radiative transfer problem for planetary atmospheres of arbitrary scattering properties became available in a form suitable to numerical solution. In that case it was planned to integrate the two programs into one, and possibly also to attempt the solution of and to devise a program for the corresponding inverse problems.

Because of its inherent mathematical difficulties, the complete solution of the general problem is not yet available and it may take some time before it can be achieved in practical form. It was therefore decided to publish all our results on polydispersed media under one cover and in usable form, in order to bring them to the attention of other workers in the field who might find them useful. We have increased the initial number of distribution models, having in mind particularly terrestrial water-droplet clouds, hazes as well as rain (irradiated by microwaves). We have also modified some of the indices of refraction in the light of more recent data, and have introduced other materials, such as clays, silicates, and iron, in order to obtain a selective yet fairly representative catalogue of theoretical scattering functions for polydispersions likely to be found in the terrestrial and planetary atmospheres and in space.

1.3 GENERAL ORGANIZATION OF THE MONOGRAPH

This work is divided into two parts, with Part II devoted to the main numerical tables. Part I is intended as an introduction to the computation, significance, and use of the tables. All important equations and expressions are numbered *consecutively* in parentheses, regardless of chapter or section number, for ease of reference.

In particular, in Chapter 2, we discuss the specific form of the Mie expressions used to compute the *single-particle* scattering parameters. We describe some features of the various related functions, avoiding duplication of already published material whenever possible, and using our own results. In discussing and comparing these with other work and in order to conserve space, we make frequent reference to van de Hulst's book [1] and his adaptation of other authors' original results, which he meticulously cites. We beg these authors' indulgence for not citing them directly here. In reproducing some of the auxiliary functions in graphical form, we admit to yielding to their aesthetic appeal quite apart from practical considerations.

In Chapter 3 we define the phase-matrix parameters, the absorption and scattering coefficients, and the albedo of single scattering for single particles and for polydispersions, and illustrate their use. The general form of the size-distribution function and the particular cases actually used are also set forth by means of equations and graphs, and their use is justified by comparison with available experimental data. The numerical integration is explained and justified on the basis of examples of the convergence of the integrals for the various parameters.

Finally, in Chapter 4 we give some examples of the uses of the tables presented in Part II and discuss their application to problems in atmospheric aerosol research; abnormal atmospheric turbid layers, such as volcanic ashes and forest fire smokes; mother-of-pearl and noctilucent clouds; radar cross section of precipitation and clouds; material in the Martian surface and atmosphere; the atmosphere of Venus; interplanetary and interstellar dust; and so forth. Much of the discussion and ideas are based on heretofore unpublished material by the author, which may become the subject of future, more detailed papers or proposals for space experiments. We hope that the reader will find a nucleus for other interesting ideas in what follows.

One important use of the tables deserves particular attention. This has to do with the so-called inverse problem of deducing the optical thickness and composition of a sunlit planetary atmosphere from its phase-dependent brightness and polarization at different wavelengths. Were a reliable and unique mathematical solution of this problem to be found, it would yield data essentially on the nature of the angular phase function, the particle density, and the albedo of single scattering for a representative sample of the medium. As we shall see in Chapter 4, this kind of information by itself is insufficient to identify the chemical composition, size range, and shape of the polydisperse particles it contains. With the help of other

pertinent criteria, the present tables should then be useful at least in choosing the most likely candidates among the innumerable possibilities.

A similar inverse problem arises in the interpretation of spectral features observed in the sunlight reflected from planetary atmospheres, in terms of the relative abundance of the responsible constituent. This problem has been discussed recently by Chamberlain [17], who also investigated a simple case with isotropic scattering and emphasized the importance of scattering on the formation of weak and strong bands in the spectrum of the main gaseous medium. In the case of water droplets, for example, our tables show the effect of weak and strong bands *within the material of the scatterers themselves* on the albedo of single scattering of the polydispersion. This information, together with the pronounced angular anisotropy, is of prime importance in interpreting planetary spectra with respect, say, to water content, since the centers of the *water-vapor* and *liquid water* bands do not coincide exactly, but often overlap. With this problem in mind, we have therefore chosen certain wavelengths in both weak and strong absorption regions. Clearly, a more complete understanding of reflected spectra in this area may also lead to important practical applications to the determination of the water content of the cloudy terrestrial atmosphere by means of satellite-borne spectrometry.

Chapter 2 Scattering on Single Particles

2.1 VARIOUS APPROXIMATIONS

Since the present monograph is not intended as a didactic or historical review of the subject, we shall merely mention some of the pertinent approximations to the single-particle scattering problem. For a more complete exposition and discussion, the interested reader is referred to van de Hulst's treatise [1] and his rather complete bibliography.

2.1.1 Rayleigh Approximation

This well-known approximation, dating from 1871 [4], is restricted to the case where the size* $x \ll 1$, that is, to particles that are very small compared to the wavelength of the incident field. Although originally only dielectric particles were considered, it has since been shown that the Rayleigh expressions apply for arbitrary m , real or complex. In the latter case whenever $|m|$ is large we have the additional condition $|mx| \ll 1$ whereby the size restriction becomes more stringent.

The Rayleigh formulation is best suited to scattering by nonpolar, idealized gas molecules, and in particular to atmospheric scattering problems whenever these assumptions may be invoked (cf. Sekera [18]). We note, however, that even gas molecules are not, strictly speaking, homogeneous and isotropic scatterers, and corrections to the Rayleigh expressions must be introduced in this case [19].

Another use of the Rayleigh approximation is in estimating the intensity

* For reasons of economy and clarity we do not define symbols unless essential, and the reader is referred to the Glossary of Symbols.

of the radar echo from water drops in clouds and precipitation, where the assumption of strictly homogeneous spheres is more nearly valid. However, care must be exercised in the case of large raindrops, where, because of the large value of $|m|$ for water in the microwave region, deviations from the Rayleigh cross section become appreciable.

2.12 Rayleigh-Gans Approximation

This can be used for somewhat larger spheres, provided their properties do not differ appreciably from those of the surrounding medium. The conditions are that both $|m - 1|$ and $2x|m - 1|$ must be small. The Rayleigh-Gans approximation has proved most useful in considering nonspherical but otherwise symmetrical scatterers, including nonhomogeneous particles.

2.13 Van de Hulst's Approximation

This represents a remarkable advance for spheres of arbitrary size but with $|m| \rightarrow 1$, first developed by van de Hulst in his doctoral thesis and described in Chapter 11 of his treatise [1]. He follows the tradition of Christian Huygens and his famous principle, clearly combining conceptualized physical principles with classical mathematical analysis to arrive at important results. It is most successful in estimating the scattering and absorption cross sections of transparent spheres and even weakly absorbing ones, of a size comparable to the wavelength and larger. Comparison with numerical results derived from the exact theory have demonstrated the power of this approach, especially when a high degree of accuracy is not essential [12].

Difficulties arise in the case when $|m - 1|$ is not small enough and the precise directional scattering pattern and polarizing properties are desired. Indeed, high accuracy could hardly be expected here when the interaction of *all* components of the electromagnetic field disturbance produced by the sphere must be correctly taken into account, rather than only a phase disturbance in the interior.

2.14 Other Approximations

In the case of very large spheres ($x \rightarrow \infty$) geometrical optics may be used to estimate the scattered field, that is, one may trace *rays* of light by the classical laws of refraction and reflection at the interface. Examples are the explanation of the rainbow and halos [2]. The combination of geometrical optics with diffraction theory (cf. Bricard [20]) increases the realm of applicability, particularly in the case of forward scattering and of reflection on

“hard” spheres, where the rays cannot penetrate the interior. The latter case, however, where $m = \infty$ is assumed, is an idealized one hardly to be found in nature. As will be shown later, the scattering properties of spheres with large but finite indices of refraction show considerable deviation from the idealized case of a totally reflecting sphere.

2.15 The Mie Solution

This was obtained by Mie [3] by applying the Maxwellian electromagnetic field theory to the problem of a homogeneous sphere irradiated by plane waves from a single direction. The method consists in expressing the incident field in terms of spherical waves centered at the sphere, fitting the appropriate boundary conditions, and solving the differential equation for the vector amplitude of the resultant field both at the surface of the sphere and at infinite distance, the so-called radiation approximation. As such, it is *the* analytical solution of the problem, in the strictest sense, since it uses a formal theory and classical mathematical analysis for an idealized sphere, in the best tradition [21]. A natural cloud droplet, for example, obviously is not a perfectly homogeneous sphere with a simple discontinuity of m at the surface going from one constant value to another. The droplet has a “skin” caused by surface tension, and at the surface itself there must be a narrow transition region where H_2O molecules are in equilibrium between the condensed and gaseous states. Since it is practically impossible to measure accurately in the laboratory the scattered field of a real, isolated water sphere, it is difficult to judge the accuracy of the Mie theory in describing light scattering on natural water drops.

For the purposes of scattering research, both in colloidal suspensions and in the atmosphere, the Mie solution has proved to be the most successful, including as it does the simpler approximations for both very small and very large particles. Since the modern computer has such an enormous capacity, there is no *practical* reason for further improving these approximations, which have already served their purpose. We believe that the extensive use of automatic computers in a judicious application of the Mie theory should not diminish its appeal as an analytical tool of research.

Derivations of the Mie solution, besides the original work [3], have been described by others, notably by Stratton [22] and by van de Hulst [7]. One of the best derivations in terms of modern notation, completeness, elegance, and clarity was given by D. S. Saxon in an unpublished report.*

* D. S. Saxon, *Lectures on the Scattering of Light*, Scientific Report No. 9, Contract AF 19(122)-239, Department of Meteorology, University of California, Los Angeles (1955), 100 pp.

Among the very first extensive tables of Mie functions are the so-called Lowan's tables [23], which were actually prepared under the late G. N. Lowan's supervision following recommendations and work by V. K. La Mer and David Sinclair. These tables, which are preceded by an excellent foreword by J. A. Stratton sketching the history of the theory, have stood the test of time in that they show a very high standard of accuracy, considering the hand-computing labor that must have been involved at the time.

For the sake of consistency with our own previously published results [16], we shall adopt essentially van de Hulst's definitions and his adaptation of the Mie expressions, as well as his notation, with minor exceptions. The reader can thus easily identify and compare our results, when appropriate, with the contents of the treatise [1]. Other authors' results may also be compared with ours on the basis of the explicit forms of the expressions shown in the following. Unless otherwise specified, all examples, graphs, and tables are based on our own numerical results.

2.2 THE BASIC MIE FUNCTIONS

The Mie problem is formulated in terms of the following basic parameters: a dimensionless size $x = kr$, where $k = 2\pi/\lambda$ is the free-space propagation constant and r is the radius of the sphere; a generally complex index of refraction of the substance of the sphere with respect to the outside medium (here assumed free space), written $m = \nu - \kappa i$; and a scattering angle θ determined by the forward direction of the incident waves, the scattering point, and the direction of observation. Generally we have set $m = 1$ for atmospheric air and we have assumed that the free-space wavelength λ is unaltered in air outside the particles. Fine corrections for the true index and wavelength for clear air of a given density are not necessary for our purposes, but must be allowed for by the reader when appropriate.

Assume the incident plane-wave radiation to be unpolarized so that the magnitude of the electric field can be represented by the sum of two mutually perpendicular and *independent* sinusoidal oscillations of unit amplitude in the xy plane, propagating in the z direction, each usually expressed in the form

$$E_{\text{inc}} = \exp[-i(kz - \omega t)]$$

where $\omega = ck$ is the circular frequency. When this field interacts with an *otherwise inactive homogeneous sphere* (i.e., a sphere composed of uncharged and unexcited matter, whose temperature is such that its Planck

emission is negligible at the given frequency), it will result in a scattered field in directions other than that of the incident field, plus the incident field itself, whose flux is diminished by the scattered energy and by the energy that is absorbed by the sphere but not *reemitted at the same or any other frequency*, as far as we are concerned here. Under these assumptions, and when we are interested only in the scattered *radiation* field, it may be expressed in terms of the two scalar components A_1 and A_2 , perpendicular and parallel, respectively, to the scattering plane (in which θ is measured) of the electric field vector amplitude \mathbf{A}_{sc} , which has no component in its direction of propagation. The results of Mie's solution [3; I, pp. 114–130] then provide the expressions for these amplitudes in the form of complex numbers given by a converging series, written

$$kA_1 \equiv S_1(m, x, \theta) = \sum_{n=1}^{\infty} \frac{2n+1}{n(n+1)} (a_n \pi_n + b_n \tau_n), \quad (1)$$

$$kA_2 \equiv S_2(m, x, \theta) = \sum_{n=1}^{\infty} \frac{2n+1}{n(n+1)} (b_n \pi_n + a_n \tau_n) \quad (2)$$

where S_1 and S_2 are dimensionless, complex amplitudes, and the n are positive integers; the other coefficients will be described later.

The meaning of the amplitudes A_1 and A_2 becomes clear when considering the energy fluxes produced by the scattering process. If one forms the Poynting vector \mathbf{N} for the incident and scattering fluxes, their ratio defines the *differential cross section* $d\sigma$ of the particle per unit solid angle, at distance R , so that

$$d\sigma(m, x, \theta) = \left| \frac{\mathbf{N}_{sc}}{\mathbf{N}_{in}} \right| R^2 d\omega$$

where

$$\mathbf{N} = \frac{1}{2} \text{Re}\{\mathbf{E} \times \mathbf{H}\}$$

is the time-averaged power flow for each field and \mathbf{H} is the magnetic field amplitude. By using the Maxwellian theory and considering the R^{-1} dependence of the amplitude of the spherical wave, it can be shown (see Section 3.22) that the differential cross section for *unit incident flux* reduces to

$$d\sigma(m, x, \theta) = \frac{1}{2} \mathbf{A}_{sc} \cdot \mathbf{A}_{sc}^*(m, x, \theta) d\omega. \quad (3)$$

Considering unpolarized incident radiation expressed as the sum of two independent and linearly polarized components of equal flux, it can finally be shown that [9]

$$\sigma_{sc}(m, x) = \int_{\Omega} d\sigma(m, x, \theta) = \frac{1}{2} \int_{\Omega} (A_1 A_1^* + A_2 A_2^*) d\omega \quad (4)$$

where $d\omega$ is an element of the solid angle and the integral is over the solid angle $\Omega = 4\pi$ of all space around the particle. The total scattering cross section σ_{sc} has the dimensions of an area. It is thus clear that the amplitudes A_1 and A_2 in expressions (1) and (2) are *meant per unit incident flux* and they are also *independent of the system of electromagnetic units used*, since these will cancel out in taking the ratio of the scattered and incident fluxes.

The scattering cross section, when normalized by the geometrical cross section, defines the dimensionless parameter

$$K_{sc}(m, x) = \sigma_{sc}(m, x)/\pi r^2,$$

(called the scattering efficiency factor Q_{sc} by van de Hulst [1]), in which case the integration (4) of the amplitudes (1) and (2) yields

$$K_{sc}(m, x) = \frac{2}{x^2} \sum_{n=1}^{\infty} (2n+1)(|a_n|^2 + |b_n|^2). \quad (5)$$

Similarly, we can define a total *extinction* cross section and efficiency factor K_{cx} , which includes the absorption contribution and which, according to the *cross-section theorem* of quantum mechanics, called the *extinction theorem* by van de Hulst and derived by him independently (cf. [1, pp. 30, 39]), is given by

$$\begin{aligned} K_{cx}(m, x) &= \frac{4}{x^2} \operatorname{Re}\{S(m, x, 0)\} \\ &= \frac{2}{x^2} \sum_{n=1}^{\infty} (2n+1) \operatorname{Re}\{a_n + b_n\}. \end{aligned} \quad (6)$$

Under the foregoing assumptions, the expressions (1), (2), (5), and (6) define the *basic Mie scattering parameters* from which all the other parameters needed to describe the intensity and polarization produced by a single particle can be derived. It will be seen that they also provide the necessary information for a representative volume of a polydispersed medium, and hence the fundamental parameters in the formulation of the radiative transfer problem in an extended medium composed of such particles.

2.21 Adaptation of Mie Expressions to Machine Computation

The evaluation of the basic functions hinges on the accurate computation of the Mie coefficients a_n , b_n , which are functions of m and x only, and of

the angular coefficients π_n and τ_n , which are functions of $\mu = \cos \theta$ only. The latter present no problems since they are defined in terms of Legendre polynomials and their derivatives, that is [1, p. 124],

$$\begin{aligned}\pi_n(\mu) &= \frac{d}{d\mu} P_n(\mu), \\ \tau_n(\mu) &= \mu \pi_n(\mu) - (1 - \mu^2) \frac{d}{d\mu} \pi_n(\mu), \quad -1 \leq \mu \leq 1,\end{aligned}\tag{7}$$

where

$$P_n(\mu) = \frac{1}{2^n n!} \frac{d^n}{d\mu^n} (\mu^2 - 1)^n$$

is the Legendre polynomial or coefficient of integer order n and real argument. By using the well-known recurrence relations between these polynomials and their derivatives it is easy to show that the coefficients (7) can also be generated by their own recursion, without reference to the Legendre polynomials per se. Thus we have

$$\begin{aligned}\pi_n(\theta) &= \cos \theta \frac{2n-1}{n-1} \pi_{n-1}(\theta) - \frac{1}{n-1} \pi_{n-2}(\theta), \\ \tau_n(\theta) &= \cos \theta [\pi_n(\theta) - \pi_{n-2}(\theta)] - (2n-1) \sin^2 \theta \pi_{n-1}(\theta) + \tau_{n-2}(\theta),\end{aligned}\tag{8}$$

$0 \leq \theta \leq \pi,$

with

$$\begin{aligned}\pi_0(\theta) &= 0, & \tau_0(\theta) &= 0, \\ \pi_1(\theta) &= 1, & \tau_1(\theta) &= \cos \theta, \\ \pi_2(\theta) &= 3 \cos \theta, & \tau_2(\theta) &= 3 \cos 2\theta,\end{aligned}$$

which can be easily programmed for machine computation. In passing, we note that in the exact forward ($\theta = 0$) and backward ($\theta = \pi$) directions, these coefficients reduce to

$$\begin{aligned}\pi_n(0) &= \tau_n(0) = \frac{n(n+1)}{2}, \\ -\pi_n(\pi) &= \tau_n(\pi) = (-1)^n \frac{n(n+1)}{2}.\end{aligned}\tag{9}$$

For example, using the first set of values in either (1) or (2), we see that $S_1(0) = S_2(0)$ and the cross-section theorem and its explicit form in (6) are immediately verified in the Mie formulation.

To adapt the coefficients a_n and b_n to computational form, we start with the Mie expressions adopted by van de Hulst [1, p. 123], written in the form

$$a_n = \frac{A_n(y)\psi_n(x) - m\psi'_n(x)}{A_n(y)\zeta_n(x) - m\zeta'_n(x)}, \quad (10)$$

$$b_n = \frac{mA_n(y)\psi_n(x) - \psi'_n(x)}{mA_n(y)\zeta_n(x) - \zeta'_n(x)}, \quad (11)$$

where the *Ricatti-Bessel functions* $\psi_n(x)$ and $\zeta_n(x)$ on the right-hand side can be written in terms of Bessel functions of the first kind of order $(n + \frac{1}{2})$ by using the definitions of spherical Bessel functions [1, p. 123; 24, pp. 52–54] as follows:

$$\begin{aligned} \psi_n(z) &= \sqrt{\frac{\pi z}{2}} J_{n+1/2}(z), \\ \zeta_n(z) &= \sqrt{\frac{\pi z}{2}} [J_{n+1/2}(z) - iN_{n+1/2}(z)] \\ &= \sqrt{\frac{\pi z}{2}} [J_{n+1/2}(z) + (-1)^n iJ_{-n-1/2}(z)]. \end{aligned} \quad (12)$$

In (10) and (11) we have further put

$$A_n(y) \equiv \frac{\psi'_n(y)}{\psi_n(y)}, \quad y \equiv mx,$$

to separate the functions with argument y from those with argument x . Whenever the index of refraction m is complex (absorbing spheres), the function $A_n(y)$ depends on Bessel functions of complex argument. The primed symbols indicate differentiation with respect to the argument.

Using the recursion formulas [24, p. 45] for Bessel functions of arbitrary order and argument, it can be shown that

$$\begin{aligned} \psi'_n(x) &\equiv \frac{d}{dx} \left[\sqrt{\frac{\pi x}{2}} J_{n+1/2}(x) \right] = \sqrt{\frac{\pi x}{2}} \left[J_{n-1/2}(x) - \frac{n}{x} J_{n+1/2}(x) \right], \\ \frac{d}{dx} \left[\sqrt{\frac{\pi x}{2}} J_{-n-1/2}(x) \right] &= -\sqrt{\frac{\pi x}{2}} \left[J_{-n+1/2}(x) + \frac{n}{x} J_{-n-1/2}(x) \right], \end{aligned}$$

and

$$\begin{aligned} \zeta'_n(x) &= \sqrt{\frac{\pi x}{2}} \left\{ J_{n-1/2}(x) - \frac{n}{x} J_{n+1/2}(x) \right. \\ &\quad \left. - (-1)^n i \left[J_{-n+1/2}(x) + \frac{n}{x} J_{-n-1/2}(x) \right] \right\}. \end{aligned}$$

Substituting these expressions into (10) and (11), collecting terms, and simplifying, we get

$$a_n(m, x) = \left\{ \left[\frac{A_n(y)}{m} + \frac{n}{x} \right] J_{n+1/2}(x) - J_{n-1/2}(x) \right\} \\ \times \left\{ \left[\frac{A_n(y)}{m} + \frac{n}{x} \right] [J_{n+1/2}(x) + (-1)^n i J_{-n-1/2}(x)] \right. \\ \left. - [J_{n-1/2}(x) - (-1)^n i J_{-n+1/2}(x)] \right\}^{-1} \quad (13)$$

and

$$b_n(m, x) = \left\{ \left[m A_n(y) + \frac{n}{x} \right] J_{n+1/2}(x) - J_{n-1/2}(x) \right\} \\ \times \left\{ \left[m A_n(y) + \frac{n}{x} \right] [J_{n+1/2}(x) + (-1)^n i J_{-n-1/2}(x)] \right. \\ \left. - [J_{n-1/2}(x) - (-1)^n i J_{-n+1/2}(x)] \right\}^{-1}. \quad (14)$$

The expressions (13) and (14) are seen to be almost identical except for the factor attached to the function $A_n(y)$.

The Bessel functions of real argument appearing in (13) and (14) can be further expressed in terms of circular functions by defining the recurring function

$$w_n(x) = \frac{2n-1}{x} w_{n-1}(x) - w_{n-2}(x) \quad (15)$$

with

$$w_0(x) = \sin x - i \cos x = \sqrt{\frac{\pi x}{2}} [J_{1/2}(x) + i J_{-1/2}(x)],$$

$$w_{-1}(x) = \cos x - i \sin x = \sqrt{\frac{\pi x}{2}} [J_{-1/2}(x) - i J_{1/2}(x)].$$

We can then verify, for example, that

$$w_1(x) = \frac{w_0(x)}{x} - w_{-1}(x) \\ = \sqrt{\frac{\pi x}{2}} [J_{3/2}(x) - i J_{-3/2}(x)], \\ w_2(x) = \frac{3}{x} w_1(x) - w_0(x) \\ = \sqrt{\frac{\pi x}{2}} [J_{5/2}(x) + i J_{-5/2}(x)],$$

and in general

$$w_n(x) = \sqrt{\frac{\pi x}{2}} [J_{n+1/2}(x) + (-1)^n i J_{-n-1/2}(x)], \quad (16)$$

according to the finite-term expansion of the functions $J_{n+1/2}(x)$ and $J_{-n-1/2}(x)$ [24, pp. 53, 54]. Comparing the function (16) with those in (13) and (14), and noting that the factor $(\pi x/2)^{1/2}$ is common to the numerators and denominators of both expressions, it is seen that the Mie coefficients may be written in the alternative form

$$a_n(m, x) = \frac{\left(\frac{A_n(y)}{m} + \frac{n}{x}\right) \operatorname{Re}\{w_n(x)\} - \operatorname{Re}\{w_{n-1}(x)\}}{\left(\frac{A_n(y)}{m} + \frac{n}{x}\right) w_n(x) - w_{n-1}(x)}, \quad (17)$$

$$b_n(m, x) = \frac{\left(m A_n(y) + \frac{n}{x}\right) \operatorname{Re}\{w_n(x)\} - \operatorname{Re}\{w_{n-1}(x)\}}{\left(m A_n(y) + \frac{n}{x}\right) w_n(x) - w_{n-1}(x)}. \quad (18)$$

Except for the coefficient $A_n(y)$, these are in a form suitable for machine computation with the help of the recursion formula (15). We note in passing that the function $w_n(x)$ is identical with the Riccati-Bessel function $\zeta_n(z)$ defined in (12), the argument being real in this case.

There remains the evaluation of the Bessel functions with complex argument involved in the factors containing $A_n(y)$. According to the definitions (12) of the Riccati-Bessel functions and their derivatives, and again using the properties of Bessel functions, we have, after simplification,

$$\begin{aligned} A_n(y) &= \frac{J_{n-1/2}(y) - \frac{n}{y} J_{n+1/2}(y)}{J_{n+1/2}(y)} \\ &= -\frac{n}{y} + \frac{J_{n-1/2}(y)}{J_{n+1/2}(y)}. \end{aligned} \quad (19)$$

This can be transformed into a recursion formula if we note that (omitting the argument for simplicity)

$$\begin{aligned} A_{n-1} &= -\frac{n-1}{y} + \frac{J_{n-3/2}}{J_{n-1/2}} \\ &= -\frac{n-1}{y} + \frac{[(2n-1)/y] J_{n-1/2} - J_{n+1/2}}{J_{n-1/2}}, \end{aligned}$$

or

$$\frac{J_{n+1/2}}{J_{n-1/2}} = \frac{n}{y} - A_{n-1}.$$

Substituting this into (19), we finally get

$$A_n(y) = -\frac{n}{y} + \left[\frac{n}{y} - A_{n-1}(y) \right]^{-1}, \quad (20)$$

which is in the form of a continued fraction. As a search of the pertinent mathematical literature reveals no practical reduction of this particular continued fraction to a form suitable for computation in the general case, we have had to rely on the recursion formula itself.

From the sequence (19) we note that

$$A_0(y) = \frac{J_{-1/2}(y)}{J_{1/2}(y)} = \cot y.$$

Putting $y \equiv mx = p - iq$, where $p = vx$ and $q = \kappa x$ with v and κ the real and imaginary parts of the index of refraction, respectively, this may be expressed in terms of circular and hyperbolic functions of real argument; after rationalization we have

$$A_0(y) = \frac{\sin p \cos p + i \sinh q \cosh q}{\sin^2 p + \sinh^2 q}. \quad (21)$$

This is the generating function actually used in combination with (20) to compute $A_n(y)$, $n = 1, 2, 3, \dots, \infty$. In passing we note from (21) that when m is real (nonabsorbing spheres), the imaginary parts of $A_0(y)$ and hence of all $A_n(y)$ vanish.

This completes the description of the computational form of the Mie expressions for the fundamental coefficients needed to obtain all pertinent scattering parameters.

2.22 Behavior of the Function $A_n(y)$

The behavior of $A_n(y)$ deserves some discussion because we have found that in certain cases it may give rise to errors if care is not taken in its exact computation. In fact, when using the recursion formulas of the previous section to obtain the scattering parameters for metallic spheres with $x > 30$, one gets physically impossible results such as $K_{ab} > K_{ex}$. The trouble may be traced to the accuracy of $A_n(y)$ when one uses the recursion formula (20) with "single precision," that is, with the normal number of significant figures in the computer.

To illustrate the difficulty let us consider iron spheres with $x = 62$ and $m = 1.28 - 1.37i$ ($\lambda 0.441 \mu$) that is, a radius of about 4.3μ . From the expression (21) for $A_0(y)$ it is easy to verify that in this case we may put $A_0(y) = i$ with a very high degree of accuracy. Upon using this

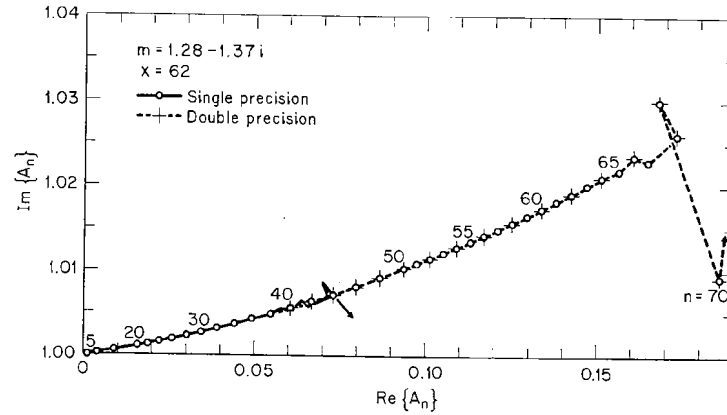


Fig. 1—Example of the complex function $A_n(y)$ for a large metallic sphere showing the accuracy of single- and double-precision routines.

generating function in the recursion formula, we note that $A_n(y)$ for small n is very near, but not quite equal to, $0 + i$, as shown in the accompanying

n	$\text{Re } \{A_n\}$	$\text{Im } \{A_n - i\}$
1	$7.4327 \cdot 10^{-5}$	$0.460 \cdot 10^{-5}$
5	$1.1148 \cdot 10^{-3}$	$0.0698 \cdot 10^{-3}$
10	$4.0871 \cdot 10^{-3}$	$0.26201 \cdot 10^{-3}$

table. It is seen that the computer cannot perform the complex arithmetic for the imaginary part with the same degree of accuracy as for the real part. These errors can thus accumulate and are eventually reflected in spurious oscillations in both parts of A_n as n increases, as well as in the values of a_n and b_n , resulting in significant errors in the basic Mie parameters. Figure 1 is a plot of A_n on the complex plane, where the solid line shows that oscillations begin for $n \geq 36$ in this case, when 8 decimal places are carried. The dashed extension of the curve shows that the trouble is

partly overcome when “double precision” is used in the program; that is, when the number of significant figures is doubled. Even then, however, rapidly increasing oscillations appear for $n \geq 64$. An analysis of differences in the real and imaginary parts of A_n as a function of n shows that small errors begin at about $n = 58$ and 51 , respectively. Second and third differences further indicate that the real part is a quadratic function of n and the imaginary part a cubic.

We have not pursued the numerical analysis further for the simple reason that double precision has proved sufficient to insure convergence of the main series in a_n and b_n for spheres large enough for our purposes. The mathematical problem itself is related to the asymptotic behavior of the Mie coefficients for large x when $n \simeq x$, originally investigated by Debye and discussed by van de Hulst [1, pp. 208 ff.]. The latter discussion is confined to real indices of refraction, however. In the metallic case, we have the problem of the ratio of two Bessel functions of large complex argument and large order of the form

$$\frac{J_\nu(y)}{J_{\nu+1}(y)}$$

where ν approaches $|y|$ from either direction. The asymptotic expansions found in Watson’s treatise [24, p. 244] may help in describing the approximate behavior of this ratio in the critical region, but there seems to be no practical way of making use of them in an exact machine program.

As seen in Fig. 1, $A_n(y)$ in the metallic case is a smooth monotonic function of n when plotted in the complex plane. In the case of moderately absorbing and nonabsorbing spheres, however, where no difficulties are found in the use of single precision with the recurrence formulas, this function shows large-amplitude oscillations. This is illustrated in Fig. 2, which shows plots of $A_n(y)$ for $x = 30$ and $m = 1.29 - 0.0472i$ on the complex plane. It is evident that if n were assumed to increase continuously (rather than by integers), a continuous curve could be made to pass through the points, as shown for $n > 20$, in the form of spiraling loops in the counterclockwise sense, of increasing amplitude with increasing n , finally “opening up” after $n > |y|$ to become a smooth curve in the positive part of the plane.

When the argument y is real, that is, when there is no absorption, $A_n(y)$ is real and its behavior as a function of n is similar to the foregoing, as shown in Fig. 3. Here we have plotted $A_n(y)$ for $m = 1.29$ and for $x = 30$, as well as the end portions for $x = 40$ and 50 . The large oscillations for $n < y$ are replaced by a monotonically increasing function that tends

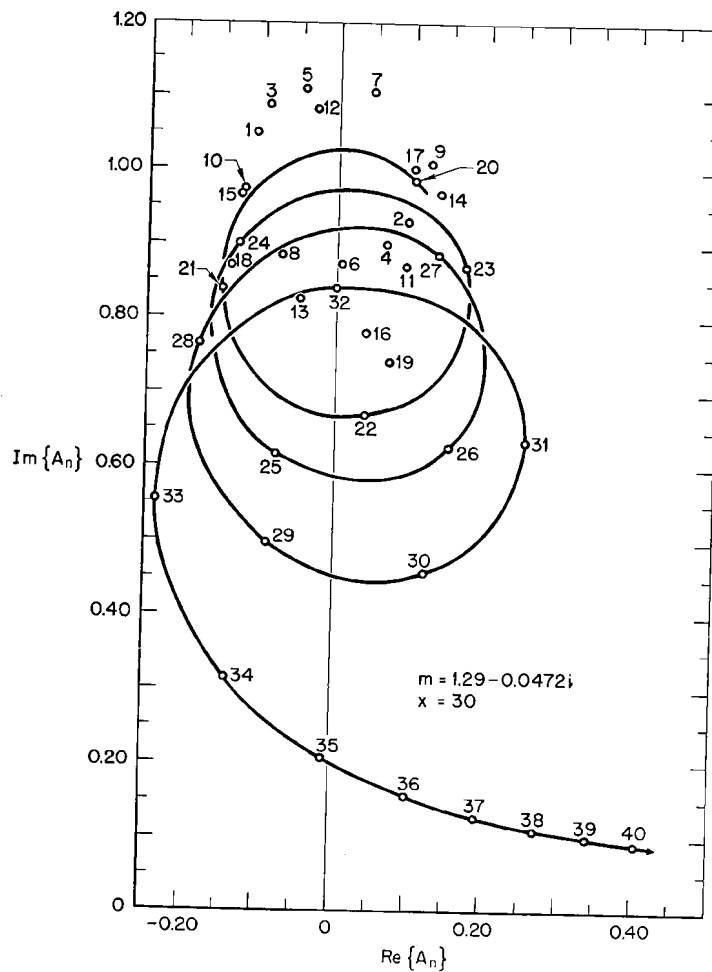


Fig. 2—Same as Fig. 1 for a dielectric sphere with moderate absorption. A continuous curve has been fitted through consecutive points with $n \geq 20$.

to a constant when $n \geq y$, a behavior related to a well-known property of Bessel functions of constant real argument and increasing order. We note in passing that the oscillations in the $n < y$ region are irregular and may become rather large since, according to (20),

$$A_n(y) \rightarrow \infty \quad \text{as} \quad \frac{n}{y} \rightarrow A_{n-1}(y).$$

Such conditions may actually be approached, but the values of the Mie coefficients themselves are apparently not affected because the factor with

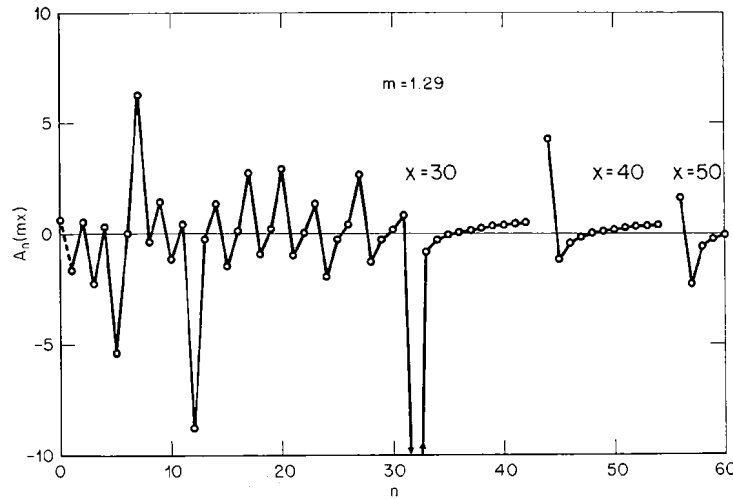


Fig. 3—The real function $A_n(y)$ for nonabsorbing dielectric spheres, with straight-line segments connecting the computed points.

$A_n(y)$ enters both numerator and denominator of expressions (17) and (18). For example, for $m = 1.29$ and $x = 46$ we find that $A_6(y) = 252.68$ but $a_6(m, x) = 0.38735 + 0.48715i$ and $b_6(m, x) = 0.38539 + 0.48669i$, both of which fall exactly on the proper circle in the complex plane (see Section 2.31, and Fig. 4).

Summarizing this section, we have found that an adequate computer program adapted to a modern electronic data-processing system should in principle encounter no difficulty with the Mie coefficients for nonabsorbing spheres of unlimited size. One might infer that in this case the modern computer eliminates Debye's problem, as shown for example in a note by

Querfeld [25], who obtained scattering functions for $x \simeq 8000$ and for m real. For large absorbing spheres, however, a problem akin to Debye's remains, and in our case, for example, using the IBM 7040/44 or a similar system, whenever $\text{Im}\{mx\} \geq 30$, one must use either double precision or some appropriate asymptotic formula in the critical regions of $n \rightarrow |mx|$; otherwise, physically unacceptable results may be obtained.

2.3 EXAMPLES OF SINGLE-PARTICLE SCATTERING PARAMETERS

Initial results related to scattering on single particles with partial absorption were described in an earlier paper [26] that was later amplified and corrected in two RAND Corporation publications of open but limited availability [27,28]. For the sake of completeness, we shall briefly review the earlier results, further amplified with the new material involved in the present work, and compare them with limiting approximations where appropriate.

2.3.1 The Mie Coefficients a_n and b_n

For nonabsorbing spheres of finite index of refraction, the coefficients a_n and b_n when plotted on the complex plane must always fall on a circle of radius 0.5 centered at the point (0.5, 0) on the real axis [1, p. 135]. This is equivalent to the conditions

$$|a_n - \tfrac{1}{2}|^2 = \tfrac{1}{4}, \quad |b_n - \tfrac{1}{2}|^2 = \tfrac{1}{4}, \quad (22)$$

which may serve as a good check on the accuracy of any computer scheme. If one plots, say, $a_1(x)$ for $m = 1.29$, as in Fig. 4a, it is seen that as x increases by constant increments, an imaginary generating point moving with variable "speed" traces the circle in the clockwise sense, as indicated by the labeled points.

The addition of a small imaginary part to the index of refraction results in a deviation from the circle spiraling inward, as indicated by the dashed and solid curves in Fig. 4a, corresponding to $a_1(x)$ and $b_1(x)$, respectively, when $m = 1.29 - 0.0472i$. Small counterclockwise loops eventually develop in these curves in precisely those regions of x where the generating point of the corresponding outer circle "slows down," so to speak, as seen in the vicinity of $x = 5, 7$, and 10 for $a_1(x)$. This feature may be related to the behavior of the corresponding function $A_n(y)$, but we have not looked into the matter further. A plot of $a_1(x)$ for $m = 2.22 - 0.022i$, as in Fig. 4b,

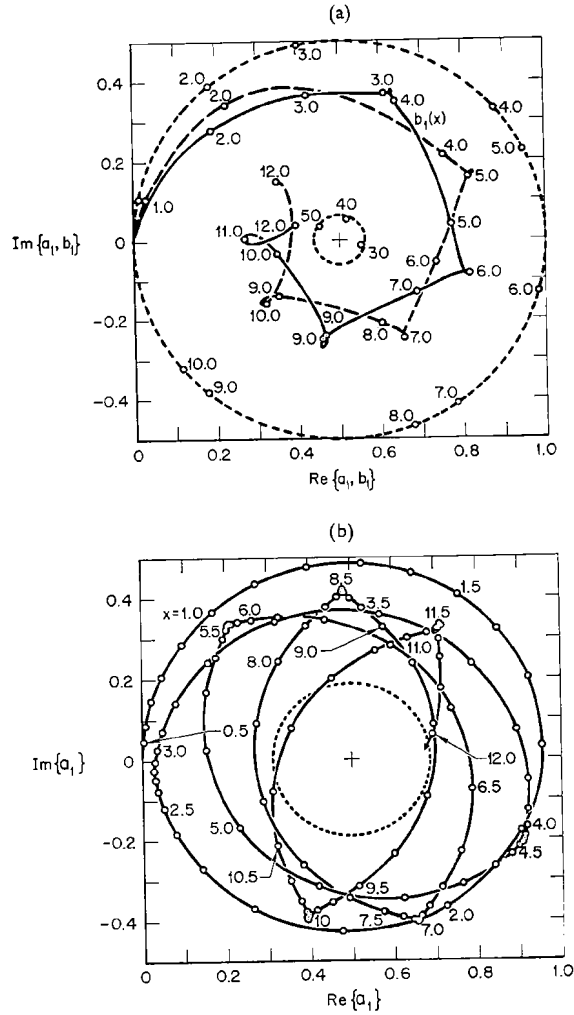


Fig. 4—Examples of the complex coefficients $a_1(x)$ and $b_1(x)$ plotted as a function of the x values indicated along the curves. (a) Outer circle (dotted line with radius 0.5): dielectric spheres with $m = 1.29$. Other curves: $a_1(x)$ (dashed line) and $b_1(x)$ (solid line) for spheres with $m = 1.29 - 0.0472i$. Radius of circle of convergence (dotted line) is $\frac{1}{2} |(m - 1)/(m + 1)| = 0.06415$. (b) $a_1(x)$ for spheres with $m = 2.22 - 0.022i$. Radius of circle of convergence (dotted line) = 0.1894.

produces another interesting pattern with regularly spaced cusps that develop into loops as x increases.

The behavior of the Mie coefficient for metallic spheres is illustrated in Fig. 5, where we have plotted $a_1(x)$ (solid line) and $b_1(x)$ (dashed line) for $m = 1.28 - 1.37i$ on the complex plane. The character of these curves is entirely different from the nonabsorbing and weakly absorbing cases. The

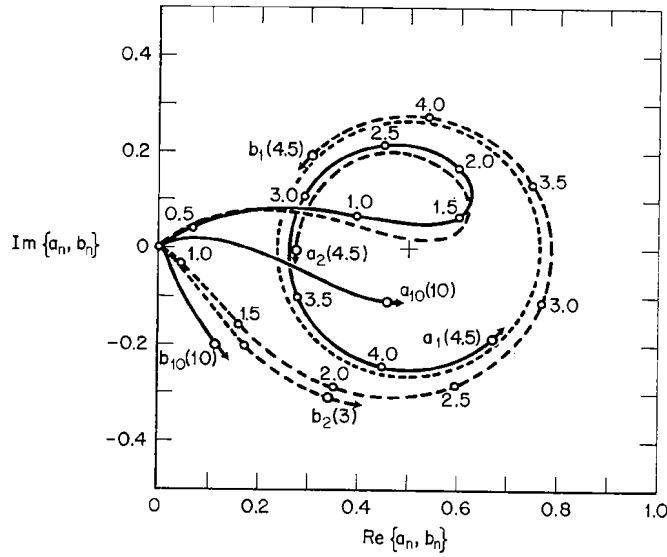


Fig. 5—Examples of $a_n(x)$ and $b_n(x)$ for metallic spheres with $m = 1.28 - 1.37i$. Radius of circle of convergence (dotted line) = 0.26285.

generating point of a_1 moves more evenly with x , forms a single loop, and then winds counterclockwise around a circle whose radius slowly increases toward an asymptotic value. The point for b_1 behaves similarly, except that the radius diminishes towards the same asymptotic value. According to van de Hulst [1, p. 279], this *circle of convergence* should have a radius given by one half the absolute value of the Fresnel reflection coefficient for the amplitude at perpendicular incidence, or (cf. expression (30) and Table 2 in Section 2.32)

$$\frac{1}{2} \left| \frac{m-1}{m+1} \right| = \frac{1}{2} \left[\frac{(v-1)^2 + \kappa^2}{(v+1)^2 + \kappa^2} \right]^{1/2}. \quad (23)$$

The position of the circle indicated in Fig. 5, which should have a radius of 0.26285, clearly demonstrates this tendency in the present example. Actually the convergence toward the circle is rather slow, as may be seen by comparing the sample values of $|a_1(x) - 0.5|^2$ and $|b_1(x) - 0.5|^2$, shown in the accompanying table, with the exact value 0.06909 of the square of the radius given by (23). The values for $x = 50, 72$ were obtained by

$$m = 1.28 - 1.37i$$

x	$a_1(x) - 0.5$	$b_1(x) - 0.5$	$ a_1(x) - 0.5 ^2$	$ b_1(x) - 0.5 ^2$
20	$-0.22686 - 0.12863i$	$0.22864 + 0.13377i$	0.06801	0.07017
30	$0.23619 - 0.11484i$	$-0.23678 + 0.11463i$	0.06898	0.06920
50	$-0.06537 + 0.25451i$	$0.06556 - 0.25462i$	0.06905	0.06913
72	$-0.06681 + 0.25418i$	$0.06690 - 0.25423i$	0.06907	0.06911

double precision. It is noteworthy that the deviations from the circle of convergence for a_1 and b_1 for a given x are almost equal and of opposite sign. Another interesting feature, not pointed out before, is that as x increases and the asymptotic circle is closely approached, a_1 and b_1 are almost exactly at diametric points with respect to the center of the circle.

In Fig. 5 we have also indicated part of the curves for the coefficients $a_n(x)$ and $b_n(x)$ for $n = 2$ and 10 to show that their loci are similar but not identical to those for $n = 1$. Thus we can make the following general statement: *for metallic spheres of finite size* and for sufficiently large x but with $n \leq x$, the points $a_n(x)$ always fall *within* the circle of convergence (defined in the foregoing); the points for $b_n(x)$ always fall *outside* this circle for all values of x and n . In the limit, provided $n/x \ll 1$, we also have

$$\begin{aligned} \lim_{x \rightarrow \infty} [a_n(x) + b_n(x)] &= 1, \\ \lim_{x \rightarrow \infty} |a_n(x) - \tfrac{1}{2}| &= \lim_{x \rightarrow \infty} |b_n(x) - \tfrac{1}{2}| = \frac{1}{2} \left| \frac{m-1}{m+1} \right|. \end{aligned} \quad (24)$$

Finally it appears that in the case of nonmetallic but moderately absorbing spheres, the a_n and b_n also tend to trace a circle of convergence as $x \rightarrow \infty$, as indicated in Fig. 4a by the points $a_1(x)$ for $x = 30, 40$, and 50 and the circle. The radius here is small, amounting to 0.06414, as given by (23) for $m = 1.29 - 0.0472i$. The limits (24) seem to apply to this case also, but they are approached more slowly. For example, for $x = 50$ we get $a_1 = 0.45160 + 0.03498i$ and $b_1 = 0.55511 - 0.04076i$. Similar remarks apply to the case shown in Fig. 4b.

2.32 The Extinction, Scattering, and Absorption Efficiencies

Once the principal Mie coefficients a_n and b_n are available, the easiest quantities to compute are the total scattering and extinction efficiencies, K_{sc} and K_{ex} , given respectively by the convergent series (5) and (6). The two efficiencies become identical for nonabsorbing spheres, and most earlier detailed computations published in the literature concern this case.

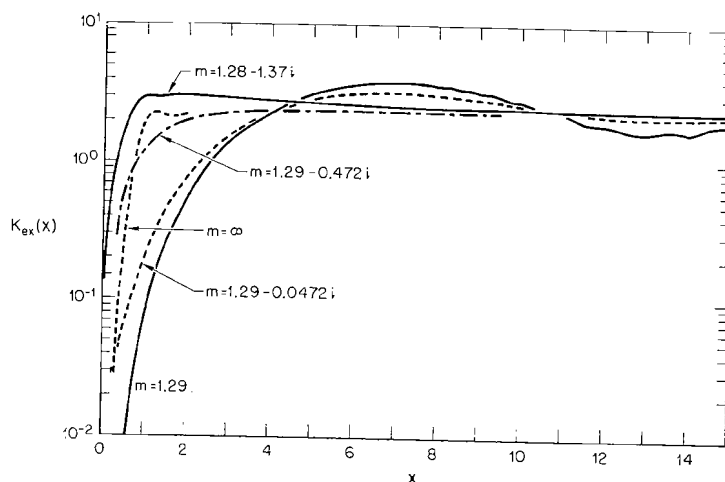


Fig. 6—The extinction efficiency $K_{ex}(m, x)$ for various types of spheres, shown in the range $0 \leq x \leq 15$.

Within the last decade, the number of computations of Mie efficiencies for single particles, including absorbing spheres, has increased considerably. It is impossible to give a complete bibliography of published and report material. A fairly complete bibliography on various Mie parameters computed up to about 1956 will be found in van de Hulst's treatise [1, pp. 167–169, 275]. For a more complete bibliography up to 1963, organized in convenient form, the reader is referred to a technical report by R. Penndorf [29], who is also the author of an early major computing program [30]. As to our own results, we have made available a number of tables of the complex amplitudes $S_1(0)$ and $S_1(\pi)$, and K_{sc} for various sizes and indices of refraction [27, 28]. From these, K_{ex} also is easily obtained by virtue of the cross-section theorem (6).

Figure 6 illustrates the behavior of the extinction efficiency as a function of x , when the real part of m is kept constant and the absorption is varied. The graphs are self-explanatory. The salient features are the considerable increase in the efficiency of the smaller particles as the absorption is increased and the damping of the maximum value occurring near $x = 7$. Also note the shift of this maximum toward a smaller size, corresponding to $x = 1.75$ as we pass to the metallic case $m = 1.28 - 137i$. A comparison with the curve for $m = \infty$ [I, p. 161] shows clearly that totally reflecting particles are not as efficient as metallic ones over a large range of sizes. Figure 6 may be compared with a similar one in a paper by Johnson and Terrell [31], who first pointed out these features (see also [I, p. 278]).

It should be mentioned here that when $|m - 1|$ is close to zero, the magnitude and broad features of the extinction efficiency can be approximated without the use of the Mie series. The complete theory was developed by van de Hulst in 1946 and is summarized in his book [I, Chapter 11]. The formulas of course are most successful for almost transparent spheres with very weak absorption. When the real and imaginary parts of m are finite, but still relatively small, it has been shown elsewhere [12] that K_{ex} may be obtained with a high degree of accuracy with the help of an *empirical* correction factor and interpolation formulas applied to van de Hulst's expression. In particular, his original formula [I, p. 179] for K_{ex} in the form

$$K_{\text{ex}}(\rho, m) = 2 - \frac{4 \cos g}{\rho} \exp(-\rho \tan g) \sin(\rho - g) + 4 \left(\frac{\cos g}{\rho} \right)^2 [\cos 2g - \exp(-\rho \tan g) \cos(\rho - 2g)], \quad (25)$$

$$|m - 1| \rightarrow 0,$$

where $\rho = 2x(\nu - 1)$ is van de Hulst's normalized size parameter and $g = \arctan \kappa/(\nu - 1)$ is his absorption parameter such that $\rho \tan g$ gives the energy absorbed along the axial ray within the sphere. Because of the assumptions of the theory, the approximation (25) overestimates the cross section for small ρ and underestimates it in varying degrees as ρ approaches and surpasses the value 4.08, which is the position for the first maximum in K_{ex} as given by (25). A correction factor $(1 + D)$, using the following expressions* for D in the indicated ranges of ρ [12], improves its accuracy

* These were obtained by this author after many trials and errors. He has no insights to offer in explaining their remarkable success.

considerably:

$$\begin{aligned}
 D_1 &= \frac{(\nu - 1)^2}{1.632\nu} [f(g) + 1] + \frac{0.2\rho - \nu + 1}{(\nu - 1)f(g)}, \quad \rho \leq 5(\nu - 1); \\
 D_2 &= \frac{\nu - 1}{8.16\nu} [f(g) + 1]\rho, \quad 5(\nu - 1) \leq \rho \leq \frac{4.08}{1 + 3 \tan g}; \\
 D_3 &= \frac{(\nu - 1)[f(g) + 1]}{2\nu(1 + 3 \tan g)}, \quad \frac{4.08}{1 + 3 \tan g} \leq \rho \leq \frac{4.08}{1 + \tan g}; \\
 D_4 &= \frac{2.04(\nu - 1)[f(g) + 1]}{\nu f(g)\rho}, \quad \rho > \frac{4.08}{1 + \tan g};
 \end{aligned} \tag{26}$$

where

$$f(g) = 1 + 4 \tan g + 3 \tan^2 g.$$

The approximation (25), together with the correction factors $1 + D$, where D is given by the appropriate value in (26), seems to work equally well for nonabsorbing spheres ($g = 0$) and in the range $1 < \nu \leq 1.50$, $0 \leq \kappa \leq 0.25$, as can be judged in the comparisons shown in Table 1.

Table 1
Comparison of approximate and exact values of K_{ex}

x	ρ	Eq. (25) $K_{\text{ex}}(\rho, m)$	Eqs. (25) and (26) $(1 + D)K_{\text{ex}}(\rho, m)$	Exact Mie value $K_{\text{ex}}(x, m)$
$m = 1.212 - 0.0601i$				
1.0	0.424	0.234	0.193	0.203
3.0	1.272	0.978	1.07	1.08
6.0	2.544	2.04	2.36	2.37
10.0	4.24	2.43	2.72	2.80
$m = 1.29$				
1.0	0.58	0.165	0.079	0.072
3.0	1.74	1.28	1.40	1.36
6.5	3.77	3.13	3.78	3.80
10.0	5.80	2.33	2.97	2.81
15.0	8.70	1.79	1.98	1.97
$m = 1.29 - 0.0472i$				
2.0	1.16	0.772	0.767	0.777
5.0	2.90	2.35	2.84	2.83
7.0	4.06	2.67	3.15	3.21
12.0	6.96	1.96	2.17	2.25

Table I—continued

x	ρ	Eq. (25) $K_{\text{ex}}(\rho, m)$	Eqs. (25) and (26) $(1 + D)K_{\text{ex}}(\rho, m)$	Exact Mie value $K_{\text{ex}}(x, m)$
$m = 1.315$				
2.0	1.26	0.727	0.648	0.642
4.0	2.52	2.22	2.55	2.63
6.5	4.095	3.17	3.93	3.94
10.0	6.30	1.99	2.30	2.45
$m = 1.308 - 0.0018i$				
1.0	0.616	0.190	0.096	0.087
3.0	1.848	1.41	1.56	1.54
6.0	3.696	3.09	3.76	3.78
10.0	6.160	2.08	2.41	2.55
$m = 1.315 - 0.0143i$				
2.0	1.26	0.769	0.717	0.717
4.0	2.52	2.18	2.53	2.59
6.5	4.095	3.00	3.66	3.72
9.0	5.670	2.38	2.76	2.89
$m = 1.315 - 0.1370i$				
2.0	1.26	1.07	1.22	1.23
4.0	2.52	1.97	2.41	2.41
6.5	4.095	2.25	2.60	2.71
9.0	5.670	2.12	2.36	2.48
$m = 1.525$				
1.0	1.05	0.518	0.322	0.237
2.0	2.10	1.72	1.76	1.98
4.0	4.20	3.17	4.23	4.09
6.0	6.30	1.99	2.43	2.52
10.0	10.5	2.39	2.71	2.87
$m = 1.525 - 0.0682i$				
1.0	1.05	0.638	0.576	0.420
2.0	2.10	1.72	1.99	2.04
4.0	4.20	2.74	3.50	3.61
6.0	6.30	2.08	2.46	2.61
10.0	10.50	2.12	2.35	2.55

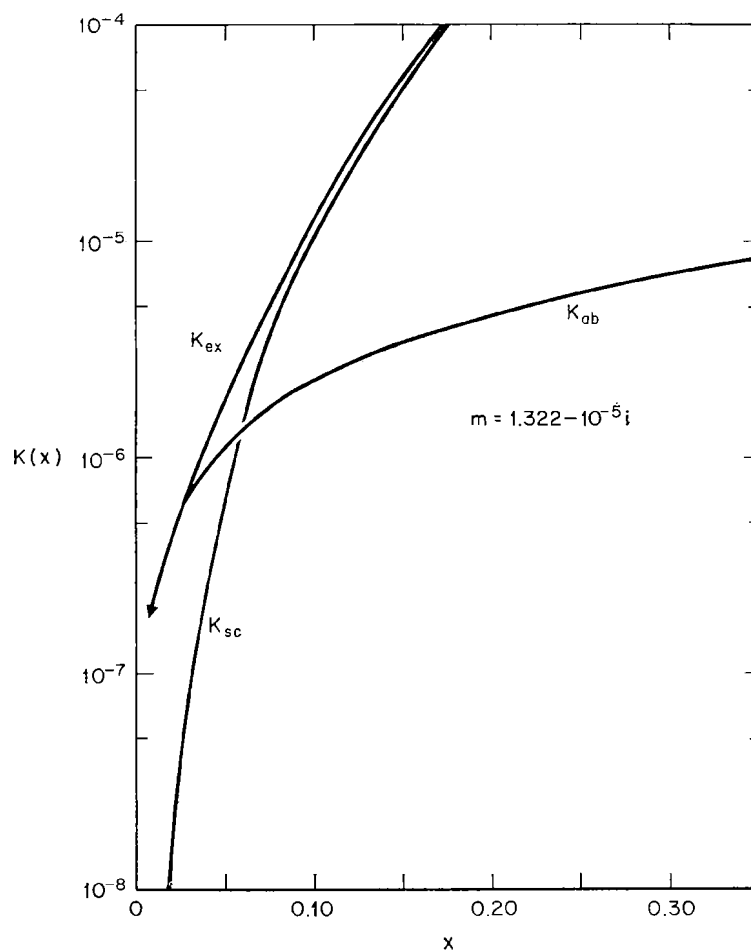


Fig. 7—The extinction, scattering, and absorption efficiencies for small but finite spheres composed of dielectric, weakly absorbing material.

The numerical examples in Table 1 show that the corrected van de Hulst formula $(1 + D)K_{ex}(\rho, m)$ is accurate within an error of about $\pm 0.05K_{ex}$ for a wide range of sizes and types of index of refraction. Note that the errors increase with ν , as should be expected, for both absorbing and nonabsorbing spheres. Moreover, for nonabsorbing spheres, the approximate formulas cannot reproduce the secondary “ripple” in the

extinction curve [1, pp. 265, 384 ff.]. Thus, within the limits indicated and in the absence of fast computers, K_{ex} can be closely estimated with very much less computing labor than for the Mie series. The accuracy is high enough for use in integrations of the extinction with respect to simple size distributions [12]. However, the approximation is not as good in estimating the relative contributions of absorption and scattering to the total cross section, except of course in the limit $x \rightarrow \infty$.

Although van de Hulst has amply covered the subject, it is worthwhile to illustrate again the relative magnitudes of the scattering and absorption efficiencies for spheres of various sizes with very weak, moderate, and very strong bulk absorption properties. Because these magnitudes change so radically from region to region, the single-scattering properties of polydispersions—for example, their scattering albedo and absorption coefficient—change considerably, depending on the size range, dominant size, and proportion of small to large particles in the distribution. In this respect, errors of judgment are common in the literature on the part of the uninitiated, for example, in the naive use of single-particle scattering concepts to deduce the atmospheric parameters of planets other than our own.

Consider, for example, dielectric particles with very weak absorption such that $m = 1.322 - 10^{-5}i$. The behavior of the three efficiencies when $x \leq 0.35$ is illustrated in Fig. 7: for $0 < x < 0.025$, $K_{\text{ex}} \simeq K_{\text{ab}}$, whereas for $x > 0.15$, $K_{\text{ex}} \simeq K_{\text{sc}}$ with $K_{\text{sc}} = K_{\text{abs}} = \frac{1}{2}K_{\text{ex}}$ at about $x = 0.06$. This behavior can be accounted for by the series expansion of the efficiency [1, p. 270]

$$K_{\text{ex}}(m, x) = -\text{Im}\left\{4x \frac{m^2 - 1}{m^2 + 2} + \frac{4}{15} x^3 \left(\frac{m^2 - 1}{m^2 + 2}\right)^2 \frac{m^4 + 27m^2 + 38}{2m^2 + 3}\right\} \\ + \frac{8}{3} x^4 \text{Re}\left\{\left(\frac{m^2 - 1}{m^2 + 2}\right)^2\right\} + \cdots \quad (27)$$

where the term in x gives the Rayleigh absorption efficiency and the term in x^4 the corresponding scattering efficiency. For x sufficiently small, the absorption term is the main contribution to K_{ex} ; but, depending on the magnitude of m , the scattering contribution in turn becomes dominant while x is still small, as shown in the example. In this case the absorption is quite negligible over a wide range of sizes, but this is not the whole story! As $x \rightarrow \infty$ we again approach the condition of equal absorption and scattering efficiencies, to wit

$$\lim_{x \rightarrow \infty} K_{\text{abs}} \leq \lim_{x \rightarrow \infty} K_{\text{sc}} = 1, \quad \kappa \ll 1, \quad (28)$$

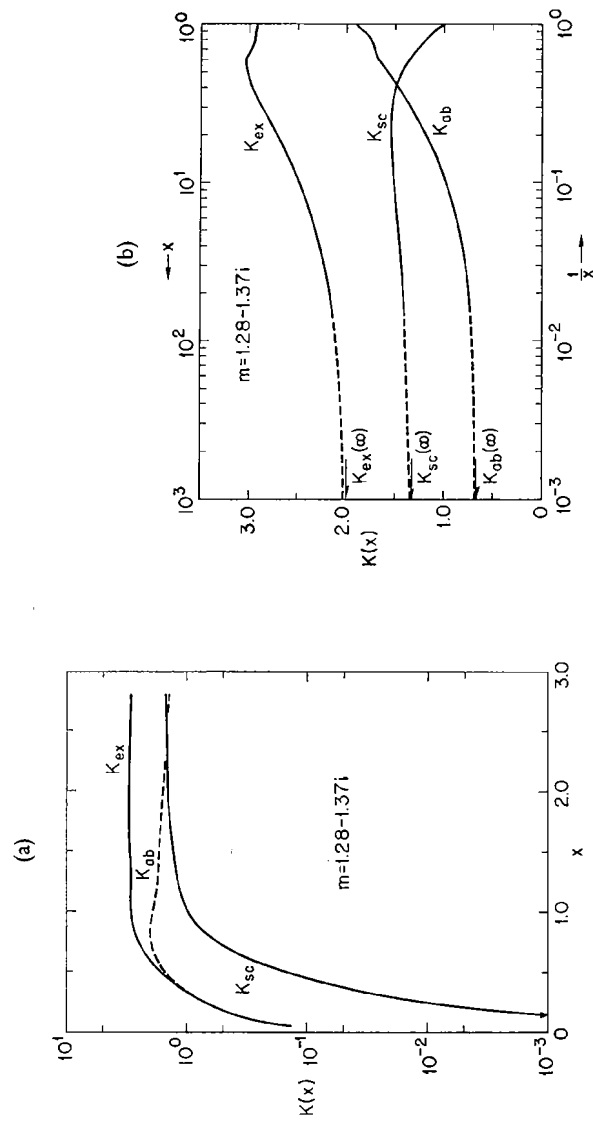


Fig. 8—(a) The three efficiencies for metallic spheres with $x < 3$. (b) The same efficiencies plotted as a function of $\log(1/x)$ showing tendency toward the asymptotic values indicated by arrows.

no matter how weak the absorption properties of the substance of the sphere. This follows the theory and asymptotic formula of van de Hulst [I, p. 181; I2], which in our notation takes the form

$$K_{ab}(\rho, m) = 1 + \frac{\exp(-2\rho \tan g)}{\rho \tan g} + \frac{\exp(-2\rho \tan g) - 1}{2(\rho \tan g)^2}. \quad (29)$$

From this we see that K_{ab} begins to approach unity when $2\rho \tan g > 1$, which in the foregoing example is equivalent to $x > 2.5 \times 10^4$, a large value due to the smallness of κ . The latter situation, by the way, that is, a sphere with radius $r > 4000\lambda$, would approach the properties of a classical blackbody, in terms of scattering theory, according to the definition given by van de Hulst [I, pp. 182, 269].

Another interesting case is that of metallic spheres, where the real and imaginary parts of m are about equal and of the order of unity. Figure 8a shows the behavior of all three efficiency factors for small and moderate metallic spheres with $m = 1.28 - 1.37i$. The efficiencies for small spheres are similar to those of weakly absorbing spheres shown in Fig. 7, except that the region where $K_{ex} \simeq K_{ab}$ extends to much larger values of x in the metallic case. We note, however, that a metallic sphere with $x = 0.10$, where the relative scattering efficiency is negligible, still shows a value $K_{sc} = 2.4 \times 10^{-4}$ compared to 10^{-5} for the equivalent dielectric sphere! The implication of this peculiarity for the nature of Martian hazes will be discussed in Section 4.42.

Figure 8a further shows that in the metallic case $K_{ab} \simeq K_{sc}$ at some moderate size, in this case where $x = 2.4$, beyond which point K_{sc} always exceeds K_{ab} ; in other words, the *albedo of single scattering* $\varpi = K_{sc}/K_{ex} > 0.5$. This is better seen in Fig. 8b, where the efficiencies are plotted against $\log(1/x)$ to show their asymptotic behavior as $x \rightarrow \infty$. The efficiencies plotted are from our own results, in this case available up to $x = 72$ (so far as we know, this is the largest x value for which there is an exact Mie series evaluation of metallic scattering). As seen in Fig. 8b, the three efficiency curves very nicely tend toward their asymptotic values indicated on the diagram. It is remarkable that van de Hulst, in a similar diagram [I, p. 276], shows the correct nature of these curves by using the then existing values for $x < 4$ only and asymptotic theory.

The asymptotic value of $K_{sc}(\infty)$ for metallic spheres is obtained [I, pp. 225, 279] by considering, in the geometric optics limit, the integral of the Fresnel reflection coefficients for the *intensity* over the illuminated sphere. The complex amplitudes r_1 and r_2 of Fresnel reflection at an

interface between vacuum and a metal are given by [1, p. 204; 32, p. 289]

$$\begin{aligned} r_1 e^{i\delta_1} &= \frac{\cos \varphi - m \cos \varphi'}{\cos \varphi + m \cos \varphi'}, \\ r_2 e^{i\delta_2} &= \frac{m \cos \varphi - \cos \varphi'}{m \cos \varphi + \cos \varphi'}, \end{aligned} \quad (30)$$

where φ is the angle of incidence (zero for normal incidence) and φ' is generally a *complex* angle of refraction, defined by a generalization of Snell's law $m = \sin \varphi / \sin \varphi'$ for complex index. Van de Hulst then shows that the scattering efficiency in this case is given by the diffraction term plus the integrated reflection, or $K_{sc}(m, \infty) = 1 + W$, where

$$W = \frac{1}{2} \int_0^{\pi/2} (|r_1|^2 + |r_2|^2) d(\cos^2 \varphi). \quad (31)$$

The asymptotic values of the efficiency factors shown in Fig. 8b were obtained by performing the integration (31), using the expressions for $|r_1|$ and $|r_2|$ and integration technique described by Irvine [33], and by putting $K_{ex}(m, \infty) = 2$, $K_{ab}(m, \infty) = 2 - K_{sc}(m, \infty)$. In Table 2 we show the results of the integration (31) for $m = 1.28 - 1.37i$ as well as some other values of m , which may complement those obtained by Irvine. For completeness Table 2 also includes values of the quantity WG defined by the integration

$$WG = \frac{1}{2} \int_0^{\pi/2} (|r_1|^2 + |r_2|^2) \cos 2\varphi d(\cos^2 \varphi). \quad (32)$$

The integral (32) provides an estimate of the *radiation pressure efficiency* $K_{pr}(m, \infty) = 1 - WG$ and the *asymmetry factor* $\overline{\cos \theta} = (1 + WG)/(1 + W)$ in the asymptotic case. For obvious reasons (no equivalent quantities can be defined for a polydispersion) we have not carried out any computations of these two parameters for finite spheres by means of the Mie series [1, p. 128; 33].

We note, by the way, that Table 2 clearly shows the tendency toward the limits (28) only when κ is very small. Also, the van de Hulst reflection criterion (31) seems to apply to weakly absorbing spheres as well. For example, our Mie calculations for $x = 150$ and $m = 1.29 - 0.0472i$ give $K_{sc} = 1.089$, $K_{ab} = 0.980$, which, though not quite in the geometrical optics range, seem to be approaching their asymptotic values of 1.060 and 0.940 according to Table 2.

Finally, the foregoing discussion of the absorption and scattering efficiencies for very large spheres disproves an inference made by Herman [34] to the effect that the absorption efficiency is given by $1 - R$, where R is the reflectivity of the substance at *perpendicular incidence*. Column 3 in Table 2 shows this quantity to differ significantly from the integrated reflection W (see also Section 2.33).

Table 2
Fresnel reflection integrals W and WG related to the scattering
and radiation pressure efficiencies for large spheres

ν	κ	$\left \frac{m-1}{m+1} \right ^2$	WG	W
1.290	0.0472	0.01646	0.03463	0.06041
1.315	0.1370	0.02194	0.03735	0.07009
1.550	0.1550	0.05003	0.04034	0.10366
1.440	0.4000	0.05784	0.04389	0.11727
1.750	0.5800	0.11380	0.04036	0.16905
2.020	0.3650	0.12683	0.03627	0.17588
2.200	0.2200	0.14467	0.03359	0.18986
2.4066	0.4771	0.18639	0.02945	0.22578
2.7589	1.2408	0.29570	0.01874	0.31943
1.28	1.37	0.27636	0.03943	0.33273
1.51	1.63	0.32567	0.03026	0.36718
1.70	1.84	0.36303	0.02385	0.39449
4.2214	2.5259	0.49810	-0.00385	0.48939

In general, the relative magnitudes of the efficiencies for extinction, absorption, and scattering in various ranges of the size parameter and refractive index cannot be described in a simple manner. Pluss [35] has recently described further features of these parameters obtained through the Mie theory.

2.33 The Backscattering or "Radar" Cross Section and Efficiency

Because of its special interest in applications to radar and pulsed-laser physics, a separate discussion of the backscattering properties of single particles is in order. The accepted definition of the radar cross section or exact backscattering cross section σ_b is 4π times the power scattered back per steradian divided by the incident flux. Van de Hulst's clear discussion

of this parameter [I, pp. 284, 223] shows that the origin of this somewhat awkward choice has to do with the definition of “gain” in radio technology. At any rate, by virtue of (3) and (1) it is evident that

$$\sigma_b(m, x) = \frac{4\pi}{k^2} |S_1(180)|^2 \quad (33)$$

where, according to (1) and (9),

$$-S_1(180) = S_2(180) = \sum_{n=1}^{\infty} (-1)^n \frac{2n+1}{2} (a_n - b_n) \quad (34)$$

is a function of the Mie coefficients only. Conceptually, by comparison of (33) with (4) we may think of σ_b as the scattering cross section of a hypothetical particle that scatters the incident energy *isotropically* with specific intensity $|S_1(180)|^2/k^2$. By analogy with the total scattering efficiency one can then define a backscattering efficiency K_b (sometimes referred to as the normalized radar cross section) by putting

$$K_b(m, x) \equiv \frac{\sigma_b}{\pi r^2} = \frac{4}{x^2} |S_1(180)|^2. \quad (35)$$

In Section 4.33 we shall define an equivalent quantity for a unit volume in a polydispersion.

In Fig. 9 we show three characteristic curves of K_b as a function of x for $x \leq 10$. The top curve is for totally reflecting spheres with $|m| = \infty$ and is based on detailed computations by J. Rheinsteint [36]; the other two curves, for a metallic and dielectric case, respectively, result from fitting smooth curves to our own data, shown by the points. The top curve shows clearly the regular and smoothly damped sine wave character of such idealized reflecting spheres (hardly likely to be found in nature in the realm of small particles illuminated by visible radiation), with K_b oscillating around its limiting value of one, in line with physical considerations [I, p. 223].

The metallic case shows the same general character (note the difference in the periodicity), but the magnitude of K_b , both for finite spheres and in the limit, is about one fourth that for totally reflecting spheres. For the purely dielectric case ($m = 1.29$) our results show a similar wave structure superposed on a longer-period oscillation with ever-increasing amplitude, without any tendency toward a limiting value for large spheres. The backscattering efficiency for weakly absorbing spheres was examined by Herman and Battan [37]. For ice spheres illuminated by microwaves ($m = 1.78 - 0.0024i$), they find a maximum value of K_b of about 38 near $x = 60$.

However, they also report that for very large x , K_b decreases monotonically, eventually reaching a value of 0.296 in the extreme point of $x = 500$ of their calculation. This brings up the question of the limiting value of K_b as $x \rightarrow \infty$.

Herman and Battan [37], on the basis of their own calculations and a discussion by J. E. McDonald [38], conjecture that this limiting value is

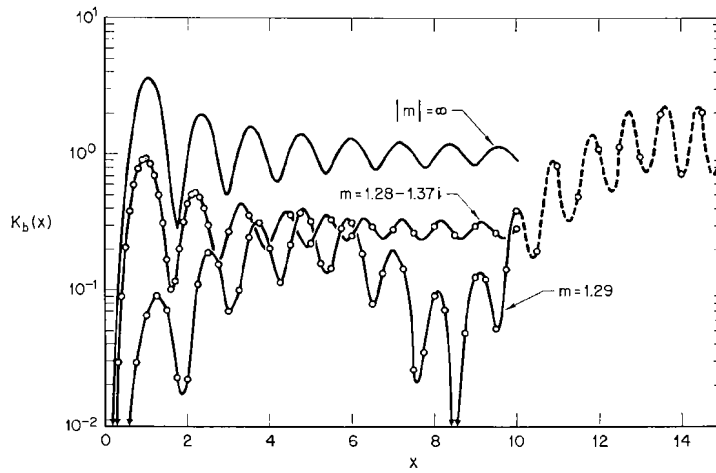


Fig. 9—The backscattering efficiency $K_b(m, x)$ for dielectric, metallic, and totally reflecting spheres. The dashed extension of the curve for $m = 1.29$ is a freehand fit to the computed points shown.

given by the Fresnel reflection coefficient for the *intensity* at perpendicular incidence; that is,

$$\lim_{x \rightarrow \infty} K_b(m, x) = \left| \frac{m - 1}{m + 1} \right|^2. \quad (36)$$

This conjecture can best be verified for the metallic case, where, as evidenced by the example in Fig. 9, K_b shows regularly damped oscillations around a limiting value that is approached for moderate values of x . In Table 3 we show examples for three types of metallic index, taken from our own results employing the double precision described in Section 2.22. The agreement with the corresponding reflection coefficients, shown in the last line, is almost perfect and the conjecture (36) must therefore be considered true. The failure of Herman and Battan's [37] results for ice

spheres to reach the limiting value of 0.0787 given by (36), even for $x = 500$, must be attributed to the fact that this size is not large enough. This is understandable, since the absorption coefficient in their case is so small that the contribution from internally reflected waves is not entirely eliminated.

Table 3
Backscattering efficiencies for metallic spheres

x	$K_b(x)$		
	$m = 1.28 - 1.37i$	$m = 1.51 - 1.63i$	$m = 1.70 - 1.84i$
32	0.2763	0.3252	0.3619
40	0.2764	0.3258	0.3634
48	0.2764	0.3258	0.3633
52	0.2764	0.3257	0.3631
56	0.2764	0.3257	
60	0.2764		
$\left \frac{m-1}{m+1} \right ^2$	0.2764	0.3257	0.3630

Although there must exist some physical or mathematical explanation of the property (36), we cannot agree with that proposed by McDonald [38]. In particular, his arguments invoking *the finite size and shape of a receiving antenna* do not seem appropriate to the problem; nor can we offer an alternative explanation. All we can say is that the property (36) is indicated by the results of the Mie theory and that it should be verified experimentally if possible. By comparing the limit (36) with (33) and (35), we can suggest the following physical interpretation: The differential cross section of a large absorbing sphere in the exact backward direction is given by $1/4\pi$ times the reflectivity of an equivalent right cylinder of the same cross-sectional area as the sphere, with its axis oriented parallel to the incident radiation.

Mathematically, the property (36) reduces to the statement

$$\lim_{x \rightarrow \infty} \frac{1}{x^2} \left| \sum_{n=1}^{\infty} (-1)^n (2n+1) [a_n(x) - b_n(x)] \right|^2 = \left| \frac{m-1}{m+1} \right|^2, \quad \text{Im}\{m\} \neq 0, \quad (37)$$

whose proof, even with the use of (24), does not appear to be simple. It should be further noted that for large absorbing spheres, including

metallic ones, the nondiffracted part of the differential scattering is never truly isotropic, even though the backscattering is given by (36). This explains why K_{sc} is *not* given by $1 + |(m-1)/(m+1)|^2$, as implied by Herman [34], except in the totally reflecting case $m = \infty$.

Finally, the Mie results indicate that, for idealized nonabsorbing dielectric spheres, a finite limit of the backscattering cross section such as (36) may not exist, an inference that appears plausible on physical grounds.

2.34 The Amplitude Components S_1 and S_2

In trying to get a clearer idea of the scattering process for various types of spheres, it is instructive to examine the behavior of the individual components of the complex amplitude for a fixed scattering angle as a function of size, and for a given sphere as a function of angle.

As we have seen, the expressions for the amplitude in the exact forward and backward directions are relatively simple and they have special physical significance. In particular, the total extinction efficiency is related to the forward amplitude by the cross section theorem (6). The form of the curve traced by the function $4x^{-2}S_1(x, 0)$ for *dielectric spheres* has been indicated by van de Hulst [I, p. 264] and others [26]. We need not reproduce the diagrams here, but recall that they show a number of major and minor oscillations of the amplitude, which are responsible for the familiar shape of the extinction curve over the range of moderate-sized spheres.

It is of some interest to look at the exact behavior of $S_1(x, 0)$ as the spheres become large and approach the geometrical optics limit, since the corresponding numerical values are now obtainable. Judging from the behavior of this amplitude for absorbing spheres, and using (1) and (9), we can make the *conjecture*

$$\lim_{x \rightarrow \infty} \frac{2}{x^2} \sum_{n=1}^{\infty} (2n+1)(a_n + b_n) = 2, \quad (38)$$

which is analogous to (37) except that in this case we are dealing with a complex limit. Again there seems to be no *mathematical* proof of (38) in the most general case, based on the behavior of the series for a_n and b_n . A proof based on physical principles has been given by van de Hulst [I, p. 107] but it is not clear that it applies to nonabsorbing spheres [I, pp. 264, 265].

Figure 10 shows a plot of the forward amplitude in the complex plane for metallic and moderately absorbing spheres. If we consider equal increments in x , the curves show very clearly the tendency of the sequence

represented by the left side of (38) to converge toward the limit. In particular, the nonmetallic case shows some "waviness" and a peculiar double looping before the curve smooths out and "points" toward the limit. The metallic case shows a smooth tendency toward the limit beginning with relatively small spheres. Both cases seem to support the conjecture (38), but the limit must be approached for rather large spheres, possibly with $x > 10^3$.

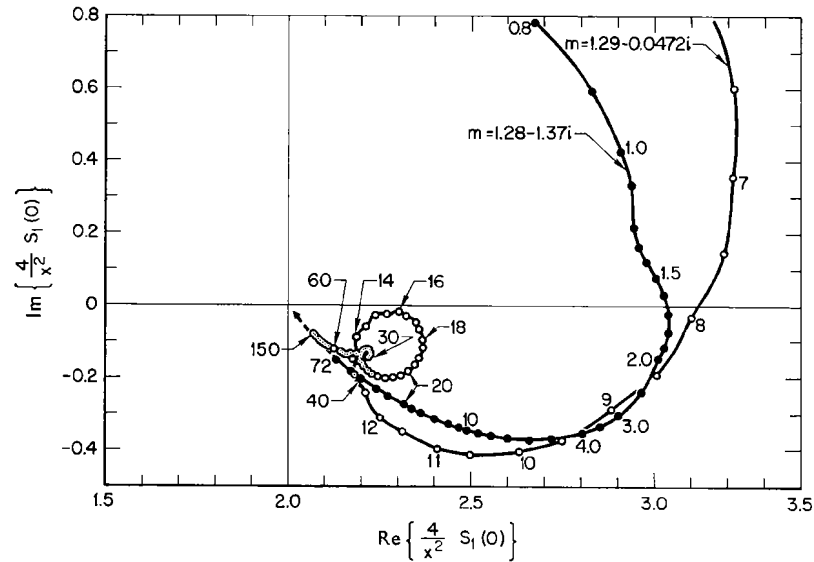


Fig. 10—Tendency toward the geometrical optics limit 2 (cross-section theorem) of the complex forward-scattering amplitude obtained by the Mie theory for dielectric and metallic spheres. Smooth curves are fitted to the computed points. The dashed portion shows extrapolation without numerical verification.

A diagram similar to Fig. 10 for nonabsorbing dielectric spheres in the same size range would be difficult to reproduce. For example, for $m = 1.29$ an extension of the previously published curve [26, Fig. 2] up to $x = 50$ shows a continuously winding shape with major and minor loops, with values lying mostly in the quarter-plane

$$\operatorname{Re} \frac{4}{x^2} S(x, 0) > 2, \quad \operatorname{Im} \frac{4}{x^2} S(x, 0) < 0,$$

and with no clear tendency toward a limiting value. Our guess is that the limit 2, if it exists, will be approached for extremely large values of x , of the order of 10^4 , with continued fine oscillations in ever smaller intervals Δx .

Figure 11 is a direct plot of the backward amplitude $S_1(x, 180^\circ)$ with continuous and hand-smoothed curves fitted to the computed points indicated, for dielectric and metallic spheres, respectively. The x^{-2}

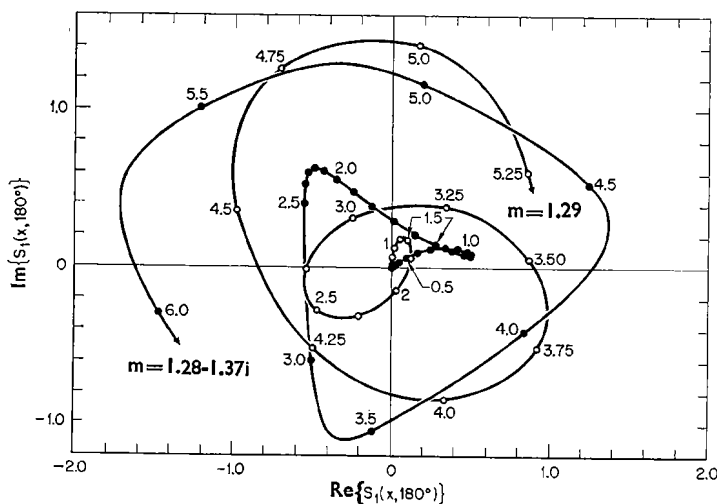


Fig. 11—Comparison of complex backscattering amplitude $S_1(180^\circ)$ for dielectric and metallic spheres. Smooth curves fitted to computed points indicated.

normalization factor has been omitted for clarity. The essentially different character of these amplitudes for the two types of material is clearly brought out, as already indicated in the corresponding backscattering efficiencies illustrated in Fig. 9. (Compare the maximum around $x = 1$ for the metallic case in both figures.)

Values of the forward and backward amplitudes for single spheres of various sizes and indices of refraction calculated by the present program have been published in report form [27,28]. In general, graphical interpolations of the complex amplitudes with respect to size by means of a diagram for a fixed scattering angle are not recommended because of the complexity of the curves [7, p. 238], as illustrated in Fig. 11.

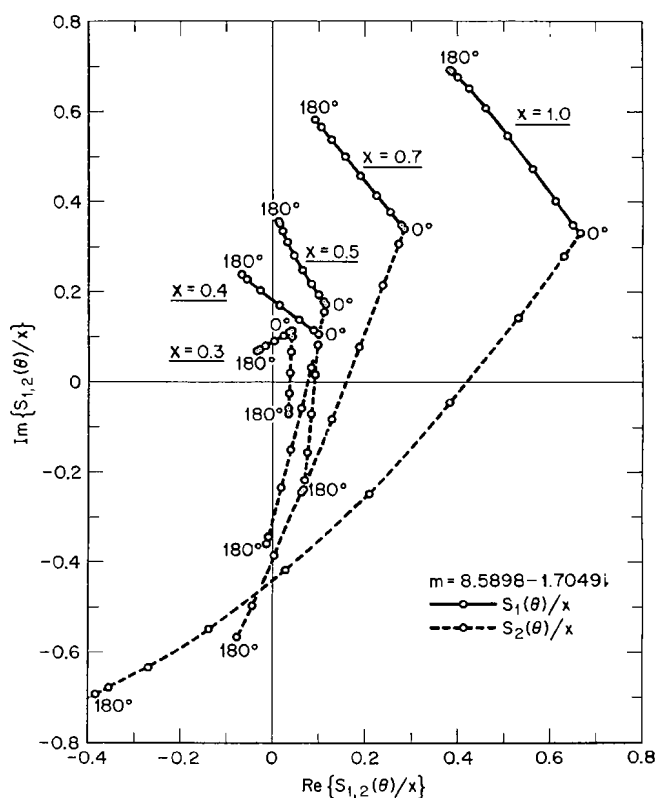


Fig. 12—Complex amplitudes $S_{1,2}(\theta)$ for small, opaque spheres of fixed radius as a function of scattering angle θ , showing deviations from the Rayleigh and the totally reflecting model (see text). The values shown have been divided by x for convenience of display.

The same applies to interpolations with respect to θ using plots of S_1 and S_2 as a function of θ for fixed values of x . The shape of the resulting curves for dielectric and absorbing spheres of moderate size has been illustrated elsewhere* [1, p. 235; 26, 27]. The curves become progressively more complicated as the spheres become large, especially in the dielectric and weakly absorbing cases.

An interesting case is that of water spheres illuminated by microwaves,

* In [27] certain errors in the diagrams of [26] have been corrected.

called "type 4" by van de Hulst in his classification of absorbing materials [1, p. 268]. When such spheres are small, they act like totally reflecting spheres with the backward amplitude considerably larger than the forward. This is clear in the plots of Fig. 12, showing the quantities S_1/x and S_2/x for $m = 8.5898 - 1.7049i$ (10°C water at $\lambda 5$ cm) and $x = 0.3, 0.4, 0.5, 0.7$, and 1.0 . The backward asymmetry $|S_1(180^\circ)| > |S_1(0^\circ)|$ starts here somewhere between $x = 0.3$ and $x = 0.4$ and disappears around $x = 1$, after which the usual forward asymmetry takes over. Note that the Rayleigh-like approximation for totally reflecting spheres [1, p. 159], given by

$$S_1(x, \theta) = ix^3(1 - \frac{1}{2} \cos \theta),$$

$$S_2(x, \theta) = ix^3(\cos \theta - \frac{1}{2})$$

would be quite inadequate in this case: the amplitudes in Fig. 12 lie considerably off the imaginary axis, they are not proportional to x^3 , and the ratio $|S_1(180^\circ)| \cdot |S_0(0^\circ)|^{-1}$ does not quite reach 3, as in the foregoing expressions. This illustrates the transition region between "soft" and totally reflecting spheres mentioned by van de Hulst [1, p. 158] and once more demonstrates the inadequacy of idealized models ($m = \infty$) to describe the scattering by real particles.

We conclude this section by reproducing in Fig. 13 the elegant curves traced by the amplitudes for a larger water sphere with $x = 4$, illuminated

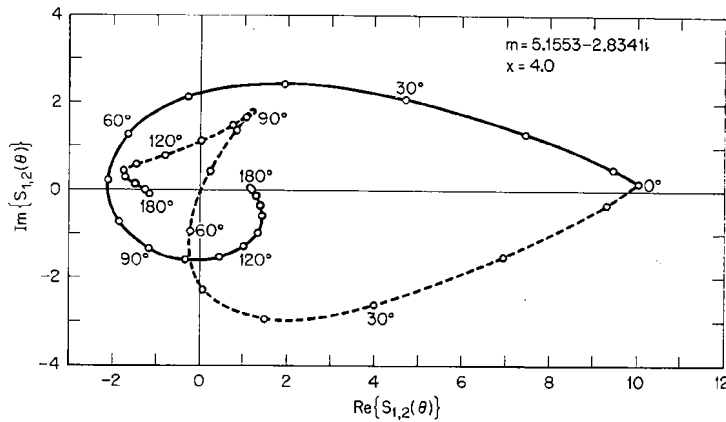


Fig. 13—Complex amplitudes $S_1(\theta)$ (solid line) and $S_2(\theta)$ (dashed line) for a single, opaque sphere of moderate size as a function of θ , with smooth curves fitted to the computed points shown.

by 21 cm radiation. This may be compared with previously published curves for more transparent spheres [26,27, Fig. 6a,b,c]. The usual forward asymmetry is apparent in Fig. 13, with $|S_1(0^\circ)|$ exceeding $|S_1(180^\circ)|$ by a factor of almost ten. A singularity in the form of a cusp or loop in $S_2(\theta)$ near $\theta = 90^\circ$ is clearly evident. This feature cannot be easily explained in terms of geometrical and physical optics. For example, the Fresnel reflection amplitudes (30), besides being difficult to evaluate in complex form [32, p. 294], have an ambiguous meaning near grazing incidence [1, p. 223], where one must consider the little-understood effects of a “creeping wave” and “spray” at the appropriate scattering angles [1, pp. 365 ff.]. We are satisfied that the numerical results based on the Mie formulas result in continuous functions for the amplitude near this critical angle.

2.35 The Dimensionless Intensity Parameters $i_1(\theta)$ and $i_2(\theta)$

Finally, we may look at some examples of the intensity parameters $i_1(m, x, \theta)$ and $i_2(m, x, \theta)$, which are related to the differential cross section (3) and are defined as follows:

$$\begin{aligned} i_1(x, m, \theta) &= k^2 A_1 A_1^* = S_1 S_1^*; \\ i_2(x, m, \theta) &= k^2 A_2 A_2^* = S_2 S_2^*. \end{aligned} \quad (39)$$

These are the quantities often tabulated in the literature to show the pattern of intensity and linear polarization (if any) produced by Mie-type scattering. In fact, when the particle is illuminated by a unit flux of unpolarized radiation, the intensity per unit solid angle scattered in any direction is given by $(i_1 + i_2)/2k^2$, and when only linear polarization is produced, as in Rayleigh scattering, the degree of polarization is simply $(i_1 - i_2)/(i_1 + i_2)$. These symbols and definitions are thus identical with those of Lowan [23] and van de Hulst [1, p. 129]. We note further that the intensity parameters (39) are directly proportional to the scattered power, *independently of the energy absorbed by the particle* whenever the index of refraction has an imaginary component.

In general, very small dielectric and nonabsorbing particles show a scattering pattern that approaches the Rayleigh limit: the intensity $i_1 + i_2$ is almost symmetrical with respect to a plane through the center of the particle and perpendicular to the incident direction and $i_2(90^\circ) \simeq 0$. As the size of the particle is increased and x approaches 1, a moderate forward asymmetry develops, although the maximum positive polarization is retained near $\theta = 90^\circ$, as shown in the lower pair of curves ($m = 1.315$)

in Fig. 14. When a strongly absorbing sphere of the same size is considered, the amount scattered in all directions is doubled, even though this represents only 0.164 of the flux incident on the particle, the rest being absorbed (upper curves in Fig. 14). The forward asymmetry is also somewhat increased. The brightness of an optically very thin layer of such absorbing particles would be about twice that of the transparent ones when viewed from any direction with respect to the illuminating parallel

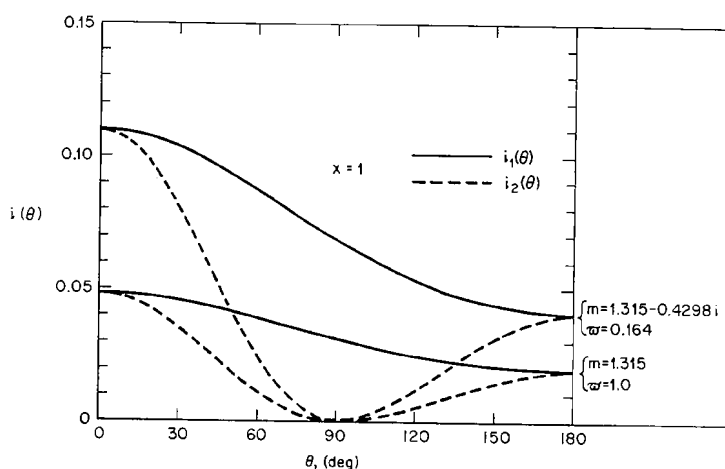
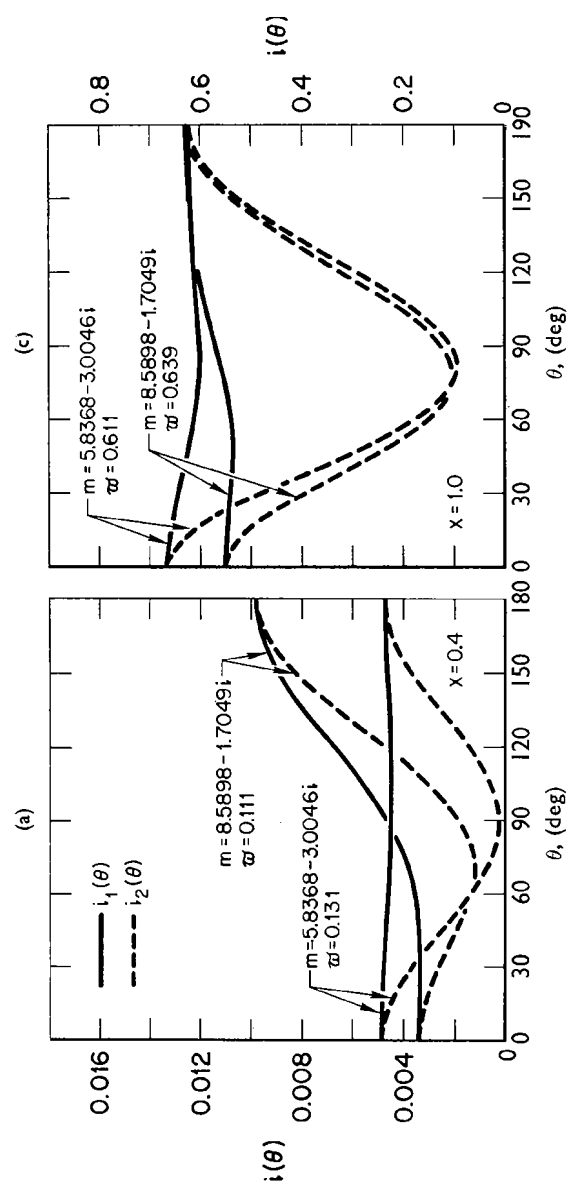


Fig. 14—Examples of dimensionless intensities $i_{1,2}(\theta)$ for a dielectric and absorbing sphere of the same small size, showing how an absorbing sphere may scatter twice as much energy in all directions as a transparent sphere.

radiation. (See Table 6, Section 3.5, for the nature of physical particles and wavelength of radiation corresponding to the indices of refraction mentioned.)

For “hard” particles, in which the real and imaginary parts are both large, as in the case of microwaves illuminating water spheres, the scattering behavior is different. In Fig. 15 we compare the situation for various small spheres with $m = 5.8 - 3i$ (softer) and $8.6 - 1.7i$ (harder), respectively. In Fig. 15a for $x = 0.4$, the softer sphere is shown to act like a Rayleigh particle, whereas the harder one shows considerable *backward* asymmetry, $i(180^\circ)$ being almost three times as intense as $i(0^\circ)$. Figure 15b shows backward asymmetry for both spheres when the relative size is doubled, the overall intensity is increased fiftyfold, and the albedo of single scattering $\varpi = K_{sc}/(K_{sc} + K_{ab})$ is increased fivefold. Furthermore,



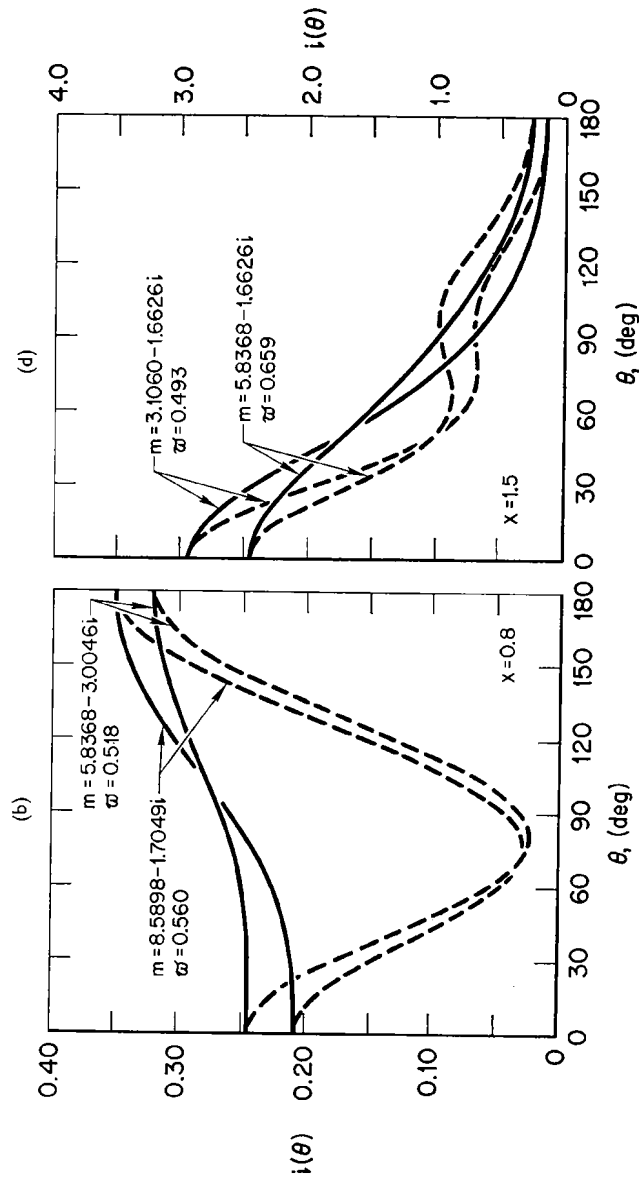


Fig. 15—Comparison of angular distribution of scattered intensities $i_{1,2}(\theta)$ of pairs of small spheres for different values of complex m . The relative size x increases from 0.4 in (a) to 1.5 in (d), as indicated on the diagrams. The curves are smooth fits to the computed points (not shown).

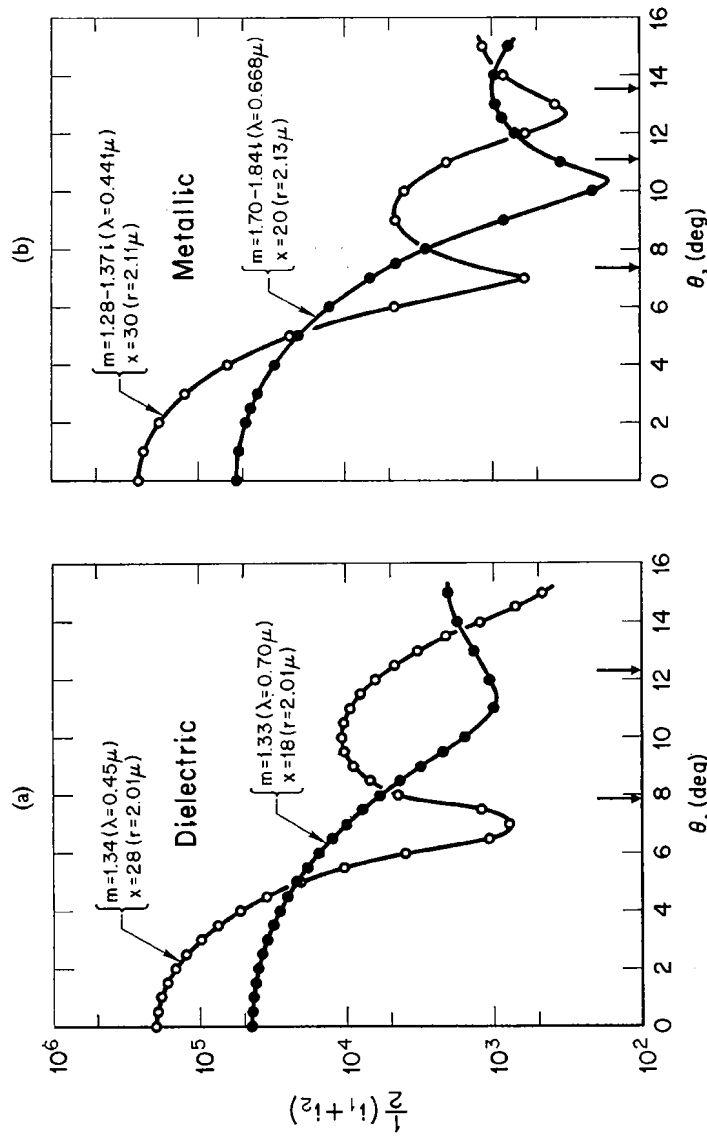


Fig. 16—The scattered intensity $(i_1 + i_2)/2$ in the aureole and corona region for unpolarized light incident on a sphere of fixed geometrical size, showing the effect of varying the relative size (or wavelength). Vertical arrows along the bottom scale show positions of diffraction minima for an opaque disk of the same radius as the sphere.

(a) Water droplet of radius about 2.0μ . (b) "Iron" sphere of radius about 2.1μ .

in the case of the harder sphere, the maximum polarization near $\theta = 90^\circ$ has a *higher* value for the larger sphere than for the smaller; that is, we observe the reverse of the situation for nonabsorbing spheres.

In Fig. 15c we see that the forward-to-backward symmetry and the polarization of the softer sphere are again almost like those of a Rayleigh particle, even though the size, $x = 1$, is not small compared to the wavelength; furthermore, the harder sphere in this case still shows some backward asymmetry but a smaller scattering efficiency than the softer sphere, a situation that is the reverse of that in Fig. 15a. Finally, in Fig. 15d for $x = 1.5$, a pronounced forward asymmetry develops in the softer sphere, and there is a reversal in the sign of polarization near $\theta = 90^\circ$, instead of a maximum there. In an even softer sphere, with $m = 3.1 - 1.7i$, the pattern is similar but more asymmetrical, although the scattered radiation represents a *smaller* percentage of the incident flux in this case (compare the values of π indicated on the diagram).

Thus the examples in Figs. 14 and 15 again (cf. Section 2.34) illustrate the fact that, for particles that are small but finite (in this case with diameters one sixth to one half the wavelength), the angular scattering pattern and polarization are rather sensitive to the relative size and to both the real and imaginary parts of the index of refraction.

The intensity distribution for single particles of larger diameter is of interest mainly to show the position and intensity of the maxima and minima responsible for the diverse corona, rainbow, and glory phenomena observed in nature. In considering these features, the reader should bear in mind that the pure monodisperse phenomenon practically never occurs in the atmosphere.

Figure 16 shows plots of the quantity $(i_1 + i_2)/2$ on a logarithmic scale versus the scattering angle in the range $0^\circ \leq \theta \leq 15^\circ$, representing the scattered intensity when the particle is illuminated by unit flux of *unpolarized* light at the wavelengths indicated. Figure 16a is for a water droplet of radius $2\ \mu$ scattering blue and red light, and Fig. 16b for an iron sphere of radius $2.1\ \mu$ (the correct x value for $\lambda 0.668\ \mu$ should be 19.8 instead of 20). The points show the actual computed values, to which smooth curves have been fitted. The vertical arrows show the position of the diffraction minima for an opaque disk of the same relative diameter that would be obtained by putting $x \sin \theta = 3.832, 7.016, 10.173$ for the first-, second-, and third-order minima, respectively [1, p. 99, Table 6]. An inspection of these diagrams reveals the following.

An optically thin layer of such monodisperse spheres illuminated by sunlight would produce a bright red corona of radius 6° to 8° , gradually

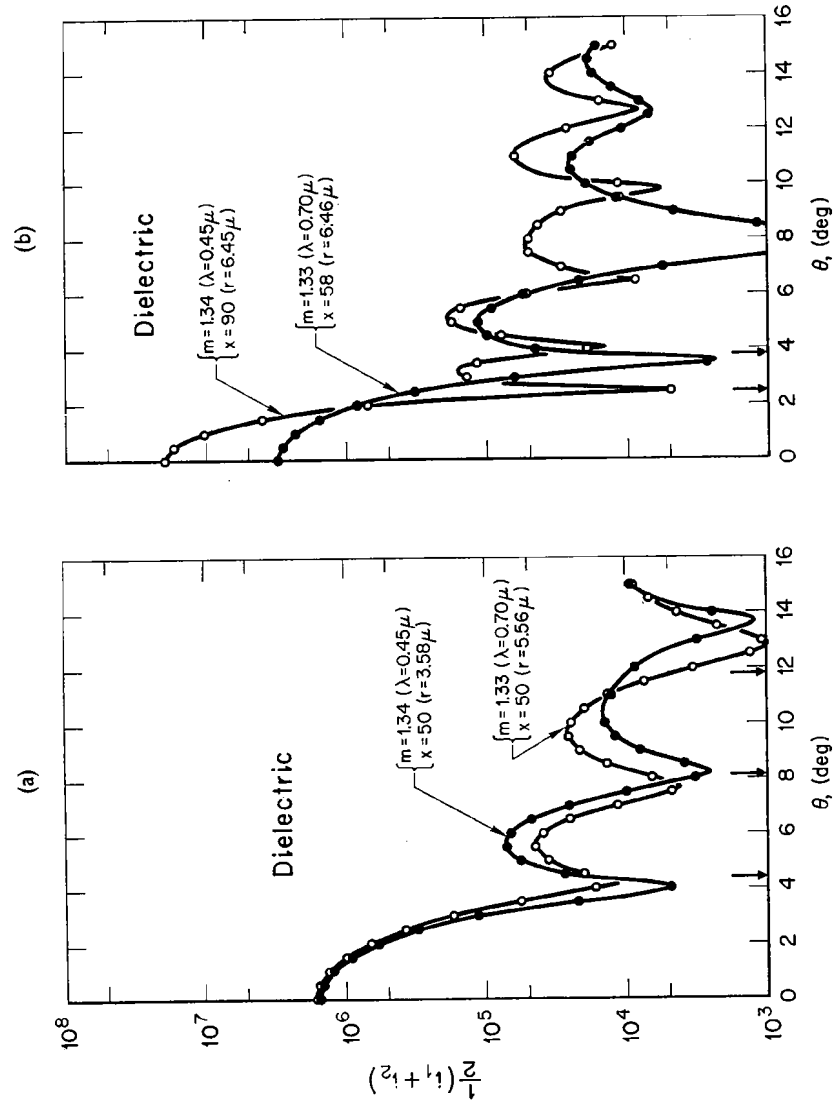


Fig. 17—Same as Fig. 16, but for larger spheres. (a) Two water spheres of the same relative size, showing the effect of varying the geometrical size (or wavelength) with little change in m . (b) A water sphere of radius about 6.5μ , showing a shift in position and number of diffraction minima with change of wavelength (relative size)

changing to an even brighter blue aureole extending to the limb of the Sun. A weaker outer blue corona with a radius of about 10° would also be observed. The radius of most common coronas produced by water clouds is smaller than this, whereas that of Bishop's rings is larger (see Section 4.31). Note that, should such a bright corona be observed (say through a volcanic dust cloud), it would be difficult to decide whether the responsible particles are transparent water drops or metallic spheres, since the absolute brightness and position of the coronas (and the deduced size of the particles) would be almost identical in both cases. However, the size of the particles, assuming a monodisperse layer, could be closely estimated on the basis of diffraction theory alone.

Figure 17a shows the effect of a small change in the refractive index keeping the *relative size of the sphere constant* (the true radii would be about 5.6μ for red light and 3.6μ for blue light, respectively). The first-order minima and maxima coincide but their intensities differ, the less refrangible sphere ($m = 1.33$) showing a *brighter* corona between 5° and 6° than the other. From this it is clear that the colored coronas are mainly a result of the relative size of the droplets in different parts of the spectrum, rather than of changes in the refrangibility of water.

Figure 17b shows the system of blue and red coronas produced respectively by two droplets of almost identical size (about 6.5μ in radius). A thin cloud composed only of such droplets would display *two* equally bright and narrow, bluish-white rings with radii of about 5° and 3° , respectively, with reddish inner borders and a much brighter blue aureole of about 2° radius around the luminary. Natural coronas around the Sun and Moon are commonly of this size and smaller, but they seldom display this degree of purity and definition because the cloud is not strictly monodisperse. Still, as we shall see later (Section 4.32), the drop sizes must be distributed in a rather narrow range around the modal size; otherwise, the corona phenomenon would be entirely washed out. We note in passing that the diffraction minima in this case coincide much better with the true scattering minima than those in Fig. 16a because of the larger spheres considered.

Figure 18 is a plot, on an expanded logarithmic scale, of the intensity $(i_1 + i_2)/2$ in the cloudbow and glory regions, for the same water drop as in Fig. 17b. We have fitted smooth, continuous curves to the computed points at 0.25° intervals shown on the diagram. It is clear that an angular resolution of 1° would prove quite inadequate to reveal the detailed character of the intensity variations for a single such sphere, particularly in the glory region. The hypothetical thin monodisperse cloud mentioned

earlier would produce a pronounced blue glory of radius 2° and a red one of radius about $3^\circ.5$, as well as a bright blue cloudbow with radius of about $37^\circ.5$. In Fig. 18 we have also shown some values of the linear polarization $(i_1 - i_2)/(i_1 + i_2)$, resulting from unpolarized incident light. Note the typically high values at the glories, where the electric vibration is mainly parallel to the plane of scattering, in contrast to the coronas, which show

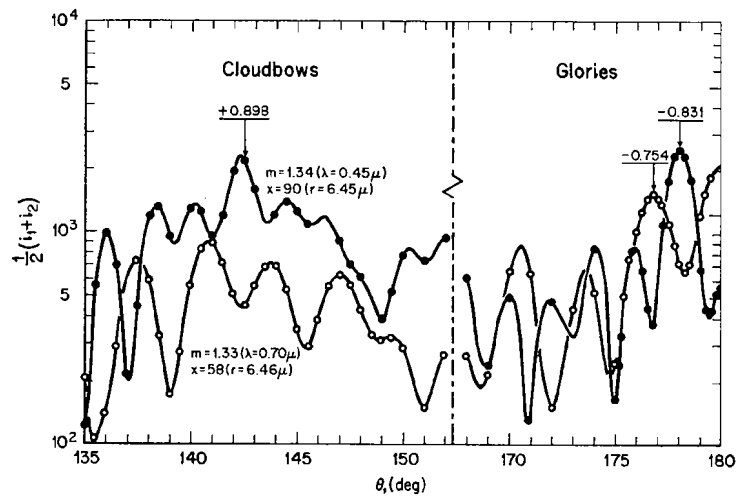


Fig. 18—Scattered intensity $(i_1 + i_2)/2$ in the backward-hemisphere cloudbow and glory region for a 6.5μ water sphere at the two wavelengths $\lambda 0.45 \mu$ and $\lambda 0.70 \mu$. Typical values of polarization produced by unpolarized incident radiation are indicated at the scattering angles shown by arrows.

practically no polarization. The Mie results, of course, corroborate that cloudbows and glories cannot be accurately described by means of geometrical optics alone, and that the relative size of the sphere is very critical in determining the position and intensity of the maxima and minima. Only very large drops of the order of 1 mm in diameter display the classical rainbow picture [cf. 25].

As a research tool, the glories seem to us to be the more important phenomenon in determining the nature of unknown particles, as for example in the atmosphere of Venus (see Section 4.41) and in Saturn's rings (Section 4.43), since they are not easily washed out by a size distribution. Note also in Fig. 18 that in this case the exact backscattering point

is an absolute maximum in red light but not in blue. This relation could be interchanged for spheres of other sizes. Thus, size-distribution effects have to be determined by means of the exact theory, since physical and geometrical optics methods seem to be unable to predict the glory phenomenon with sufficient accuracy [1, pp. 249–258].

Chapter 3 Single Scattering on Many Particles

3.1 CHOICE OF CHARACTERISTIC PARAMETERS

In considering the quantitative description of a stream of electromagnetic energy of arbitrary characteristics, one may choose from several existing schemes, depending on the nature of the problem. Some of these have clearly historical origins or are related to human vision, whereas others are dictated by the mathematical formalism required by a particular theory, or by the requirements of experimental techniques. Classical nomenclature and symbolism have changed and continue to change as attempts are made to achieve the most general description, often at the expense of physical understanding of the particular problem at hand.

We do not attempt to present here a comprehensive review and comparison of the several existing schemes. A brief description of some of these is given by Shurcliff [39]. With a minor modification we adopt the Stokes vector representation and the corresponding matrix operator, following such authors as Chandrasekhar [40], van de Hulst [1], Sekera [41,42], and others, whose main interest has been in atmospheric scattering and optical phenomena. This choice, besides avoiding the lamentable and often unnecessary introduction of innovation in concepts, units, and symbols, is a good compromise in that it is best suited to the theoretical *and* experimental description of the *incoherent, partially polarized light* resulting from the interaction of sunlight with a scattering planetary atmosphere.

The close relation between the Stokes parameters and observable quantities, on the one hand, and those given by the theory of primary and

multiple scattering on the other, is clear and unambiguous. The scheme has the added advantage that all the Stokes parameters or their equivalents have the same physical dimensions and the parameters for coincident streams are usually simply additive. Naturally, the Stokes system has some disadvantages; for example, the wave amplitude and phase are not explicit, as they are in the so-called Jones vector and matrix representation [39, p. 25; *I*, p. 49]. So far, however, in scattering experiments it has been impossible to determine amplitudes and phases, but only energies. In *atmospheric* problems, even if this were possible with the use of laser light as a source, it is doubtful whether the amplitude and phase of the light waves scattered by a volume element of the order of cubic meters can be usefully interpreted.

3.2 THE STOKES PARAMETERS FOR A SINGLE PARTICLE

The particular forms of the Stokes vector and the scattering matrix adopted here were used earlier by this author [9], and they represent a modification based on the analysis of Perrin [43] and Perrin and Abragam [44]. They are eminently suited to a well-known model of atmospheric scattering, namely, a mixture of idealized Rayleigh particles and larger particles composed of optically homogeneous and isotropic material with perfect spherical symmetry. Under these conditions an elementary scattering process can be described by an almost diagonal matrix operating on the vector representing the incident radiation, itself in an arbitrary state of polarization. Symbolically, we write

$$\mathbf{I}(\theta) \Delta\omega = \boldsymbol{\sigma}(\theta) \cdot \mathbf{I}_0 \Delta\omega_0 \quad (40)$$

where \mathbf{I}_0 and $\mathbf{I}(\theta)$ are column vectors of the form $\{I_1, I_2, U, V\}$ corresponding to the incident and emergent streams of radiation, respectively, and $\boldsymbol{\sigma}(\theta)$ is a 4 by 4 matrix operator of the form

$$\boldsymbol{\sigma}(\theta) \equiv \begin{pmatrix} \sigma_1(\theta) & 0 & 0 & 0 \\ 0 & \sigma_2(\theta) & 0 & 0 \\ 0 & 0 & \sigma_3(\theta) & \sigma_4(\theta) \\ 0 & 0 & -\sigma_4(\theta) & \sigma_3(\theta) \end{pmatrix}. \quad (41)$$

The dimensions of \mathbf{I}_0 and \mathbf{I} are those of energy flux and scattering intensity, respectively, *per unit area* and *per unit solid angle* in whatever physical units one chooses. In Eq. (40) $\Delta\omega_0$ is the (small) solid angle occupied by

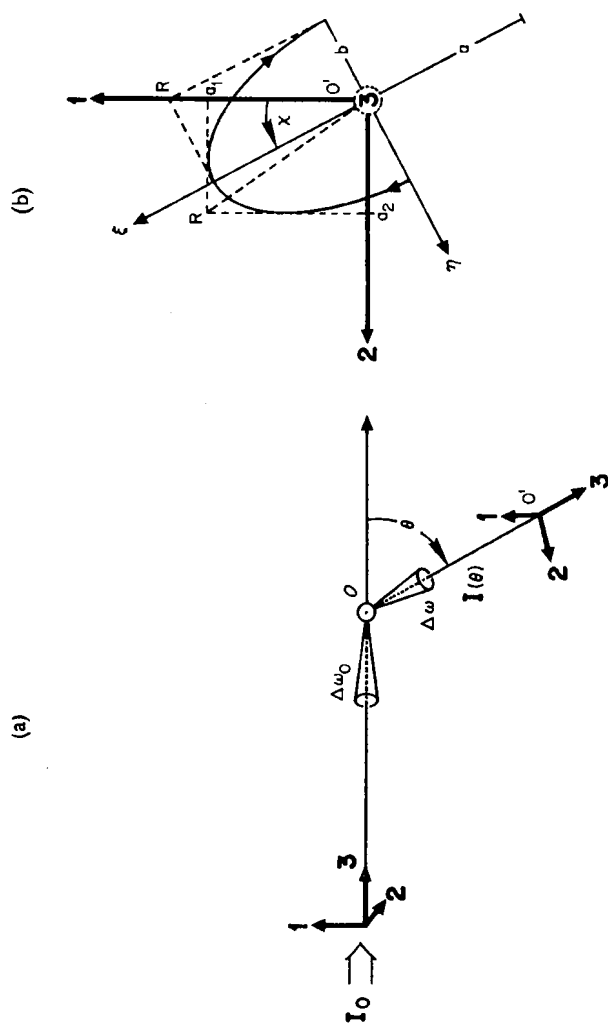


Fig. 19—Schematic diagrams illustrating an elementary scattering process and defining the coordinates. (a) Right-handed orthogonal coordinate systems for incident and scattered radiation, definition of scattering angle θ and elementary solid angles. (b) Polarization ellipse as seen against the direction of propagation, reference coordinate system, axes, and other parameters discussed in the text.

the illuminating source, assumed to be far enough so that the illuminating energy is practically in the form of "parallel rays" or plane waves from a fixed direction, and $\Delta\omega$ is the small solid angle in which the scattering is considered (see Fig. 19a). It is further assumed that we are dealing with quasi-monochromatic radiation in the wavelength interval $\Delta\lambda$. The dimensions of the elements $\sigma_i(\theta)$ of the matrix (41) are those of a differential cross section for scattering in a unit solid angle in the manner defined by Eq. (3).

The scattering element considered here, situated at the point O in the schematic diagram of Fig. 19a, may be a single spherical homogeneous particle endowed with the idealized optical properties mentioned earlier. It may also be a small *spherical* volume element of space occupied by a number of such particles, of various sizes and optical properties, whose positions are not fixed but must be in random motion within the time interval in which an observation is to be made.* Indeed, to be quite rigorous one must endow this element with somewhat inconsistent properties: The volume of space must be large enough so that a perfect sample of all the particles of the larger medium it represents are included; it must be small enough so that the source radiation entering from one hemisphere illuminates the particles in the other hemisphere with essentially unaltered intensity and state of polarization; the particles should be not only in random motion but also sufficiently sparse in the volume so that there is no self-illumination after a primary scattering process; finally, there should be absolutely no inhomogeneities with respect to size or type of particle anywhere within the sphere, so that the scattering process is invariant with respect to the directions of incidence and emergence provided the angle between them remains fixed.

As mentioned in the introduction, we eliminate one of the degrees of freedom in the element by restricting ourselves to scattering particles composed of the same material, that is, having fixed optical constants at the given wavelength but of variable size, with the particle concentration depending on the size. The foregoing considerations therefore will apply only to this characteristic. Despite these highly idealized requirements for the elementary scattering volume and, as in the mathematical analysis of other linear processes, for purposes of integration, the abstraction from the physical to a mathematical element for differential scattering is known to lead to meaningful results. This is eminently true in atmospheric scattering, for example, where the assumption of a linear process in the

* Otherwise the scattering process would have to be defined in terms of the interaction between the complex *amplitudes* rather than the intensities.

form of independent or incoherent scattering is almost always realized. Naturally the magnitude of the geometrical volume of the element considered may be varied according to the particle sizes and concentrations involved. In the case of well-mixed "clear" air near the earth's surface, containing micron-sized aerosol particles, the volume may be taken to be of the order of a few cubic centimeters. The same applies to moderately dense but stable stratiform clouds. However, in the case of dense cumulus clouds, the size-distribution law may change within distances of the order of meters, in which case a volume element of 1 cm^3 must be assigned a size distribution and concentration that is typical within a volume of several cubic meters. In the case of raindrops illuminated by microwave radiation, the volume element is usually of the order of cubic meters. In the case of the interplanetary dust particles responsible for the zodiacal light, one may have to consider a volume of several hundred cubic kilometers as a representative element; and so on for interstellar and intergalactic particles.

3.21 Derivation and Properties of the Stokes Parameters

Since a complete derivation of the Stokes parameters is not readily available in one place in the recent literature, it may be useful to outline the major steps leading to the relations between these parameters and the state of polarization of a stream of radiation. Consider an elementary scattering process on a single particle at the point O in Fig. 19a and assume that this results in a *fully polarized* pencil of monochromatic radiation such that the polarization ellipse has an arbitrary orientation, propagating in the direction 3 (*out* of the page in Fig. 19b). This direction, together with that of propagation of the source radiation I_0 and the point O , define the *scattering plane*. The other two directions 1 and 2 , which together with 3 form a right-handed orthogonal coordinate system centered at the observation point O' , are always chosen so that they are perpendicular and parallel, respectively, to the scattering plane.

In order to find the relation between the Stokes elements of I_0 and I connected by the scattering matrix (41), and the complex amplitudes S_1 and S_2 given by the theory, we first make two quite valid assumptions: (i) on the experimental side, that we can determine (e.g., by means of analyzers and retardation plates) *time-average* intensities and phase differences related to the electric field vibration along the directions 1 and 2 [cf. 45, p. 688]; and (ii) on the theoretical side, that we can express the values of the complex amplitudes along the same directions in terms of the amplitudes of the source radiation, which is in fact what the Mie theory does. Considering the field along a *fixed* plane through the point O'

(sufficiently removed from O so that the radiation conditions are fulfilled) as in Fig. 19b, and assuming the usual harmonic time oscillation of the electric field \mathbf{E} , of angular frequency ω , we can write

$$\begin{aligned} E_1 &= a_1 \sin(\omega t - \varphi_1) = a_1 \sin \psi, \\ E_2 &= a_2 \sin(\omega t - \varphi_2) = a_2 \sin(\psi + \delta), \end{aligned} \quad (42)$$

where

$$\psi \equiv \omega t - \varphi_1, \quad \delta \equiv \varphi_1 - \varphi_2$$

for its components along **1** and **2**, respectively; a_1 and a_2 are the maximum amplitude components along these axes; and φ_1 and φ_2 are phase angles related in such a way that $\varphi_1 - \varphi_2 = \delta \neq 0$ is a constant. By the foregoing assumption a_1 and a_2 must have fixed magnitudes. The second form on the right-hand side of expression (42) is the parametric representation of the resultant of two *coupled* harmonic motions along **1** and **2** describing an ellipse. To see this, one can eliminate ψ by using trigonometric identities, and after algebraic simplification one gets from (42)

$$\left(\frac{E_1}{a_1}\right)^2 + \left(\frac{E_2}{a_2}\right)^2 - 2 \frac{E_1 E_2}{a_1 a_2} \cos \delta = \sin^2 \delta. \quad (43)$$

This is the general equation of an ellipse traced by the end point of the electric field vector, whose major and minor axes along ξ and η , respectively, do not necessarily coincide with those of the coordinate system **1**, **2**, but make an angle χ with them. To find χ , we perform the standard rotation of axes, represented by the operation

$$\begin{pmatrix} E_\xi \\ E_\eta \end{pmatrix} = \begin{pmatrix} \cos \chi & \sin \chi \\ -\sin \chi & \cos \chi \end{pmatrix} \begin{pmatrix} E_1 \\ E_2 \end{pmatrix},$$

which yields the field components along ξ and η , namely, from (42),

$$\begin{aligned} E_\xi &= a_1 \sin \psi \cos \chi + a_2 \sin(\psi + \delta) \sin \chi, \\ E_\eta &= -a_1 \sin \psi \sin \chi + a_2 \sin(\psi + \delta) \cos \chi. \end{aligned}$$

After expanding $\sin(\psi + \delta)$, these may be written in the form

$$\begin{aligned} E_\xi &= A_1 \sin \psi + A_2 \cos \psi, \\ E_\eta &= A_3 \sin \psi + A_4 \cos \psi \end{aligned} \quad (44)$$

with

$$\begin{aligned} A_1 &\equiv a_1 \cos \chi + a_2 \sin \chi \cos \delta, \\ A_2 &\equiv a_2 \sin \delta \sin \chi, \\ A_3 &\equiv -a_1 \sin \chi + a_2 \cos \chi \cos \delta, \\ A_4 &\equiv a_2 \sin \delta \cos \chi. \end{aligned} \quad (45)$$

Eliminating ψ from the system (44) and simplifying, we get

$$\frac{A_3^2 + A_4^2}{A^2} E_\xi^2 + \frac{A_1^2 + A_2^2}{A^2} E_\eta^2 - 2 \frac{A_1 A_3 + A_2 A_4}{A^2} E_\xi E_\eta = 1 \quad (46)$$

where, by virtue of (45) and after simplification, we have put

$$\begin{aligned} A^2 &\equiv (A_1 A_4 - A_2 A_3)^2 \\ &= (a_1 a_2 \sin \delta)^2 \neq 0. \end{aligned}$$

We note first that (46) has no meaning if $A^2 = 0$, that is, when $\sin \delta = 0$ or $\delta = n\pi$, where n is any integer or zero. (Actually this latter case represents a degenerate ellipse, where the minor axis vanishes.) Next we note that by definition of the foregoing rotation of axes, (46) must be in the so-called normal form of the equation of an ellipse,

$$\left(\frac{\xi}{a}\right)^2 + \left(\frac{\eta}{b}\right)^2 = 1$$

centered at the origin with the semimajor axis a along ξ and the semiminor axis b along η . By comparison with (46) we note that the third term on the left must vanish, or

$$A_1 A_3 + A_2 A_4 = 0,$$

which, from (45), after rearrangement and simplification, reduces to

$$a_1 a_2 \cos 2\chi \cos \delta = \frac{1}{2}(a_1^2 - a_2^2) \sin 2\chi$$

or

$$\tan 2\chi = \frac{2a_1 a_2 \cos \delta}{a_1^2 - a_2^2}. \quad (47)$$

The relation (47) may be assumed to hold even when $a_1 = \pm a_2$ or $\cos 2\chi = 0$, in which case $\chi = (2n + 1)\pi/4$, and there is an ambiguity regarding the quadrant of **1, 2** plane in which the major axis lies. This ambiguity is resolved by a knowledge of the phase difference δ .

We obtain further relations by identifying the semimajor and minor axes of the ellipse from (46). With (47) remaining valid, we have

$$a^2 = \frac{A^2}{A_3^2 + A_4^2}, \quad b^2 = \frac{A^2}{A_1^2 + A_2^2},$$

or

$$\frac{1}{a^2} + \frac{1}{b^2} = \frac{A_1^2 + A_2^2 + A_3^2 + A_4^2}{A^2}.$$

But from the definitions (45) we note that the numerator on the right-hand side in the preceding equation reduces to $a_1^2 + a_2^2$. Hence, using also the value of A^2 already noted, we have

$$\frac{a^2 + b^2}{a^2 b^2} = \frac{a_1^2 + a_2^2}{(a_1 a_2 \sin \delta)^2}. \quad (48)$$

Now it can be shown analytically (and neither the statement nor the derivation of this theorem is to be found in modern college texts on analytical geometry) that for a given ellipse, *the length of the diagonal D (corresponding to $2(O'R)$ in Fig. 19b) of any circumscribed rectangle is an invariant given by*

$$D^2 = (2a)^2 + (2b)^2$$

for all angles χ . From this it follows that for all χ

$$a_1^2 + a_2^2 = a^2 + b^2 \quad (49)$$

and hence, by comparison with (48),

$$ab = \pm a_1 a_2 \sin \delta. \quad (50)$$

The important relations (47), (49), and (50) are derived in a somewhat different way by Born and Wolf [45, pp. 26, 27] and Chandrasekhar [40, pp. 25–29], who is generally credited with reviving the use of Stokes parameters in radiative transfer problems.

Before arriving at the expressions for the Stokes parameters proper, we need a few additional relations. Define an angle β such that

$$\frac{b}{a} = \tan \beta, \quad -\frac{\pi}{4} \leq \beta \leq \frac{\pi}{4},$$

whence, by the usual properties of ratios and trigonometric identities, we obtain

$$\pm \frac{2ab}{a^2 + b^2} = \sin 2\beta; \quad \frac{a^2 - b^2}{a^2 + b^2} = \cos 2\beta. \quad (51)$$

Similarly, introduction of another auxiliary angle α such that

$$\frac{a_2}{a_1} = \tan \alpha, \quad 0 \leq \alpha \leq \frac{\pi}{2},$$

yields

$$\frac{2a_1 a_2}{a_1^2 + a_2^2} = \sin 2\alpha; \quad \frac{a_1^2 - a_2^2}{a_1^2 + a_2^2} = \cos 2\alpha, \quad (52)$$

which, when replaced in (47), results in

$$\tan 2\chi = \tan 2\alpha \cos \delta. \quad (53)$$

Finally, division of (50) by (49) yields

$$\pm \frac{2ab}{a^2 + b^2} = \frac{2a_1a_2}{a_1^2 + a_2^2} \sin \delta \quad (54)$$

or, by (51) and (52),

$$\sin 2\beta = \sin 2\alpha \sin \delta. \quad (55)$$

In order to obtain the relations among the *four Stokes parameters* I , Q , U , V , for a fully polarized stream and the polarization parameters represented by the angles χ and β , we first *identify* the former as follows*:

$$\begin{aligned} I &\equiv a_1^2 + a_2^2, \\ Q &\equiv a_1^2 - a_2^2, \\ U &\equiv 2a_1a_2 \cos \delta, \\ -V &\equiv 2a_1a_2 \sin \delta, \end{aligned} \quad (56)$$

where an appropriate conversion factor between the energy fluxes on the left-hand sides and the squared amplitudes of the electric field on the right-hand sides, respectively, has been omitted for simplicity. Squaring and adding all four parameters in (56), we note that

$$I^2 = Q^2 + U^2 + V^2, \quad (57)$$

which is *valid only when no unpolarized radiation is present in the stream considered*.

Next, from (47), (51), and (54) we have

$$U = Q \tan 2\chi,$$

$$V = I \sin 2\beta,$$

which, when substituted into (57), yield

$$Q^2(1 + \tan^2 2\chi) = I^2(1 - \sin^2 2\beta)$$

or

$$Q^2 = (I \cos 2\beta \cos 2\chi)^2.$$

* We are indebted to J. W. Hovenier and H. C. van de Hulst (private communication) for the negative sign of V here [43, p. 418; 41, p. 48; I , p. 41] for consistency with our representation of the phase angles and their difference as in (42).

Thus we can write down the expressions for the four Stokes parameters in two convenient forms that fully describe the state of polarization, namely,

$$I = I_1 + I_2, \quad (58a)$$

$$Q = I_1 - I_2 = I \cos 2\chi \cos 2\beta, \quad (58b)$$

$$U = Q \tan 2\chi = I \sin 2\chi \cos 2\beta, \quad (58c)$$

$$V = Q \frac{\tan 2\beta}{\cos 2\chi} = I \sin 2\beta. \quad (58d)$$

There remains the question of the sense of rotation of the end point of the electric vector describing the ellipse. From the expressions (42) for the components E_1 and E_2 , we note that if $0 < \delta < \pi$, the end point of the resultant electric field vector will trace the ellipse in the *clockwise* sense in the fixed plane through O' , as indicated by the arrows on the ellipse of Fig. 19b. Shurcliff [39, p. 3] justifies the nomenclature *right-handed polarization* for this situation, by pointing out that at a *fixed time instant* the end points of the vectors in a continuous wave train would trace a right-handed helix or screw thread without ambiguity. The polarization would be left-handed (counterclockwise in the plane of Fig. 19b) if $-\pi < \delta < 0$.

Through (55) and (58d), since $\sin 2\alpha > 0$ by definition, it is clear that the sign of the Stokes parameter V determines the sense of rotation, the polarization being right-handed in the sense explained in the preceding paragraph whenever $V > 0$ or $\sin 2\beta > 0$ and $0 < \beta < \pi/2$. However, since we have defined β such that $|\tan \beta| \leq 0$ is always the ratio of the minor to the major axis of the ellipse, these conditions become

$$0 < \delta < \pi, \quad 0 < \beta \leq \frac{\pi}{4}, \quad \text{right-handed polarization;}$$

$$-\pi < \delta < 0, \quad -\frac{\pi}{4} \leq \beta < 0, \quad \text{left-handed polarization.}$$

From symmetry considerations, we can also eliminate the ambiguity regarding χ mentioned after Eq. (47) by restricting this angle to values $-\pi/2 \leq \chi \leq \pi/2$.

Thus the state of polarization of a given stream is completely specified by the four Stokes parameters, obtained either experimentally by measuring the two amplitude components a_1 and a_2 and their phase difference δ , according to (56), or theoretically by determining the elements of the transformation matrix (41), given the state of polarization of the incident

stream. Table 4 is a convenient listing of selected types of complete polarization with typical values of the three polarization parameters Q , U , V and the corresponding values of the auxiliary angles χ , β , and δ . This table may be compared with a similar one given by Shurcliff [39, p. 23] and graphical examples in Born and Wolf's text [45, p. 29], noting the differences that arise from our particular choice of coordinates. This

Table 4
Examples of completely polarized light

Type	Q/I	U/I	V/I	χ	β	δ	Description of polarization
(i)	1	0	0	0	0	0	Linear, vertical
(ii)	-1	0	0	$\frac{\pi}{2}$	0	0	Linear, horizontal
(iii)	0	1	0	$\frac{\pi}{4}$	0	0	Linear, 1st and 3rd quadrants
(iv)	0	-1	0	$-\frac{\pi}{4}$	0	0	Linear, 2nd and 4th quadrants
(v)	0	0	1		$\frac{\pi}{4}$	$\frac{\pi}{2}$	Circular, right-handed
(vi)	0	0	-1		$-\frac{\pi}{4}$	$-\frac{\pi}{2}$	Circular, left-handed
(vii)	$\frac{1}{4}$	$\frac{\sqrt{3}}{4}$	$\frac{\sqrt{3}}{2}$	$\frac{\pi}{6}$	$\frac{\pi}{6}$	$\arcsin \sqrt{\frac{4}{5}}$	Elliptical, right-handed, 1st and 3rd quadrants
(viii)	$-\frac{1}{4}$	$-\frac{\sqrt{3}}{4}$	$-\frac{\sqrt{3}}{2}$	$-\frac{\pi}{6}$	$-\frac{\pi}{6}$	$-\arcsin \sqrt{\frac{4}{5}}$	Elliptical, left-handed, 2nd and 4th quadrants

latter choice has been made mainly in deference to the best-known type of scattering polarization, discovered by Lord Rayleigh [5], which with natural sunlight always results in positive linear polarization, or $Q/I > 0$ and $\chi = 0$, provided multiple scattering may be neglected. The same is true of polarization produced by reflection on an ideal flat interface between a dielectric and free space.

Two additional properties of the Stokes parameters must be mentioned, remembering that these parameters are true operational physical concepts in the sense of P. W. Bridgman [46]. In fact, the usefulness of the Stokes

parameters hinges entirely on our ability to measure, by available techniques of optical analysis, intensities in any two fixed and mutually perpendicular directions **1** and **2** and their difference, as well as an apparent phase difference between them (over a time interval that is generally much longer than the period of vibration). It is evident, therefore, that this definition introduces a certain degree of arbitrariness, depending for example on the limitations imposed by the time constant of sensors. In a similar fashion, “*natural*” or *unpolarized light* may be operationally defined in terms of our inability to determine a finite intensity difference Q and phase difference δ for *any* fixed orientation of the axes **1** and **2**. In terms of the Stokes parameters, this definition is equivalent to the ideal condition

$$Q = U = V = 0. \quad (59)$$

However, in the preceding derivation of the Stokes parameters we have assumed a strictly monochromatic radiation of a fixed angular frequency ω , which may always be expressed in terms of the *coupled* harmonic oscillations as in (42). But this type of radiation will always display a state of pure polarization conforming to one of the types illustrated in Table 4, and the condition (59) is never realized. The only condition under which unpolarized yet strictly monochromatic radiation may be visualized is by the *addition of two uncoupled and oppositely polarized streams*, as exemplified by the pairs (i), (ii); (iii), (iv); (v), (vi); and (vii), (viii) in Table 4. It is difficult to devise a technique to accomplish this experimentally.

Actually, since strictly monochromatic light is seldom found in nature, the state of polarization will never be pure, in which case we speak of *partial polarization*. This brings us to the second property of the parameters first pointed out by Stokes, according to Chandrasekhar [40, pp. 31–33], who also gives its proof. This property allows any stream of quasi-monochromatic light to be represented as a mixture of an unpolarized component $I^{(N)}$ of the type (59) and a purely polarized component $I^{(II)}$ of the types in Table 4, in which case

$$(I^{(N)} + I^{(II)})^2 = I^2 > Q^2 + U^2 + V^2. \quad (60)$$

The *degree of partial polarization* Π may then be defined unambiguously by means of the positive ratio

$$0 \leq \frac{I^{(II)}}{I^{(II)} + I^{(N)}} \equiv \Pi = \frac{(Q^2 + U^2 + V^2)^{1/2}}{I} < 1, \quad (61)$$

and the Stokes vector for a partially polarized stream may be separated into its two components by putting

$$\begin{aligned}\mathbf{I}^{(N)} &= \{I - (Q^2 + U^2 + V^2)^{1/2}, 0, 0, 0\}, \\ \mathbf{I}^{(II)} &= \{(Q^2 + U^2 + V^2)^{1/2}, Q, U, V\}.\end{aligned}\quad (62)$$

Summarizing this section, we have outlined the steps leading to the expressions for the Stokes parameters by considering an idealized electromagnetic oscillation at a single frequency. We have described their properties and relations, in particular the two most important ones resulting from their operational definition: the additivity of the parameters for two independent streams of light that have been made to coincide in direction and sense of propagation; and the possibility of representing an arbitrary state of partial polarization, such as is likely to be found in nature, in terms of the parameters for two idealized component streams, corresponding to purely unpolarized and purely polarized states, respectively. Both properties are basic to the definition of Stokes parameters for polydisperse media.

3.22 The Stokes Matrix for Mie Scattering

We are now in a position to identify the elements of the matrix (41) in terms of the Mie parameters. The form of this matrix was first derived by Perrin [43] in a very clear and elegant paper based on the idealized optical properties of the Mie scatterers. In brief, his derivation is based on P. Solleilet's* principle that the transformation of the Stokes intensity vector by a generally *homogeneous* and *linear* optical process may be represented by 16 independent coefficients arranged in a 4 by 4 matrix. If the process takes place in an isotropic medium, at any given frequency the coefficients will be functions only of the angle θ between the incident and emergent radiation. The number of independent coefficients is then successively reduced to:

- 10, by considering the principle of reciprocity (no fluorescence or Raman effect);
- 8, by considering mirror symmetry in the medium;
- 6, by considering no rotatory power in the medium; and finally
- 4, by considering spherical symmetry in addition to the foregoing

which results in the form shown in (41).

* According to a 1929 paper cited by Perrin [43].

In a later paper, which is more interesting for our purposes (and which is not mentioned by van de Hulst [1, pp. 46 ff.] in his perspicuous interpretation of these properties), Perrin and Abragam [44] pursue the analysis further. They point out that in deriving his original expressions, Mie [3] either explicitly or implicitly assumed a transformation of the incident stream corresponding to pure scattering only, on a homogeneous sphere of otherwise optically inactive material, characterized only by a difference in (complex) refractive index with respect to the surrounding medium, and possessing all the symmetries mentioned above. Since under these assumptions any scattering plane is also a plane of symmetry, they demonstrate that only two complex numbers operating on the amplitudes perpendicular and parallel to this plane are sufficient to describe the complete scattering transformation of the Stokes vector of the incident stream. These numbers are identified as the original Mie amplitude functions given in Section 2.2 by the expressions (1) and (2) and having the property (4), and it is shown [44] that the elements of the matrix (41) are

$$\begin{aligned}\sigma_1(\theta) &= A_1 A_1^*, \\ \sigma_2(\theta) &= A_2 A_2^*, \\ \sigma_3(\theta) &= \frac{1}{2} (A_1 A_2^* + A_2 A_1^*) = \operatorname{Re}\{A_1 A_2^*\}, \\ \sigma_4(\theta) &= \frac{i}{2} (A_1 A_2^* - A_2 A_1^*) = -\operatorname{Im}\{A_1 A_2^*\},\end{aligned}\tag{63}$$

in which the last two relations follow from the property of complex numbers

$$\begin{aligned}\operatorname{Re}\{A_1 A_2^*\} &= \operatorname{Re}\{A_2 A_1^*\}, \\ \operatorname{Im}\{A_1 A_2^*\} &= -\operatorname{Im}\{A_2 A_1^*\}.\end{aligned}$$

Hence an elementary scattering process on a *single* particle of this sort (or per particle in a small collection of *identical* particles under conditions of independent scattering as in Section 3.2), according to (40), (41), and (63), is described by the matrix equation

$$\begin{pmatrix} I_1 \\ I_2 \\ U \\ V \end{pmatrix} = \begin{pmatrix} A_1 A_1 & 0 & 0 & 0 \\ 0 & A_2 A_2^* & 0 & 0 \\ 0 & 0 & \operatorname{Re}\{A_1 A_2^*\} & -\operatorname{Im}\{A_1 A_2^*\} \\ 0 & 0 & \operatorname{Im}\{A_1 A_2^*\} & \operatorname{Re}\{A_1 A_2^*\} \end{pmatrix} \begin{pmatrix} I_{01} \\ I_{02} \\ U_0 \\ V_0 \end{pmatrix}, \tag{64}$$

or, carrying out the multiplication and using the symbols in (63) for

simplicity, we have

$$\begin{aligned}
 I_1 &= \sigma_1 I_{01}, \\
 I_2 &= \sigma_2 I_{02}, \\
 U &= \sigma_3 U_0 + \sigma_4 V_0, \\
 V &= -\sigma_4 U_0 + \sigma_3 V_0.
 \end{aligned} \tag{65}$$

Note, in passing, that in (41) and (64) we have replaced the two first Stokes parameters I and Q by the set I_1 and I_2 , which simplifies the form of the scattering matrix and operations. The two sets are entirely equivalent by virtue of the expressions (58a) and (58b), whereby $I_1 = \frac{1}{2}(I + Q)$ and $I_2 = \frac{1}{2}(I - Q)$. For the sake of uniformity, we shall henceforth use the *modified set of Stokes parameters and matrix*, represented by (I_1, I_2, U, V) and (41), respectively, rather than the primitive set favored by the authors quoted in this section. (This convention is also followed in the tabulations.) It is easy to verify that in this system the criteria for full or partial polarization respectively reduce to

$$\frac{4I_1 I_2}{U^2 + V^2} \geq 1 \tag{66}$$

but the degree of partial polarization is always defined by the ratio (61).

In the above-mentioned paper, Perrin and Abragam [44] derived a relation between the elements $\sigma_j(\theta)$ that has a consequence for polydisperse scattering not pointed out in the literature, so far as we know. This relation in the present notation reduces to

$$\frac{\sigma_1 \sigma_2}{\sigma_3^2 + \sigma_4^2} = 1 \tag{67}$$

and is *valid only for a single Mie scatterer or for a collection of scatterers identical in size and optical properties*. Forming the ratio (66) using (65) and simplifying, we get

$$\frac{4I_1 I_2}{U^2 + V^2} = \frac{4I_{01} I_{02}}{U_0^2 + V_0^2} \frac{\sigma_1 \sigma_2}{\sigma_3^2 + \sigma_4^2}. \tag{68}$$

It is then clear from (66), (67), and (68) that *if the incident radiation is fully polarized, the process of primary scattering on a single Mie particle will yield fully polarized light in all directions*. It is also evident, however, that unpolarized incident light does not necessarily yield unpolarized

scattered light, except in the forward and backward directions, since generally $\sigma_1 \neq \sigma_2$ for single spheres. Furthermore, if the incident light is either unpolarized or linearly polarized, as in examples (i) and (ii) of Table 4, the scattering will produce partial or full *linear* polarization. Moreover, from the relations (65) it is seen that elliptically polarized light can result only by scattering of fully or partially polarized incident light, as in the examples (iii) through (viii) in Table 4.

The corollary to the property (67), also derived by the same authors [44], is even more interesting for our purposes. According to this, for a *collection of scatterers that is heterogeneous*, by virtue of variations in either their size or optical properties, or both, the ratio (67) always exceeds unity; or, borrowing the notation to be introduced later (cf. Section 3.32),

$$\frac{P_1(\theta)P_2(\theta)}{P_3^2(\theta) + P_4^2(\theta)} > 1, \quad (69)$$

where the $P_j(\theta)$ are the scattering elements for a polydispersion equivalent to the $\sigma_j(\theta)$ for single particles. It then follows immediately from the relation (68) that, in this case, the resultant stream will be only partially polarized even if the incident light is fully polarized. In other words, *a single act of scattering of fully polarized light on a polydispersion of Mie-type particles results in some depolarization at all scattering angles except the exact forward and backward directions*. This does not apply to particle polydispersions that are all in the Rayleigh range, however, in which case the ratio (69) will be very close to unity.

This important property is verified by our numerical results as presented in the tables. Some examples were shown in the appendix of a report on microwave scattering [47, pp. 36, 37]. For single spheres the relation (67) should of course always hold, and this would provide a good check on the numerical accuracy of Mie amplitudes obtained by the present or other computational schemes.

The foregoing polarization properties also suggest an experimental application: Assuming that very nearly monochromatic and fully polarized light can be produced (e.g., laser light) and the polarization of the scattered light can be exactly determined experimentally, the observed degree of depolarization could be a measure of the heterogeneity of a collection of scatterers otherwise assumed to be identical or monodisperse. This technique could be especially valuable when the scatterers cannot be isolated and examined as to size and composition, but are available only as colloidal suspensions, hydrosols, or aerosols.

3.3 THE STOKES MATRIX ELEMENTS FOR A POLYDISPERSION

In most problems of atmospheric scattering we have to deal with a collection of particles within the illuminated volume. Since the incident energy may be of arbitrary magnitude, expressed in a particular system of physical units governed by experimental conditions and the preferences of the researcher, it is convenient to normalize the incident flux to unity. On the other hand, since the number concentration and size distribution of the scatterers per unit volume is arbitrary, it is also useful to separate these parameters in the elements of the scattering matrix from those describing the angular distribution and the polarization. Furthermore, the directionally scattered intensity can itself be normalized with respect to the total flux scattered in all directions.

These three normalizations are necessary not only in understanding the elementary scattering process, but also in the mathematical formulation of the transfer problem in extended media.

3.31 Normalization and Separation in Monodisperse Systems

The first normalization mentioned above is readily performed, for a quasi point source like the Sun, by setting in (40)

$$\lim_{\Delta\omega_0 \rightarrow 0} I_0 \Delta\omega_0 = F \quad (70)$$

where I_0 is a Dirac delta function in the direction of the Sun and F is the flux or incident power per unit area expressed in some appropriate physical units. The single scattering process (40) may then be expressed in the form

$$\mathbf{I}(\theta) = F\boldsymbol{\sigma}(\theta) \cdot \mathbf{F}_0 \quad (71)$$

where \mathbf{F}_0 is the dimensionless Stokes vector $\{F_{01}, F_{02}, U_0, V_0\}$ such that $F_{01} + F_{02} = 1$ always, and any one of the types of radiation illustrated in Table 4, or pairs thereof corresponding to unpolarized light, may be substituted for \mathbf{F}_0 , provided we set $I = 1$ in that table.

To accomplish the second type of normalization we proceed as follows. For a single particle and in analogy with (39) we first extend the definitions of the Mie intensity functions by setting

$$\begin{aligned} \sigma_1(\theta) &= A_1 A_1^* = k^{-2} i_1(\theta), \\ \sigma_2(\theta) &= A_2 A_2^* = k^{-2} i_2(\theta), \\ \sigma_3(\theta) &= \text{Re}\{A_1 A_2^*\} = k^{-2} i_3(\theta), \\ \sigma_4(\theta) &= -\text{Im}\{A_1 A_2^*\} = k^{-2} i_4(\theta). \end{aligned} \quad (72)$$

Using these expressions in the integral (4) and dividing both sides by $\pi r^2 K_{sc}(x) = \sigma_{sc}(x)$, we obtain the *normalization condition*,

$$\begin{aligned} 1 &= \frac{1}{2\pi} \int_{\Omega} \left(\frac{A_1 A_1^*}{r^2 K_{sc}} + \frac{A_2 A_2^*}{r^2 K_{sc}} \right) d\omega \\ &= \frac{1}{4\pi} \int_{\Omega} \left[\frac{2i_1(\theta)}{x^2 K_{sc}} + \frac{2i_2(\theta)}{x^2 K_{sc}} \right] d\omega \end{aligned} \quad (73)$$

where the integration is with respect to solid angle over all directions around the point occupied by the particle. The expression

$$\frac{2}{x^2 K_{sc}(x)} [i_1(\theta) + i_2(\theta)] \equiv \frac{1}{2} [P_1(\theta) + P_2(\theta)] \quad (74)$$

has been called the *normalized phase function* for scattering because its integral over all directions gives the number 4π , that is, the solid angle corresponding to all space around a point. Our choice of symbols on the right-hand side of (74) has been dictated by considerations of continuity and uniformity with our own previous work [9,10,15,28,47], which conforms to the notation introduced by Chandrasekhar [40] and adopted by Sekera [41]. (The quantity (74) is entirely equivalent to the “indicatrix of scattering,” a term preferred by Soviet authors such as Ambartsumyan [48] and Sobolev [49], who use the symbols $x(\cos \gamma)$ and $x(\gamma)$, respectively.)

At any rate, if we define four dimensionless quantities $P_j(\theta)$ by putting

$$P_j(\theta) = \frac{4i_j(\theta)}{x^2 K_{sc}(x)} = \frac{4\sigma_j(\theta)}{r^2 K_{sc}(x)}, \quad j = 1, 2, 3, 4, \quad (75)$$

according to (72) and (74) the scattering matrix (41) may be rewritten in the form

$$\sigma(\theta) = \frac{\pi r^2 K_{sc}(x)}{4\pi} \begin{pmatrix} P_1(\theta) & 0 & 0 & 0 \\ 0 & P_2(\theta) & 0 & 0 \\ 0 & 0 & P_3(\theta) & P_4(\theta) \\ 0 & 0 & -P_4(\theta) & P_3(\theta) \end{pmatrix}, \quad (76)$$

which completes the separation and the two normalizations mentioned above for the case of a single particle. For N identical particles per unit volume, which are such that the principle of additivity mentioned in Section 3.22 can be invoked, the elementary scattering process (40), with

the use of (71) and (76), takes the form

$$\begin{aligned} \mathbf{I}(\theta) &= FNr^2 \frac{K_{sc}(x)}{4} \mathbf{P}(\theta) \cdot \mathbf{F}_0 \\ &= F\beta_{sc}(N, x) \frac{\mathbf{P}(\theta) \cdot \mathbf{F}_0}{4\pi} \end{aligned} \quad (77)$$

where $\mathbf{P}(\theta)$ is the part within brackets of the matrix in (76), and where we have defined a *scattering cross section per unit volume of space* containing N particles of relative size $x = 2\pi r/\lambda$ by setting

$$\beta_{sc}(N, x) = N\pi r^2 K_{sc}(x). \quad (78)$$

Note that by virtue of the definition of \mathbf{F}_0 in (71), the sum of the first two elements of the Stokes vector $\mathbf{P} \cdot \mathbf{F}_0$ automatically satisfies the normalization condition (73).

As we shall see, in the case of a polydispersion, the foregoing separation of the scattering cross section from the angular scattering and polarization properties of the medium is useful even in problems involving optically thin media. In media of finite optical thickness, where higher-order scattering must be considered, the separation is essential, even in the homogeneous and monodisperse case, for the mathematical treatment of the problem of diffuse reflection and transmission.

3.32 Extension to Polydisperse Systems

The extension to polydisperse systems in the sense used here, that is, to spheres of identical optical constants but differing in size only, follows easily from the previous discussion. When the volume contains particles distributed in discrete sizes, the quantities N , $P_j(\theta)$, β_{sc} will be replaced by the corresponding summations, with the latter two properly weighted by the number of particles in each size range. However, as suggested by Sekera [18], it is both more elegant and more practical to replace the summations by integrals, since particle counts in most atmospheric suspensions do indicate a continuous size distribution. Actually, this question is not a simple one, being related to difficulties in the reliable collection and analysis of particle counts, especially in the free and undisturbed atmosphere and in clouds. We shall prefer the integral representation here, assuming that the distribution may indeed be represented by a continuous function of the radius within any given range of interest $r_1 \leq r \leq r_2$. The total number of particles per unit volume will thus be given by the integral

$$N = \int_{r_1}^{r_2} n(r) dr,$$

where $n(r)$ is a continuous and integrable function defined within the range, representing the partial concentration per unit volume and per unit increment of the radius r .

It is more convenient to redefine the *distribution function* $n(r)$ in terms of the Mie size parameter $x = kr = 2\pi r/\lambda$, thus introducing the wavelength λ as an independent parameter. This is necessary since for most materials the refractive index m depends on the wavelength. If, further, we can find a distribution function that takes into account *all sizes* within the volume, then the foregoing integral may be written in the form

$$N = k^{-1} \int_0^{\infty} n(x) dx \quad (79)$$

where $n(x)$ has the same form as $n(r)$ after the change of variable. Substituting (79) into (78), we immediately obtain the expression

$$\beta_{sc}[\lambda, n(x)] = \pi k^{-3} \int_0^{\infty} x^2 n(x) K_{sc}(x) dx \quad (80)$$

for the volume scattering cross section.

Similarly, by multiplying numerator and denominator of the right-hand side of (75) by $\pi k^{-3} n(x)$ and integrating them separately, we get

$$P_j(\theta) = \frac{4\pi}{k^3 \beta_{sc}} \int_0^{\infty} n(x) i_j(\theta) dx, \quad j = 1, 2, 3, 4, \quad (81)$$

for the corresponding elements of the normalized scattering matrix for the polydispersion. The functions (80) and (81) must be used to obtain the Stokes parameters for the elementary scattering process represented by (77) in the case of a polydispersion.

It remains to specify the arbitrary distribution functions $n(r)$, which so far we have only required to be continuous and integrable in the range of interest.

3.4 FORM AND PROPERTIES OF THE DISTRIBUTION FUNCTION

As in our preliminary results [15], we choose a family of distribution functions of the general form

$$n(r) = ar^{\alpha} \exp(-br^{\nu}), \quad 0 \leq r < \infty, \quad (82)$$

which vanishes at $r = 0, \infty$, and which we shall call a *modified gamma distribution* in analogy with the so-called gamma distribution, to which it

reduces when $\gamma = 1$. The four constants a , α , b , and γ are positive and real, and α is an integer. They are not independent of each other, and are related to quantities in the frequency distribution, which can be determined by measurements. For example, upon integration over the entire range of radii, we get

$$\begin{aligned} N &= a \int_0^\infty r^\alpha \exp(-br^\gamma) dr \\ &= a\gamma^{-1}b^{-(\alpha+1)/\gamma}\Gamma\left(\frac{\alpha+1}{\gamma}\right), \end{aligned} \quad (83)$$

which shows that the constant a is essentially given by N , the total number of particles per unit volume. Furthermore, differentiation of (82) with respect to r yields

$$\frac{d}{dr} n(r) = ar^{\alpha-1}(\alpha - \gamma br^\gamma)\exp(-br^\gamma), \quad (84)$$

which has three zeros, two of which are at $r = 0$ (provided $\alpha > 1$) and at $r = \infty$, respectively. If $\alpha = 1$, the derivative at the origin is equal to a . The third zero is found by putting the last factor in (84) equal to zero, which determines the absolute maximum of the function (82), whence

$$b = \frac{\alpha}{\gamma r_c^\gamma} \quad (85)$$

with

$$n(r_c) = ar_c^\alpha \exp\left(-\frac{\alpha}{\gamma}\right), \quad (86)$$

where r_c is the *mode radius* or size of maximum frequency in the distribution, obtainable from the particle counts. Thus the constant b is determined by r_c , provided α and γ are fixed or otherwise obtained from the shape of the experimental distribution curve.

One can enumerate other properties of the modified gamma distribution, such as the mean, variance, skewness, and so on, commonly used to describe statistical distribution functions, but these are not of particular interest here. A quantity of some interest is the total volume V_p occupied by the particles per unit volume of space, whence the mass of the particles may be obtained. This is also given by a definite integral, obtained after multiplying $n(r)$ by $(4/3)\pi r^3$ and integrating:

$$\begin{aligned} V_p &= \frac{4}{3}a\pi \int_0^\infty r^{\alpha+3} \exp(-br^\gamma) dr \\ &= \frac{4}{3}a\pi\gamma^{-1}b^{-(\alpha+4)/\gamma}\Gamma\left(\frac{\alpha+4}{\gamma}\right). \end{aligned} \quad (87)$$

For the case $\gamma = 1$, using the functional equation for gamma functions and by virtue of (83), (87) reduces to

$$V_p = \frac{4\pi}{3} b^{-3} N(\alpha + 1)(\alpha + 2)(\alpha + 3), \quad \gamma = 1. \quad (88)$$

Another quantity of interest is the logarithmic derivative of $n(r)$, which allows comparison with power law distributions, where $n(r)$ is assumed to vary as some negative power of the radius. Differentiating the logarithm of (82) with respect to $\ln r$, we get, by using (85),

$$\begin{aligned} r \frac{d}{dr} [\ln n(r)] &= \alpha - b\gamma r^\gamma \\ &= \alpha \left[1 - \left(\frac{r}{r_c} \right)^\gamma \right], \end{aligned} \quad (89)$$

which represents the slope of the curve $\log n(r)$ versus $\log r$. This also shows that for $\alpha > 0$, such logarithmic plots of $n(r)$ for all functions (82) are convex curves with no inflection points, having a slope given by α at $r = 0$ and approaching $-\infty$ as $r \rightarrow \infty$.

3.41 Actual Distribution Functions Used

One may construct a great variety of specific distributions based on the general form (82). Since our intention here is to present detailed tables of all Stokes matrix elements for each of these, the problem is one of judicious choice, so that the number of tables is kept within reasonable bounds while covering a sufficient range of distribution models likely to be most useful in problems of atmospheric and space particle scattering. After careful consideration of experimental data on distributions, we have chosen six basic models, which are described in Table 5 and presented graphically in Figs. 20 and 21.

Table 5 lists the numerical parameters used in constructing the models on the basis of Eq. (82). Column 1 shows the name or designation of the distribution, which also appears in the title of the main tables in Part II. Column 2 lists the total number of particles N assigned to the unit volume indicated. Column 3 shows the corresponding constant a determined by means of (83) and the other constants of the model. Columns 4 to 7 list the specific values of the parameters in (82), and column 8 includes the specific concentration, per unit volume and radius increment, at the mode radius r_c , as given by (86). In the last column of this table, we have shown the relative volume V_p occupied by the totality of the particles in the distribution, according to (87) and (88). This quantity, when multiplied by any unit volume of space and by the density of the substance of the particles, should yield the actual mass of the particles in the unit volume

Table 5
Size-distribution models used in the tables

Distribution type	N	a	r_c	α	γ	b	$n(r_c)$	$-\frac{r}{dr} \frac{d[\ln n(r)]}{dr} \geq 4$	V_p
Haze M	100 cm^{-3}	$5.3333 \cdot 10^4$	0.05μ	1	$\frac{1}{2}$	8.9443	$360.9 \text{ cm}^{-3} \mu^{-1}$	$r \geq 1.25 \mu$	$4.948 \cdot 10^{-11}$
Rain M	1000 m^{-3}	$5.3333 \cdot 10^5$	0.05 mm	1	$\frac{1}{2}$	8.9443	$3609 \text{ m}^{-3} \text{mm}^{-1}$	$r \geq 1.25 \text{ mm}$	$4.948 \cdot 10^{-7}$
Haze L	100 cm^{-3}	$4.9757 \cdot 10^6$	0.07μ	2	$\frac{1}{2}$	15.1186	$446.6 \text{ cm}^{-3} \mu^{-1}$	$r \geq 0.63 \mu$	$1.167 \cdot 10^{-11}$
Rain L	1000 m^{-3}	$4.9757 \cdot 10^7$	0.07 mm	2	$\frac{1}{2}$	15.1186	$4466 \text{ m}^{-3} \text{mm}^{-1}$	$r \geq 0.63 \text{ mm}$	$1.167 \cdot 10^{-7}$
Haze H	100 cm^{-3}	$4.0000 \cdot 10^5$	0.10μ	2	1	20.0000	$541.4 \text{ cm}^{-3} \mu^{-1}$	$r \geq 0.30 \mu$	$3.142 \cdot 10^{-12}$
Hail H	10 m^{-3}	$4.0000 \cdot 10^4$	0.10 cm	2	1	20.0000	$54.14 \text{ m}^{-3} \text{cm}^{-1}$	$r \geq 0.30 \text{ cm}$	$3.142 \cdot 10^{-7}$
Cumulus cloud, C.1	100 cm^{-3}	2.3730	4.00μ	6	1	$\frac{3}{2}$	$24.09 \text{ cm}^{-3} \mu^{-1}$	$r \geq 6.67 \mu$	$6.255 \cdot 10^{-8}$
Corona cloud, C.2	100 cm^{-3}	$1.0851 \cdot 10^{-2}$	4.00μ	8	3	$\frac{1}{24}$	$49.41 \text{ cm}^{-3} \mu^{-1}$	$r \geq 4.58 \mu$	$3.016 \cdot 10^{-8}$
MOP cloud, C.3	100 cm^{-3}	5.5556	2.00μ	8	3	$\frac{1}{3}$	$98.82 \text{ cm}^{-3} \mu^{-1}$	$r \geq 2.29 \mu$	$3.770 \cdot 10^{-9}$
Double corona cloud, C.4	100 cm^{-3}	5.5556	4.00μ	8	3	$\frac{1}{3}$	$98.82 \text{ cm}^{-3} \mu^{-1}$	$r \geq 4.29 \mu$	

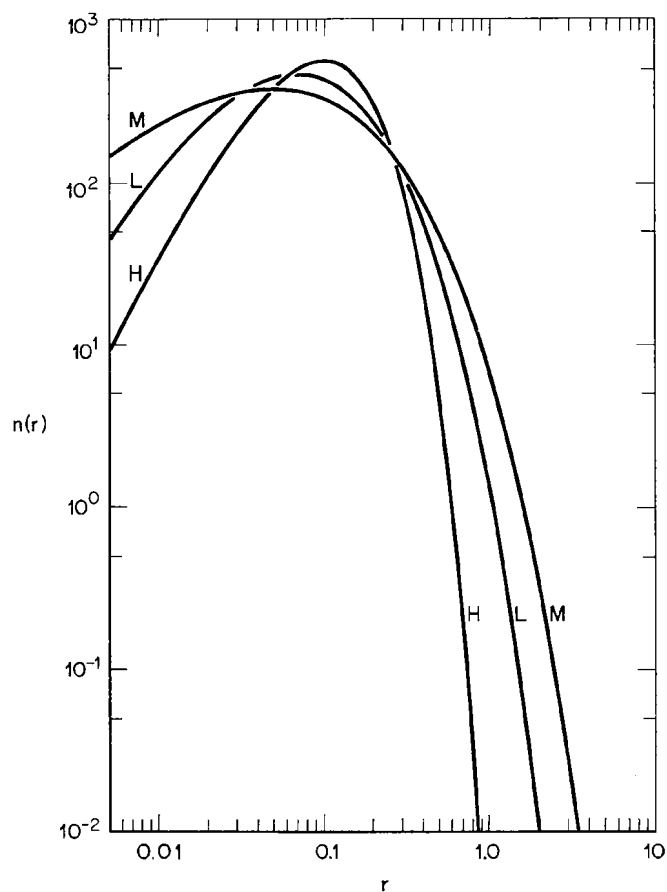


Fig. 20—Haze-type distribution functions used. The units for the radius r and for the unit volume in $n(r)$ depend on the particular model (see Table 5).

chosen. For example, for the cloud model C.1, we obtain a liquid water content of 0.063 g m^{-3} .

Finally, in column 9 we have indicated the values of the radius for which the negative logarithmic slope of the distribution equals or exceeds 4. From (89) this condition becomes

$$r \geq r_0 \left(1 + \frac{4}{\alpha} \right)^{1/\gamma}. \quad (90)$$

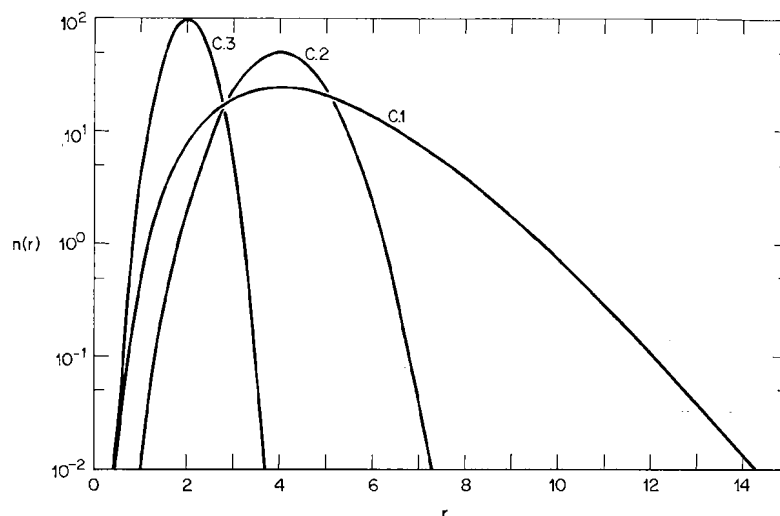


Fig. 21—Cloud-type distribution functions. The scale for the radius r is linear here, rather than logarithmic as in Fig. 20.

The corresponding point on the distribution curve is interesting for two reasons. In the case of aerosol or haze models, it indicates the region where the distribution may be approximated by a “model C” power law of the form $n(r) \propto r^{-4}$, supposed to be characteristic of continental aerosols. Second, for any of the models in Table 5, it shows the point in the distribution beyond which the integrals (81) for $\theta = 0$ begin to converge. This behavior, which has been pointed out before [9,10,26], has to do with the fact that at and near zero scattering angles the intensity parameter $i_s(x, \theta)$ varies as x^4 . Therefore, when a power distribution law is assumed, with a negative exponent not exceeding 4, the matrix elements $P_j(\theta)$ near the forward directions are not uniquely determined by the shape of the distribution alone, but are also functions of the upper limit in size in the integrations (80) and (81). In our own early work we introduced discontinuous distributions based on power laws in various regions of the size spectrum, including what we called a model C haze [10,11,12,16], which later was adopted by others. We have since abandoned these awkward distributions in favor of the continuous ones, which are more appealing analytically as well as more practical, since they do not depend on the meaningless extra parameters needed in the former to fit actual distributions.

A brief word to justify the choice of models. *Haze M* was first introduced to reproduce marine or coastal types of distributions [15,16]. By changing the size and wavelength unit from microns to millimeters and by reducing N as shown in Table 5, we were able to fit the model to certain natural raindrop distributions, and hence it was also found useful in computing microwave scattering parameters [47]. (For economy, the Stokes matrix elements corresponding to rain model M are not included in the present tabulation since they are presented in detail for various microwave frequencies in a published report [47].)

Haze L has been adopted to represent the continental-type aerosol distributions, replacing the model C power law mentioned earlier. As can be seen in Fig. 20, the number of particles for $r > 1.0 \mu$ is much smaller than in model M, and the correct logarithmic slope lies in the important region around $r = 0.63 \mu$. (We have plotted the three haze distributions on log-log coordinates in Fig. 20 for a better appreciation of the logarithmic slopes.) Applying the same transformation as above, we also adopt a *rain model L*, which approximates the drop size distribution in light and moderate rain, in better agreement with raindrop counts than the original model M. Our choice of raindrop size distributions is not as fortuitous as it may appear, for we have carefully considered existing field measurements. A survey of the extensive literature on the subject shows, in fact, that there is little agreement among various authors, and that there is no distribution that might be considered standard for any given rainfall rate. This situation is not surprising in view of the diverse natural rain-producing mechanisms and situations, levels and methods of observation, and interpretations. We have therefore limited ourselves to two models that may approximate conditions in moderate and light rain aloft [cf. 47], and leave it to the reader to decide on their validity by comparing them with observations or with other models, on the basis of the parameters in Table 5 and the curves in Fig. 20.

The *haze H* model also serves a double purpose. With a proper choice of units, it may be used to represent high-level or stratospheric aerosol or "dust" layers composed of submicron particles. A comparison with the average of several size spectra deduced by Junge, Chagnon, and Manson [50, Fig. 23], for example, shows that our model is in close agreement with the upper size limit of particles considered by these authors to be of stratospheric origin. Here again, actual measurements are scarce and standard distributions can hardly be postulated. Changing the size and wavelength unit to centimeters converts this model to a hailstone distribution, called here *hail H*. The situation regarding actual hailstone size distributions

seems to be worse than that of raindrops. In our choice we have been somewhat guided by the recent work of Battan and Theiss [51,52], which suggests that hailstones aloft may contain a larger proportion of smaller stones than indicated by ground collectors.

As to cloud droplet distributions, *model C.1* is identical with our original one [13,15,16], developed to represent *cumulus clouds* of moderate thickness. This model contains the widest distribution among all our models. Although actual counts show that distributions in thicker cumulus and in stratiform clouds and fog may be wider, with a larger mode radius, it is impractical to include such models in the present work. The general trend in the variation of scattering properties as the size distribution becomes wider is sufficiently illustrated by the models considered here. Incidentally, model C.1 has the highest liquid water content among the four cloud models considered and is the most skewed toward large drops, as can be appreciated from Fig. 21. (The cloud distributions are plotted on semilog coordinates for better display.)

What we have called *corona cloud*, or *model C.2*, has the same mode radius of 4μ as in C.1, but the distribution is much narrower and almost symmetrical. To our knowledge there are no observations of cloud drop size indicating that such a distribution actually exists in nature. As the name indicates, we have chosen this distribution in our attempt to find a model whose integrated angular scattering properties will indicate colored coronas of the right radius. The question of coronas will be discussed further later, in Section 4.32.

The *mother-of-pearl*, or *model C.3* cloud, we devised in an attempt to reproduce the color phenomena observed when these high-altitude clouds are present at twilight. To our knowledge, the actual capture and the analysis of the nature and size of such cloud particles have never been reported. This model may also be used to investigate the phenomenon of the Bishop's ring (see Section 4.31), since the model's mode radius of 2μ is close to the characteristic sizes attributed to the responsible particles. The distribution here is extremely narrow and practically symmetrical, with almost all the particles contained within the range $1 \leq r \leq 3 \mu$, but it is not strictly monodisperse with respect to scattering effects.

Finally, the *double corona* or *model C.4* cloud distribution (not shown on Fig. 21) is identical to that in C.3 and is obtained by a translation of the origin of the sizes to the left by two units. The actual distribution function used is given by

$$n(r) = 5.5556(r - 2)^8 \exp \left[-\frac{1}{3}(r - 2)^3 \right] \mu^{-1}\text{cm}^{-3} \quad (91)$$

where the constant a is the same as for model C.3, as determined from (83) on the basis of $N = 100 \text{ cm}^{-3}$. We have put model C.4 to a very limited use (see Tables T.70 and T.71 in Part II), mainly to reproduce the rare phenomenon of a clearly defined double or triple corona around the sun. We have not computed the exact volume V_p for this model, but it should be about eight times that shown for model C.3.

In general, although we have had to limit the number of models used in the tables of Part II, our manner of presentation and tabulation affords the reader considerable latitude and flexibility. First of all, the standard concentration N can of course be adjusted by a factor to fit any desired value, in which case β_{ex} (and β_{sc}) will change by the same factor, while the P_j and ϖ values will remain unaltered. More important, additional *composite size-distribution models* can be generated by addition and subtraction, in any desired proportion, of those listed in Table 5. By virtue of the additivity of the Stokes parameters, the corresponding scattering parameters can be easily evaluated from the tabulated ones, provided they are properly weighted (see Section 4.31).

3.5 CHOICE OF REFRACTIVE INDICES (OPTICAL CONSTANTS)

In Chapter 2 we described the sensitivity of all the Mie scattering parameters to variations in both the real and imaginary parts of the index of refraction, as well as in the relative size of the scattering sphere. As we shall see, the corresponding integrated parameters are also sensitive not only to the shape of the distribution function and to the relative size of all the contributing particles, but also to variations in either or both optical constants of the substance of the particles, for any given distribution and wavelength. Therefore it is dangerous to make generalizations about these parameters on the basis of a limited number of models.

In trying to arrive at a judicious choice of specific values of the refractive index to be used in the model distributions, one is faced with a dilemma. Most known substances likely to form atmospheric suspensions vary in their optical constants, not only with chemical composition, but also with the wavelength. Moreover, there is often little agreement in the values of these constants obtained independently by various authors, especially in the case of absorbing dielectrics and metals. Even for that most important and common substance, liquid water, there are significant discrepancies in the absorption data, particularly in the infrared region beyond $\lambda 6 \mu$. As for "dust" particles in interplanetary and interstellar

space, not only is their nature unknown (this being precisely what is sought by analysis of their scattering and absorption properties; see Section 4.5), but the relevant conjectures put forth by different authors vary widely. Thus it would be pointless to consider more than one or two examples representing each of the types of substance suggested in the literature, such as pure and absorbing dielectrics, opaque earths, ices, and metals. From the corresponding scattering and absorption properties of polydisperse—or monodisperse—populations, one may then hope to reduce the number of choices and to pursue the research by more refined analysis of the astronomical data.

Our choice for the final tables presented here has been guided by various considerations. First of all, for obvious reasons we have tried to cover liquid water in most detail from the visible into the middle infrared, as well as the microwave region in the millimeter and centimeter range. The ice phase is not so well covered because common ice clouds are not composed of spherical particles, and the optical constants of ice in the infrared are not well known. As for other solid or liquid particles, we have limited our choice to certain materials only, such as silicates, certain clays (limonites) assumed by various authors to be present on the surface of Mars, and metals (iron). Space does not permit the inclusion of all likely materials. We have preferred instead to offer complete tables of all the scattering parameters for specific cases, letting the reader draw his own conclusions for other materials by considering the trends as one varies the optical constants that determine the real and imaginary parts of the index of refraction.

Table 6 lists the real and imaginary parts of the complex index of refraction, $m = \nu - i\kappa$, actually adopted in this work, together with the wavelength and the corresponding bulk absorption coefficient $\gamma_b = 4\pi\kappa/\lambda$. Except for liquid water in the visible and near infrared, where there is general experimental agreement, the substances indicated for other wavelengths and indices should not be taken too literally. Some remarks on our criteria for the choices follow.

For *liquid water* in the visible and near infrared, we have been mainly guided by Centeno's [53] compilation, especially for the real part of m , and have used graphical interpolation to get the values at the particular wavelengths shown in Table 6. The latter were chosen to coincide with regions of maxima and minima in the absorption spectrum. The values of γ at $\lambda 1.19$, 1.45 , 1.94 , and 2.25μ have been adapted from those given by Curcio and Petty [54] for triply distilled water at 20°C . These seemed more suitable for our purposes than the more recent determination of

Bayly, Kartha, and Stevens [55] at 25°C, in which the degree of purity of the water sample is not clearly stated. At 22.25μ we show two indices, with and without a weak absorption, respectively, to examine the effect of its neglect on the scattering and albedo of a polydispersion. In the remaining part of the infrared spectrum the values are mostly adapted from Centeno [53], except at 23.0μ . At 28.15μ we also adopt two values for κ , the second of which (i.e., $\kappa = 0.0236$) is used to show the effect of halving the absorption in this region, as suggested by McDonald [56] (see Section 4.31).

After having computed and prepared tables for all additional cases with liquid water in the infrared, based on Centeno's data as previously [16], we discovered a very recent set of consistent values for m in the range $1.0 \leq \lambda \leq 40 \mu$, published by Pontier and Dechambenoy [57]. These are based on new infrared oblique reflection measurements, and the complex index is deduced, in part, following the method proposed by Queney [58]. A comparison with the older set revealed no significant departures in the real and imaginary parts of m except around 23.0μ , where the new value shows an absorption some five times the old. Since this is in agreement with other measurements [55], we had to revise all our tables corresponding to water at 23.0μ on the basis of the new data, leaving other wavelengths unchanged. Incidentally, the newer measurements [57] near 28.15μ show an absorption that is in better agreement with Centeno's [53] rather than with McDonald's [56] preference.

The temperature dependence of the liquid water absorption coefficient in the infrared is often not explicitly stated in the literature. Hence we show no temperatures in this case in Table 6, where most values may be assumed to apply to room temperature or 20°C [53,54], and to 35°C at 23.0μ [57].

The values for liquid water at 0°C and 10°C in the millimeter and centimeter regions were computed on the basis of the Debye formula, as given by Saxton and Lane and used in our previous work [47]. According to a recent note by Lane [59], it appears that the original formula closely reproduces experimental values in the far infrared region as well. Therefore the values listed in Table 6 may be considered as reliable in the whole range $0.10 \leq \lambda \leq 8 \text{ cm}$. For ice at 0°C we have adopted a constant index of refraction for the same range, following an earlier work [47], since no new determinations have come to our attention.

For *iron* in the visible we have adopted two sets of values for the three wavelengths shown in Table 6. The first set, with the lower values for ν and κ , is identical with that used in our previous work [26,27,28] and follows closely the values mentioned by van de Hulst [1, p. 273]. The

Table 6
Indices of refraction used in the tables

Substance	λ	n	κ	γ_b (cm ⁻¹)	Source and comments
Liquid water	0.45 μ	1.3400	0.	0.	Centeno [53]
	0.70 μ	1.3300	0.	0.	Centeno [53]
	1.19 μ	1.3220	0.00001	1.056	Curcio & Petty [54], near max. absorption
	1.45 μ	1.3180	0.00030	26.000	Curcio & Petty [54], near max. absorption
	1.61 μ	1.3150	0.	0.	Centeno [53], no absorption
	1.94 μ	1.3080	0.00180	116.6	Curcio & Petty [54], near max. absorption
	2.25 μ	1.2900	0.	0.	Centeno [53], no absorption
	2.25 μ	1.2900	0.00035	19.55	Curcio & Petty [54], near min. absorption
	3.00 μ	1.3640	0.30600	12820.0	Pontier & Dechambenoy [57], max. absorption
	3.90 μ	1.3530	0.00590	190.1	Centeno [53], near min. absorption
	5.30 μ	1.3150	0.01430	339.1	Centeno [53], near min. absorption
	6.05 μ	1.3150	0.13700	2846.	Centeno [53], near max. absorption
	8.15 μ	1.2900	0.04720	727.8	Centeno [53], near min. absorption
	8.15 μ	1.2900	0.02360	363.9	McDonald [56], reduced absorption
	10.00 μ	1.2120	0.06010	755.2	Centeno [53]
	11.50 μ	1.1110	0.18310	2001.	Centeno [53]
0°C liquid water	16.60 μ	1.4400	0.40000	3028.	Centeno [53]
	0.1 cm	2.4066	0.4771	59.95	Saxton & Lane formula (as used in [47])
	0.2 cm	2.5604	0.8947	56.22	Saxton & Lane formula (as used in [47])
	0.3 cm	2.7589	1.2408	51.97	Saxton & Lane formula (as used in [47])
	0.5 cm	3.1918	1.7657	44.38	Saxton & Lane formula (as used in [47])
	1.0 cm	4.2214	2.5259	31.74	Saxton & Lane formula (as used in [47])

Table 6 (continued)

Substance	λ	ν	κ	γ_b (cm ⁻¹)	Source and comments
0°C liquid water	2.0 cm	5.8368	3.0046	18.88	Saxton & Lane formula (as used in [47])
	3.3 cm	7.1755	2.8642	10.91	Saxton & Lane formula (as used in [47])
	5.0 cm	8.1084	2.4102	6.058	Saxton & Lane formula (as used in [47])
	8.0 cm	8.7889	1.7531	2.754	Saxton & Lane formula (as used in [47])
10°C liquid water	0.1 cm	2.4806	0.7050	88.59	Saxton & Lane formula (as used in [47])
	0.3 cm	3.1060	1.6626	69.64	Saxton & Lane formula (as used in [47])
	1.0 cm	5.1553	2.8341	35.61	Saxton & Lane formula (as used in [47])
	3.3 cm	8.0253	2.2727	8.654	Saxton & Lane formula (as used in [47])
	8.0 cm	8.9218	1.1423	1.794	Saxton & Lane formula (as used in [47])
0°C ice	0.2 cm	1.7800	0.0024	0.1508	Previously used value [47]
	0.5 cm	1.7800	0.0024	0.06032	Previously used value [47]
	1.0 cm	1.7800	0.0024	0.03016	Previously used value [47]
	3.3 cm	1.7800	0.0024	0.00914	Previously used value [47]
	8.0 cm	1.7800	0.0024	0.00377	Previously used value [47]
Iron	0.441 μ	1.2800	1.3700	$3.904 \cdot 10^5$	Van de Hulst [1]; Handbook [62]
	0.589 μ	1.5100	1.6300	$3.478 \cdot 10^5$	Van de Hulst [1]; Handbook [62]
	0.668 μ	1.7000	1.8400	$3.461 \cdot 10^5$	Van de Hulst [1]; Handbook [62]
	0.441 μ	2.6600	3.8400	$1.094 \cdot 10^6$	Yolken & Kruger [60]
	0.559 μ	3.4600	3.8800	$8.278 \cdot 10^5$	Yolken & Kruger [60]
Silicate	0.668 μ	3.5700	4.0300	$7.581 \cdot 10^5$	Yolken & Kruger [60]
	0.450 μ	1.5600	0.	0.	Handbook
	0.589 μ	1.5500	0.	0.	Handbook
	0.700 μ	1.5400	0.	0.	Handbook
	0.589 μ	1.5500	0.0155	$3.307 \cdot 10^3$	Handbook
Limonite	0.589 μ	1.5500	0.1550	$3.307 \cdot 10^4$	Handbook
	0.589 μ	2.2000	0.	0.	Handbook
	0.589 μ	2.2000	0.0220	$4.694 \cdot 10^3$	Handbook
	0.589 μ	2.2000	0.2200	$4.694 \cdot 10^4$	Handbook

second set, in which the optical constants are about double those of the first, was adapted (by graphical interpolation) from recent determinations by Yolken and Kruger [60]. However, the latter do not seem to quite agree with another, independent set of recent determinations by Lenham and Treherne [61]. According to private communications from the authors of both papers, it appears that the values of the optical constants are in this case quite sensitive to the method of preparation and purity of the sample, as well as to other experimental constraints. As the scattering properties of iron or other metallic particles are of interest mainly in research on interplanetary and interstellar matter, where the conditions of condensation are unknown, it is doubtful whether the use of exact laboratory-derived values is crucial. We have prepared scattering tables for a few polydispersions on the basis of only the two sets of optical constants mentioned, hoping they will be of some use in this type of research.

As for *silicates*, our criterion in choosing an appropriate index of refraction has been to include some sort of glasslike material. In view of the numerous values for quartz and other optical materials quoted in the literature [62], we have adopted a hypothetical dielectric material with a likely refrangibility in the visible that approximates the optical properties of quartz at $\lambda 0.589 \mu$. We have also included "dirty" silicates to examine the effects of including some absorption equivalent to κ/ν equals 0.01 and 0.10, respectively.

Finally, we have used a refractive index $m = 2.2$ to represent *limonite* [62], with and without absorption, to simulate Martian dust. Again, this value should not be taken literally as characteristic of this substance, but only as an example of the scattering properties of earthlike opaque minerals.

Combining the fifty indices of refraction listed in Table 6 with the seven distribution models of Table 5, we have produced over one hundred tables of complete scattering parameters. These should be adequate to cover a wide range of problems connected with scattering, absorption, and radiative transfer in polydisperse media. In the following chapter we shall illustrate some of the applications and suggest methods to generate composite models on the basis of the tabulated data.

3.6 PREPARATION OF THE TABLES

The generation of the Mie functions used in the integrals (80) and (81) is essentially as described previously [27], except that it is now written in

FORTRAN for the current IBM 7040/7044 system in use at The RAND Corporation. Whenever $\kappa x > 30$, it automatically incorporates the double-precision subroutine mentioned in Section 2.22. It has been checked repeatedly and has been found adequate for our purposes.

The present program is set up so that for each case one has to specify the following sets of parameters: $\nu, \kappa, \lambda, n(x); x_1, \Delta x, x_2; \theta_1, \Delta\theta, \theta_2$, where x_1 and x_2 are the integration limits and Δx is the integration interval, which may be changed three times for any particular run. Note that λ is the only dimensional parameter, and the choice of its units determines also the true size r of the particles in the distribution $n(x)$. The trapezoidal rule is used with a sufficiently small summation interval Δx in each case to ensure a continuous integral as a function of x , taking into account all the contributing particles in the distribution. Also θ_1 and θ_2 are the initial and final scattering angles, usually set equal to 0° and 180° , respectively, and $\Delta\theta$ (which can also be varied three times for each case), the angular interval for which data are required. The memory capacity of the system imposes a limitation for each case, so that the number of angles θ to be displayed times the number of terms to be summed in the series for $a_n(x_2)$ and $b_n(x_2)$ must not exceed 10^4 . Otherwise there is no limitation on the size x , except in the case of large absorbing spheres, where the double-precision routine itself fails, as mentioned in Section 2.22.

It is understood that for each $x + \Delta x$ specified, the computer correctly evaluates all the scattering parameters for the individual sphere on the basis of the proper Mie series, as described in Section 2.2. Only at specified intervals, which are multiples of Δx , are the results displayed on two separate pages: on the first page the computer prints the individual values of $S_1(\theta)$, $S_2(\theta)$ (as complex numbers), K_{ex} , K_{sc} , K_{ab} , and $i_j(\theta)$, ($j = 1, 2, 3, 4$) as defined in (39) and (72), for the sphere of the particular x , m and the angles specified. On a second page are printed the values of the integrals with respect to $n(x)$ of the type

$$\beta[m, n(x), \lambda, x_1, x] = \pi k^{-3} \int_{x_1}^x x^2 n(x) K(m, x) dx \quad (92)$$

where β may be the volume scattering, absorption, or extinction cross section, according as K_{sc} , K_{ab} , or K_{ex} is used in the integrand on the right-hand side; and the values of $P_j(\theta)/4\pi$ given by the integral (81) over the same limits as in (92) and for the same angles as on the first page. The convergence of these integrals can thus be easily checked to verify the choice of the upper limit of integration x_2 .

As for machine time, the longest case with $x_2 = 160$, which had to be

split into two runs because of the above-mentioned memory limitation (see Table T.35), took just under 36 minutes for all operations including printout.

Due to the sensitivity of the Mie functions to size, one has to choose Δx so that the integral takes into account all their major and minor oscillations. We have no uniform scheme to offer for the best choice of Δx , except for a "feel" developed after trying various values and comparing

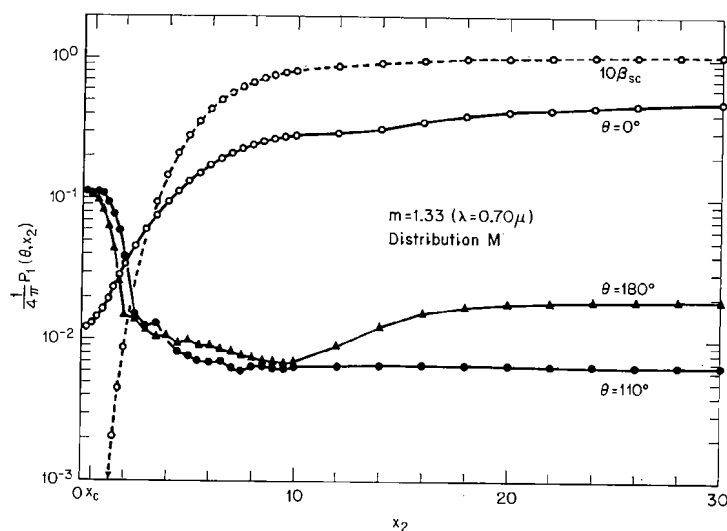


Fig. 22—Examples of the convergence of the integrals (80) and (81) toward a definite value for finite limits x_2 of integration. For convenience of display the actual values for $\theta = 0^\circ$ were multiplied by 10^{-1} before plotting, and those for β_{sc} by 10.

the smoothness and convergence of the integral curves toward the asymptotes representing the definite integrals (80) and (81). Figure 22 illustrates the manner of convergence with a partial plot of some of the integrals that make up the values shown in Table T.2 for a haze M distribution. The curves marked $\theta = 0^\circ$, 110° , and 180° correspond to the function $P_1(\theta, x)/4\pi$ for these angles as a function of upper limit x . For $\theta = 0^\circ$, the intensity function (reduced by a factor of 10 for display) rises smoothly from its Rayleigh value near the origin, with just the indication of a relative minimum around $x = 12$, reflecting the strong minimum in the function $i_1(x, 0^\circ)$ that exists in this region [cf. 9, Fig. 2]. The curve is still

rising at $x = 30$, and the integration in this case was actually carried up to $x = 50$, ensuring full convergence in the value shown in Table T.2. The curve for $\theta = 110^\circ$ seems to attain its asymptotic value very quickly near $x = 10$, whereas that for $\theta = 180^\circ$ shows a minimum in this region and then rises again, in opposite phase to the tendency in the curve for $\theta = 0^\circ$. Note that both curves for $\theta = 110^\circ$ and 180° show that the normalized intensity functions here first drop from their Rayleigh value near the origin, showing the effects of increased forward anisotropy as progressively larger

Table 7
Comparison of integration with fine and gross intervals
for water cloud model C.1 at $\lambda 0.70 \mu$

x	$P_1(5^\circ, x)/4\pi$		$P_1(180^\circ, x)/4\pi$	
	Gross	Fine	Gross	Fine
10	3.731	3.730	0.01087	0.00665
20	7.331	7.445	0.07028	0.06845
30	6.124	6.143	0.03914	0.05007
40	3.247	3.233	0.04776	0.04724
80	2.212	2.209	0.04786	0.05008
110	2.155	2.152	0.04851	0.05055

particles are taken into account. The volume scattering cross section $\beta_{sc}(x)$ is also shown (value in km^{-1} increased by a factor of 10 for display) to rise steeply and smoothly from its zero value at the origin, without any indication of the well-known, numerous major and minor oscillations in the curve $K_{so}(x)$ for water droplets.

In Fig. 22 we have fitted smooth curves to the *printout points* only at x : 0.25(0.25)2(0.5)10(2)30, indicated by dots, in the case of β_{sc} and $\theta = 0^\circ$, but for $\theta = 110^\circ$ and 180° we have joined the points with straight line segments without curve fitting. Had we used a finer printout interval, approaching the integration interval indicated in Table T.2, these latter curves would show smoother oscillations, reflecting more faithfully the behavior of dielectric spheres indicated in Fig. 9. Because of the nature of the distribution function $n(x)$, it is clear that these oscillations are damped out upon integration to a large limiting size x_2 .

Finally, in Table 7 we show the effect of a change in integration interval on the partial and final integrals for the two intensity functions for the cloud distribution C.1 (see Table T.36). The columns marked "gross"

were obtained by using the intervals $x: 1(1)40(0.5)110$ and the column marked "fine" with $x: 0.25(0.25)110$. Clearly, there is very little improvement in the forward area ($\theta = 5^\circ$) if the integration interval is quartered, whereas in the backward area ($\theta = 180^\circ$) the gross interval of $\Delta x = 1$ is not adequate, especially for a small range of integration. For the complete integral with $x_2 = 110$, the backscattering intensity is underestimated by about 4 percent. We have used the fine interval in preparing Table T.36.

The main tables, numbered consecutively from T.1 to T.125 (to distinguish them from tables appearing in Part I) and reproduced in Part II, are arranged according to increasing wavelength and grouped by substance and distribution model. They contain all the information needed by the reader on the complete volume scattering parameters of the polydispersion. In the heading of each table we have indicated: the complex index of refraction m and wavelength λ , also appearing in Table 6; the size-distribution model, identified in Table 5; the lower and upper limits of integration, as well as the various intervals used within the range; and the volume extinction cross section β_{ex} and albedo ω . These are given with sufficient accuracy to allow the reader to obtain the scattering and absorption cross sections separately to at least three significant figures.

In the final tabulation of the angle-dependent scattering matrix elements, we have tried to choose in each case a sufficient number of angles between 0° and 180° to cover in detail the oscillations primarily of the main intensity functions, $P_1(\theta)/4\pi$ and $P_2(\theta)/4\pi$, so that when plotted as in Fig. 28, the computed points can be fitted with smooth curves by the reader for further graphical interpolation. Thus the adopted angular interval $\Delta\theta$ (not necessarily the same as in the original computation) is often variable within each table, depending on the nature of the angular dependence in each region. For example, in Table T.51 for the corona cloud C.2 at $\lambda 0.45 \mu$, we have tabulated values every 0.5° in the range 4° to 10° and every 1° in 170° to 180° , to display the coronas and glories that are produced within very narrow angles by this model. For the same cloud illuminated by infrared at $\lambda 16.6 \mu$ (Table T.58), a tabulation every $\Delta\theta = 10^\circ$ is more than adequate to show the smoothly varying character of the intensity functions.

Derived quantities, such as the asymmetry factor $\overline{\cos \theta}$, which according to van de Hulst's definition [1, p. 128] and Eq. (74) is given by the integral

$$\overline{\cos \theta} = \frac{1}{4} \int_0^\pi [P_1(\theta) + P_2(\theta)] \cos \theta \sin \theta d\theta$$

for a polydispersion, can be easily obtained from the tabulations by

graphical or numerical integration. The same applies to integrations of the intensities over a range of scattering angles, as in the problem of the zodiacal light (see Section 4.51).

All the tabulated values of these functions have been carefully edited and rounded off to *four significant figures* from the original machine tabulation in six figures. To save space, we have further limited the individual tabulations to *six decimal places* in the case of zeros and of relatively small quantities. The intensities $P_1(\theta)/4\pi$ and $P_2(\theta)/4\pi$ are of course positive by definition, but the remaining two matrix elements may have either sign. Where applicable, we have indicated only the negative sign determined by the definitions adopted here according to (72) and (81).

Chapter 4 Discussion and Applications of the Results

4.1 GENERAL REMARKS

As noted in the Introduction, the prime purpose of this monograph is to investigate the elementary scattering and absorption properties of polydispersions of Mie particles. The principal results are presented in the form of numerical tables, extracted and reproduced in Part II. Most of the original results have not been previously published by the author, either in the form of RAND reports for limited circulation, or in the open scientific literature. We believe that the numerical tables constitute a versatile and powerful experimental tool for the further investigation of aggregates of particles illuminated by electromagnetic radiation of various frequencies. At the same time, considerable new information on the scattering behavior of polydispersions is contained in the tables, either explicitly or implicitly. We do not intend to analyze and describe all of it in detail here, hoping to expand on particular features in future studies as the occasion may arise.

In this chapter we wish merely to discuss some of the salient features of our results and to illustrate by means of examples a few of their more immediate applications. By proper analysis of the results, the reader may discover other features and uses, whose omission here does not necessarily mean that they have been overlooked by the author.

4.2 EQUATION OF RADIATIVE TRANSFER

One important use of the numerical results in the form presented in Part II is as input parameters in solving the equation of radiative transfer

in extended scattering media. To illustrate this use, we shall briefly recall one particular form of this equation, since we are not concerned here with its solution and discussion. This form is often used when a planetary atmosphere is modeled as a locally plane-parallel, horizontally homogeneous medium, which scatters the externally incident radiation without change of wavelength or resonant effects, and contains no internal emitters of radiation, of thermal or other origin. Denoting by h the height or distance normal to the planes of stratification, measured from the boundary that receives no direct incident radiation (e.g., the Earth's surface in the terrestrial case), we have, for a small volume element embedded in the medium,

$$\mu \frac{d\mathbf{I}(h; \mu, \varphi)}{dh} = -\beta_{\text{ex}}(h)\mathbf{I}(h; \mu, \varphi) + \beta_{\text{sc}}(h)\mathbf{J}(h; \mu, \varphi) \quad (93)$$

for quasi-monochromatic radiation of central wavelength λ (not shown explicitly in the symbols but implied). In this equation, which applies to the diffuse or scattered field only, μ is a direction cosine referred to the local zenith, φ is an azimuth, and \mathbf{J} is the Stokes vector corresponding to the so-called source function in this type of formulation. The physical interpretation and explanation of this formulation is available in various papers, as for example in recent publications by Sekera [63,64,65]. If the height is a single-valued, continuous function of the normal optical thickness τ , so that

$$dh = -\frac{d\tau(h)}{\beta_{\text{ex}}(h)} \quad (94)$$

and the local albedo of single scattering ϖ is defined as

$$\varpi(\tau) = \frac{\beta_{\text{sc}}(\tau)}{\beta_{\text{ex}}(\tau)} \quad (95)$$

then (93) may be rewritten in terms of the dimensionless independent parameter τ , in the simpler form

$$\mu \frac{d}{d\tau} \mathbf{I}(\tau; \mu, \varphi) = \mathbf{I}(\tau; \mu, \varphi) - \varpi(\tau)\mathbf{J}(\tau; \mu, \varphi), \quad (96)$$

where the source function has the explicit form

$$\mathbf{J}(\tau; \mu_0, \mu, \varphi) = \frac{\mathbf{P}(\theta)}{4\pi} \cdot \mathbf{F}_0 \exp\left(-\frac{\tau}{\mu_0}\right) + \frac{1}{4\mu} \int_{\Omega} \mathbf{P}(\psi) \cdot \mathbf{I}(\tau; \mu', \varphi') d\omega \quad (97)$$

which is valid for unit incident flux $F = 1$. Here μ_0 is the absolute value of the direction cosine for the incident radiation, μ' , φ' denote the direction

of incident diffuse radiation (self-illumination); and ψ is the scattering angle between the directions μ' , φ' and μ , φ . The remaining symbols are as before. Note that for an *isolated* volume element, (97) and (93) reduce to (77) since $\tau \rightarrow 0$ and there is no diffuse field.

The complete solution of the integrodifferential equation (96), with the source function (97) for homogeneous atmospheres of arbitrary optical thickness but with a Rayleigh-type scattering only, has recently been the subject of considerable study. For example, the method first proposed by Chandrasekhar [40] has been further developed by Mullikin [66] and Sekera [65], and complete numerical tables and their analyses have been published by Sekera and Kahle [67,68].

Equation (96) can also be solved in a first approximation under conditions where multiple scattering (self-illumination) may be neglected. This amounts to neglecting the second term on the right-hand side of Eq. (97), and we have the first-order linear differential equation

$$\mu \frac{d\mathbf{I}(\tau; \mu, \varphi)}{d\tau} = \mathbf{I} - \frac{\varpi(\tau)}{4\pi} \mathbf{P}(\theta) \cdot \mathbf{F}_0 \exp\left(-\frac{\tau}{\mu_0}\right). \quad (98)$$

In an arbitrarily mixed atmosphere, particularly if, due to the presence of some absorbing molecular layer, $\varpi(\tau)$ is not a single-valued function of h , (98) may not have an analytical solution. If, however, the albedo is constant throughout the medium, then we have the well-known solutions

$$\begin{aligned} \mathbf{I}_{tr}(\tau_1; -\mu, -\mu_0) &= \frac{\varpi}{4\pi} \mathbf{P}(\theta) \cdot \mathbf{F}_0 \frac{\mu_0}{\mu_0 - \mu} \left[\exp\left(-\frac{\tau_1}{\mu_0}\right) - \exp\left(-\frac{\tau_1}{\mu}\right) \right], \\ \mathbf{I}_{re}(0; \mu, -\mu_0) &= \frac{\varpi}{4\pi} \mathbf{P}(\theta) \cdot \mathbf{F}_0 \frac{\mu_0}{\mu_0 + \mu} \left[1 - \exp\left(-\tau_1 \frac{\mu_0 + \mu}{\mu_0 \mu}\right) \right] \end{aligned} \quad (99)$$

for the transmitted and reflected diffuse field, respectively, where τ_1 denotes the total normal optical thickness. Under the conditions mentioned above, since independent scattering is assumed and there are no higher-order scattering effects, solutions of the type (99) may be obtained separately for each component of the medium and the results added to obtain the total field. It is evident that these solutions, which are fairly good approximations for media whose total optical thickness (absorption plus scattering attenuation) is small, say $\tau \leq 0.10$, depend on the directions of incidence and emergence as well as the albedo of single scattering.

Finally, if $\tau \ll 1$ and the arguments of the exponentials in (99) are sufficiently small (i.e., barring near-grazing incidence and emergence),

the two solutions reduce to a single one, given by

$$\begin{aligned} \mathbf{I}(\tau_{sc}, \mu) &= \frac{\omega\tau_1}{4\pi\mu} \mathbf{P}(\theta) \cdot \mathbf{F}_0 \\ &= \tau_{sc} \frac{\mathbf{P}(\theta)}{4\pi\mu} \cdot \mathbf{F}_0 \end{aligned} \quad (100)$$

where τ_{sc} is the scattering optical thickness. This solution says in effect that the diffuse field, both transmitted and reflected, *depends only on the total scattering cross section, the scattering angle θ , and the direction of emergence of the radiation*, but it is independent of the albedo of single scattering. This property in turn shows that the true nature of the particles in an optically thin scattering medium cannot be deduced from photopolarimetric data on the diffuse field alone. The total extinction or the true absorption cross section must be determined independently in order to deduce the complex index of refraction of the particles.

In general, in media that admit the solution (99) or (100), it is clear from their form that the nature of the diffuse field will be mainly governed by the scattering matrix $\mathbf{P}(\theta)$ as well as by the volume scattering and absorption cross sections. All three in turn depend critically on the size distribution and nature of the particles. As we shall see, there are a number of outstanding geophysical and astronomical problems that may be included in this category.

Thanks to the separation and normalizations discussed in Sections 3.31 and 3.32, the tabulated material compiled in Part II can be used directly in the equation of transfer by choosing the appropriate model or combination of models to simulate a given atmosphere. Conversely, provided all observable parameters are available for an unknown atmosphere, it should be possible in principle to derive the form of the phase matrix and volume scattering and absorption cross sections, whence the tables will provide some indication of the nature and size distribution of the individual scatterers.

4.3 APPLICATIONS TO THE TERRESTRIAL ATMOSPHERE

The terrestrial atmosphere obviously is the best medium for a direct application of our results. Its diverse optical phenomena and their variations during daylight, twilight, and night conditions must have been subject to observation and interpretation from the beginning of human life. Whereas their systematic study during historical times was confined

to the analysis of observations made from the surface, the atmosphere has been subject to observation from outside only within the last decade. Despite the impressive recent advances in refined instrumentation and in mobility of the platforms on which they may be mounted, much remains to be done before we are able to completely understand the interactions of solar energy with the earth-atmosphere system. In particular, the initial drastic simplifications introduced by the great pioneers of the nineteenth century, to interpret the gross features of the atmosphere *as a scattering medium*, are no longer sufficient to make full use of the very detailed observational data now available and potentially available in the near future. These must include the information obtainable from artificial satellites and by means of artificial sources of optical, infrared, and microwave coherent radiation of high intensity confined in a narrow beam.

The particular aspects of the terrestrial problem in which polydisperse scattering is involved include the cloudless sunlit atmosphere; the particulate layers in the stratosphere and mesosphere; water-droplet and ice clouds; and disturbed conditions produced by major volcanic eruptions, forest fires, and man-made pollution. The appropriate forms of the equation of transfer for each of these varies from problem to problem, some being amenable to immediate solution and interpretation while others are as yet practically intractable. In the following sections we illustrate the use of the tables for some of the simpler cases.

4.31 Aerosol, Haze, and Dust Layers

On cloudless days the skylight distribution may be explained in a first approximation in terms of an optically homogeneous, sunlit medium with a single type of scattering characteristic of nonpolar molecules (Rayleigh scattering). A careful examination of the diffuse skylight, however, reveals considerable departures from this model, especially in the increased brightness within a wide circle around the sun, called the aureole. These departures are mainly due to the presence of several other types of large scattering particles whose concentration and nature, for any given location, vary both vertically and horizontally, and of course with time.

It would be impossible to incorporate all these variations in a theoretical model to obtain the diffuse field, and various simplifications have been tried. One such simplification assumes a mixture of two types of scattering only, corresponding to a Rayleigh and a Mie component. Using the subscripts R and M for these components, respectively, and none for the mixture, and using the source function for *primary scattering* only, we

may rewrite Eq. (93) in the form

$$\mu \frac{d\mathbf{I}}{dh} = -\beta_{\text{ex}}\mathbf{I} + \frac{1}{4\pi}(\beta_{\text{scR}}\mathbf{P}_{\text{R}} + \beta_{\text{scM}}\mathbf{P}_{\text{M}}) \cdot \mathbf{F}_0 \exp\left(-\frac{\tau}{\mu_0}\right) \quad (101)$$

where

$$\begin{aligned} \beta_{\text{ex}}(h) &= \beta_{\text{exR}}(h) + \beta_{\text{exM}}(h), \\ \beta_{\text{sc}}(h) &= \beta_{\text{scR}}(h) + \beta_{\text{scM}}(h), \end{aligned} \quad (102)$$

and

$$\tau(h) = \int_h^\infty \beta_{\text{ex}}(h) dh. \quad (103)$$

To solve (101) it should be written in the form (98); that is,

$$\mu \frac{d\mathbf{I}}{\beta_{\text{ex}}(h) dh} = -\mathbf{I} + \frac{\varpi(h)}{4\pi} \left(\frac{\beta_{\text{scR}}}{\beta_{\text{sc}}} \mathbf{P}_{\text{R}} + \frac{\beta_{\text{scM}}}{\beta_{\text{sc}}} \mathbf{P}_{\text{M}} \right) \cdot \mathbf{F}_0 \exp\left(-\frac{\tau}{\mu_0}\right) \quad (104)$$

where

$$\varpi(h) = \frac{\beta_{\text{sc}}(h)}{\beta_{\text{ex}}(h)}. \quad (105)$$

We then note from (104) that the analytical solutions in (99) cannot be obtained in this case unless both the albedo of single scattering ϖ and the scattering mixing ratios per unit volume $\beta_{\text{scR}}/\beta_{\text{sc}}$ and $\beta_{\text{scM}}/\beta_{\text{sc}}$ are independent of the total optical thickness of the mixture. Even if we assume a constant size distribution for the Mie particles, this is equivalent to the condition that their number concentration vary with height as the density of molecular air. It is well known that this condition is not satisfied in our atmosphere.

However, provided we can neglect multiple scattering effects, and we are not interested in the variation of the diffuse field *within* such an atmosphere, but only in what emerges from the boundaries, the actual Mie component can always be replaced by an equivalent one having the same total concentration per unit column and a scale height equal to that of the molecular atmosphere. The whole atmosphere then becomes an optically homogeneous one, and we revert to the solutions (99) in terms of the total optical thickness τ , remembering that the scattering matrix must be properly weighted; that is,

$$\mathbf{P}(\theta) = \frac{\beta_{\text{scR}}\mathbf{P}_{\text{R}} + \beta_{\text{scM}}\mathbf{P}_{\text{M}}}{\beta_{\text{sc}}}. \quad (106)$$

The foregoing separation can of course be extended to any number of different types of scatterers and size distributions. It can be easily shown

that the first two elements of the *weighted* scattering matrix (106) for any mixture fulfill the normalization condition (73), which, from (74) and (81), takes the form

$$1 = \frac{1}{8\pi} \int_{\Omega} [P_1(\theta) + P_2(\theta)] d\omega. \quad (107)$$

In an earlier attempt to estimate the role of aerosols in the formation of the aureole around the sun [8,9,10], we had used a slightly different but equivalent technique, originally suggested by Sekera [41]. This procedure consisted in treating the aerosol effect as a perturbation on the known Rayleigh diffuse field. If only primary scattering of sunlight is considered, it can be shown that Eq. (104) takes the alternate form

$$\mu \frac{d\mathbf{I}}{\beta_{\text{ex}}(h) dh} = -\mathbf{I} + \frac{\varpi(h)}{4\pi} \left(\mathbf{P}_R + \frac{\beta_{\text{scM}}}{\beta_{\text{scR}} + \beta_{\text{scM}}} \mathbf{P}_D \right) \cdot \mathbf{F}_0 \exp\left(-\frac{\tau}{\mu_0}\right) \quad (108)$$

where

$$\mathbf{P}_D \equiv \mathbf{P}_M - \mathbf{P}_R. \quad (109)$$

Here again the scattering matrix in parentheses on the right-hand side of Eq. (108) is the same as (106) and fulfills the normalization condition (107), whereas the integral of the components ($P_{1D} + P_{2D}$) of the deviation matrix (109) over all space is by definition equal to zero. When the aerosol component is small, the form (108) has certain advantages, especially in directions other than those in the vicinity of incoming sunlight. There is a single mixing ratio $\beta_{\text{scM}}/(\beta_{\text{scR}} + \beta_{\text{scM}})$, which may be considered as a *turbidity coefficient* and which is a function of h or τ in the lower atmosphere. When only primary scattering is considered, as in the above-mentioned study [10], this coefficient may be kept constant in an equivalent homogeneous atmosphere.

In the more general case, when the optical thickness of the aerosols is of the same order as that of the air molecules, and when multiple-scattering effects are to be included, the separation of $P(\theta)$ as in (108) offers little advantage. Furthermore, the introduction of negative intensities, which the latter method entails, is not physically attractive.

At any rate, in the case of the aureole, it is evident that the Mie component will dominate the Rayleigh component of the scattering matrix for scattering angles $0 \leq \theta \leq 40^\circ$. This is illustrated in Fig. 23, where we have plotted the scattering matrix components $P_1(\theta)$ and $P_2(\theta)$ for sea-level air containing 100 water particles distributed as in the haze L model (see

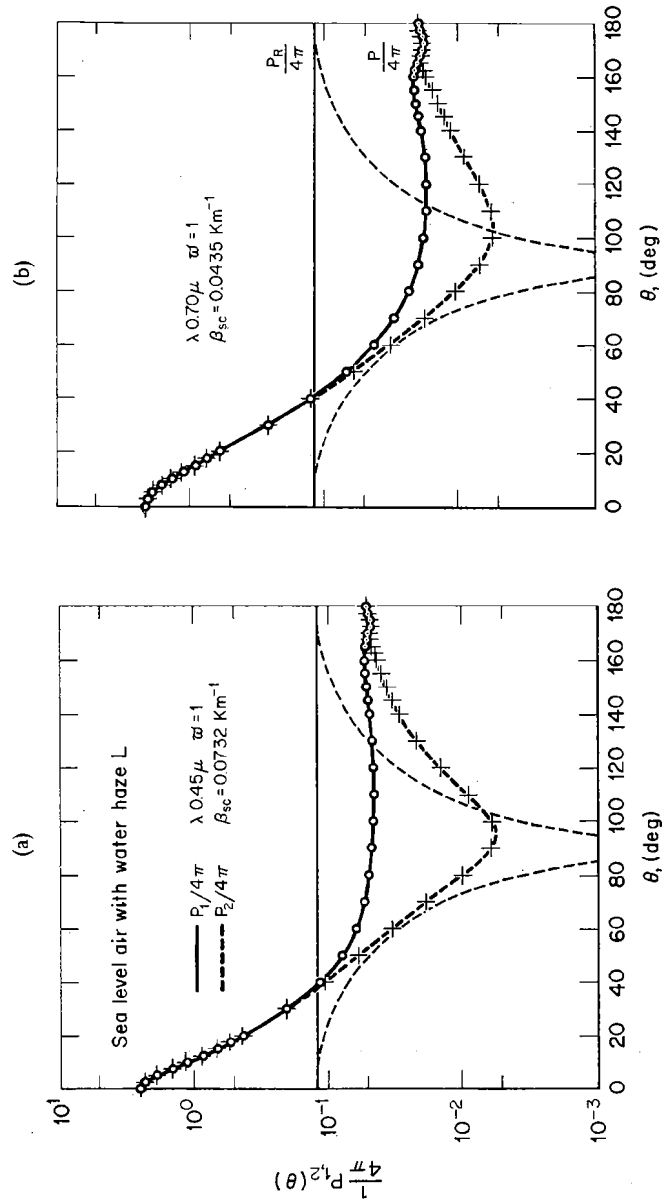


Fig. 23—Examples of the two intensity elements $P_1(\theta)/4\pi$ and $P_2(\theta)/4\pi$ of the scattering matrix for sea-level air containing a water haze as in model L, illuminated by unpolarized incident radiation. (a) At 0.45μ . (b) At 0.70μ . The purely Rayleigh case is indicated by thinner traces for comparison. The values of β_{sc} shown correspond to the composite models. Smooth curves have been fitted.

Tables 5, T.16, and T.17). For the mixing ratios in (106), we used values of β_{scR} of 0.0252 and 0.0040 km^{-1} [69] for $\lambda 0.450 \mu$ and $\lambda 0.700 \mu$, respectively, and β_{scM} from the corresponding tables. In blue light, Fig. 23a shows the aureole effect in the forward area, but in the region around $60^\circ \leq \theta \leq 160^\circ$ a Rayleigh-type scattering and polarization result because of its high mixing ratio. In red light (Fig. 23b), the Rayleigh effect is much weaker. (In both these figures we also show the pure Rayleigh functions P_{1R} and P_{2R} for comparison.)

These two examples give an indication of the aureole brightness gradients to be expected with this type of aerosol. As already pointed out elsewhere [16], our original attempt using a diffraction approximation for the forward scattering [10] was in error because a factor of 4π was omitted in P_{1M} and P_{2M} and the brightness gradient near $\theta = 0^\circ$ was overestimated by the diffraction approximation. A recomputation of the aureole using the same method but with the more exact curves of Fig. 23 would give a more realistic picture, with a flatter gradient near the Sun's limb and a broader aureole region around the Sun, in better agreement with photometric observations.

Figure 24 shows what could be a typical phase function for stratospheric air at 20 km. The Rayleigh components of β_{sc} at this level are $1.87 \cdot 10^{-3}$ and $0.295 \cdot 10^{-3} \text{ km}^{-1}$ at $\lambda 0.450 \mu$ and $\lambda 0.700 \mu$, respectively [69], and the Mie component has been taken as 1/10 of that given by a model H distribution of silicate particles (Tables T.102 and T.103). (Actually the concentration of 10 particles per cubic centimeter is rather high for normal stratospheric conditions, and may be more typical of volcanic dust layers producing anomalous twilights.) It is seen that even with this size distribution, containing practically no particles with radii greater than 0.5μ , there is a considerable aureole effect. The variations of the natural aureole with height in the stratosphere have been demonstrated by the excellent balloon measurements of Newkirk and Eddy [70].

In general, Figs. 23 and 24 indicate the inhomogeneity in scattering properties to be expected in the natural, cloudless atmosphere on the clearest days, far from intense sources of pollution. Thus in solving the direct problem there seems to be no alternative but to introduce the complete scattering matrix of the mixed atmosphere characteristic of each layer and to integrate step by step. In this respect the techniques proposed by van de Hulst [71] seem to offer the best hope. On the other hand, the solution of inverse problems is made more difficult by the number of independent variables sought, such as the mixing ratio, size distribution, and optical constants of the aerosol components, and their

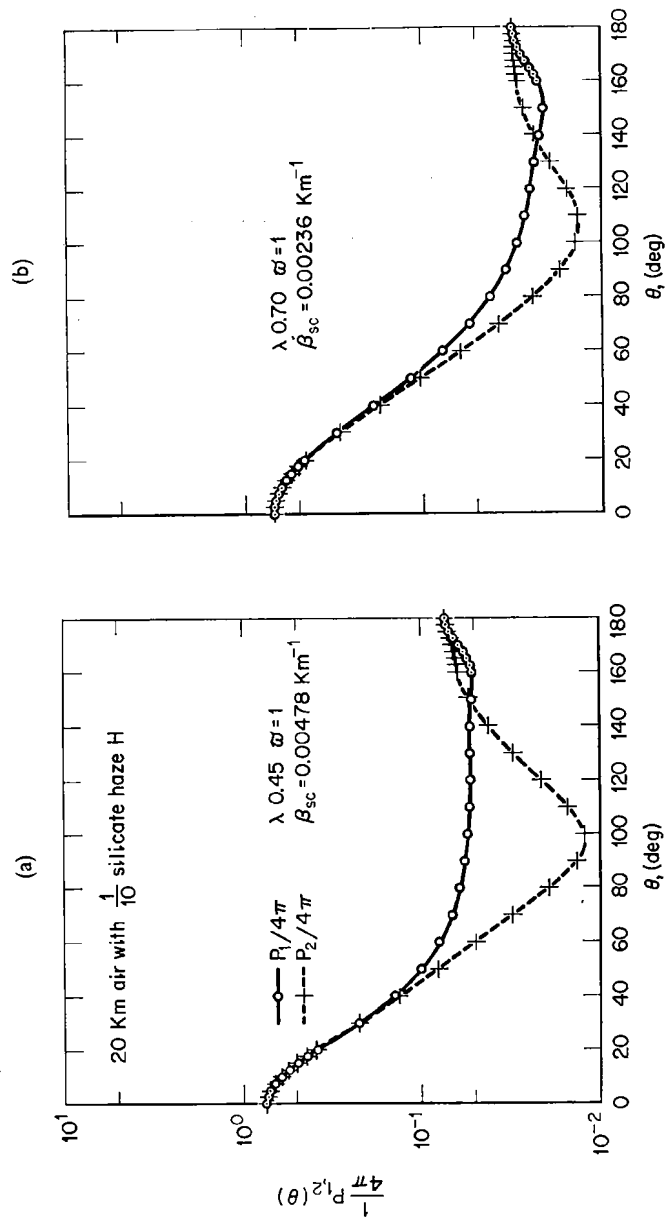


Fig. 24—Examples of the same elements as in Fig. 23 for air at 20 km containing 10 silicate particles per cm^3 distributed according to model H. (a) At 0.45μ . (b) At 0.70μ ; note the marked deviation in intensity and polarization from the Rayleigh model in this case.

stratification. It is necessary to rely on all variables amenable to observation, both in diffuse reflection and transmission, to obtain anything like a unique solution. Sekera [72] has discussed some of these problems in connection with satellite observations of reflected sunlight. It is clear that a number of models of the scattering function, such as those produced in this monograph, representing likely aerosol distributions, will be of great help in making judicious choices in both the direct and the inverse problem.

A few comments about polarization effects are in order. In this country, Sekera and his collaborators [18,41,73] have for several years conducted detailed measurements of the polarization of the cloudless skylight. Soviet scientists, notably G. V. Rozenberg [74], have undertaken similar studies. These observations, when compared with the Rayleigh theoretical model as to degree of polarization, positions of the maximum polarization and of the neutral points, and the wavelength dependence of these and other details, reveal significant discrepancies. The polarization of the light diffusely reflected from the top of our atmosphere has not been observed, but because of the important ground reflection effects it should reveal even greater departures from the Rayleigh model, as shown, for example, by Fraser [75].

It is evident from an inspection of the curves in Figs. 23 and 24 that the presence of aerosols must contribute significantly to the general polarization field. Outside the aureole region an analysis of their effect on various polarization features is not straightforward, as these are mainly the result of higher-order scattering and surface reflection. A detailed discussion cannot be undertaken here, but it is clear that a proper analysis of these effects requires a set of complete scattering elements for each aerosol model. For example, the data presented here suggest that some ellipticity may be present in the turbid atmosphere. However, this should be a rather weak effect because (a) no ellipticity is produced by primary scattering of the unpolarized incident sunlight on Mie particles, and (b) even with multiple scattering, the ellipticity parameters $P_3(\theta)$ and $P_4(\theta)$ for air are considerably diluted by the Rayleigh components when properly weighted as in (106). These and other considerations indicate that the elliptical polarization of the cloudless sky should be greatest in red light and during late twilight in certain directions.

Since the discovery of the laser effect allows the use of almost monochromatic and fully polarized light beams, a study of the ellipticity parameters is most useful in the analysis of Mie polydispersions in the laboratory. An interesting feature, already mentioned in Section 3.22, is the depolarizing effect of the inhomogeneity in the size of the particles.

We may introduce a *depolarization factor*, $0 \leq D(P) < 1$, by forming the ratio

$$D(P) \equiv \frac{P_1 P_2 - (P_3^2 + P_4^2)}{P_1 P_2 + (P_3^2 + P_4^2)} \quad (110)$$

on the basis of inequality (69). In the ideal case of purely polarized monochromatic incident light, the quantity $D(P)$ as here defined indicates the degradation of the degree of polarization, in the strict sense of the definitions (61) and (62) of partial polarization. In this sense, the depolarization factor $D(P)$ also indicates the *degree of incoherence* introduced by the polydispersion, in which the particles are assumed to be randomly distributed in time and space, when illuminated by a continuous monochromatic and *coherent* stream of radiation. The factor (110) therefore has an operational significance in connection with laser experiments.

It is evident that $D(P)$ will be a function of the nature and size distribution of the particles as well as of the scattering angle θ . Figure 25 illustrates this for two models and for two types of particles represented in Tables T.1, T.112, T.27, and T.120, as indicated along the curves. The water particles (curves 1 and 27) show maximum depolarization in the backward area, and there seems to be no correlation of the curves with the polarizing property of the particles when illuminated by unpolarized light. Curves 112 and 120 for metallic spheres show maximum depolarization in the forward area, precisely where the partial linear polarization $(P_1 - P_2)/(P_1 + P_2)$ is at a maximum. It is interesting that in this case the greater depolarization occurs for the narrower distribution H (curve 120), contrary to what might be expected.

These features also suggest that the assumption of a Lambert-type reflection for the Earth's or other planets' surfaces is of questionable value, especially in a discussion of its effects on the polarization of the diffuse radiation of the overlying atmosphere. In fact, the concept of Lambert reflection, as introduced by Chandrasekhar [40], assumes that all incident radiation is completely depolarized (i.e., $D(P) = 1$) at all angles of incidence and reflection, regardless of its initial state of polarization. This assumption is necessary to simplify the solution of the corresponding equation of transfer for thin and moderately thick atmospheres, and it has meaning only as a rough approximation for a reflecting surface of chaotic structure and composition. If the surface is fairly homogeneous and composed of fine grains of solid particles or a dense layer of cloud droplets, for example, the assumption may result in misleading interpretations of the polarization of the diffusely reflected radiation in terms of the mass of an overlying molecular atmosphere.

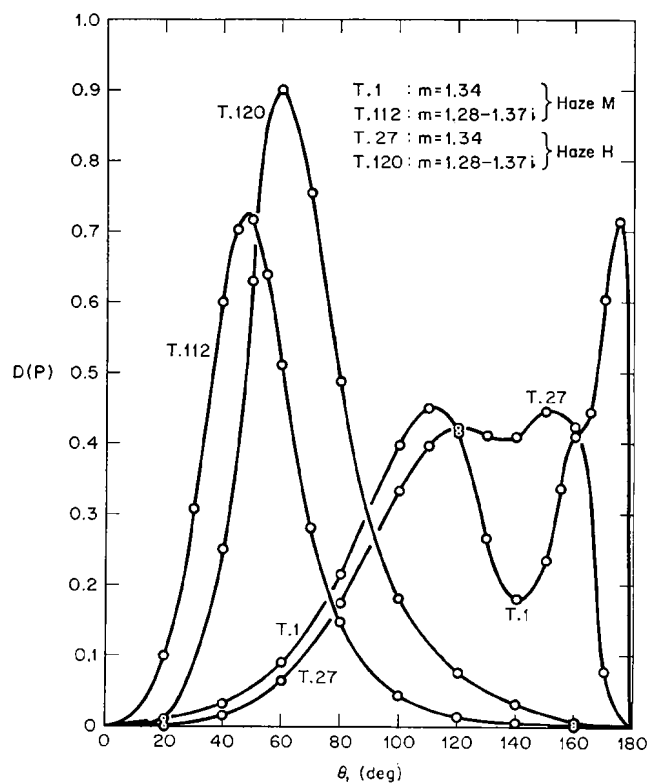


Fig. 25—Examples of the depolarization factor $D(P)$ at various angles for two distributions of dielectric and metallic particles. Labels along the curves refer to the tables in Part II.

Another important area where complete models of aerosol scattering are necessary is in the twilight method of atmospheric probing. As Rozenberg [74] points out in his excellent monograph, twilight conditions are eminently suited to the study of high atmospheric layers by means of ground, balloon, and satellite photometric observations. In the analysis of such data, since primary scattering is the main component, all the elements of the models are directly usable. Noctilucent clouds, which have recently become the subject of systematic observations [76], must be included in this category.

Finally, we should mention disturbed or abnormal optical conditions

produced by great volcanic explosions or extensive forest fires on otherwise cloudless days. The classical example of the former is the Krakatoa event of 1883, whose very widespread effects are so admirably described in the Royal Society's report [77] prepared five years later. A remarkable example of extensive fire smoke occurred in September, 1950, during the widespread forest fires in Alberta, Canada, which produced such phenomena as the "blue" or "violet" sun observed as far downwind as England and Western Europe [78,79].

In addition to anomalous twilight displays, the Krakatoa phenomenon also produced the so-called Bishop's rings and "blue" and "green" suns. We have devised the models represented by Tables T.104, T.105, T.110, T.111, T.124, and T.125 in an attempt to reproduce some of these phenomena. Figure 26 shows the intensity element $(P_1 + P_2)/8\pi$ for unpolarized light taken from Tables T.104 and T.105 for silicate spheres at $\lambda 0.45 \mu$ and $\lambda 0.70 \mu$, respectively. It is seen that a Bishop's ring effect does exist, as indicated by the intensity curves in the aureole region. The anomalies in gradient should result in color differentiation within the well-defined aureole region, and the overall effect may well account for the "reddish-brown" Bishop's ring of 10° to 12° radius mentioned by

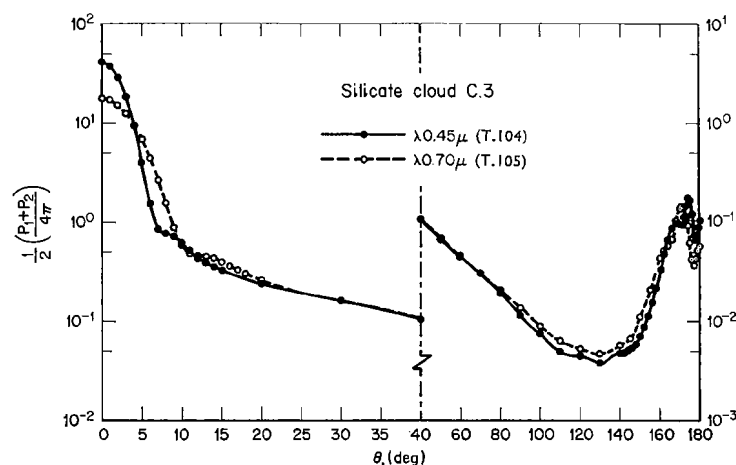


Fig. 26—Detail of the normalized scattering intensity for a cloudlike polydispersion of silicate spheres, illuminated by unpolarized radiation at two wavelengths in the visible. Note change of both scales in the two parts of the diagram. Smooth curves are fitted.

Humphries [80]. In the backward hemisphere, Fig. 26 shows a weaker ring of about 10° radius around the antisolar point, which also agrees with the Krakatoa observations.

The curves for Tables T.110 and T.111 for more opaque material ($m = 2.2$) show very similar effects in the forward and backward scattering areas, whereas those for Tables T.124 and T.125 for "metallic" spheres show no maximum around the antisolar point. From this, one might conclude that the Krakatoa dust was mainly composed of dielectric particles with radii between 1 and $3\ \mu$ distributed around a mode radius of $2\ \mu$ according to our model. However, this subject needs a thorough analysis before more definite conclusions can be drawn. For example, the model must also explain the green sun phenomenon and the reported anomalous polarization effects, and it is possible that absorbing particles may have to be included. The effects of nonspherical or irregular particles must also be considered, although there is evidence that these may not be important, at least in the forward area $0^\circ < \theta < 90^\circ$ [Hodkinson in 15, p. 87; 81]. We cannot go into these matters here, but it is evident that the use of polydisperse models of spherical particles should give better results than the monodisperse, opaque-disk diffraction theory considered in the original interpretations [77,80].

Similar remarks apply to the case of forest fire smoke and other disturbed conditions in the optical state of the cloudless atmosphere. In all cases one must bear in mind that conditions are seldom duplicated. Each case shows quite individual characteristics that depend on the nature of the source of the turbidity, local meteorological conditions, geographical position, and so on.

4.32 Natural Water Clouds

Because natural clouds are, in general, dense aggregates of rather large water droplets and ice crystals, a cloud depth of a few hundred meters suffices to give a large optical thickness. This means considerable multiple-scattering effects, which will tend to suppress the single-scattering features, such as coronas, cloudbows, and glories with their variable polarization, as pointed out elsewhere [Deirmendjian in 15, p. 171; 16]. Hence the single-scattering matrix elements in our models will be most useful in the direct interpretation of phenomena produced by optically thin cloud elements illuminated by sunlight or other sources.

A good example of the latter is mother-of-pearl or nacreous clouds. Hesstvedt [82,83] has published a thorough description of their numerous occurrences in Norway, with emphasis on the mechanism of their

formation. A thorough analysis of the related optical phenomena with respect to scattering theory is still lacking. Although we do not intend to undertake this here, some ideas can be advanced on the basis of the present work. We have adopted the distribution C.3 (Table 5 and Fig. 21) to simulate mother-of-pearl clouds with a mode radius of 2μ , in accordance with estimates in the literature [82]. Water droplets with this distribution (Tables T.59 and T.60) yield intensity functions very similar to those reproduced in Fig. 26. It is seen that there is only one tenuous corona formed at each wavelength between $\theta = 8^\circ$ and 14° . It would seem that even this narrow distribution does not explain the vivid and alternating colors reported in the literature [2,82]. As pointed out in Section 2.35 and demonstrated in Fig. 17, multiple coronas are possible only with strictly monodisperse particles. In fact, this may be the case in mother-of-pearl clouds, indicating a remarkably uniform mechanism of formation for the particles, with the size depending on position within the cloud, as pointed out by Hesstvedt [83]. This would also explain why the color bands often follow the contour of the cloud rather than arcs of equal scattering angle. In any case, one may assert that the responsible particles must be spherical, whether composed of vitreous ice or supercooled liquid water.

The very common phenomenon of iridescent clouds must be akin to that of nacreous clouds, although the former occur much lower in the atmosphere than the latter. However, the characteristic droplet radii may be larger in the case of iridescent clouds.

Another phenomenon associated with optically thin clouds is the colored coronas commonly observed around the sun and moon. As so aptly described by Minnaert [2], the coronas are highly variable in intensity, number of rings, color, and radius. The most clearly defined are those around the full moon seen through so-called *altocumulus stratiformis perlucidus* [84,85], when these clouds are so optically thin that bright stars are visible through them. Because of the weak illumination and dark background, the colors are then easily discernible. Since in most cases the radius of these rings does not exceed 4° to 6° , the responsible droplets cannot be very small. The cloud models C.2 and C.4 were carefully chosen with this type of cloud in mind.

In Fig. 27 we reproduce the intensity for a water cloud with a C.2 distribution (Tables T.51 and T.52) illuminated by unpolarized radiation. The effect of the change in intensity gradient within the aureole region, seen around $\theta = 4^\circ$ to 5° in blue and $\theta = 6^\circ$ to 7° in red, would result in a visual impression of colored rings around the luminary, surrounding less defined rings of red and bluish light. The graphs imply, of course, that

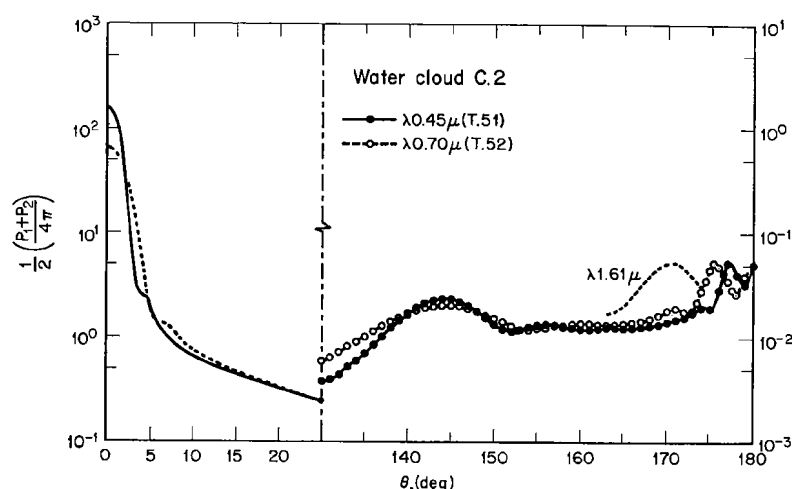


Fig. 27—Detail of the scattering intensity for water droplets with a narrow distribution around $r = 4 \mu$ showing coronas, cloudbows, and glories. The dotted fragment of curve marked 1.61μ is drawn to the same scale and refers to the same cloud as do the other curves.

there will be a gradual transition through a green ring between these. Comparing Fig. 27 with Fig. 26, we note that the rings have wider radii in the latter because the predominant particle size of 2μ is one half that for Fig. 27, with an almost inverse variation between these two parameters. The whole region of steepest intensity gradient in both sets of curves is really the aureole, giving the visual impression of a bright bluish-white inner ring surrounded by a fainter reddish ring [2, p. 214].

True maxima in intensity, corresponding to sharply defined coronas, appear only with the much narrower distribution C.4, as indicated in Fig. 28 (see Tables T.70 and T.71). These peaks are centered around $\theta = 5^\circ$ and 7.5° , respectively, for the blue and red rings, and the latter is superposed on a secondary maximum in blue. There is an indication of a fainter system between 11° and 13° , which, together with the bright red ring between 2.5° and 4° , coinciding with a deep minimum in blue, should result in a triple system of colored coronas in this case. Such occurrences are not very common. The author witnessed a brilliant display at Santa Monica, California, one spring afternoon (April 14, 1963) after a rain shower. Within a few minutes, in rapid succession, there

was brilliant iridescence on high clouds near the sun; then, as a homogeneous veil of altostratus approached the sun, first there were two systems of colored bands *parallel to the contour of the cloud*, which then evolved into a system of three perfectly defined colored corona systems as the cloud covered the Sun. I estimated the radius of the outer red corona at 5° to 6° . The visual impression was that each red ring had a beautiful inner greenish ring, and I noted that the limb of the Sun was clearly defined through the cloud rather than washed out by the aureoling effect. In this case the predominant droplets must have had a radius of from 6 to $8\ \mu$, judging from the radii of the coronas. The whole phenomenon lasted less than 15 minutes. It would be interesting to speculate on the mechanism of cloud formation during this display. Perhaps a vertical wave was present in the wind field, as in the case of mother-of-pearl clouds, producing large, almost uniform droplets in a very shallow layer. A strictly monodisperse cloud, however, would be ruled out, as pointed out previously (see Section 2.35).

Turning to features in the backward-scattering hemisphere, we have the cloudbows and glories already mentioned in regard to single-particle scattering (Section 2.35 and Fig. 18). Both are regions of maxima in the

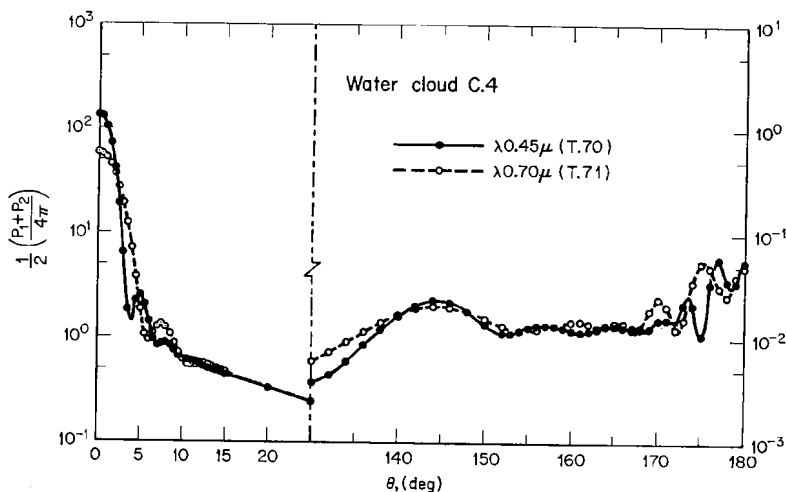


Fig. 28—Same as Fig. 27, but for a narrower distribution of droplets, showing the appearance of clearly defined double coronas and glories at each wavelength. The polarizations in this as well as in Figs. 26 and 27 may be evaluated from the corresponding tables in Part II.

scattering intensity in the backward hemisphere, which appear at various angles, depending on the refractive index and the relative size of the dielectric sphere, but can be distinguished by their polarization: In the cloudbows the electric vector is predominantly perpendicular to the scattering plane (positive polarization with $P_1 > P_2$ in the sense defined in Section 3.21), whereas in the glories, which appear closer to the backward direction, the predominant vibration is parallel to the scattering plane (negative polarization with $P_2 > P_1$). In polydispersions there are, of course, many superpositions of both these features, but the net result is that some of them are enhanced to produce a single cloudbow or glory effect in the integrated intensities. This was first pointed out by this author [13; 15, p. 171] on the basis of the Mie theory and cloud model C.1; but experimental verification, especially observations of the polarization in the cloudbow and glory of natural water clouds, seems to be lacking.

Such features become more pronounced as the cloud-drop distribution is made narrower, as shown in Figs. 27 and 28, corresponding to cloud models C.3 and C.4, respectively. In both cases there is a broad cloudbow between 140° and 150° where there is no separation of colors (in agreement with visual observations), but there is considerable positive polarization, as can be seen from the corresponding Tables T.51, T.52, T.70, and T.71. These tables also show that the relatively flat region in the intensity curves of Figs. 27 and 28, roughly between 150° and 170° , is actually one in which the individual polarized components vary considerably. For example, if a thin cloud conforming to the model of Fig. 28 were observed through a properly oriented polarizing filter, it would display a colored bow with the blue maximum at about 158° and a red maximum at 164° , whereas the principal "white" cloudbow would persist at 145° . After the axis of the polarizer is turned by 90° , the principal cloudbow would disappear and a blue bow would form at about 153° and a red bow at 158° .

Figures 27 and 28 also show well-defined, true glories with considerable dispersion between 5° and 3° from the backward direction. (The high degree of negative polarization in these regions may be appreciated from the corresponding tables.) Figure 28 in addition shows a second glory system with a larger radius. On the other hand, a very similar feature seen in Fig. 26 for silicate spheres is not a true glory but a cloudbow, according to the polarization criterion mentioned earlier. The reason for this is the higher refractive index for silicates, which results in a migration of the cloudbows toward larger scattering angles. Water clouds with the same distribution as in Fig. 26 do show a true colored glory with a radius between 9° and 5° in addition to a pronounced cloudbow at $\theta = 150^\circ$

(see Tables T.59 and T.60) Here we have a beautiful example, by the way, of how the classical Maxwellian theory of light, properly applied, provides a good explanation of a natural phenomenon that eludes a simpler analysis [cf. 1, pp. 249–258].

The wider cloud distribution C.1, whose matrix elements are given here (see Tables T.35 through T.50) in greater detail than in the earlier publication [16], shows no indication of a corona, but the cloudbows and glories do appear. A plot of the intensity elements P_1 and P_2 would show two distinct cloudbows in blue, centered respectively at $\theta = 122^\circ$ and 143° and a single glory of radius 2° in blue and 4° in red. This corresponds to the colored glory commonly observed around the shadowpoint of aircraft overflying altocumulus clouds.

The very steep and narrow aureole region displayed by the cumulus model C.1 in the visible (see T.35 and T.36) needs some comment. This phenomenon would be rather difficult to observe instrumentally because of the small scattering angle ($\theta < 3^\circ$) and the problem of eliminating the direct sunlight. The only possibility would be the use of a coronagraph-type instrument, at the moment when the thin border of a cumulus cloud approaches the Sun to form the proverbial “silver lining.” At any rate it is certain that this extremely intense aureole exists, judging from the almost perfect matching in the range $2^\circ \leq \theta \leq 170^\circ$ of our theoretical model with detailed nephelometer observations in fog performed by Pritchard and Elliott [86]. In this connection an interesting phenomenon, which we shall call *the filtered-sun effect*, must also be mentioned. This is a rather common occurrence along the California coast when the Sun is obscured by a uniform layer of low stratus cloud. When the cloud has the proper thickness, one is able to see the Sun’s disk perfectly defined, with no aureoling effect at the limb, surrounded by a *uniform* field of cloud light of low brightness. When a thinner part of the cloud passes in front of the sun, the effect disappears and the limb is washed out by the appearance of an aureole. At other moments the Sun becomes invisible, but its position can still be estimated by the sensation of infrared radiation on one’s face. The filtered-sun phenomenon has been noted by Ambartsumyan [48, p. 571].

The phenomenon may be explained qualitatively if one considers the high intensity of the source, that is, the Sun. The fact that we seek a coherent image of the disk (it would be interesting to photograph the Sun under such conditions to see if sunspots are also discernible) indicates that we are looking at directly transmitted sunlight of greatly reduced flux, which only slightly exceeds the diffuse cloud-light background. Now the

sky brightness on a clear day with high Sun is of the order of 10^{-6} of the apparent surface brightness of the Sun. Let us assume that under overcast conditions the diffuse cloud brightness is about 10^{-7} that of the Sun, and the barely visible disk of the filtered Sun is of this same order of brightness. This provides a rough estimate of the slant optical thickness of the responsible cloud, or $-\ln(10^{-7}) \simeq 16$. From Table T.35 we note that a homogeneous cloud of that type with a geometrical thickness of 1 km or 10^7 droplets per square centimeter column yields just this optical thickness. The *geometrical* depth seems too great for California stratus. However, considering that stratus droplets are larger than those in our cumulus model, and that their number density may exceed 100 cm^{-3} , a correspondingly shallower layer cloud may provide the required optical thickness.

At any rate, the foregoing line of reasoning brings out an important characteristic of highly asymmetrical scattering in deep media. That is, the medium must have a rather large optical thickness, of the order of 16 or more in the case of a model C.1 type of cloud, before the intense forward lobe is completely suppressed in diffuse transmission by the multiple scattering. This *critical thickness* may be more precisely determined from the actual cloud density and thickness when the filtered Sun is seen. Its value, of course, will depend on the size distribution of the droplets in the cloud, as well as on the intensity of the illuminating source.

Most of the features observed in diffuse transmission and reflection of sunlight on thin clouds may be treated quantitatively by solving the first-order approximation for a mixed medium, as in (104), using our models for the scattering matrix. For clouds of finite optical thickness, smaller than some critical value such as suggested by the foregoing criterion, the complete equation must be solved rigorously, including the polarization effects. A priori assumptions and simplifications may lead to serious errors owing to the complex nature of the scattering mechanism. For the radiation emerging from deeper media, it may be possible to introduce simplifications on the basis of semi-infinite models, provided the effects of the albedo of single scattering are well understood.

In this connection, we should mention another area of research in which our models, particularly those for water clouds in the infrared region, must have important applications. This area has to do with the effect of cloud and other absorbing particulate layers on the radiation balance and thermal structure of the atmosphere. Closely related to this is the effect of scattering on the absorption bands of H_2O , CO_2 , and other molecular bands, as well as the bands in liquid water and ice. In both cases

it is essential to have exact values of the albedo of single scattering for the polydispersion in the region of the water and ice bands.

As we have pointed out elsewhere [12], the absorption through a given mass of a solid or liquid substance in the *polydispersed state* is not equal to the absorption through the same mass in the condensed or bulk state. This is related to the behavior of the single-particle absorption efficiencies discussed in Section 2.32. The examples in Table 8 clearly demonstrate

Table 8
Comparison of bulk and scattering mass absorption coefficients for water clouds

λ (μ)	γ_b (cm^{-1})	Cloud C.1		Cloud C.3		Haze M		Haze L	
		$1 - \tau$	γ_{sc} (cm^{-1})	$1 - \tau$	γ_{sc} (cm^{-1})	$1 - \tau$	γ_{sc} (cm^{-1})	$1 - \tau$	γ_{sc} (cm^{-1})
1.45	26.00	0.0151	42.69			0.0026	40.08		
1.94	116.6	0.0605	174.6			0.0151	168.6	0.0196	150.5
6.05	2846.	0.4567	1450.	0.5454	2657	0.7028	626.9	0.8687	2658.
16.6	3028.	0.6051	1641.	0.8456	2643	0.9253	2514.	0.9985	2440.

this inequality. To determine the *scattering mass absorption coefficient* γ_{sc} , we simply multiply the volume absorption coefficient β_{ab} , from the corresponding table in Part II, by $1/V_p$ from the last column in Table 5, that is, the volume of space needed to get unit volume of condensed particles. The value of γ_{sc} thus obtained is entirely equivalent to the bulk absorption coefficient γ_b , shown in Table 6 and repeated in column 2 of Table 8 for comparison. For each model we also show the parameter $(1 - \tau) = \beta_{ab}/\beta_{sc}$ in Table 8. In the examples it is seen that $\gamma_{sc} > \gamma_b$ at the shorter wavelengths and in the weak water absorption bands at 1.45μ and 1.94μ , whereas $\gamma_{sc} < \gamma_b$ in the stronger absorption region farther in the infrared spectrum. A knowledge of the so-called liquid water content of a given cloud would be of little help in estimating the absorption of infrared radiation by a cloud element. The important criteria here are the relative size, size distribution, and concentration, as well as the strength of the band at the particular wavelength. When multiple scattering is taken into account, these effects become more complex and generalizations more dangerous. The intensification or weakening of a given water (or ice) band must also depend on the scattering angle, since, for example, absorption has little effect on forward scattering at small angles, whereas

it suppresses the cloudbows and glories in the backward area. (The effects on water vapor and other molecular bands are excluded from the foregoing discussion.)

Some of these problems have been mentioned in a survey article by E. M. Feigelson [87], who arrives at similar "negative" conclusions. From her own references to the Soviet literature* it is evident that her remarks on the problems of cloud scattering are based on considerable experimental and theoretical research. As mentioned in our prefatory remarks to the present monograph, language barriers have unfortunately prevented us from adequately discussing this work and comparing it with ours.

For the cloud and haze models used here, the graphs in Fig. 29 are intended to show the wavelength dependence of the extinction coefficient over the entire range $0.45 \leq \lambda \leq 16.6 \mu$. All the curves correspond to a single substance, liquid water. These have been fit "by eye" to the computed points shown, and they may be used for a fairly good interpolation at other wavelengths. Figure 29 may be compared with a similar diagram in an earlier work [12], which was based on the modified van de Hulst approximation described in Section 2.32. The differences are due to the different distribution functions used in each case, rather than to failures in the approximation.

For a given number concentration of water particles (i.e., $N = 100 \text{ cm}^{-3}$) the family of curves in Fig. 29 demonstrates the wide range of variation in the extinction—over several orders of magnitude—resulting from changes in the particle size and size distribution only. The lowest straight line, labeled $\beta_R(0)$, corresponds to nonabsorbing air molecules at sea level, with the well-known λ^{-4} dependence. As we pass to the unmixed-haze models, the absolute slope with respect to λ decreases as the proportion of larger particles increases, as indicated by the next three curves above the Rayleigh line. In all three curves there is a minimum at about 2.4μ , followed by a maximum at about 3.0μ , roughly following the variations in the imaginary part κ of the index. These features are clearly absent in the cloud extinction curves.

The three cloud curves in the upper part of the diagram are first of all separated from the haze curves by a large gap on the diagram, equivalent to several orders of magnitude and reflecting the abrupt change in the size and mode radius of the particles in the two types of distribution. The

* E. M. Feigelson, *Radiation Processes in Stratified Clouds*, Moscow, 1964; G. V. Rozenberg, in *Spectroscopy of Scattering Media*, Minsk, 1963 (see also W. M. Irvine, *Astron. Papers Transl. from Russian No. 9*, Smiths. Inst. Astroph. Obs., 1966).

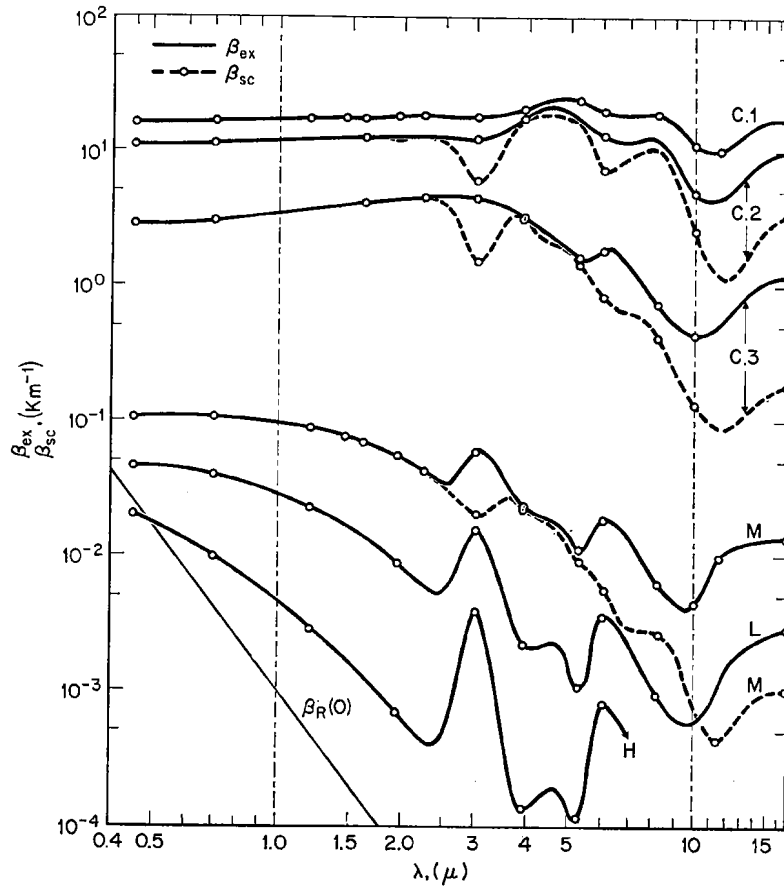


Fig. 29—Wavelength dependence of the volume extinction coefficient (solid line) and, in some cases, of the scattering coefficient (dashed line) for various distributions of water spheres equivalent to 100 particles per cm^3 in each case.

slope of all three curves in the visible and near infrared is small but positive and the maximum extinction occurs in cloud C.1 near 25.0μ . In some of the cases we have added the dashed curve to indicate the form of the scattering coefficient β_{sc} . It is clear that the relative value of the difference, $\beta_{ex} - \beta_{sc} = \beta_{ab}$, depends critically on the distribution model. Furthermore, in the region $8.0 < \lambda < 12 \mu$ there is a relative minimum in

the extinction for all cases, but this could hardly be called a "window," even without the inclusion of water-vapor wing absorption, except in the case of very tenuous clouds and haze layers. When the total concentration N is changed by some factor for any given model, the corresponding curve in Fig. 29 will be shifted vertically without change of shape.

Yamamoto *et al.* [88] have recently published an interesting discussion of the radiation to be expected from a cloud in this so-called window region, taking into consideration the temperature of the underlying surface. As pointed out by these authors, the albedo of single scattering ϖ is an essential parameter in the problem, and we have shown that its value depends on the drop-size distribution function as well as on the imaginary part κ of the index of refraction. For this reason in certain cases we have used two alternative values for water at $\lambda 8.15 \mu$ (see Table 6), which differ by a factor of two. The effect on the extinction and albedo in two of our models, other things remaining equal, is shown in the accompanying table. It is clear from this comparison that the value of κ

κ	Haze L		Cloud C.1	
	$\beta_{ex} \text{ (km}^{-1}\text{)}$	ϖ	$\beta_{ex} \text{ (km}^{-1}\text{)}$	ϖ
0.0472	$9.424 \cdot 10^{-4}$	0.156	18.75	0.746
0.0236	$5.465 \cdot 10^{-4}$	0.269	19.30	0.854

strongly affects the extinction and albedo in the haze model, where the droplets are small, whereas in the cloud model, the effect is much smaller: halving the value of κ increases the albedo of single scattering by only 15 percent and the extinction also *increases*, contrary to the case in the haze model.

In the $\lambda 3.0 \mu$ region, the changeover from the old value of $m = 1.525 - 0.0682i$ to the new one of $m = 1.364 - 0.306i$ (see Section 3.5) hardly affected the extinction coefficient and the albedo in the cloud C.1 model, reducing them by a mere 3 percent and 7 percent, respectively (compare old values [16] with new in Table T.42). The aureole in the region $0^\circ < \theta < 20^\circ$ was unaffected by this change; however, the linear polarization increased from the maximum of 0.28 at $\theta = 50^\circ$ to one of 0.85 at $\theta = 80^\circ$, the broad glory around $\theta = 160^\circ$ disappeared, and the intensity at $\theta = 180^\circ$ was reduced by 72 percent. These features have important implications in the search for water clouds on Venus (see Section 4.41).

These examples also indicate that layers of small, absorbing haze particles may have a stronger effect on the local air temperature than thin layers of cloud droplets of an equivalent optical thickness.

The cloud models bring out a number of other interesting points that are inherent in the numerical results compiled in Part II, such as the effect of various amounts of absorption on the coronas, cloudbows, and glories. These visible features also exist in the near infrared, in regions of minimum absorption, as seen for example in model C.1 at $\lambda 1.61$ and 2.25μ (Tables T.39 and T.41). We shall not describe these and other features in detail here, since most of them can easily be found by the reader from appropriate plots of our results.

In general, the foregoing discussion provides an idea of the difficulties involved in so-called inverse problems, where one wishes to obtain all the physical data on otherwise inaccessible atmospheric particles from spectrophotometric and polarimetric parameters alone. To do this it is evident that one must have a complete set of scattering and absorption measurements, even if multiple scattering may be neglected. This is tantamount to requiring that the air sample be available in the laboratory, which is self-defeating. It follows that the optical method of atmospheric probing, either with sunlight or with an artificial source of illumination, is a limited tool of research in this respect, but useful in complementing other sources of information. A mathematical analysis of some of these inverse problems has been developed by K. S. Shifrin and his collaborators in a series of papers, a résumé of which has been given recently by Shifrin and Perelman [89].

4.33 Microwave Scattering Properties of Natural Precipitation

As mentioned in an earlier study [47], in the field of radio meteorology, the radar reflectivity of precipitation particles represents a particular case of scattering on polydispersions. In Section 2.33 we defined the so-called radar cross section of a single particle in terms of the backscattering intensity in the present context. To find the equivalent cross section per unit volume in a polydispersion, we rewrite the expression (33) for σ_b in the form

$$\begin{aligned}\sigma_b(x) &= \frac{4\pi}{k^2} i_1(x, 180^\circ) \\ &= \pi r^2 K_{sc}(x) \frac{4i_1(x, 180^\circ)}{k^2 r^2 K_{sc}(x)}.\end{aligned}$$

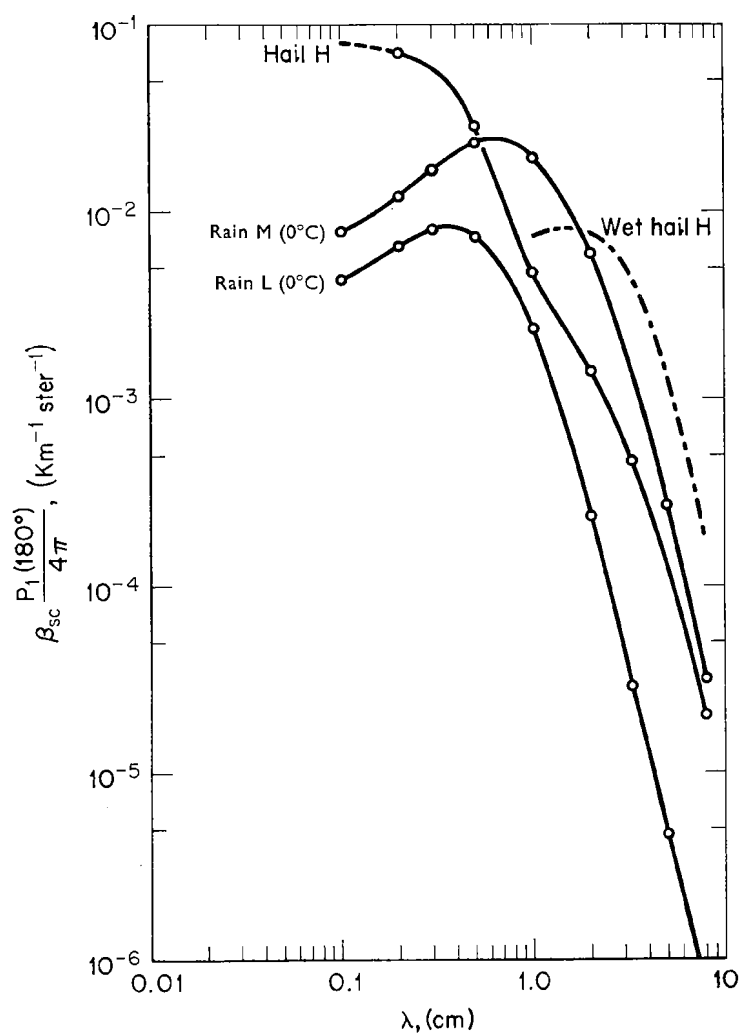


Fig. 30—Wavelength dependence of the backscattering intensity function for 1000 particles per m^3 in the microwave region for the four precipitation models indicated. The dashed portion of the curve marked “hail H” indicates graphical extrapolation. The curve marked “rain M” is adapted from previous work [47] not included in the present volume.

For N identical particles in a unit volume, a comparison of the last expression above with (75) and (78) yields

$$N\sigma_b(x) = \beta_{sc}(N, x)P_1(x, 180^\circ),$$

which is expressed in terms of the volume scattering cross section and the first element of the normalized scattering matrix. According to (77), the preceding expression represents 4π times the intensity scattered in the exact backward direction, just as in the case of σ_b . The extension to a polydispersion follows immediately from Section 3.32, and we have

$$\int_{r_1}^{r_2} n(r)\sigma_b(x) dr = \beta_{sc}P_1(180) \quad (111)$$

where the quantities on the right-hand side are obtainable directly from our tables for a particular wavelength and distribution $n(r)$. The expression (111) is then the *radar cross section per unit volume* for N particles following the distribution $n(r)$, and is equivalent to the single-particle radar cross section σ_b customarily used in radio meteorology.

Primary scattering theory is eminently applicable here, and the radar echo intensity is given directly by Eq. (100) with $\theta = 180^\circ$ and $|\mu| = 1$, provided the two-way path attenuations are properly accounted for.

In Fig. 30 we have plotted the true intensity function for backscattering, $\beta_{sc}P_1(180)/4\pi$, on logarithmic scales as a function of the wavelength. The units for the ordinate are square centimeters per 10^6 cm^3 per steradian. The curve marked "rain M" is taken from the previous model [47], which is not included here, whereas the other curves are taken directly from the corresponding tables in Part II. Provided no other effects are taken into account, it is seen that, for equal incident energies, the radar cross section has a maximum at about $\lambda 0.35 \text{ cm}$ for model L (light rain) and at $\lambda 0.60 \text{ cm}$ for the heavier rain, model M; that is, both maxima are in the millimeter region. Presumably this peak will migrate toward still longer wavelengths for heavier rain containing a greater proportion of larger drops. Otherwise the two curves are quite similar in slope. There is more than an order of magnitude difference between the two when $\lambda > 1 \text{ cm}$, which means that meteorological radar systems in existence are well adapted to discriminate between rain intensities.

The hail model H shows a different wavelength dependence, and there is no absolute maximum in radar reflectivity within the range displayed. There is a change of curvature and a weak relative minimum near $\lambda 1 \text{ cm}$ in the radar cross section, which reflects the pronounced minimum in $K_b(x)$ for single dielectric particles near $x = 1.8$ displayed in Fig. 9. This

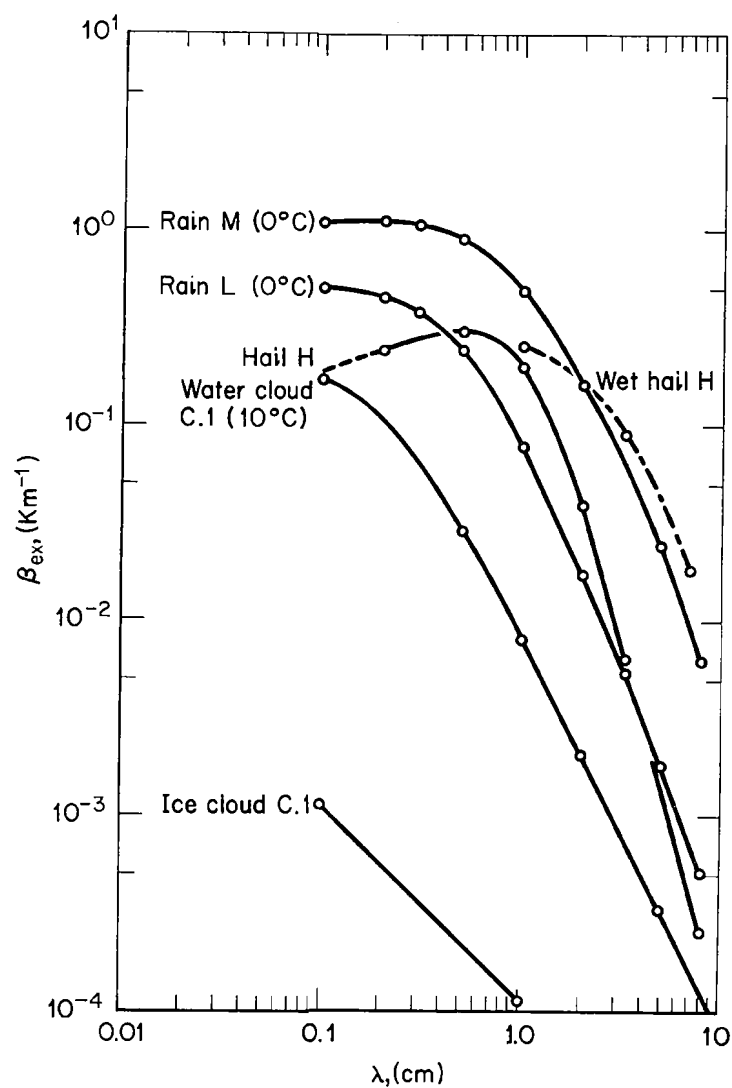


Fig. 31—Wavelength dependence of the volume extinction coefficients corresponding to the precipitation models of Fig. 30. Also included are the microwave extinctions for two cloud models adapted from previous work [47].

behaviour is due to the narrow size distribution adopted for the hail model, whose mode radius almost coincides with the x value for minimum K_i near $\lambda 1$ cm. A comparison of the hail curve with those for the two rain models shows that, other things being equal, a *multiwavelength* meteorological radar system could discriminate between hail and rain in a given cloud.

In Fig. 30 we also show a curve marked "wet hail H" fitted to three points only. This was obtained by considering water spheres with the same distribution as for hail (see Tables T.96 and T.97). Although free-falling water spheres with diameters near 1 cm may not be stable, their reflectivity may give a good indication of that of ice spheres coated with water. The comparison of the wet-hail with the dry-hail curve shows that the radar cross section of the former is larger by an order of magnitude, with a maximum near $\lambda 2$ cm. (Note the backward asymmetry in angular scattering displayed in Tables T.96 and T.97.) A hail model with *size distribution* has never been used before, so far as we know, and the corresponding integrated scattering and absorption properties, on the basis of the exact Mie theory as given here, are new.

Finally, in Fig. 31, we have plotted a set of curves displaying the wavelength dependence of the extinction coefficient for all our models in the centimeter and millimeter region. These curves also include the previous determinations for a water and ice cloud in the same region [47]. The extinction curves in Fig. 31 may be compared with those in Fig. 29 for haze and cloud in the infrared, the ratio of particle size to wavelength being analogous in both cases. The marked differences in the shape and slope of the curves in the two sets are due mainly to the wavelength dependence of the index of refraction in each case.

On the basis of our results one may, of course, set up radiative transfer equations for precipitating clouds illuminated by microwaves, using a properly weighted scattering function and mixing ratio, just as in the case of visible radiation and haze discussed earlier (Section 4.31). The angular dependence of the scattered radiation and the polarization parameters, including the ellipticity, become especially important in interpretations of data obtained with so-called bistatic radar systems, when the distance between emitter and receiver is comparable to that of the "target" and the scattering angle is less than 180° . In such situations the path attenuation of the transmitted and reflected pulse by different cloud formations and precipitation areas also becomes important. Similar remarks apply to the problem of the radar cross section and microwave emission spectrum of Venus, whose atmosphere might contain precipitating water clouds (see Section 4.41).

Further interesting features of the microwave scattering parameters, inherent in our present results, may be found by the reader, for example by comparing the new models with our own previous results [47] and related work by other authors.

4.34 Laser Applications

A new technique for remote atmospheric probing was introduced with the detection of high-level scattering layers by means of pulsed-laser light, first announced by Fiocco and Smullin [90]. This expected application of the newly discovered optical maser has great potentialities for future atmospheric research, especially when multiwavelength systems and their adaptation to space vehicles are perfected. However, as we shall see, the present technique cannot by itself provide all the data on atmospheric scattering layers unless it is used in conjunction with other information and independent criteria.

The detection of aerosol or other scattering layers embedded in the molecular atmosphere by means of pulsed monochromatic visible radiation (optical radar) is entirely analogous to the detection of precipitation by means of microwaves, and the corresponding theory follows immediately from the discussion of the previous section. An important difference is that, under normal conditions, the air molecules themselves present a strong backscattering cross section, and the aerosol component in general represents only a small increase over the background signal. In radar, on the other hand, the echo from precipitation particles is so strong, compared to that from air and even cloud particles, that the latter may be neglected.

Since the pulse duration in the laser system is of the order of 10^{-8} sec, the probed layer is of the order of tens of meters thick and its optical thickness is infinitesimal. Hence, for the intensity reflected *at the mixed layer itself*, we may use Eq. (100) directly; that is,

$$I(\tau_{sc}, \mu) = \frac{\tau_{sc}}{\mu} \frac{P_1(180^\circ)}{4\pi} F \quad (112)$$

where F is the flux in the laser beam incident on the layer *after attenuation through the atmosphere below*, and the other quantities apply to the layer only. Separating the latter into two components, as in expressions (102) and (106), we can get the ratio I/I_R , which after simplification becomes

$$\frac{I}{I_R} = 1 + \frac{\beta_{scM} P_M(180^\circ)}{\beta_{scR} P_R(180^\circ)} \geq 1. \quad (113)$$

Here, I is the actual reflected intensity received and I_R is the equivalent value for molecular air of the same thickness in the absence of aerosols. The latter quantity is presumably known from theory and from standard data on the air density at the level in question. Hence it should be possible in principle to obtain the value of the product $\beta_{scM}P_M(180^\circ)$ from the measurements and Eq. (113).

In actual fact, even if this product could be determined, it is impossible to obtain the value of the individual factors, as we have pointed out elsewhere [91]. It follows from the discussion of our results that, in the case of a polydispersed layer, the product $\beta_{scM}P_M(180^\circ)$ cannot determine a unique size distribution and index of refraction. If a monodisperse aerosol can be assumed, the situation is not much better because there are still four unknown quantities inherent in this product, namely, the number of particles N per unit volume, the size r of the particles, and the real and imaginary parts of the complex index of refraction. The latter two quantities cannot be determined because, as shown in Eq. (100), the theory of very thin scattering layers does not involve the albedo of single scattering (ϖ). A determination of $\varpi < 1$ is important because it implies a value of $\kappa \neq 0$, which in turn affects the backscattering cross section. Thus it is clear that the optical radar method has several limitations in determining the *nature* of an unknown scattering layer, but its usefulness for *detection* and range mapping, especially at night, cannot be denied.

A bistatic system might provide additional parameters by monitoring changes in the polarization of the source laser. In that case an equation similar to (113), written for the polarized components, may be used in the analysis of the data. However, difficulties similar to those in the case of bistatic radar (Section 4.33) will have to be faced. Of course, a multi-wavelength *and* bistatic system, if feasible, should offer the best possibilities.

Another possible future use of the laser is in communications. For visible wavelengths and in atmospheric transmission, this application is beset with difficulties such as the loss of power due to atmospheric attenuation, divergence of the beam, and loss of coherence. Consortini *et al.* [92], for example, have pointed out that the monochromaticity of the laser beam will deteriorate on account of the scattering on the air molecules in thermal motion, without even mentioning aerosol effects. It is evident that the latter will further deteriorate the quality of the beam, mainly as a result of forward scattering. The conservation of coherence and polarization is of course crucial here. We have shown that in polydispersions, at least of spherical particles, these properties are conserved in exact forward

scattering. However, it may be possible in the future to consider also scatter-propagation techniques at small angles, as in conventional radio propagation [93]. In that case the depolarization factors, as shown in Fig. 25 for hazes, must be considered.

Our results suggest that scatter propagation by reflection from water-droplet clouds might conceivably be used for laser communications, for example at scattering angles where the intensity is maximized. These occur in the aureole, corona, cloudbow, and glory regions, and the corresponding depolarization $D(P)$ may be evaluated by means of Eq. (110) and

Table 9
Selected values of depolarization $D(P)$ for the water cloud models C.1, 2, 3, 4 at the scattering angles shown in parentheses

Feature	0.70 μ				1.61 μ		
	C.1	C.2	C.3	C.4	C.1	C.2	C.3
Aureole and coronas	(6°) 0.005	(6°5) 0.005	(13°) 0.014	(7°5) 0.002	(10°) 0.014	(10°) 0.019	(25°) 0.011
Cloudbow (max.)	(145°) 0.491	(144°) 0.247	(150°) 0.320	(144°) 0.185	(147°5) 0.416	(150°) 0.202	(160°) 0.104
Glory (max.)	(177°) 0.431	(176°) 0.287	(171°) 0.638	(175°) 0.254	(172°5) 04.51	(170°) 0.312	

our tables. All the cloud models show near-zero depolarization in the steepest and brightest part of the aureole region. We show samples of the depolarization in this and other regions in Table 9 for the cloud models indicated, at two wavelengths: $\lambda 0.70 \mu$, near that of the ruby laser, and $\lambda 1.61 \mu$, where absorption is at a minimum. It is clear from the table that the aureole and corona regions show negligible depolarizations, and since the corresponding scattering intensity is near maximum, it is quite possible that water clouds might be used in scatter propagation in a laser link. On the other hand, both the cloudbow and glory areas show rather high depolarization, which limits their usefulness. At any rate, since new laser sources are rapidly being developed, it should be possible to select a particular wavelength in the infrared region that gives maximum transmission, freedom from noise, and potential for scatter propagation by means of clouds.

We note, by the way, that Rozenberg and Gorchakov have recently reported [94] very careful experimental determinations of the Stokes parameters for scattered light on small volumes of atmospheric air. From

these they have determined a quantity they call "the degree of uniformity," which appears to be equivalent to the reciprocal of the depolarization factor $D(P)$ defined here. Comparison of their experimental results [94, Fig. 7] with our theoretical curve 1 in Fig. 25 for water haze M shows excellent agreement, all things considered, particularly in the relative minimum of depolarization in the region $130^\circ < \theta < 150^\circ$. It follows that experiments on natural water clouds should show an equally good agreement with the predicted values of Table 9. This means that in this case, although the cloudbow is a region of low depolarization, it may not be suitable for scatter propagation, except possibly in clouds of the type C.4 and with the use of infrared lasers. Similar remarks apply to the depolarization in the glory region.

Since laser light is highly monochromatic and coherent, it was initially thought that scattering with the use of this source may show characteristics different from those observed when an incoherent source is used. As a matter of fact, we have shown in Section 3.2 that the nature of scattering on the type of polydispersions considered here does not depend on the degree of coherence of the source (the Mie theory does in fact assume coherent initial illumination), but on the random distribution of the scatterers. Experiments conducted with both types of sources have indeed shown no significant differences in either transmission or angular scattering [95,96]. It is possible, however, that some differences may indeed be detected when such sources are used to illuminate highly concentrated, strictly monodisperse particle samples, especially if coherent multiple-scattering effects are present.

4.4 OTHER PLANETARY ATMOSPHERES

While models for the complete scattering properties of Mie polydispersions are useful in refining our understanding of the physics of the well-known terrestrial atmosphere, such models are indispensable in advancing reasonable conjectures on the basic characteristics of other planetary atmospheres that have not yet been directly probed. Those of the terrestrial planets Venus and Mars have naturally received most attention in the literature because of the possibility of future spacecraft landings. The composition and mass of the Martian atmosphere is now essentially known, but the main features of the bulk of the Venusian atmosphere remain a mystery. Among the other solar planets, Saturn's rings are also of particular interest since they are related to scattering phenomena.

4.41 Venus

We shall devote some space to this atmosphere because it presents by far the most fascinating problem from the point of view of electromagnetic scattering phenomena, where practically all of our results are applicable to some degree. There is evidence that its mass exceeds that of our own atmosphere, and there are quantities of large scattering particles in suspension. As to composition, CO_2 and traces of H_2O have been definitely identified spectroscopically in the upper layers, but their relative abundance in the entire atmosphere with respect to other constituents remains unknown. Other than these items, and the apparent high temperature close to some unspecified solid or liquid surface of the planet, there are no reliable data on the atmosphere of Venus. Despite considerable research efforts to devise models based on available data, and despite one successful flyby space probe (the United States' *Mariner 2*), there is little agreement among scientists on the main characteristics of this atmosphere, as evidenced by the proceedings of two recent specialized conferences on the subject [97,98]. (In yet another specialized conference held in Tucson, Arizona (March, 1968) after the manuscript of this book had been completed, results obtained by two recent Venus probes, the United States' *Mariner 5* and the Soviet Union's *Venera 4*, were discussed and compared, reducing some of the aforementioned uncertainties.)

One reason for this state of affairs is a curious attitude prevalent among scientists in regard to Venus, which may be partly attributed to the pressures of the so-called space age. This attitude, which is hardly in harmony with the precepts of the scientific *method*, induces the use of all manner of ad hoc simplifying assumptions leading to hasty inferences (alas, often published and later cited uncritically) on the origin of the visible, infrared, and microwave radiations emanating from Venus, despite the many known difficulties in the use of such data to obtain useful information about our own atmosphere. Interestingly enough, the scientists most concerned with radiative transfer in sunlit planetary atmospheres have so far refrained from setting up theoretical models for that of Venus. Furthermore, one finds some rather careless and misleading statements in the recent literature as to the possible local scattering properties and their implications for the transfer of solar radiation. For example, in an effort to justify a so-called greenhouse explanation of the apparent high surface temperature, the forward anisotropy of large-particle scattering has been proposed as a mechanism that allows a considerable amount of diffuse solar energy to reach the surface, despite the presence of a very thick atmosphere. However, experience shows that an optical thickness of 16

is sufficient to eliminate the most extreme anisotropy from the diffuse field (cf. the filtered-sun effect mentioned in Section 4.32).

Similar remarks apply to interpretations of the observed microwave radiation of Venus in the range $4 \text{ mm} < \lambda < 10 \text{ cm}$, which has been the subject of numerous papers. We need not review these here, since they also are extensively discussed in the above-mentioned conference proceedings [97,98] and in the references cited therein. In essence, the problem reduces to the following; the millimeter and centimeter emissions conform to the tail end of the curve for a 600° to 700°K blackbody surface at the longer wavelengths, and to that for a 400° to 500°K surface at the shorter wavelengths. The wavelength dependence is smooth and efforts to detect discrete emission or absorption lines or bands have failed so far. Aside from the problem of the source of this apparent high temperature, the question of the differential temperature of emission within the range mentioned needs explanation.

As long ago as 1963 [99], we pointed out that *if* the atmosphere contained water in amounts not much in excess of those in our own, a continuous cloud layer on Venus was quite plausible, and consequently, given the proper cloud thickness, a continuous layer of *raindrop-size* condensation products, which never reach the surface, could also be postulated. The optical thickness of this mixed medium in the microwave region could be of the same magnitude as that of our own cloudless atmosphere in the visible. One may then formulate a problem in radiative transfer analogous to that of the sunlit terrestrial atmosphere, with the important difference that the external parallel illumination and the plane-atmosphere model must be replaced by one with an internal source surrounded by a spherical atmospheric shell. Clearly the latter problem—especially if radial inhomogeneities in the shell and thermal radiation effects are considered in addition to scattering—is by no means trivial, but rather more complex than the first problem. In our original papers [99,100] we demonstrated that in the very first approximation, considering only extinction but no diffuse transmission, such a model was capable of faithfully reproducing the microwave emission of Venus through *differential attenuation* of the radiation emitted at a *uniform blackbody temperature* at some lower surface of the planet. The assumption of large raindrops was crucial in this model, since together with the much smaller cloud droplets, and taking into account the exact wavelength dependence of the complex dielectric constant of water at the wavelengths in question, it yielded just the right magnitude and variation in microwave optical thickness to fit the data without the assumption of a massive atmosphere.

We felt at that time that this agreement could not be dismissed as mere coincidence, especially since the additional assumption of high-level water-and-ice clouds, similar to terrestrial mother-of-pearl and noctilucent clouds, could also provide an explanation of the brightness, broad spectrum, and polarization of the planet in the visible and near-infrared range. As we pointed out [100], the existence of considerable amounts of water in the lower "invisible" part of the atmosphere cannot be excluded, notwithstanding the negative spectroscopic evidence in the near infrared and the absence of the $\lambda 1.35$ water-vapor resonance feature in the microwave data. Since our deep-cloud hypothesis resulted in an atmosphere practically opaque to solar visible and infrared radiation, we also advanced the conjecture that the high surface temperature must be attributed to an internal heat source rather than a greenhouse effect [99,100].

Our increasing capabilities to detect and analyze radar echos from Venus will no doubt provide further information on her atmosphere. Recently, Evans *et al.* [101] obtained echos at the short wavelength of $\lambda 3.8$ cm. Although these may be interpreted mainly in terms of reflection from a compact spherical planetary surface, an atmospheric component may have been present, as the authors themselves point out. Their interpretation of the data, based on a simple absorbing layer, results in a minimum normal optical thickness of $\tau = 0.46$ for this wavelength. Considering the difficulties of deducing such a parameter from radar echos alone, this value is in good agreement with that of 0.10 given by our own models in this region. In general, the $\lambda 3.8$ cm results lend further support to the existence of microwave scatterers in the form of large hydrometeors [100].

Without elaborating on the foregoing ideas, it is clear that a knowledge of the microwave scattering parameters for large polydisperse hydrometeors is essential in the analysis of this and related problems. For example, the models for Venus's atmosphere may be further refined by a proper combination of extinction curves, as in Fig. 31, to obtain even better agreement with existing observational data than that achieved earlier [100]. The presence of hail-like particles cannot be excluded, given the possibility of intense vertical convective cells implied by the deep-cloud model. Also, considerations of atmospheric scattering effects may suggest explanations other than that proposed by Clark and Kuz'min [102,103] for the weak differential polarization observed at $\lambda 10.6$ cm by interferometry, simply by assuming an asymmetrical distribution of large hydrometeors over the planet at the time of observation. Similar remarks apply to the apparent variations of surface temperature deduced by

various authors on the basis of differential microwave emissions as a function of planetary phase. For the proposed Venus radio occultation experiment (see opening paragraph, Section 4.41) similar to the *Mariner 4* Mars experiment [104,105], our microwave scattering models should be particularly useful in the analysis of the data once they become available.

Returning to the planetary brightness and polarization data in the visible and infrared, the possibility of obtaining complete information on the deeper layers of the Venusian atmosphere by means of their analysis is rather small. Even if a set of complete solutions for the problem of diffuse reflection on highly inhomogeneous, deep atmospheres with asymmetrical scattering were available, there is little likelihood that a single model would fit the observations. Once we know more about the basic parameters of the atmosphere, however, such solutions are essential in understanding the energy budget and hence the dynamics of the atmosphere.

In any event, although the question of the composition of the upper and lower cloud particles remains unsolved, the single-scattering models can still be used to obtain some insights here. This could be accomplished, for example, by means of photometric and polarimetric observations around the subsolar point from a close flyby or an orbiting space platform [106]. The purpose would be to detect the glory phenomenon, which, as we have seen, is present even against the background produced by multiple scattering in diffuse reflection. If a glory is detected, either in the visible or near infrared with the help of polarizing filters (cf. the glory at $\lambda 1.61 \mu$ indicated in Fig. 27) it would imply the existence of *spherical* dielectric particles of the right size, which would in turn be a strong argument in favor of water or other material condensed in this form in the Venusian environment. As we have pointed out [106], this type of observation cannot be carried out by terrestrial telescoping because of the small angular size of the planet.

The possible existence of a halo effect *in diffuse reflection*, suggested recently by O'Leary [107] as an indication of the presence of ice-crystal clouds, is physically and theoretically untenable. Any halolike brightness enhancement observed on the whole planet at the proper phase angle should be related to the form of the scattering function in a layer of considerable optical depth, rather than to the properties of a thin upper layer of ice crystals, as suggested by O'Leary.

The presence of ice crystals was recently inferred by J. Strong on the basis of low-resolution, infrared reflection spectra obtained by balloon [97, pp. 147, 151]. It follows from our discussion in Section 4.32 of the mass absorption coefficient for water droplets that the analysis of such

data is by no means simple. A band such as 13.0μ should be most intense near low planetary phase angles.

Somewhat similar remarks apply to the planet's polarization as a function of phase angle: The variation cannot be related directly to single scattering and thence to the nature of the responsible particles. In attempting to match Lyot's famous observations discussed by van de Hulst [108], we found the closest agreement *in the sign* of polarization with that for cloud model C.1 at 13.9μ (Table T.43). The scattering properties of the model are not altered if both wavelength and particle size are multiplied, say, by 0.25. Hence, *if* Lyot's hypothesis were strictly valid (which we doubt), that is, if multiple scattering merely reduces the degree of polarization in *all directions* by a *constant positive factor* [108], one could interpret his visual observations in terms of a cloud of spherical particles with predominant radii around 0.5μ and complex index of refraction $m = 1.353 - 0.0059i$. Because of its very tentative nature, this result, presented at a meeting of the American Geophysical Union in December, 1961 [109], was never formally published. Gehrels and Samuelson [110] have since published preliminary results of photometric polarimetry with various filters covering the ultraviolet through the near infrared, which show considerable dispersion in the polarization versus phase curves of Venus. The interpretation of these interesting observations is not straightforward since they refer to the whole illuminated planet. Again, data on the distribution of the polarization (and brightness) field over the planet, obtained from a close-in space platform, would be very helpful here.

4.42 Mars

Although our present knowledge of the constitution and mass of the tenuous Martian atmosphere is practically complete, it appears that a few questions still remain [98]. For example, the nature and size of the particles making up the colored and opaque hazes, long observed by astronomers, are still undetermined.

Chamberlain and Hunten in a recent review [111] have discussed the comparative merits of various techniques used in investigations of the Martian atmosphere, suggesting that photopolarimetric methods are less reliable than spectroscopic ones in estimating the mass (a conclusion that we had indicated in an unpublished note* in 1961). Nevertheless, as these authors have pointed out [111], the photopolarimetric method cannot be

* *Quarterly Technical Progress Report*(3), RM-2769-JPL, The RAND Corporation, Santa Monica, April 28, 1961, p. 74.

rejected outright, particularly if the molecular and atomic components are separated from the aerosol component and the effects of surface reflection. This separation should not present major problems, since the atmosphere is optically thin (no multiple scattering) and the effects of primary scattering and ground reflection are simply additive. However, for Earth-based observations, the planet does not present the most favorable phase angles (close to 180°) at which the aerosol component can best be detected by forward scattering. Near superior conjunction, on the other hand, when observing conditions are optimized, we have backscattering conditions (plus maximum surface reflection), which are least favorable in separating the Rayleigh and aerosol contributions, as noted in our discussion of the pulsed laser technique (see Section 4.34). Thus, here too, relatively simple photometric experiments carried on a space probe to obtain the proper conditions of illumination would provide much meaningful information.

The question of the nature of the Martian surface material and its relation to atmospheric dusts has received much attention recently. Attempts to resolve these questions by polarimetric and photometric methods have been carried out, notably by A. Dollfus [112,113]. Nor is the problem solved by the spectacular technological feat of the transmission of television photos aboard the *Mariner 4* space probe [114], which was not designed as an experiment for this purpose. Barring an actual instrument landing on the surface for sampling purposes, photometric studies of the atmospheric dusts, presumably blown up from the surface by Martian winds, still offer a good means of learning about their size and nature. It is of course conceivable that some of the Martian hazes are of interplanetary origin, and their formation is akin to that of terrestrial noctilucent clouds, as suggested by Vestine and Deirmendjian [115]; or they may be local condensations of some atmospheric constituent. In either case their characteristics may not be directly related to the surface material, but can best be determined by light-scattering methods, just as in the case of terrestrial stratospheric aerosols.

For this purpose, in addition to our silicate and iron models, we have included some models (see Tables T.106 and T.111) corresponding to the limonite particles proposed by Dollfus as a possible surface and airborne material. These should help in the interpretation of future, more detailed, photopolarimetric data. Regarding the often reported obscuration of Martian surface features by dust storms, the discussion in Section 2.32 and Figs. 7 and 8a should provide some insight into the question of absorbing particles, discussed for example by Öpik [116]. In particular,

the steep rise with relative size in the albedo of single scattering for weakly absorbing particles indicated in these figures has some interesting implications for the possibility of condensation in the rarefied Martian atmosphere and the maintenance of a low particle temperature in a radiation field.

4.43 Saturn's Rings

These rings represent another fascinating problem that bears re-examination in the light of the present results. From a recent comprehensive review, by Alexander [117], of all available observations of the planet, its rings, and its satellites, it appears that there has been little progress in our knowledge and understanding of the rings in the past fifty years. The two main difficulties here are connected with observational problems on account of the distance of the planet from Earth and the small range in phase angle, about 0° to 6° , available to us. The first factor results in insufficient accuracy and resolution in the photometry of stars during their occultation by the rings, and the second in a severe limitation on scattering angles needed to reconstruct the phase function of the particles in the rings.

In view of this situation it is not surprising that there is little agreement in the literature on the density, size, shape, and concentration of the particles in the various rings of Saturn. Ever since Laplace's classical work, the most serious theoretical studies are still concerned with the dynamic stability of the rings, as illustrated by a recent reexamination of the problem [118]. Even such a fundamental quantity as the transverse and axial optical thickness of the various rings has not been determined with sufficient accuracy. Cook and Franklin [119] have attempted to make a better estimate by re-analyzing older reports of star occultations and the eclipse of the satellite Iapetus by the shadow of the ring. The latter method is not straightforward, since it depends on *ad hoc* assumptions about the reflectivity of the satellite as well as on the unknown optical thickness of the ring itself and the nature of the shadow it produces. The refinements introduced by Cook and Franklin by considering the effects of the finite size and light curve of Iapetus and of a limb-darkened Sun do not go to the heart of the problem.

Quite apart from the aforementioned observational difficulties it seems to us that the quite logical assumption of polydisperse ring particles and the variety of scattering properties for various types of particles and distributions have not, in general, been seriously considered in existing interpretations of the data. Alexander's account [117, pp. 338 ff.] of the

earlier attempts makes interesting reading here, and it reveals that, even in the more recent ones, there is a singular attachment to traditional notions [120]. In fact, the earlier gross assumptions regarding the nature of the ring material (either boulders or fine dust) could be refined by considering just primary scattering, as in Eq. (99), but including the important effects of size, size distribution, concentration, and complex index of refraction on the scattering matrix for polydispersions. These parameters may also vary with radial distance from the planet along the axis of the rings, as in the case of the zodiacal particles. The apparent secondary gaps within rings A and B, variously reported for example by Lyot [113, pp. 567 ff.] and others [117], rather than being devoid of particles, may then be explained by the existence of locally larger particles for a given ring mass, resulting in a relative minimum in backscattered light compared to the brighter parts of the ring. Similarly, the radial striations sometimes reported along a given ring might be due to higher local concentrations of particles (other things remaining equal) produced by a convergence-divergence wave traveling around the ring.

The actual composition of the particles cannot be guessed at without a knowledge of their index of refraction, and hence of the albedo of single scattering ϖ . This, in turn, is difficult to determine from observations of the brightness of the sunlit ring, especially for the outer and thinner ring A, since this is essentially governed by τ_{sc} as in Eq. (100), where ϖ is implicit only. Nor is it possible to obtain the total extinction τ_{ex} separately by monitoring the passage of a star behind the ring, particularly if the particle sizes are of the order of terrestrial cloud droplets or larger. In this case, due to the observing conditions, the whole phenomenon will be within the most intense part of the diffraction aureole, with $P_1(0)/4\pi \simeq 300$ (cf. Table T.35). The unresolved image of the star must include both its directly attenuated light and the forward-scattered component, with the result that the image may appear hardly diminished when passing behind the rings. As a matter of fact, the whole system of rings (subtending at most 47 seconds of arc) should appear uniformly brighter when "occulting" a bright star, although this has never been reported. In this respect, Ainslie and Knight's report of a visual observation of the passage of a star behind ring A [117, p. 340] is rather interesting. The apparent momentary *brightenings* of the star (which itself remained visible throughout the event) could indicate the existence of local rings of larger particles that may be the same as Enke's and other "divisions," normally appearing as *darker* bands within ring A in reflected sunlight.

As to the middle ring B, its superior brightness may be attributable to a

greater optical thickness than ring A, a higher albedo, finer particles per unit mass and volume, or a combination of all three. Here again it is difficult to separate these effects by observation. For example, the extinction optical thickness cannot easily be evaluated from star occultations, for reasons similar to those just given; namely, the formation of an intense diffraction aureole even by absorbing or opaque particles. The solutions (99) of the transfer equation, which would probably be more applicable to the ring B situation, in combination with some of our models, may suggest some of the likely alternatives and help narrow down the choice of models on the basis of all available criteria. There is no doubt that the whole ring complex, seen edgewise, must present a considerable extinction in order to account for the well-observed shadow on the body of the planet. This may very well indicate the presence of considerable absorption within the particles.

The shape of the ring particles is even more problematical than their size and nature. One meager piece of information is provided by Lyot's and Dollfus's polarization data [113, p. 395] indicating a glory effect, in which case spherical dielectric particles may have to be postulated (see Section 4.32).

Of course, if Saturn could be observed at large phase angles in the direction of the Sun, or from a flyby space probe, the nature of the ring material could be discussed with much more confidence. The relative brightness of the rings would then be enhanced, probably by an order of magnitude or more and by a different factor for each ring, revealing the characteristic sizes of the constituent particles. Such an experiment seems to be conceivable as a technological possibility within the next decade or two [121]. In the meantime, we believe that our present uncertainties in the subject may be further reduced by more careful analyses of existing and future observations in terms of polydisperse scattering theory in conjunction with improved resolution and photometry from Earth or its vicinity.

4.5 INTERPLANETARY AND INTERSTELLAR DUST

Lastly, we must comment on the relevance of our results to the problem of interplanetary and interstellar dust, whose existence in very low concentrations in circumsolar and galactic space is revealed only by the cumulative extinction, brightness, and polarization effects observed over vast spaces. Multiple scattering is out of the question here, but there are other important difficulties. Aside from the problem of separating these

effects from the background produced by other sources, the observing conditions also impose a limitation on the number of scattering parameters needed in each case to deduce the nature of the particle cloud without ambiguity. In the case of interplanetary particles, we can detect their tenuous brightness (and polarization) over a wide angular range in the form of the zodiacal light and gegenschein. The existence of interstellar grains is mainly surmised through their differential attenuation of starlight, but their angular scattering properties cannot be measured directly.

These problems and our state of knowledge just prior to the advent of the space age were reviewed in the 1954 Liège Colloquium "*Les particules solides dans les astres*" [122] with wide participation of international authorities on the subject. The proceedings of this important conference reveal, among other things, that a knowledge of the nature of interstellar and interplanetary condensations is of fundamental importance in the theory of star and planet formation.

4.51 Zodiacal Light

Interest in this phenomenon of the deep twilight sky at low latitudes, already known to observers in antiquity, has recently revived. The earlier controversy on the question whether the zodiacal light originates in the scattering of sunlight by electrons or by dust seems to have been settled in favor of the latter after the notable work of the Cambridge Observatories Chacaltaya expedition in 1958. In particular, Blackwell and Ingham [123], after a careful reduction of their own spectra of the zodiacal light, showed conclusively that the solar Fraunhofer lines were reproduced quite faithfully, and hence the contribution of electron scattering to the brightness and polarization should be minor. Thus the zodiacal light may be interpreted mainly on the basis of the theory of primary scattering of sunlight on a cloud of large particles concentrated in the ecliptic plane, of unknown shape, size, size spectrum, and concentration, and the variation of these parameters with radial distance from the sun.

Although the mathematical formulation of the problem should be simple, there are numerous difficulties related to both the observational uncertainties and the choice of models. The lack of agreement in both areas was patent during a recent international symposium on the subject [124]. We cannot undertake a detailed discussion of all the pertinent problems here, but merely wish to point out the relevance of our numerical experiments.

The main interest in the zodiacal light is of course in deducing the nature, amount, and distribution of the responsible particles. Here the problem is

somewhat akin to that of Saturn's rings, except that the observing situation is vastly different. Whereas in the case of Saturn the totality of the ring particles is observed through backscattering of sunlight at a constant scattering angle along the rings, the zodiacal light is seen from a platform (the Earth) imbedded within the originating cloud of particles in orbit around the illuminating source. Hence, as pointed out by Giese [14,125], the contribution to the brightness and polarization of the phenomenon in any particular direction must come from scattering over a wide range of angles, since it depends on the intersection of the "line of sight" with various parts of the zodiacal cloud. It is thus evident that the number of differential parameters needed to construct models of the latter exceed the number of observable integral quantities. It is therefore essential to have as many models as possible in order to approach a solution by trial and error and by checking for consistency and agreement with other theoretical criteria. In particular, we believe that the definite distribution models and substances presented here, even though limited to spherical particles, should help broaden the likely choices over and above the limited cases considered in the literature (e.g., power-law distributions).

Again, it is clear that space platforms could be very helpful here, particularly if photopolarimetric scans of the zodiacal light could be obtained at distances from the Sun greater than the Earth's. The analysis of such data should narrow down the choice of models. As a matter of fact, the single "multiple outer-planet swingby" mentioned by Hunter [121, p. 626] could serve as an excellent platform for critical observations of both the zodiacal light and Saturn's rings, as well as of other outer-planet atmospheres, at phase angles unavailable from Earth's vicinity.

In the meantime, recent systematic terrestrial observing programs, such as from the Haleakala site [Weinberg in 124], and special expeditions [123; Wolstencroft and Brandt in 124], as well as rocket data [126], are providing a set of more reliable and detailed data than was available, say, ten years ago. The detection by the rocket and the newer Chacaltaya expedition of a slight ellipticity in the polarization of the zodiacal light, if corroborated, supplies an additional parameter related to the nature of the zodiacal particles. As mentioned in Section 4.31, although no ellipticity can be produced by primary scattering of sunlight on *spherical particles*, the observed ellipticity might, at least in one case [Wolstencroft and Brandt in 124], be attributed to rescattering of the polarized terrestrial light on high stratospheric particles within the solid angle subtended by the photometer.

At any rate, the observed linear polarization curve of the zodiacal light,

which seems fairly well established over a wide range of elongations [123,126], cannot be explained in terms of a single *substance* and distribution model. In particular, the considerable positive polarization at small elongations with a maximum at about 75° requires a considerable proportion of metallic (iron) particles [125,126] in addition to the dielectric ones considered initially. As a matter of fact, our iron haze M models (see Tables T.112 to T.114) do show a high maximum polarization of about 0.5 at scattering angles $60^\circ < \theta < 80^\circ$, supporting the suggestion [126] that a greater proportion of *fine* metallic particles should be included in the original models.

In any discussion of the zodiacal light, the existence of the gegenschein cannot be overlooked. If this well-known phenomenon is related to the zodiacal cloud particles—rather than to a “tail” of other material in the close vicinity of Earth—then dielectric spherical particles must be included to explain the enhanced brightness around the antisolar point (see, e.g., our water-cloud models). Strong arguments in favor of the latter may be advanced also on the basis of the maximum negative polarizations obtained by the rocket photometer [126] near 170° in the region of the glory (see Section 4.32). If the elliptical polarization reported in the latter is not further verified, it may just be possible to explain all the known major features of the outer corona, zodiacal light, and gegenschein on the basis of a single (not necessarily unique) model of *spherical* particles, consisting of a properly weighted mixture of our dielectric and metallic distribution models in combination with a reasonable radial distribution law.

4.52 Interstellar Particles

An excellent introduction to this subject is provided by the late Jean Dufay's lucid monograph [127], Parts 2 and 3 of which are of particular relevance here. The author presents a fascinating account of the step-by-step and painstaking astronomical detective work which, during the past two or three decades, established the existence of small interstellar *grains of matter*, quite apart from atoms and molecules, covering a remarkably narrow range of sizes rather than a continuous population up to asteroidal chunks of matter. The main evidence in our own local galaxy (Milky Way) comes from the differential extinction (reddening) of starlight in certain regions of the sky, as well as its polarization. The responsible material is spread within spaces measured in parsecs ($\sim 3 \cdot 10^{13}$ km) rather than astronomical units ($\sim 1.5 \cdot 10^8$ km) as in the zodiacal cloud. These interstellar grains appear to be mainly concentrated in the denser cloud regions, in the

form of diffuse and dark nebulosities, but are thought to exist also in much smaller concentrations in the space between these.

When the differential extinction, deduced by an indirect but consistent line of reasoning and expressed in terms of magnitude differences between unattenuated and attenuated stars of the same type at a normalized distance, is plotted linearly as a function of the inverse of the wavelength, a characteristic S-shaped curve is obtained [1, p. 448]. This has become the standard representation on which practically all discussions of the problem are based. The invariable adherence to this rather awkward method and terminology (the reddening of stars by *extinction* is called “color excess” despite the implied contradiction!) must be attributed to the tradition-mindedness of astronomers rather than to a devotion to scientific clarity. A more cogent justification may be the following: *Provided the size and refractive index are assumed constant*, this method of plotting allows at once both the determination of a characteristic size for the grains and a matching of the wavelength dependence by comparing with theoretical extinction efficiency curves plotted against the size parameter x . Van de Hulst was among the first to examine carefully the implications of scattering theory in this problem and has since given excellent reviews of his own and other authors’ work [1, pp. 446–452; 128]. In particular he believes that homogeneous spherical particles are incapable of providing a coherent explanation of all the observations, especially the polarization.

It would indeed be surprising if, from the interstellar extinction and polarization so far observed over only a rather narrow spectrum, one should be able to deduce uniquely the size, shape, and constitution of the responsible particles, formed at astronomical distances under unknown conditions. The possibility of ever sampling these particles for laboratory analysis is quite remote, and the difficulties in solving an inverse problem are even greater than for atmospheric particles (cf. Section 4.32). Nevertheless, it is fitting to conclude the discussion of our results with the problem of interstellar grains, since their discovery is a triumph of light-scattering theory.

Although we are inclined to agree with van de Hulst that “the Mie theory . . . can better tell us the size of fat globules in real milk than the size of solid particles in the Milky Way” [128], we still believe that its usefulness, particularly in combinations of various types of size distribution and complex index of refraction, has not been exhausted. We have not included in Part II any specific models with this problem in mind, but intend to discuss it separately in the future. Some of our models, using both the old and new optical constants for pure iron (see Table 6) with

characteristic sizes within the range attributed to interstellar particles (cf. Tables T.115 to T.123), do show that the extinction is almost independent of wavelength. This is mainly due to the variation of both parts of m with λ . Our calculations further show that this result is unaltered if one stops the integration at a smaller limiting radius r_2 for each wavelength than indicated by x_2 in the tables. For example, by graphical interpolation (extrapolation) in curves such as shown in Fig. 22, we obtain, for model haze L and iron particles, the values for $\beta_{\text{ex}}(r_2)$ shown in the accompanying table, the last line of which corresponds to the values shown in Tables

r_2	$\lambda 0.441 \mu$	$\lambda 0.589 \mu$	$\lambda 0.668 \mu$
0.1μ	(0.145)	(0.140)	$(0.137) \cdot 10^{-3}$
0.2μ	0.760	0.750	$(0.748) \cdot 10^{-3}$
0.3μ	1.65	1.64	$1.62 \cdot 10^{-3}$
$> 2.5 \mu$	4.78	4.79	$4.81 \cdot 10^{-3}$

T.117 to T.119. This example lends support to van de Hulst's original deduction that the interstellar grains are dielectric rather than metallic in nature. Our own results, for instance, corroborate that waterlike particles with the same size distribution (see curves for haze H and L in Fig. 29) do show the right type of wavelength dependence in the extinction.

Our aforementioned metallic models further show that, although the extinction is virtually unaffected by changes in the real and imaginary parts of m (compare Tables T.115 and T.116 with Tables T.117 and T.119), they do alter significantly the albedo, asymmetry, and polarization of the scattered light. Hence any deductions about the specific chemical composition of the interstellar grains (iron, graphite, etc.) on the basis of extinction alone must be considered extremely tentative. Also, more recent observations reveal that neither the wavelength dependence of the extinction [129] nor that of the degree of polarization [130] are really uniform for all regions of the sky. This implies, among other things, that there may be variations in the characteristic size and size distribution of the grains in different regions of the Milky Way. At any rate, the question of plausible values for m and $n(r)$ in general is still very much an open one.

One interesting property of the type of distribution function used in our models has to do with the total mass of particles producing the desired type of extinction for a particular distribution law. This is given by the integral (87), Section 3.4, and is shown in Table 5 for each model. It is

evident from the discussion of our results and the nature of this integral that, whereas particles larger than a limiting size r_2 will not contribute to the extinction coefficient or optical thickness, they will contribute materially to the mass integral up to a larger size than r_2 because of the factor r^3 in (87). This means that, should the interstellar grains follow such distribution laws, the resulting extinction does not allow an accurate determination of their mass and the *possible existence of larger than typical particles cannot be precluded*. This applies equally to the intensity and polarization of the scattered light and hence bears on the existence of a certain number of large "chunks" of otherwise undetected matter in the zodiacal cloud. The relative mass and number of these additional particles may be easily assessed in our models. The possible mass-size distribution of interstellar grains corresponding to a given extinction has been used in the formulation of theories on their mode of formation, stability, and lifetime [127, pp. 222 and 248 ff.].

The fairly well-established existence of starlight polarization presents yet another puzzling problem that has brought forth various more or less sophisticated hypotheses regarding the possible shape and optical properties of the responsible particles, and the nature of possible interstellar magnetic and kinematic fields [122, 127, 128]. Reliable criteria for a choice among these are not readily available, nor are we in a position to discuss the various theories. We wonder, however, whether simpler explanations may not still be available. For example, barring some esoteric reason not explicitly mentioned in the literature, we do not see why nonspherical *distributions* of spherical grains, concentrated, say, in a disklike region around stars—similar to the zodiacal dust cloud around the ecliptic plane—cannot be considered. Would not such concentrations, including invisible systems of planets with their own atmospheres, produce the observed polarization effects without recourse to particle alignment? A recent paper on the intrinsic polarization of the eclipsing binary β Lyrae [131] contains some interesting suggestions along these lines.

We believe that these and other interesting problems still offer a fruitful field of research that has not yet been fully exploited by means of the theory of polydisperse Mie scattering. Hence our present laborious—but otherwise modest—efforts.

References

1. H. C. van de Hulst, *Light Scattering by Small Particles*, John Wiley and Sons, Inc., New York, 470 pp. (1957).
2. M. Minnaert, *Light and Colour in the Open Air*, Dover Publications, Inc., New York, 362 pp. (1954).
3. G. Mie, *Ann. Physik.*, **25**, 377–445 (1908).
4. J. W. Strutt (Lord Rayleigh), *Phil. Mag.*, **41**, 107–120, 274–279, (1871). *Scientific Papers, I*, Dover Publications, Inc., New York, 87–103 (1964).
5. —, *Phil. Mag.*, **12**, 81–101 (1881). *Scientific Papers, I*, Dover Publications, Inc., New York, 518–536 (1964).
6. —, *Phil. Mag.*, **47**, 375–384 (1899). *Scientific Papers, III*, Dover Publications, Inc., New York, 396–405 (1964).
7. V. Twersky, *Phys. Today*, **13**, 30–36 (1960).
8. D. Deirmendjian, *Atmospheric Scattering of Light and the Sun's Aureole*. Dissertation, University of California, Los Angeles, 79 pp. (1956).
9. —, *Ann. Geophys.*, **13**, 286–306 (1957).
10. —, *Ann. Geophys.*, **15**, 218–249 (1959).
11. —, *Quart. J. Roy. Meteorol. Soc.*, **85**, 404–411 (1959).
12. —, *Quart. J. Roy. Meteorol. Soc.*, **86**, 371–381 (1960).
13. —, Paper presented at the Vienna Conference of the Radiation Commission, IUGG (1961).
14. R. H. Giese, *Z. Astrophys.*, **51**, 119–147 (1961).
15. M. Kerker (ed.), *ICES Electromagnetic Scattering*, Pergamon Press, Oxford, 592 pp. (1963).
16. D. Deirmendjian, *Appl. Optics*, **3**, 187–196 (1964).
17. J. Chamberlain, *Ap. J.*, **141**, 1184–1205 (1965).
18. Z. Sekera, in *Hand. der Physik.*, **48**, S. Flugge (ed.), 288–328, Springer Verlag, Berlin (1957).

19. J. Cabannes, *La Diffusion Moléculaire de la Lumière*, Presses Universitaires, Paris (1929).
20. J. Bricard, in *Hand. der Physik.*, **48**, S. Flugge (ed.), 329–369, Springer Verlag, Berlin (1957).
21. N. A. Logan, *J. Opt. Soc. Am.*, **52**, 342 (1962).
22. J. A. Stratton, *Electromagnetic Theory*, McGraw-Hill Book Co., New York, 615 pp. (1941).
23. A. N. Lowan, *Tables of Scattering Functions for Spherical Particles*, Natl. Bu. Stds., Washington, D.C., *Appl. Math.*, Ser. 4, 119 pp. (1949).
24. G. N. Watson, *A Treatise on the Theory of Bessel Functions* (2nd ed.), The Macmillan Co., New York, 752 pp. (1944).
25. C. W. Querfeld, *J. Opt. Soc. Am.*, **55**, 105–106 (1965).
26. D. Deirmendjian, R. Clasen, and W. Viezee, *J. Opt. Soc. Am.*, **51**, 620–633 (1961).
27. D. Deirmendjian and R. Clasen, *Light Scattering on Partially Absorbing Homogeneous Spheres of Finite Size*, The RAND Corporation, R-393-PR, 44 pp. (1962).
28. D. Deirmendjian, *Tables of Mie Scattering Cross Sections and Amplitudes*, The RAND Corporation, R-407-PR, 34 pp. (1963).
29. R. Penndorf, *Research on Aerosol Scattering in the Infrared, Final Report*, AFCRL-63-668, Bedford, Massachusetts, June 1963. (Obtainable from U.S. Department of Commerce, Office of Technical Services, Washington 25, D.C.)
30. —, *J. Opt. Soc. Am.*, **47**, 1010–1015 (1957).
31. J. C. Johnson and J. R. Terrell, *J. Opt. Soc. Am.*, **45**, 451–454 (1955).
32. A. Vašíček, *Optics of Thin Films*, trans. from Czech by H. Watney-Kaczer, North-Holland Publishing Co., Amsterdam, 403 pp. (1960).
33. W. Irvine, *J. Opt. Soc. Am.*, **55**, 16–21 (1965).
34. B. M. Herman, *Quart. J. Roy. Meteorol. Soc.*, **88**, 143–150 (1962).
35. G. N. Plass, *Appl. Optics*, **5**, 279–285 (1966); **7**, 985 (1968).
36. J. Rheinstein, *Tables of the Amplitude and Phase of the Backscatter from a Conducting Sphere*, Lincoln Laboratory, Report 22-G-16, 44 pp. (June 1963).
37. B. M. Herman and L. J. Battan, *Quart. J. Roy. Meteorol. Soc.*, **87**, 223–230 (1961).
38. J. E. McDonald, *Quart. J. Roy. Meteorol. Soc.*, **88**, 183–186 (1962).
39. W. A. Shurcliff, *Polarized Light*, Harvard University Press, Cambridge, 207 pp. (1962).
40. S. Chandrasekhar, *Radiative Transfer*, Clarendon Press, Oxford, 385 pp. (1950); Dover Publications, Inc., New York (1960).
41. Z. Sekera, *Adv. Geophys.*, **III**, 43–104 (1956).
42. —, *J. Opt. Soc. Am.*, **56**, 1732–1740 (1966).
43. F. Perrin, *J. Chem. Phys.*, **10**, 415–427 (1942); *J. Phys. et Rad.*, Ser. 8, **3**, 41–51 (1942).

44. F. Perrin and A. Abragam, *J. Phys. et Rad.*, Ser. 8, **12**, 69–73 (1951).
45. M. Born and E. Wolf, *Principles of Optics*, Pergamon Press, Oxford, 803 pp. (1959).
46. P. W. Bridgman, *The Logic of Modern Physics*, The Macmillan Co., New York, 228 pp. (1927).
47. D. Deirmendjian, *Radio Science*, **69D**, 893–897 (1965). See also *Complete Microwave Scattering and Extinction Properties of Polydispersed Cloud and Rain Elements*, The RAND Corporation, R-422-PR, 54 pp. (1963).
48. V. A. Ambartsumyan (ed.), *Theoretical Astrophysics*, trans. from Russian by J. B. Sykes, Pergamon Press, Inc., New York, 645 pp. (1958).
49. V. V. Sobolev, *A Treatise on Radiative Transfer*, trans. from Russian by S. I. Gaposchkin, D. Van Nostrand Company, Inc., Princeton, 319 pp. (1963).
50. C. E. Junge, C. W. Chagnon, and J. E. Manson, *J. Meteorol.*, **18**, 81–108 (1961).
51. L. J. Battan and J. B. Theiss, *J. Atmos. Sci.*, **23**, 78–87 (1966).
52. L. J. Battan, private communication (1966).
53. M. Centeno, *J. Opt. Soc. Am.*, **31**, 244–247 (1941).
54. J. A. Curcio and C. C. Petty, *J. Opt. Soc. Am.*, **41**, 302–304 (1951).
55. J. G. Bayly, V. B. Kartha, and W. H. Stevens, *Infrared Physics*, **3**, 211–223 (1963).
56. J. E. McDonald, *J. Meteorol.*, **17**, 232–238 (1960).
57. L. Pontier and C. Dechambenoy, *Ann. Geophys.*, **22**, 633–641 (1966).
58. P. Queney, *Ann. Geophys.*, **22**, 628–632 (1966).
59. J. A. Lane, *J. Opt. Soc. Am.*, **56**, 1398–1399 (1966).
60. H. T. Yolken and J. Kruger, *J. Opt. Soc. Am.*, **55**, 842–844 (1965).
61. A. P. Lenham and D. M. Treherne, in *Optical Properties and Electronic Structure of Metals and Alloys*, F. Abeles (ed.), 196–201, North Holland Publishing Co., Amsterdam (1966).
62. *American Institute of Physics Handbook*, McGraw-Hill Book Company, Inc., New York (1957).
63. Z. Sekera, *Radiative Transfer in a Planetary Atmosphere with Imperfect Scattering*, The RAND Corporation, R-413-PR, 64 pp. (1963).
64. —, *Rev. Geophys.*, **4**, 101–111 (1966).
65. —, *Reduction of the Equations of Radiative Transfer for a Plane-Parallel, Planetary Atmosphere, Parts I and II*, The RAND Corporation, RM-4951-PR and RM-5056-PR, 78 pp. and 57 pp. (1966). (Submitted to *Ap. J.*)
66. T. W. Mullikin, *Ap. J.* **145**, 886–931 (1966).
67. Z. Sekera and A. B. Kahle, *Scattering Functions for Rayleigh Atmospheres of Arbitrary Thickness*, The RAND Corporation, R-452-PR, 73 pp. (1966).
68. A. B. Kahle, *Intensity of Radiation from a Rayleigh Scattering Atmosphere*, The RAND Corp., RM-5620-PR (1968).
69. D. Deirmendjian, *Archiv. Meteor. Geophys. Bioklim.*, **B**, **6**, 452–461, (1955).
70. G. Newkirk and J. A. Eddy, *J. Atmos. Sci.*, **21**, 35–60 (1964).

71. H. C. van de Hulst and K. Grossman, *Multiple Light Scattering in Planetary Atmospheres*, paper presented at KPNO-NASA Conference, Tucson, February 1967 (see [98] 35-55).
72. Z. Sekera, *Icarus*, **6**, 348-359 (1967).
73. G. C. Holzworth and C. R. Nagaraja Rao, *J. Opt. Soc. Am.*, **55**, 403-408 (1965).
74. G. V. Rozenberg, *Twilight*, trans. from Russian (1963) by R. B. Rodman, Plenum Press, New York, 358 pp. (1966).
75. R. S. Fraser, *J. Opt. Soc. Am.*, **54**, 157-168 (1964).
76. B. Fogle and B. Haurwitz, *Space Sci. Rev.*, **6**, 279-340 (1966).
77. G. J. Symons (ed.), *The Eruption of Krakatoa and Subsequent Phenomena*, Truber and Co., London, 494 pp. (1888).
78. H. Wexler, *Weatherwise*, **3**, 129-134, 142 (1950).
79. R. Wilson, *M.N.R.A.S.*, **111**, 478-489 (1951).
80. W. J. Humphries, *Physics of the Air*, Dover Publications, Inc., New York, 676 pp. (1920, 1964).
81. A. C. Holland and J. S. Draper, *Appl. Optics*, **6**, 511-518 (1967).
82. E. Hesstvedt, Mother of Pearl Clouds in Norway, *Geofysiske Publikasjoner*, **20**, No. 10, 29 pp. (1959).
83. —, *Tellus*, **14**, 297-300 (1962).
84. F. H. Ludlam and R. S. Scorer, *Cloud Study. A Pictorial Guide*, John Murray, London, 80 pp. (1957).
85. R. S. Scorer and H. Wexler, *A Colour Guide to Clouds*, Pergamon Press, London, 61 pp. (1964).
86. B. S. Pritchard and W. G. Elliott, *J. Opt. Soc. Am.*, **50**, 191-202 (1960).
87. E. M. Feigelson, *Cosmic Res.*, **2**, 388-393 (1964).
88. G. Yamamoto, M. Tanaka, and K. Kamitani, *J. Atmos. Sci.*, **23**, 305-313 (1966).
89. K. S. Shifrin and A. Y. Perelman, *Tellus*, **18**, 566-572 (1966).
90. G. Fiocco and L. D. Smullin, *Nature*, **199**, 1275-1276 (1963).
91. D. Deirmendjian, *J. Geophys. Res.*, **70**, 743-745 (1965).
92. A. Consortini, L. Ronchi, A. M. Scheggi, and G. Toraldo di Francia, *Radio Science*, **1** (new series), 523-529 (1966).
93. M. King and S. Kainer, *Proc. IEEE*, **53**, 137-141 (1965).
94. G. I. Gorchakov and G. V. Rozenberg, *Izv. Atmos. Ocean. Phys.* (in Eng. transl.), **1**, No. 12, 752-756 (1965).
95. R. F. Hopfield, *Appl. Optics*, **6**, 171-172 (1967).
96. F. S. Harris, Jr., G. C. Sherman, and F. L. Morse, *IEEE Trans. Anten. and Propag.*, **AP-15**, 141-147 (1967).
97. H. Brown, G. J. Stanley, D. O. Muhleman, and G. Munch (eds.), *Proc. Caltech-JPL Lunar and Planetary Conf.*, September 1965, 307 pp. Tech. Memo. No. 33-266 (1966).
98. J. C. Brandt and M. B. McElroy (eds.), *The Atmospheres of Mars and Venus*, Gordon and Breach, New York, 288 pp. (1968).

99. D. Deirmendjian in *Les Spectres Infrarouges des Astres (1963)*, **26**, 397–405, Université de Liège (1964).
100. —, *Icarus*, **3**, 109–120 (1964).
101. J. V. Evans, R. P. Ingalls, L. R. Rainville, and R. R. Silva, *Astron. J.*, **71**, 902–915 (1966).
102. B. G. Clark and A. D. Kuz'min, *Ap. J.*, **142**, 23–44 (1965); *Astron. Zhurnal*, **42**, 595–617 (1965).
103. A. D. Kuz'min and B. G. Clark, *Soviet Physics Doklady*, **10**, 180–181 (1965) (tr. *Dokl. Ak. N. SSSR*, **161**, 551–552 (1965)).
104. A. Kliore, D. L. Cain, G. S. Levy, Von R. Eshleman, G. Fjeldbo, and F. D. Drake, *Science*, **149**, 1243–1248 (1965).
105. A. Kliore, D. A. Tito, D. L. Cain, and G. S. Levy, *J. Spacecraft Rockets*, **4**, 1339–1346 (1967).
106. D. Deirmendjian, in *Proc. XVII IAF Congress, (Madrid 1966)*, O. Wolczek (ed.), 27–32, Polish Sc. Publ., Warsaw (1968).
107. B. T. O'Leary, *Ap. J.*, **146**, 754–766 (1966).
108. H. C. van de Hulst in *The Atmospheres of the Earth and Planets*, G. Kuiper (ed.), 49–111, University of Chicago Press, Chicago (1952).
109. D. Deirmendjian, *J. Geophys. Res.*, **67**, 1635 (1962).
110. T. Gehrels and R. E. Samuelson, *Ap. J.*, **134**, 1022–1024 (1961).
111. J. W. Chamberlain and D. M. Hunten, *Rev. Geophys.*, **3**, 299–317 (1965).
112. A. Dollfus, *Ann. d'Astrophys.*, **28**, 722–747 (1965).
113. —, in *Planets and Satellites*, G. P. Kuiper and B. M. Middlehurst (eds.), 343–399, 534–571, University of Chicago Press, Chicago (1961).
114. R. B. Leighton, B. C. Murray, R. P. Sharp, J. D. Allen, and R. K. Sloan, *Science*, **149**, 627–630 (1965).
115. D. Deirmendjian and E. H. Vestine, *Planet. Space Sci.*, **1**, 146–153 (1959).
116. E. J. Öpik, *J. Geophys. Res.*, **65**, 3057–3063 (1960).
117. A. F. O'D. Alexander, *The Planet Saturn*, Faber and Faber, London 474 pp. (1962).
118. A. F. Cook and F. A. Franklin, *Astron. J.*, **69**, 173–200 (1964).
119. —, *Smithsonian Contr. to Astroph.*, **2**, No. 13, 377–383 (1958).
120. F. A. Franklin and A. F. Cook, *Astron. J.*, **63**, 398–400 (1958).
121. M. W. Hunter, *Space Sci. Rev.*, **6**, 601–654 (1967).
122. Les particules solides dans les astres, *Mem. Soc. Roy. Sci. Liège*, 4th series, **15** (Fascicule unique), 687 pp., Université de Liège (1955).
123. D. E. Blackwell and M. F. Ingham, *Contributions from the Cambridge Observatories Nos. 36–39, M.N.R.A.S.*, **122**, 113–176 (1961).
124. J. L. Weinberg (ed.), *The Zodiacal Light and the Interplanetary Medium*, NASA SP-150, Govt. Print. Off., Wash. D.C., 430 pp. (1968).
125. R. H. Giese, *Space Sci. Rev.*, **1**, 589–611 (1963).
126. R. D. Wolstencroft and L. J. Rose, *Ap. J.*, **147**, 271–292 (1967).
127. J. Dufay, *Galactic Nebulae and Interstellar Matter*, trans. from French by A. J. Pomerans, Philosophical Library, New York, 352 pp. (1957).

128. H. C. van de Hulst, "Light Scattering by Interstellar Grains," lecture reprint from *Publ. Royal Observatory, Edinburgh*, IV (1964).
129. J. B. Whiteoak, *Ap. J.*, **144**, 305-317 (1966).
130. G. V. Coyne and T. Gehrels, *Astron. J.*, **71**, 355-363 (1966).
131. I. Appenzeller and W. A. Hiltner, *Ap. J.*, **149**, 353-362 (1967).

PART II
NUMERICAL TABLES

Table T.I

$m = 1.34$
 $\lambda = 0.45 \mu$

Model: Water haze M
 $x: 0.1(0.1)12.0(0.2)68$

$\beta_{ex} = 0.1056 \text{ km}^{-1}$
 $\varpi = 1.0$

θ	$P_1/4\pi$	$P_2/4\pi$	$P_3/4\pi$	$P_4/4\pi$
0.0	10.31	10.31	10.31	0
2.5	7.386	7.409	7.397	-0.05662
5.0	4.027	4.063	4.039	-0.08973
7.5	2.324	2.349	2.327	-0.07824
10.0	1.484	1.501	1.482	-0.05634
12.5	1.029	1.046	1.029	-0.04014
15.0	0.7612	0.7769	0.7621	+0.02902
17.5	0.5881	0.6028	0.5891	-0.02059
20.0	0.4665	0.4817	0.4683	-0.01421
30.0	0.2108	0.2259	0.2139	-0.002744
40.0	0.1044	0.1168	0.1068	0.000838
50.0	0.05445	0.06353	0.05562	0.001983
60.0	0.02999	0.03620	0.03000	0.002198
70.0	0.01758	0.02169	0.01675	0.002141
80.0	0.01115	0.01383	0.009759	0.002042
90.0	0.007968	0.009528	0.006013	0.002039
100.0	0.006599	0.007211	0.003930	0.002243
110.0	0.006286	0.006197	0.002693	0.002727
120.0	0.006752	0.006307	0.001949	0.003715
130.0	0.008783	0.007764	0.001701	0.005906
132.5	0.009838	0.008350	0.001726	0.006784
135.0	0.01123	0.008974	0.001789	0.007802
137.5	0.01299	0.009586	0.001901	0.008929
140.0	0.01510	0.01010	0.002079	0.01007
142.5	0.01745	0.01040	0.002336	0.01105
145.0	0.01980	0.01042	0.002700	0.01167
147.5	0.02179	0.01019	0.003178	0.01174
150.0	0.02314	0.009882	0.003791	0.01127
152.5	0.02375	0.009747	0.004517	0.01042
155.0	0.02379	0.009980	0.005397	0.009418
157.5	0.02351	0.01086	0.006472	0.008524
160.0	0.02322	0.01260	0.007732	0.007898
162.5	0.02317	0.01531	0.009201	0.007637
165.0	0.02355	0.01925	0.01087	0.007496
167.5	0.02353	0.02382	0.01219	0.006437
170.0	0.02194	0.02602	0.01146	0.002993
172.5	0.01927	0.02278	0.006826	-0.003082
175.0	0.01927	0.01921	-0.004026	-0.006738
177.5	0.02587	0.02369	-0.02176	-0.004213
180.0	0.03261	0.03261	-0.03261	0

Table T.2

$m = 1.33$
 $\lambda = 0.70 \mu$

Model: Water haze M
 $x: 0.1(0.1)10.0(0.2)50$

$\beta_{ex} = 0.1055 \text{ km}^{-1}$
 $w = 1.0$

θ	$P_1/4\pi$	$P_2/4\pi$	$P_3/4\pi$	$P_4/4\pi$
0.0	5.176	5.176	5.176	0
2.5	4.478	4.484	4.480	-0.02026
5.0	3.238	3.252	3.243	-0.04563
7.5	2.267	2.288	2.273	-0.05258
10.0	1.620	1.644	1.627	-0.04891
12.5	1.196	1.218	1.202	-0.04218
15.0	0.9068	0.9284	0.9130	-0.03461
17.5	0.7023	0.7235	0.7084	-0.02770
20.0	0.5528	0.5732	0.5587	-0.02206
30.0	0.2341	0.2494	0.2381	-0.007954
40.0	0.1093	0.1194	0.1112	-0.002190
50.0	0.05528	0.06148	0.05566	0.000165
60.0	0.03030	0.03388	0.02962	0.001129
70.0	0.01806	0.02003	0.01672	0.001531
80.0	0.01177	0.01277	0.01000	0.001727
90.0	0.008553	0.008878	0.006400	0.001912
100.0	0.007013	0.006824	0.004367	0.002217
110.0	0.006508	0.005916	0.003179	0.002741
120.0	0.006859	0.005921	0.002482	0.003685
130.0	0.008524	0.006738	0.002160	0.005381
132.5	0.009263	0.007036	0.002129	0.005956
135.0	0.01016	0.007339	0.002121	0.006580
137.5	0.01123	0.007617	0.002137	0.007225
140.0	0.01244	0.007830	0.002185	0.007841
142.5	0.01374	0.007941	0.002277	0.008361
145.0	0.01506	0.007942	0.002425	0.008718
147.5	0.01631	0.007849	0.002639	0.008852
150.0	0.01737	0.007715	0.002944	0.008715
152.5	0.01815	0.007686	0.003361	0.008331
155.0	0.01863	0.007925	0.003874	0.007808
157.5	0.01890	0.008563	0.004490	0.007234
160.0	0.01901	0.009835	0.005254	0.006663
162.5	0.01888	0.01190	0.006085	0.006164
165.0	0.01842	0.01442	0.006715	0.005613
167.5	0.01744	0.01665	0.006723	0.004350
170.0	0.01534	0.01715	0.005214	0.001470
172.5	0.01269	0.01474	0.000910	-0.002529
175.0	0.01254	0.01268	-0.006657	-0.004315
177.5	0.01627	0.01560	-0.01524	-0.002131
180.0	0.01922	0.01922	-0.01922	0

Table T.3

$m = 1.322 - 0.00001i$ Model: Water haze M $\beta_{\text{ex}} = 0.08823 \text{ km}^{-1}$
 $\lambda = 1.19 \mu$ $x: 0.01(0.01)1(0.1)5(0.2)29$ $\varpi = 0.9999$

θ	$P_1/4\pi$	$P_2/4\pi$	$P_3/4\pi$	$P_4/4\pi$
0.0	2.862	2.862	2.862	0
2.5	2.719	2.721	2.720	-0.005714
5.0	2.367	2.375	2.371	-0.01780
7.5	1.956	1.968	1.961	-0.02817
10.0	1.578	1.593	1.584	-0.03385
12.5	1.262	1.278	1.268	-0.03554
15.0	1.006	1.022	1.011	-0.03457
17.5	0.8016	0.8172	0.8068	-0.03205
20.0	0.6402	0.6544	0.6445	-0.02872
30.0	0.2700	0.2769	0.2705	-0.01559
40.0	0.1233	0.1250	0.1215	-0.007309
50.0	0.06182	0.06088	0.05888	-0.002936
60.0	0.03410	0.03203	0.03075	-0.000707
70.0	0.02063	0.01822	0.01719	0.000441
80.0	0.01367	0.01126	0.01022	0.001081
90.0	0.009951	0.007650	0.006437	0.001518
100.0	0.007994	0.005777	0.004284	0.001923
110.0	0.007113	0.004908	0.002994	0.002407
115.0	0.006982	0.004739	0.002544	0.002713
120.0	0.007049	0.004711	0.002181	0.003082
125.0	0.007331	0.004807	0.001879	0.003527
130.0	0.007854	0.004998	0.001617	0.004050
135.0	0.008643	0.005249	0.001382	0.004628
140.0	0.009683	0.005508	0.001168	0.005186
145.0	0.01088	0.005744	0.000993	0.005597
150.0	0.01203	0.006026	0.000896	0.005700
152.5	0.01249	0.006262	0.000884	0.005610
155.0	0.01284	0.006629	0.000898	0.005422
157.5	0.01301	0.007197	0.000926	0.005145
160.0	0.01296	0.007985	0.000918	0.004787
162.5	0.01264	0.008951	0.000805	0.004307
165.0	0.01198	0.009931	0.000439	0.003576
167.5	0.01088	0.01050	-0.000456	0.002403
170.0	0.009502	0.01027	-0.002088	0.000758
172.5	0.008429	0.009406	-0.004487	-0.000846
175.0	0.008566	0.009051	-0.007382	-0.001384
177.5	0.009993	0.01007	-0.009907	-0.000622
180.0	0.01092	0.01092	-0.01092	0

Table T.4

$m = 1.318 - 0.0003i$
 $\lambda = 1.45 \mu$

Model: Water haze M
 $x: 0.04(0.04)5(0.16)25$

$\beta_{ex} = 0.07633 \text{ km}^{-1}$
 $w = 0.9974$

θ	$P_1/4\pi$	$P_2/4\pi$	$P_3/4\pi$	$P_4/4\pi$
0.0	2.423	2.423	2.423	0
2.5	2.335	2.336	2.335	-0.003792
5.0	2.105	2.110	2.107	-0.01264
7.5	1.809	1.817	1.813	-0.02174
10.0	1.511	1.521	1.515	-0.02822
12.5	1.241	1.252	1.245	-0.03164
15.0	1.010	1.020	1.013	-0.03252
17.5	0.8176	0.8272	0.8204	-0.03157
20.0	0.6608	0.6689	0.6626	-0.02946
30.0	0.2861	0.2870	0.2838	-0.01803
40.0	0.1324	0.1289	0.1280	-0.009302
50.0	0.06703	0.06193	0.06194	-0.004265
60.0	0.03728	0.03199	0.03219	-0.001545
70.0	0.02271	0.01781	0.01783	-0.000075
80.0	0.01510	0.01076	0.01045	0.000764
90.0	0.01097	0.007150	0.006432	0.001315
100.0	0.008714	0.005307	0.004126	0.001766
105.0	0.008041	0.004786	0.003343	0.001993
110.0	0.007596	0.004455	0.002723	0.002235
115.0	0.007352	0.004279	0.002220	0.002507
120.0	0.007296	0.004233	0.001802	0.002816
125.0	0.007428	0.004296	0.001439	0.003170
130.0	0.007753	0.004449	0.001109	0.003566
135.0	0.008274	0.004669	0.000793	0.003983
140.0	0.008972	0.004938	0.000480	0.004371
145.0	0.009772	0.005255	0.000170	0.004650
150.0	0.01054	0.005683	-0.000126	0.004724
155.0	0.01104	0.006388	-0.000421	0.004518
160.0	0.01102	0.007551	-0.000822	0.003976
165.0	0.01011	0.008905	-0.001751	0.002853
170.0	0.008369	0.009105	-0.004037	0.000714
175.0	0.008050	0.008555	-0.007570	-0.000686
180.0	0.009517	0.009517	-0.009517	0

Table T.5

$m = 1.315$
 $\lambda = 1.61 \mu$

Model: Water haze M
 $x: 0.05(0.05)4.0(0.2)20$

$\beta_{\text{ex}} = 0.06909 \text{ km}^{-1}$
 $\varpi = 1.0$

θ	$P_1/4\pi$	$P_2/4\pi$	$P_3/4\pi$	$P_4/4\pi$
0.0	2.224	2.224	2.224	0
2.5	2.156	2.157	2.156	-0.003009
5.0	1.974	1.978	1.976	-0.01042
7.5	1.727	1.733	1.730	-0.01877
10.0	1.465	1.472	1.468	-0.02535
12.5	1.219	1.227	1.222	-0.02929
15.0	1.003	1.011	1.006	-0.03087
17.5	0.8202	0.8262	0.8215	-0.03067
20.0	0.6679	0.6722	0.6681	-0.02922
30.0	0.2952	0.2922	0.2911	-0.01895
40.0	0.1383	0.1315	0.1323	-0.01024
50.0	0.07062	0.06290	0.06415	-0.004956
60.0	0.03949	0.03217	0.03326	-0.002002
70.0	0.02414	0.01768	0.01832	-0.000351
80.0	0.01610	0.01052	0.01064	0.000608
90.0	0.01170	0.006884	0.006447	0.001219
100.0	0.009247	0.005054	0.004030	0.001689
110.0	0.007966	0.004230	0.002546	0.002154
120.0	0.007521	0.004023	0.001550	0.002703
130.0	0.007809	0.004238	0.000775	0.003368
140.0	0.008768	0.004750	0.000042	0.004037
145.0	0.009407	0.005114	-0.000340	0.004259
150.0	0.01001	0.005607	-0.000733	0.004305
155.0	0.01039	0.006343	-0.001164	0.004109
160.0	0.01030	0.007436	-0.001735	0.003592
162.5	0.009998	0.008042	-0.002173	0.003148
165.0	0.009485	0.008584	-0.002806	0.002526
167.5	0.008808	0.008890	-0.003708	0.001690
170.0	0.008112	0.008807	-0.004925	0.000693
172.5	0.007734	0.008525	-0.006373	-0.000156
175.0	0.008020	0.008526	-0.007783	-0.000444
177.5	0.008763	0.008915	-0.008801	-0.000203
180.0	0.009169	0.009169	-0.009169	0

Table T.6

$m = 1.308 - 0.0018i$
 $\lambda = 1.94 \mu$

Model: Water haze M
 $x: 0.025(0.025)6(0.10)18$

$\beta_{ex} = 0.05546 \text{ km}^{-1}$
 $\varpi = 0.9849$

θ	$P_1/4\pi$	$P_2/4\pi$	$P_3/4\pi$	$P_4/4\pi$
0.0	1.939	1.939	1.939	0
2.5	1.893	1.893	1.893	-0.002156
5.0	1.764	1.765	1.764	-0.007720
7.5	1.580	1.582	1.581	-0.01461
10.0	1.374	1.376	1.374	-0.02083
12.5	1.169	1.170	1.169	-0.02531
15.0	0.9810	0.9809	0.9800	-0.02786
17.5	0.8157	0.8137	0.8134	-0.02873
20.0	0.6745	0.6703	0.6708	-0.02830
30.0	0.3117	0.3004	0.3037	-0.02040
40.0	0.1506	0.1365	0.1408	-0.01195
50.0	0.07864	0.06495	0.06895	-0.006288
60.0	0.04471	0.03265	0.03574	-0.002926
70.0	0.02763	0.01743	0.01948	-0.000971
80.0	0.01849	0.009996	0.01103	0.000194
90.0	0.01338	0.006300	0.006394	0.000936
100.0	0.01045	0.004498	0.003698	0.001473
105.0	0.009502	0.004016	0.002769	0.001707
110.0	0.008813	0.003724	0.002021	0.001934
115.0	0.008337	0.003582	0.001401	0.002161
120.0	0.008046	0.003561	0.000870	0.002394
125.0	0.007919	0.003642	0.000395	0.002632
130.0	0.007944	0.003815	-0.000051	0.002874
135.0	0.008094	0.004068	-0.000491	0.003100
140.0	0.008353	0.004410	-0.000945	0.003292
145.0	0.008659	0.004848	-0.001429	0.003402
150.0	0.008946	0.005425	-0.001960	0.003393
155.0	0.009080	0.006185	-0.002574	0.003198
160.0	0.008931	0.007115	-0.003361	0.002745
165.0	0.008383	0.007992	-0.004507	0.001896
170.0	0.007706	0.008274	-0.006175	0.000637
175.0	0.007933	0.008314	-0.007904	-0.000103
180.0	0.008604	0.008604	-0.008604	0

Table T.7

$m = 1.29 - 0.000035i$
 $\lambda = 2.25 \mu$

Model: Water haze M
 $x: 0.25(0.25)4.0(0.10)16$

$\beta_{ex} = 0.04238 \text{ km}^{-1}$
 $\varpi = 0.9968$

θ	$P_1/4\pi$	$P_2/4\pi$	$P_3/4\pi$	$P_4/4\pi$
0.0	1.776	1.776	1.776	0
2.5	1.740	1.740	1.740	-0.001629
5.0	1.637	1.637	1.637	-0.005955
7.5	1.487	1.486	1.486	-0.01162
10.0	1.312	1.310	1.311	-0.01715
12.5	1.133	1.129	1.131	-0.02154
15.0	0.9636	0.9571	0.9596	-0.02441
17.5	0.8106	0.8014	0.8050	-0.02581
20.0	0.6772	0.6653	0.6700	-0.02598
30.0	0.3238	0.3040	0.3117	-0.02003
40.0	0.1603	0.1387	0.1468	-0.01232
50.0	0.08528	0.06539	0.07234	-0.006786
60.0	0.04915	0.03214	0.03739	-0.003342
70.0	0.03066	0.01656	0.02011	-0.001273
80.0	0.02064	0.009070	0.01108	-0.000017
90.0	0.01494	0.005451	0.006102	0.000781
100.0	0.01161	0.003776	0.003189	0.001335
110.0	0.009682	0.003134	0.001359	0.001771
120.0	0.008663	0.003088	0.000081	0.002157
130.0	0.008292	0.003436	-0.000961	0.002500
140.0	0.008369	0.004117	-0.001979	0.002725
145.0	0.008495	0.004601	-0.002525	0.002745
150.0	0.008587	0.005206	-0.003124	0.002656
155.0	0.008603	0.005961	-0.003794	0.002442
160.0	0.008432	0.006825	-0.004607	0.002040
165.0	0.008086	0.007654	-0.005625	0.001401
170.0	0.007753	0.008088	-0.006917	0.000533
175.0	0.008048	0.008494	-0.008072	0.000021
180.0	0.008494	0.008494	-0.008494	0

Table T.8

$m = 1.364 - 0.3060i$
 $\lambda = 3.00 \mu$

Model: Water haze M
 $x: 0.025(0.025)2(0.1)10$

$\beta_{ex} = 0.05932 \text{ km}^{-1}$
 $\varpi = 0.3466$

θ	$P_1/4\pi$	$P_2/4\pi$	$P_3/4\pi$	$P_4/4\pi$
0.0	1.103	1.103	1.103	0
5.0	1.053	1.045	1.049	-0.005210
10.0	0.9229	0.8972	0.9097	-0.01743
15.0	0.7574	0.7112	0.7331	-0.02975
20.0	0.5972	0.5349	0.5632	-0.03749
25.0	0.4628	0.3905	0.4219	-0.04019
30.0	0.3574	0.2805	0.3123	-0.03941
40.0	0.2155	0.1407	0.1680	-0.03279
50.0	0.1346	0.06909	0.08930	-0.02462
60.0	0.08795	0.03347	0.04642	-0.01765
70.0	0.06016	0.01620	0.02275	-0.01235
80.0	0.04302	0.008201	0.009391	-0.008518
90.0	0.03209	0.004912	0.001703	-0.005794
100.0	0.02489	0.004004	-0.002818	-0.003867
110.0	0.02002	0.004276	-0.005536	-0.002503
120.0	0.01666	0.005112	-0.007220	-0.001538
130.0	0.01432	0.006182	-0.008309	-0.000863
140.0	0.01268	0.007313	-0.009058	-0.000411
150.0	0.01156	0.008396	-0.009602	-0.000141
160.0	0.01084	0.009344	-0.009993	-0.000020
170.0	0.01044	0.01004	-0.01023	0.000004
180.0	0.01031	0.01031	-0.01031	0

Table T.9

$m = 1.353 - 0.0059i$ $\lambda = 3.9 \mu$		Model: Water haze M $x: 0.0125(0.0125)1.0(0.1)9$		$\beta_{ex} = 0.02355 \text{ km}^{-1}$ $\omega = 0.9477$
θ	$P_1/4\pi$	$P_2/4\pi$	$P_3/4\pi$	$P_4/4\pi$
0.0	0.9216	0.9216	0.9216	0
5.0	0.8882	0.8864	0.8873	-0.002139
10.0	0.7986	0.7919	0.7952	-0.007387
15.0	0.6779	0.6642	0.6708	-0.01318
20.0	0.5524	0.5310	0.5410	-0.01740
25.0	0.4392	0.4108	0.4237	-0.01933
30.0	0.3449	0.3110	0.3260	-0.01935
40.0	0.2108	0.1711	0.1876	-0.01616
50.0	0.1312	0.09140	0.1066	-0.01157
60.0	0.08466	0.04813	0.06045	-0.007490
70.0	0.05706	0.02520	0.03403	-0.004317
80.0	0.04030	0.01339	0.01863	-0.002017
90.0	0.02981	0.007645	0.009406	-0.000366
100.0	0.02310	0.005234	0.003688	0.000813
110.0	0.01874	0.004714	-0.000050	0.001672
120.0	0.01590	0.005310	-0.002683	0.002297
130.0	0.01410	0.006637	-0.004775	0.002726
140.0	0.01303	0.008465	-0.006716	0.002904
145.0	0.01271	0.009507	-0.007726	0.002859
150.0	0.01252	0.01059	-0.008789	0.002693
155.0	0.01243	0.01164	-0.009932	0.002350
160.0	0.01245	0.01254	-0.01115	0.001806
165.0	0.01269	0.01323	-0.01233	0.001146
170.0	0.01322	0.01372	-0.01331	0.000540
175.0	0.01384	0.01402	-0.01392	0.000137
180.0	0.01412	0.01412	-0.01412	0

Table T.10

$m = 1.315 - 0.0143i$
 $\lambda = 5.30 \mu$

Model: Water haze M
 $x: 0.0125(0.0125)1.0(0.10)7$

$\beta_{ex} = 0.01123 \text{ km}^{-1}$
 $\varpi = 0.8263$

θ	$P_1/4\pi$	$P_2/4\pi$	$P_3/4\pi$	$P_4/4\pi$
0.0	0.6851	0.6851	0.6851	0
5.0	0.6689	0.6663	0.6676	-0.001062
10.0	0.6233	0.6138	0.6185	-0.003859
15.0	0.5572	0.5379	0.5474	-0.007423
20.0	0.4814	0.4515	0.4659	-0.01069
25.0	0.4058	0.3657	0.3847	-0.01293
30.0	0.3368	0.2883	0.3108	-0.01393
40.0	0.2281	0.1691	0.1950	-0.01311
50.0	0.1550	0.09343	0.1183	-0.01051
60.0	0.1074	0.04877	0.06972	-0.007530
70.0	0.07659	0.02395	0.03947	-0.004846
80.0	0.05646	0.01108	0.02058	-0.002709
90.0	0.04309	0.005219	0.008637	-0.001081
100.0	0.03408	0.003392	0.000930	0.000107
110.0	0.02793	0.003856	-0.004206	0.000932
120.0	0.02371	0.005600	-0.007797	0.001463
130.0	0.02084	0.008011	-0.01049	0.001731
140.0	0.01899	0.01072	-0.01268	0.001737
145.0	0.01836	0.01209	-0.01366	0.001632
150.0	0.01790	0.01341	-0.01460	0.001451
155.0	0.01761	0.01464	-0.01548	0.001199
160.0	0.01749	0.01573	-0.01628	0.000893
165.0	0.01754	0.01664	-0.01697	0.000569
170.0	0.01769	0.01733	-0.01748	0.000278
175.0	0.01784	0.01776	-0.01780	0.000073
180.0	0.01791	0.01791	-0.01791	0

Table T.II

$m = 1.315 - 0.1370i$
 $\lambda = 6.05 \mu$

Model: Water haze M
 $x: 0.01(0.01)1.0(0.10)5$

$\beta_{ex} = 0.01893 \text{ km}^{-1}$
 $w = 0.2972$

θ	$P_1/4\pi$	$P_2/4\pi$	$P_3/4\pi$	$P_4/4\pi$
0.0	0.5279	0.5279	0.5279	0
5.0	0.5198	0.5169	0.5184	-0.000819
10.0	0.4967	0.4856	0.4911	-0.003088
15.0	0.4613	0.4383	0.4495	-0.006300
20.0	0.4175	0.3809	0.3986	-0.009790
25.0	0.3697	0.3197	0.3434	-0.01292
30.0	0.3218	0.2601	0.2886	-0.01523
40.0	0.2363	0.1593	0.1925	-0.01684
50.0	0.1716	0.08960	0.1217	-0.01537
60.0	0.1261	0.04642	0.07347	-0.01267
70.0	0.09453	0.02169	0.04136	-0.009845
80.0	0.07241	0.008928	0.02012	-0.007271
90.0	0.05689	0.003598	0.006145	-0.005073
100.0	0.04595	0.002666	-0.003088	-0.003322
110.0	0.03814	0.004220	-0.009262	-0.002007
120.0	0.03253	0.007073	-0.01346	-0.001062
130.0	0.02851	0.01046	-0.01637	-0.000422
140.0	0.02566	0.01389	-0.01844	-0.000043
145.0	0.02460	0.01550	-0.01924	0.000060
150.0	0.02374	0.01699	-0.01991	0.000114
155.0	0.02305	0.01833	-0.02046	0.000126
160.0	0.02253	0.01948	-0.02091	0.000109
165.0	0.02215	0.02042	-0.02125	0.000075
170.0	0.02189	0.02112	-0.02150	0.000038
175.0	0.02174	0.02155	-0.02164	0.000010
180.0	0.02169	0.02169	-0.02169	0

Table T.12

$m = 1.29 - 0.0472i$
 $\lambda = 8.15 \mu$

Model: Water haze M
 $x: 0.01(0.01)1.0(0.1)5$

$\beta_{ex} = 0.006244 \text{ km}^{-1}$
 $\varpi = 0.4103$

θ	$P_1/4\pi$	$P_2/4\pi$	$P_3/4\pi$	$P_4/4\pi$
0.0	0.4154	0.4154	0.4154	0
10.0	0.3968	0.3881	0.3924	-0.001318
20.0	0.3483	0.3181	0.3328	-0.004315
30.0	0.2861	0.2316	0.2571	-0.007055
40.0	0.2258	0.1520	0.1847	-0.008266
50.0	0.1756	0.09074	0.1251	-0.007942
60.0	0.1367	0.04881	0.08010	-0.006729
70.0	0.1076	0.02287	0.04731	-0.005209
80.0	0.08597	0.008745	0.02390	-0.003700
90.0	0.07003	0.002788	0.007357	-0.002357
100.0	0.05829	0.002148	-0.004308	-0.001264
110.0	0.04965	0.004750	-0.01257	0.000453
120.0	0.04331	0.009137	-0.01847	0.000088
130.0	0.03869	0.01428	-0.02273	0.000389
140.0	0.03540	0.01944	-0.02585	0.000483
150.0	0.03318	0.02406	-0.02810	0.000411
160.0	0.03181	0.02772	-0.02966	0.000241
170.0	0.03110	0.03007	-0.03058	0.000071
180.0	0.03088	0.03088	-0.03088	0

Table T.13

$m = 1.212 - 0.0601i$ Model: Water haze M $\beta_{\text{ex}} = 0.004487 \text{ km}^{-1}$
 $\lambda = 10.0 \mu$ $x: 0.005(0.005)1.0(0.05)4$ $w = 0.1786$

θ	$P_1/4\pi$	$P_2/4\pi$	$P_3/4\pi$	$P_4/4\pi$
0.0	0.3256	0.3256	0.3256	0
10.0	0.3160	0.3079	0.3119	-0.000567
20.0	0.2899	0.2606	0.2749	-0.001972
30.0	0.2535	0.1981	0.2240	-0.003530
40.0	0.2141	0.1353	0.1700	-0.004606
50.0	0.1772	0.08269	0.1206	-0.004924
60.0	0.1457	0.04424	0.07962	-0.004583
70.0	0.1203	0.01951	0.04743	-0.003857
80.0	0.1003	0.006063	0.02294	-0.003007
90.0	0.08483	0.001006	0.004630	-0.002194
100.0	0.07283	0.001741	-0.008931	-0.001493
110.0	0.06360	0.006133	-0.01891	-0.000930
120.0	0.05650	0.01252	-0.02621	-0.000511
130.0	0.05122	0.01963	-0.03152	-0.000228
140.0	0.04728	0.02656	-0.03536	-0.000064
150.0	0.04448	0.03260	-0.03805	0.000006
160.0	0.04261	0.03726	-0.03984	0.000018
170.0	0.04155	0.04020	-0.04087	0.000007
180.0	0.04120	0.04120	-0.04120	0

Table T.14

$$m = 1.111 - 0.1831i$$

$$\lambda = 11.5 \mu$$

Model: Water haze M
 $x: 0.005(0.005)0.5(0.05)3.5$

$$\beta_{\text{ex}} = 0.009734 \text{ km}^{-1}$$

$$w = 0.04417$$

θ	$P_1/4\pi$	$P_2/4\pi$	$P_3/4\pi$	$P_4/4\pi$
0.0	0.2667	0.2667	0.2667	0
10.0	0.2612	0.2535	0.2573	-0.000478
20.0	0.2459	0.2177	0.2314	-0.001716
30.0	0.2236	0.1688	0.1942	-0.003237
40.0	0.1980	0.1177	0.1525	-0.004537
50.0	0.1722	0.07281	0.1117	-0.005300
60.0	0.1485	0.03869	0.07537	-0.005465
70.0	0.1280	0.01624	0.04488	-0.005149
80.0	0.1108	0.004213	0.02030	-0.004534
90.0	0.09674	0.000443	0.000961	-0.003785
100.0	0.08540	0.002637	-0.01400	-0.003016
110.0	0.07632	0.008713	-0.02542	-0.002295
120.0	0.06914	0.01692	-0.03404	-0.001659
130.0	0.06354	0.02585	-0.04046	-0.001127
140.0	0.05927	0.03444	-0.04515	-0.000704
150.0	0.05613	0.04187	-0.04847	-0.000386
160.0	0.05399	0.04756	-0.05067	-0.000168
170.0	0.05275	0.05112	-0.05193	-0.000042
180.0	0.05234	0.05234	-0.05234	0

Table T.15

$n = 1.44 - 0.4000i$
 $\lambda = 16.6 \mu$

Model: Water haze M
 $x: 0.005(0.005)0.5(0.05)2.5$

$\beta_{ex} = 0.01345 \text{ km}^{-1}$
 $\tau = 0.07473$

θ	$P_1/4\pi$	$P_2/4\pi$	$P_3/4\pi$	$P_4/4\pi$
0.0	0.1986	0.1986	0.1986	0
10.0	0.1964	0.1910	0.1937	-0.000488
20.0	0.1901	0.1700	0.1798	-0.001817
30.0	0.1806	0.1394	0.1585	-0.003635
40.0	0.1687	0.1045	0.1325	-0.005498
50.0	0.1557	0.07056	0.1042	-0.007011
60.0	0.1425	0.04165	0.07598	-0.007926
70.0	0.1298	0.02019	0.04935	-0.008168
80.0	0.1182	0.007005	0.02533	-0.007808
90.0	0.1080	0.001714	0.004394	-0.007000
100.0	0.09913	0.003143	-0.01340	-0.005922
110.0	0.09164	0.009710	-0.02821	-0.004736
120.0	0.08544	0.01969	-0.04029	-0.003569
130.0	0.08040	0.03141	-0.04992	-0.002510
140.0	0.07644	0.04330	-0.05740	-0.001613
150.0	0.07346	0.05402	-0.06296	-0.000906
160.0	0.07139	0.06249	-0.06678	-0.000402
170.0	0.07016	0.06790	-0.06902	-0.000100
180.0	0.06976	0.06976	-0.06976	0

Table T.16

$m = 1.34$
 $\lambda = 0.45 \mu$

Model: Water haze L
 $x: 0.10(0.10)12(0.2)36$

$\beta_{\text{ex}} = 0.04797 \text{ km}^{-1}$
 $\varpi = 1.0$

θ	$P_1/4\pi$	$P_2/4\pi$	$P_3/4\pi$	$P_4/4\pi$
0.0	3.725	3.725	3.725	0
2.5	3.438	3.443	3.440	-0.01105
5.0	2.798	2.811	2.804	-0.03099
7.5	2.149	2.167	2.155	-0.04298
10.0	1.627	1.649	1.634	-0.04542
12.5	1.238	1.262	1.246	-0.04267
15.0	0.9526	0.9767	0.9605	-0.03775
17.5	0.7422	0.7655	0.7497	-0.03205
20.0	0.5845	0.6068	0.5915	-0.02647
30.0	0.2444	0.2606	0.2488	-0.01091
40.0	0.1130	0.1232	0.1150	-0.003766
50.0	0.05706	0.06306	0.05738	-0.000638
60.0	0.03140	0.03475	0.03065	0.000722
70.0	0.01885	0.02061	0.01745	0.001338
80.0	0.01241	0.01322	0.01058	0.001663
90.0	0.009068	0.009235	0.006843	0.001923
100.0	0.007386	0.007113	0.004704	0.002252
110.0	0.006711	0.006148	0.003441	0.002758
120.0	0.006880	0.006046	0.002712	0.003618
130.0	0.008182	0.006690	0.002325	0.005089
135.0	0.009463	0.007215	0.002224	0.006110
140.0	0.01126	0.007748	0.002192	0.007245
145.0	0.01349	0.008151	0.002288	0.008270
150.0	0.01582	0.008391	0.002627	0.008846
155.0	0.01774	0.008865	0.003371	0.008735
157.5	0.01835	0.009498	0.003922	0.008431
160.0	0.01862	0.01057	0.004534	0.008000
162.5	0.01849	0.01206	0.005076	0.007381
165.0	0.01774	0.01369	0.005251	0.006293
167.5	0.01602	0.01468	0.004506	0.004250
170.0	0.01338	0.01401	0.002151	0.001098
172.5	0.01103	0.01195	-0.002128	-0.002090
175.0	0.01103	0.01120	-0.007929	-0.003108
177.5	0.01390	0.01375	-0.01353	-0.001394
180.0	0.01592	0.01592	-0.01592	0

Table T.17

$m = 1.33$
 $\lambda = 0.70 \mu$

Model: Water haze L
 $x: 0.05(0.05)6(0.2)26$

$\beta_{\text{ex}} = 0.03953 \text{ km}^{-1}$
 $\omega = 1.0$

θ	$P_1/4\pi$	$P_2/4\pi$	$P_3/4\pi$	$P_4/4\pi$
0.0	2.415	2.415	2.415	0
2.5	2.331	2.332	2.332	-0.003833
5.0	2.110	2.114	2.112	-0.01290
7.5	1.819	1.828	1.823	-0.02250
10.0	1.521	1.533	1.526	-0.02957
12.5	1.249	1.262	1.254	-0.03338
15.0	1.014	1.028	1.019	-0.03435
17.5	0.8189	0.8323	0.8234	-0.03327
20.0	0.6596	0.6719	0.6632	-0.03092
30.0	0.2816	0.2872	0.2814	-0.01829
40.0	0.1286	0.1293	0.1262	-0.009006
50.0	0.06442	0.06273	0.06103	-0.003878
60.0	0.03550	0.03292	0.03185	-0.001225
70.0	0.02147	0.01870	0.01781	0.000173
80.0	0.01425	0.01155	0.01062	0.000956
90.0	0.01037	0.007825	0.006711	0.001459
100.0	0.008275	0.005882	0.004467	0.001888
110.0	0.007271	0.004962	0.003113	0.002373
120.0	0.007076	0.004698	0.002241	0.003009
130.0	0.007671	0.004924	0.001616	0.003871
135.0	0.008289	0.005184	0.001343	0.004382
140.0	0.009115	0.005517	0.001079	0.004902
145.0	0.01009	0.005922	0.000825	0.005353
150.0	0.01109	0.006452	0.000593	0.005620
155.0	0.01182	0.007261	0.000369	0.005575
157.5	0.01198	0.007827	0.000222	0.005387
160.0	0.01190	0.008499	-0.000006	0.005040
162.5	0.01151	0.009199	-0.000408	0.004471
165.0	0.01076	0.009742	-0.001115	0.003591
167.5	0.009716	0.009894	-0.002255	0.002343
170.0	0.008617	0.009556	-0.003881	0.000867
172.5	0.007999	0.009024	-0.005883	-0.000346
175.0	0.008362	0.008969	-0.007913	-0.000719
177.5	0.009428	0.009591	-0.009450	-0.000319
180.0	0.01002	0.01002	-0.01002	0

Table T.18

$m = 1.322 - 0.00001i$
 $\lambda = 1.19 \mu$

Model: Water haze L
 $x: 0.05(0.05)5(0.2)17$

$\beta_{ex} = 0.02218 \text{ km}^{-1}$
 $\varpi = 0.9999$

θ	$P_1/4\pi$	$P_2/4\pi$	$P_3/4\pi$	$P_4/4\pi$
0.0	1.520	1.520	1.520	0
2.5	1.495	1.495	1.495	-0.001327
5.0	1.422	1.422	1.422	-0.004929
7.5	1.314	1.313	1.313	-0.009860
10.0	1.183	1.181	1.182	-0.01503
12.5	1.044	1.040	1.042	-0.01957
15.0	0.9071	0.9009	0.9033	-0.02299
17.5	0.7786	0.7702	0.7734	-0.02514
20.0	0.6626	0.6518	0.6560	-0.02610
30.0	0.3345	0.3166	0.3233	-0.02213
40.0	0.1704	0.1504	0.1574	-0.01446
50.0	0.09167	0.07300	0.07938	-0.008299
60.0	0.05297	0.03688	0.04145	-0.004259
70.0	0.03297	0.01958	0.02261	-0.001770
80.0	0.02208	0.01109	0.01271	-0.000235
90.0	0.01589	0.006882	0.007233	0.000758
100.0	0.01228	0.004857	0.004031	0.001457
110.0	0.01019	0.004017	0.002023	0.002008
120.0	0.009059	0.003907	0.000628	0.002506
125.0	0.008764	0.004058	0.000043	0.002751
130.0	0.008617	0.004332	-0.000513	0.002992
135.0	0.008595	0.004726	-0.001074	0.003220
140.0	0.008672	0.005245	-0.001669	0.003414
145.0	0.008807	0.005897	-0.002331	0.003538
150.0	0.008939	0.006683	-0.003100	0.003535
155.0	0.008986	0.007583	-0.004029	0.003324
160.0	0.008876	0.008488	-0.005190	0.002793
165.0	0.008659	0.009185	-0.006624	0.001876
170.0	0.008680	0.009496	-0.008191	0.000772
175.0	0.009329	0.009695	-0.009421	0.000104
180.0	0.009864	0.009864	-0.009864	0

Table T.19

$m = 1.308 - 0.0018i$
 $\lambda = 1.94 \mu$

Model: Water haze L
 $x: 0.025(0.025)6(0.1)10$

$\beta_{\text{ex}} = 0.008947 \text{ km}^{-1}$
 $\omega = 0.9804$

θ	$P_1/4\pi$	$P_2/4\pi$	$P_3/4\pi$	$P_4/4\pi$
0.0	0.9252	0.9252	0.9252	0
5.0	0.8930	0.8905	0.8918	-0.001820
10.0	0.8063	0.7972	0.8017	-0.006316
15.0	0.6887	0.6706	0.6794	-0.01138
20.0	0.5648	0.5373	0.5505	-0.01522
25.0	0.4513	0.4155	0.4322	-0.01717
30.0	0.3552	0.3133	0.3325	-0.01740
40.0	0.2169	0.1695	0.1899	-0.01466
50.0	0.1342	0.08813	0.1064	-0.01050
60.0	0.08583	0.04466	0.05916	-0.006715
70.0	0.05732	0.02222	0.03247	-0.003790
80.0	0.04010	0.01104	0.01716	-0.001681
90.0	0.02943	0.005836	0.008142	-0.000200
100.0	0.02265	0.003829	0.002640	0.000834
110.0	0.01827	0.003558	-0.000900	0.001554
120.0	0.01544	0.004278	-0.003372	0.002047
130.0	0.01364	0.005610	-0.005320	0.002338
140.0	0.01258	0.007360	-0.007094	0.002400
145.0	0.01225	0.008341	-0.007996	0.002314
150.0	0.01206	0.009356	-0.008928	0.002132
155.0	0.01198	0.01036	-0.009891	0.001835
160.0	0.01204	0.01129	-0.01087	0.001418
165.0	0.01224	0.01207	-0.01179	0.000923
170.0	0.01261	0.01267	-0.01254	0.000452
175.0	0.01300	0.01305	-0.01302	0.000119
180.0	0.01318	0.01318	-0.01318	0

Table T.20

$m = 1.364 - 0.3060i$
 $\lambda = 3.00 \mu$

Model: Water haze L
 $x: 0.025(0.025)2(0.1)4$

$\beta_{ex} = 0.01571 \text{ km}^{-1}$
 $\varpi = 0.2359$

θ	$P_1/4\pi$	$P_2/4\pi$	$P_3/4\pi$	$P_4/4\pi$
0.0	0.4411	0.4411	0.4411	0
5.0	0.4362	0.4333	0.4347	-0.000796
10.0	0.4219	0.4110	0.4164	-0.003047
15.0	0.3995	0.3767	0.3879	-0.006380
20.0	0.3709	0.3338	0.3516	-0.01027
25.0	0.3382	0.2863	0.3107	-0.01414
30.0	0.3037	0.2383	0.2681	-0.01750
40.0	0.2365	0.1517	0.1874	-0.02150
50.0	0.1796	0.08740	0.1218	-0.02163
60.0	0.1362	0.04590	0.07407	-0.01918
70.0	0.1046	0.02185	0.04117	-0.01577
80.0	0.08192	0.009520	0.01894	-0.01238
90.0	0.06549	0.004604	0.003998	-0.009372
100.0	0.05352	0.004158	-0.006018	-0.006808
110.0	0.04478	0.006215	-0.01272	-0.004708
120.0	0.03841	0.009515	-0.01722	-0.003068
130.0	0.03377	0.01328	-0.02027	-0.001857
140.0	0.03044	0.01702	-0.02237	-0.001018
150.0	0.02810	0.02038	-0.02380	-0.000484
160.0	0.02657	0.02307	-0.02473	-0.000182
170.0	0.02570	0.02481	-0.02525	-0.000040
180.0	0.02542	0.02542	-0.02542	0

Table T.21

$m = 1.353 - 0.0059i$
 $\lambda = 3.90 \mu$

Model: Water haze L
 $x: 0.025(0.025)3$

$\beta_{\text{ex}} = 0.002219 \text{ km}^{-1}$
 $w = 0.08931$

θ	$P_1/4\pi$	$P_2/4\pi$	$P_3/4\pi$	$P_4/4\pi$
0.0	0.3458	0.3458	0.3458	0
10.0	0.3361	0.3289	0.3325	-0.000628
20.0	0.3090	0.2832	0.2958	-0.002245
30.0	0.2700	0.2207	0.2440	-0.004187
40.0	0.2257	0.1557	0.1871	-0.005713
50.0	0.1825	0.09913	0.1337	-0.006327
60.0	0.1446	0.05654	0.08884	-0.005921
70.0	0.1138	0.02840	0.05418	-0.004722
80.0	0.09018	0.01229	0.02878	-0.003122
90.0	0.07269	0.004920	0.01069	-0.001499
100.0	0.05997	0.003368	-0.002115	-0.000125
110.0	0.05077	0.005446	-0.01128	0.000855
120.0	0.04418	0.009622	-0.01796	0.001397
130.0	0.03956	0.01481	-0.02289	0.001526
140.0	0.03643	0.02020	-0.02655	0.001327
150.0	0.03444	0.02514	-0.02923	0.000925
160.0	0.03328	0.02909	-0.03107	0.000475
170.0	0.03270	0.03164	-0.03216	0.000129
180.0	0.03252	0.03252	-0.03252	0

Table T.22

$m = 1.315 - 0.0143i$
 $\lambda = 5.30 \mu$

Model: Water haze L
 $x: 0.0125(0.0125)4$

$\beta_{\text{ex}} = 0.001088 \text{ km}^{-1}$
 $\varpi = 0.6345$

θ	$P_1/4\pi$	$P_2/4\pi$	$P_3/4\pi$	$P_4/4\pi$
0.0	0.2891	0.2891	0.2891	0
10.0	0.2820	0.2754	0.2787	-0.000396
20.0	0.2625	0.2381	0.2500	-0.001383
30.0	0.2346	0.1871	0.2094	-0.002490
40.0	0.2034	0.1335	0.1645	-0.003258
50.0	0.1730	0.08595	0.1214	-0.003460
60.0	0.1459	0.04894	0.08353	-0.003136
70.0	0.1230	0.02353	0.05219	-0.002473
80.0	0.1042	0.008634	0.02719	-0.001682
90.0	0.08923	0.002242	0.007720	-0.000920
100.0	0.07739	0.002156	-0.007210	-0.000279
110.0	0.06814	0.006336	-0.01855	0.000194
120.0	0.06103	0.01305	-0.02711	0.000483
130.0	0.05566	0.02088	-0.03353	0.000593
140.0	0.05173	0.02873	-0.03830	0.000549
150.0	0.04898	0.03572	-0.04174	0.000399
160.0	0.04719	0.04120	-0.04407	0.000211
170.0	0.04619	0.04468	-0.04543	0.000058
180.0	0.04587	0.04587	-0.04587	0

Table T.23

$m = 1.315 - 0.1370i$ Model: Water haze L $\beta_{\text{ex}} = 0.003571 \text{ km}^{-1}$
 $\lambda = 6.05 \mu$ $x: 0.01(0.01)3$ $w = 0.1313$

θ	$P_1/4\pi$	$P_2/4\pi$	$P_3/4\pi$	$P_4/4\pi$
0.0	0.2430	0.2430	0.2430	0
10.0	0.2390	0.2327	0.2358	-0.000410
20.0	0.2274	0.2042	0.2155	-0.001496
30.0	0.2102	0.1638	0.1855	-0.002896
40.0	0.1897	0.1195	0.1504	-0.004186
50.0	0.1682	0.07828	0.1144	-0.005044
60.0	0.1476	0.04479	0.08059	-0.005335
70.0	0.1289	0.02105	0.05089	-0.005101
80.0	0.1128	0.007009	0.02592	-0.004492
90.0	0.09922	0.001333	0.005584	-0.003685
100.0	0.08810	0.002172	-0.01063	-0.002835
110.0	0.07911	0.007589	-0.02335	-0.002047
120.0	0.07194	0.01580	-0.03319	-0.001383
130.0	0.06632	0.02525	-0.04069	-0.000865
140.0	0.06203	0.03466	-0.04628	-0.000492
150.0	0.05888	0.04302	-0.05030	-0.000245
160.0	0.05674	0.04954	-0.05301	-0.000098
170.0	0.05549	0.05367	-0.05457	-0.000023
180.0	0.05508	0.05508	-0.05508	0

Table T.24

$m = 1.29 - 0.0472i$
 $\lambda = 8.15 \mu$

Model: Water haze L
 $x: 0.01(0.01)3$

$\beta_{\text{ex}} = 0.0009424 \text{ km}^{-1}$
 $\varpi = 0.1560$

θ	$P_1/4\pi$	$P_2/4\pi$	$P_3/4\pi$	$P_4/4\pi$
0.0	0.1971	0.1971	0.1971	0
10.0	0.1950	0.1897	0.1923	-0.000094
20.0	0.1889	0.1688	0.1786	-0.000347
30.0	0.1796	0.1384	0.1576	-0.000678
40.0	0.1681	0.1037	0.1319	-0.000993
50.0	0.1554	0.06972	0.1040	-0.001211
60.0	0.1426	0.04067	0.07591	-0.001292
70.0	0.1302	0.01904	0.04936	-0.001237
80.0	0.1189	0.005762	0.02530	-0.001079
90.0	0.1089	0.000546	0.004227	-0.000861
100.0	0.1001	0.002236	-0.01376	-0.000630
110.0	0.09272	0.009205	-0.02877	-0.000420
120.0	0.08657	0.01965	-0.04104	-0.000250
130.0	0.08157	0.03180	-0.05084	-0.000129
140.0	0.07764	0.04405	-0.05845	-0.000055
150.0	0.07469	0.05503	-0.06410	-0.000017
160.0	0.07264	0.06366	-0.06800	-0.000003
170.0	0.07143	0.06915	-0.07028	0.000000
180.0	0.07103	0.07103	-0.07103	0

Table T.25

$m = 1.29 - 0.0236i$ Model: Water haze L $\beta_{ex} = 0.0005465 \text{ km}^{-1}$
 $\lambda = 8.15 \mu$ $x: 0.01(0.01)3$ $\tau = 0.2688$

θ	$P_1/4\pi$	$P_2/4\pi$	$P_3/4\pi$	$P_4/4\pi$
0.0	0.1977	0.1977	0.1977	0
10.0	0.1956	0.1902	0.1929	-0.000170
20.0	0.1894	0.1693	0.1791	-0.000255
30.0	0.1800	0.1388	0.1581	-0.000493
40.0	0.1683	0.1040	0.1323	-0.000709
50.0	0.1555	0.06997	0.1042	-0.000842
60.0	0.1426	0.04085	0.07608	-0.000864
70.0	0.1302	0.01915	0.04948	-0.000782
80.0	0.1188	0.005829	0.02541	-0.000626
90.0	0.1087	0.000574	0.004332	-0.000437
100.0	0.09990	0.002229	-0.01365	-0.000254
110.0	0.09248	0.009167	-0.02864	-0.000103
120.0	0.08633	0.01958	-0.04090	0.000000
130.0	0.08134	0.03171	-0.05068	0.000055
140.0	0.07743	0.04393	-0.05828	0.000069
150.0	0.07449	0.05488	-0.06392	0.000055
160.0	0.07244	0.06349	-0.06782	0.000030
170.0	0.07124	0.06897	-0.07010	0.000008
180.0	0.07085	0.07085	-0.07085	0

Table T.26

$m = 1.44 - 0.4000i$
 $\lambda = 16.6 \mu$

Model: Water haze L
 $x: 0.005(0.005)0.5(0.05)1.5$

$\beta_{\text{ex}} = 0.002889 \text{ km}^{-1}$
 $\varpi = 0.001468$

θ	$P_1/4\pi$	$P_2/4\pi$	$P_3/4\pi$	$P_4/4\pi$
0.0	0.1393	0.1393	0.1393	0
10.0	0.1389	0.1348	0.1369	-0.000070
20.0	0.1378	0.1222	0.1298	-0.000270
30.0	0.1361	0.1030	0.1184	-0.000567
40.0	0.1339	0.07985	0.1034	-0.000917
50.0	0.1311	0.05571	0.08545	-0.001267
60.0	0.1281	0.03352	0.06547	-0.001568
70.0	0.1249	0.01581	0.04432	-0.001784
80.0	0.1216	0.004376	0.02281	-0.001888
90.0	0.1183	0.000123	0.001682	-0.001875
100.0	0.1152	0.003042	-0.01844	-0.001752
110.0	0.1123	0.01229	-0.03703	-0.001539
120.0	0.1097	0.02636	-0.05371	-0.001264
130.0	0.1074	0.04331	-0.06818	-0.000960
140.0	0.1055	0.06102	-0.08022	-0.000658
150.0	0.1040	0.07739	-0.08970	-0.000390
160.0	0.1029	0.09055	-0.09652	-0.000180
170.0	0.1022	0.09906	-0.1006	-0.000046
180.0	0.1020	0.1020	-0.1020	0

Table T.27

$m = 1.340$
 $\lambda = 0.45 \mu$

Model: Water haze H
 $x: 0.05(0.05)2(0.10)18$

$\beta_{\text{ex}} = 0.02014 \text{ km}^{-1}$
 $\varpi = 1.0$

θ	$P_1/4\pi$	$P_2/4\pi$	$P_3/4\pi$	$P_4/4\pi$
0.0	1.666	1.666	1.666	0
2.5	1.641	1.641	1.641	-0.001436
5.0	1.568	1.568	1.568	-0.005441
7.5	1.456	1.456	1.456	-0.01120
10.0	1.317	1.316	1.316	-0.01762
12.5	1.162	1.161	1.161	-0.02365
15.0	1.004	1.003	1.003	-0.02848
17.5	0.8531	0.8513	0.8511	-0.03165
20.0	0.7143	0.7120	0.7116	-0.03308
30.0	0.3246	0.3206	0.3199	-0.02647
40.0	0.1462	0.1414	0.1408	-0.01490
50.0	0.07121	0.06640	0.06603	-0.007041
60.0	0.03852	0.03398	0.03374	-0.002795
70.0	0.02314	0.01898	0.01872	-0.000612
80.0	0.01532	0.01155	0.01114	0.000550
90.0	0.01111	0.007688	0.007030	0.001239
100.0	0.008790	0.005633	0.004655	0.001735
110.0	0.007585	0.004588	0.003189	0.002190
120.0	0.007129	0.004193	0.002201	0.002696
130.0	0.007242	0.004339	0.001433	0.003310
140.0	0.007725	0.005130	0.000649	0.004018
150.0	0.008001	0.006748	-0.000626	0.004503
160.0	0.007208	0.008594	-0.003448	0.003622
162.5	0.006967	0.008881	-0.004462	0.003053
165.0	0.006862	0.009064	-0.005534	0.002389
167.5	0.006982	0.009162	-0.006590	0.001701
170.0	0.007368	0.009215	-0.007549	0.001074
172.5	0.007971	0.009257	-0.008337	0.000577
175.0	0.008640	0.009305	-0.008911	0.000241
177.5	0.009167	0.009349	-0.009254	0.000057
180.0	0.009367	0.009367	-0.009367	0

Table T.28

$m = 1.33$
 $\lambda = 0.70 \mu$

Model: Water haze H
 $x: 0.05(0.05)2(0.10)14$

$\beta_{\text{ex}} = 0.009888 \text{ km}^{-1}$
 $\varpi = 1.0$

θ	$P_1/4\pi$	$P_2/4\pi$	$P_3/4\pi$	$P_4/4\pi$
0.0	0.9544	0.9544	0.9544	0
5.0	0.9267	0.9241	0.9254	-0.001804
10.0	0.8495	0.8400	0.8447	-0.006517
15.0	0.7385	0.7199	0.7290	-0.01243
20.0	0.6129	0.5855	0.5986	-0.01768
30.0	0.3801	0.3418	0.3591	-0.02211
40.0	0.2176	0.1789	0.1951	-0.01903
50.0	0.1225	0.08934	0.1018	-0.01316
60.0	0.07092	0.04452	0.05313	-0.007822
70.0	0.04340	0.02285	0.02828	-0.003975
80.0	0.02842	0.01239	0.01538	-0.001452
90.0	0.01996	0.007329	0.008396	0.000166
100.0	0.01502	0.004960	0.004376	0.001234
110.0	0.01204	0.004039	0.001851	0.001986
120.0	0.01021	0.004017	0.000033	0.002553
130.0	0.009060	0.004671	-0.001575	0.002965
140.0	0.008334	0.005901	-0.003360	0.003122
150.0	0.008047	0.007535	-0.005586	0.002789
160.0	0.008582	0.009208	-0.008114	0.001805
165.0	0.009243	0.009918	-0.009267	0.001165
170.0	0.01003	0.01047	-0.01018	0.000571
175.0	0.01069	0.01083	-0.01076	0.000151
180.0	0.01095	0.01095	-0.01095	0

Table T.29

$m = 1.322 - 0.00001i$ Model: Water haze H $\beta_{\text{ex}} = 0.002877 \text{ km}^{-1}$
 $\lambda = 1.19 \mu$ $x: 0.05(0.05)8$ $\varpi = 0.9999$

θ	$P_1/4\pi$	$P_2/4\pi$	$P_3/4\pi$	$P_4/4\pi$
0.0	0.4633	0.4633	0.4633	0
5.0	0.4582	0.4560	0.4571	-0.000333
10.0	0.4434	0.4348	0.4391	-0.001275
15.0	0.4202	0.4019	0.4109	-0.002672
20.0	0.3903	0.3604	0.3750	-0.004305
25.0	0.3560	0.3139	0.3341	-0.005940
30.0	0.3194	0.2658	0.2911	-0.007367
35.0	0.2825	0.2191	0.2483	-0.008435
40.0	0.2469	0.1760	0.2078	-0.009064
45.0	0.2137	0.1379	0.1708	-0.009240
50.0	0.1836	0.1055	0.1380	-0.009002
55.0	0.1570	0.07884	0.1097	-0.008422
60.0	0.1338	0.05753	0.08584	-0.007590
65.0	0.1140	0.04098	0.06601	-0.006594
70.0	0.09716	0.02848	0.04977	-0.005514
75.0	0.08302	0.01932	0.03662	-0.004415
80.0	0.07121	0.01283	0.02605	-0.003347
85.0	0.06139	0.008440	0.01760	-0.002346
90.0	0.05324	0.005661	0.01086	-0.001435
95.0	0.04651	0.004106	0.005490	-0.000628
100.0	0.04094	0.003466	0.001189	0.000068
105.0	0.03634	0.003504	-0.002275	0.000651
110.0	0.03256	0.004040	-0.005094	0.001122
120.0	0.02691	0.006093	-0.009365	0.001734
130.0	0.02323	0.008875	-0.01247	0.001927
140.0	0.02100	0.01191	-0.01488	0.001745
150.0	0.01986	0.01483	-0.01680	0.001278
160.0	0.01947	0.01728	-0.01826	0.000687
170.0	0.01946	0.01893	-0.01919	0.000193
180.0	0.01951	0.01951	-0.01951	0

Table T.30

$m = 1.308 - 0.0018i$
 $\lambda = 1.94 \mu$

Model: Water haze H
 $x: 0.025(0.025)5$

$\beta_{ex} = 0.0006960 \text{ km}^{-1}$
 $\varpi = 0.9443$

θ	$P_1/4\pi$	$P_2/4\pi$	$P_3/4\pi$	$P_4/4\pi$
0.0	0.2546	0.2546	0.2546	0
10.0	0.2504	0.2441	0.2472	-0.000127
20.0	0.2385	0.2150	0.2264	-0.000458
30.0	0.2205	0.1736	0.1956	-0.000866
40.0	0.1986	0.1276	0.1591	-0.001205
50.0	0.1752	0.08429	0.1213	-0.001364
60.0	0.1522	0.04879	0.08570	-0.001300
70.0	0.1310	0.02338	0.05446	-0.001042
80.0	0.1124	0.008116	0.02850	-0.000663
90.0	0.09659	0.001580	0.007826	-0.000253
100.0	0.08359	0.001687	-0.008110	0.000109
110.0	0.07317	0.006277	-0.02009	0.000368
120.0	0.06498	0.01344	-0.02892	0.000500
130.0	0.05869	0.02163	-0.03533	0.000509
140.0	0.05400	0.02967	-0.03990	0.000424
150.0	0.05063	0.03670	-0.04307	0.000287
160.0	0.04838	0.04212	-0.04513	0.000144
170.0	0.04710	0.04552	-0.04630	0.000039
180.0	0.04668	0.04668	-0.04668	0

Table T.31

$m = 1.364 - 0.3060i$
 $\lambda = 3.00 \mu$

Model: Water haze H
 $x: 0.025(0.025)3$

$\beta_{ex} = 0.003897 \text{ km}^{-1}$
 $\varpi = 0.08142$

θ	$P_1/4\pi$	$P_2/4\pi$	$P_3/4\pi$	$P_4/4\pi$
0.0	0.1737	0.1737	0.1737	0
10.0	0.1725	0.1676	0.1701	-0.000185
20.0	0.1691	0.1506	0.1596	-0.000703
30.0	0.1638	0.1252	0.1432	-0.001450
40.0	0.1568	0.09539	0.1223	-0.002286
50.0	0.1488	0.06534	0.09848	-0.003065
60.0	0.1400	0.03875	0.07345	-0.003665
70.0	0.1311	0.01832	0.04861	-0.004009
80.0	0.1224	0.005487	0.02509	-0.004073
90.0	0.1142	0.000470	0.003654	-0.003876
100.0	0.1066	0.002494	-0.01523	-0.003471
110.0	0.09991	0.01012	-0.03139	-0.002925
120.0	0.09408	0.02154	-0.04483	-0.002310
130.0	0.08918	0.03489	-0.05570	-0.001693
140.0	0.08521	0.04841	-0.06419	-0.001126
150.0	0.08216	0.06055	-0.07053	-0.000651
160.0	0.08000	0.07011	-0.07489	-0.000294
170.0	0.07872	0.07620	-0.07745	-0.000074
180.0	0.07829	0.07829	-0.07829	0

Table T.32

$m = 1.353 - 0.0059i$
 $\lambda = 3.90 \mu$

Model: Water haze H
 $x: 0.025(0.025)2$

$\beta_{\text{ex}} = 0.0001317 \text{ km}^{-1}$
 $\varpi = 0.05876$

θ	$P_1/4\pi$	$P_2/4\pi$	$P_3/4\pi$	$P_4/4\pi$
0.0	0.1515	0.1515	0.1515	0
10.0	0.1509	0.1466	0.1487	0.000003
20.0	0.1491	0.1324	0.1405	0.000011
30.0	0.1463	0.1111	0.1275	0.000023
40.0	0.1425	0.08556	0.1104	0.000040
50.0	0.1381	0.05926	0.09045	0.000058
60.0	0.1331	0.03541	0.06864	0.000076
70.0	0.1279	0.01664	0.04608	0.000093
80.0	0.1226	0.004635	0.02374	0.000105
90.0	0.1174	0.000088	0.002412	0.000111
100.0	0.1125	0.002697	-0.01730	0.000110
110.0	0.1080	0.01137	-0.03498	0.000102
120.0	0.1039	0.02445	-0.05038	0.000088
130.0	0.1004	0.03999	-0.06336	0.000070
140.0	0.09753	0.05601	-0.07390	0.000050
150.0	0.09525	0.07062	-0.08202	0.000030
160.0	0.09362	0.08226	-0.08776	0.000014
170.0	0.09264	0.08974	-0.09118	0.000004
180.0	0.09231	0.09231	-0.09231	0

Table T.33

$m = 1.315 - 0.0143i$
 $\lambda = 5.30 \mu$

Model: Water haze H
 $x: 0.01(0.01)1.5$

$\beta_{ex} = 0.0001142 \text{ km}^{-1}$
 $\varpi = 0.1677$

θ	$P_1/4\pi$	$P_2/4\pi$	$P_3/4\pi$	$P_4/4\pi$
0.0	0.1363	0.1363	0.1363	0
20.0	0.1351	0.1196	0.1271	-0.000003
40.0	0.1319	0.07820	0.1016	-0.000010
60.0	0.1272	0.03269	0.06448	-0.000017
80.0	0.1216	0.004064	0.02222	-0.000020
100.0	0.1160	0.003152	-0.01911	-0.000017
120.0	0.1111	0.02701	-0.05477	0.000012
140.0	0.1072	0.06230	-0.08174	-0.000006
160.0	0.1048	0.09233	-0.09837	-0.000002
180.0	0.1040	0.1040	-0.1040	0

Table T.34

$m = 1.315 - 0.1370i$
 $\lambda = 6.05 \mu$

Model: Water haze H
 $x: 0.01(0.01)1.5$

$\beta_{ex} = 0.0008008 \text{ km}^{-1}$
 $\varpi = 0.01680$

θ	$P_1/4\pi$	$P_2/4\pi$	$P_3/4\pi$	$P_4/4\pi$
0.0	0.1323	0.1323	0.1323	0
20.0	0.1314	0.1163	0.1236	-0.000050
40.0	0.1290	0.07629	0.09921	-0.000172
60.0	0.1254	0.03202	0.06338	-0.000302
80.0	0.1212	0.003950	0.02187	-0.000377
100.0	0.1169	0.003260	-0.01951	-0.000363
120.0	0.1130	0.02767	-0.05592	-0.000271
140.0	0.1100	0.06405	-0.08392	-0.000145
160.0	0.1080	0.09523	-0.1014	-0.000040
180.0	0.1074	0.1074	-0.1074	0

Table T.35

$m = 1.34$
 $\lambda = 0.45 \mu$

Model: Water cloud C.I
 $x: 0.25(0.25)60(0.50)160$

$\beta_{\text{ex}} = 16.33 \text{ km}^{-1}$
 $\varpi = 1.0$

θ	$P_1/4\pi$	$P_2/4\pi$	$P_3/4\pi$	$P_4/4\pi$
0.0	313.6	313.6	313.6	0
1.0	140.8	140.9	140.9	-0.9193
2.0	21.94	21.91	21.91	-0.4747
3.0	5.369	5.315	5.330	-0.1072
4.0	2.590	2.537	2.555	-0.03771
5.0	1.616	1.575	1.589	-0.01870
6.0	1.171	1.136	1.149	-0.01197
7.0	0.9335	0.9018	0.9133	-0.007486
8.0	0.7932	0.7678	0.7767	-0.005416
9.0	0.7020	0.6778	0.6861	-0.004902
10.0	0.6313	0.6163	0.6206	-0.004102
11.0	0.5811	0.5636	0.5692	0.000698
12.0	0.5432	0.5262	0.5319	-0.003656
13.0	0.5022	0.4986	0.4975	-0.000433
14.0	0.4735	0.4650	0.4667	0.001042
15.0	0.4454	0.4420	0.4411	-0.001713
20.0	0.3298	0.3337	0.3294	0.000177
25.0	0.2429	0.2522	0.2450	0.001153
30.0	0.1756	0.1875	0.1784	0.001882
35.0	0.1252	0.1384	0.1283	0.001758
40.0	0.08809	0.1008	0.09096	0.001645
45.0	0.06152	0.07262	0.06360	0.001629
50.0	0.04213	0.05193	0.04375	0.001358
55.0	0.02924	0.03650	0.02981	0.001304
60.0	0.01974	0.02551	0.01980	0.001088
65.0	0.01259	0.01835	0.01268	0.000292
70.0	0.009010	0.01186	0.007978	0.000644
75.0	0.006492	0.007668	0.004809	0.000374
80.0	0.004743	0.005057	0.002773	0.000292
85.0	0.003611	0.003358	0.001428	0.000247
90.0	0.002973	0.002407	0.000690	0.000186
95.0	0.002614	0.001817	0.000194	0.000211
100.0	0.002393	0.001639	0.000016	0.000200
105.0	0.002240	0.001604	-0.000126	0.000293
110.0	0.002262	0.001740	0.000042	0.000226
115.0	0.003598	0.002083	0.000608	0.000268
120.0	0.005559	0.001784	0.000717	0.001243
122.0	0.005790	0.001796	0.000456	0.001499

TABLE T.35

θ	$P_1/4\pi$	$P_2/4\pi$	$P_3/4\pi$	$P_4/4\pi$
124.0	0.005598	0.001778	0.000163	0.001618
126.0	0.005166	0.001819	-0.000191	0.001707
128.0	0.004789	0.001809	-0.000426	0.001703
130.0	0.004612	0.001987	-0.000530	0.001886
132.0	0.005103	0.002396	-0.000616	0.002186
134.0	0.006797	0.002971	-0.000308	0.003205
136.0	0.01126	0.004090	0.000338	0.005368
138.0	0.01887	0.005499	0.001815	0.008378
139.0	0.02554	0.006086	0.002397	0.009854
140.0	0.03058	0.005605	0.004450	0.01065
141.0	0.03760	0.005978	0.005218	0.01118
142.0	0.04338	0.005211	0.006355	0.01006
143.0	0.04588	0.004408	0.007622	0.007422
144.0	0.04523	0.004129	0.008179	0.003547
145.0	0.04125	0.004590	0.007800	-0.000592
146.0	0.03390	0.006071	0.007191	-0.004185
147.0	0.02537	0.008230	0.006071	-0.005499
148.0	0.01822	0.01060	0.004914	-0.005074
149.0	0.01373	0.01255	0.004072	-0.002826
150.0	0.01220	0.01326	0.003521	-0.000348
152.0	0.01300	0.01284	0.003086	0.002328
154.0	0.01373	0.01172	0.002962	0.002489
156.0	0.01291	0.01177	0.002848	0.001786
158.0	0.01178	0.01217	0.002543	0.001374
160.0	0.01085	0.01261	0.002167	0.001423
162.0	0.01022	0.01262	0.001918	0.001359
164.0	0.009510	0.01309	0.001716	0.001260
166.0	0.009168	0.01350	0.001645	0.001303
168.0	0.008951	0.01396	0.001860	0.001346
170.0	0.009386	0.01550	0.002047	0.001480
172.0	0.009436	0.01749	0.002882	0.001824
174.0	0.01089	0.02082	0.004268	0.002049
176.0	0.01482	0.03004	0.009039	0.002877
177.0	0.02156	0.04157	0.01662	0.003132
178.0	0.03577	0.05156	0.02723	0.000238
179.0	0.04157	0.02090	-0.005092	-0.005588
180.0	0.05022	0.05022	-0.05022	0

Table T.36

$m = 1.33$
 $\lambda = 0.70 \mu$

Model: Water cloud C.I
 $x: 0.25(0.25)110$

$\beta_{ex} = 16.73 \text{ km}^{-1}$
 $\tau = 1.0$

θ	$P_1/4\pi$	$P_2/4\pi$	$P_3/4\pi$	$P_4/4\pi$
0.0	133.7	133.7	133.7	0
1.0	94.25	94.30	94.27	-0.3803
2.0	35.94	36.01	35.96	-0.5669
3.0	10.54	10.56	10.53	-0.3055
4.0	3.900	3.881	3.876	-0.1192
5.0	2.152	2.112	2.121	-0.05086
6.0	1.483	1.448	1.458	-0.02761
7.0	1.140	1.107	1.117	-0.01722
8.0	0.9335	0.9062	0.9147	-0.01071
9.0	0.8009	0.7765	0.7832	-0.006069
10.0	0.7092	0.6887	0.6945	-0.004903
15.0	0.4684	0.4624	0.4619	-0.001724
25.0	0.2440	0.2530	0.2452	0.001089
35.0	0.1242	0.1361	0.1264	0.002622
45.0	0.06121	0.07150	0.06255	0.002202
55.0	0.02894	0.03683	0.02973	0.001548
65.0	0.01417	0.01847	0.01359	0.001145
75.0	0.007188	0.009110	0.005735	0.000596
85.0	0.004092	0.004565	0.002149	0.000404
95.0	0.002788	0.002652	0.000617	0.000355
105.0	0.002416	0.002064	0.000035	0.000337
107.5	0.002410	0.002007	0.000154	0.000332
110.0	0.002711	0.002038	0.000217	0.000337
112.5	0.003195	0.002020	0.000440	0.000467
115.0	0.003854	0.002053	0.000509	0.000711
117.5	0.004508	0.002046	0.000597	0.001047
120.0	0.005096	0.002064	0.000499	0.001424
122.5	0.005509	0.002131	0.000276	0.001746
125.0	0.005758	0.002335	0.000104	0.002151
127.5	0.006005	0.002638	-0.000051	0.002497

TABLE T.36

θ	$P_1/4\pi$	$P_2/4\pi$	$P_3/4\pi$	$P_4/4\pi$
130.0	0.007082	0.003284	-0.000065	0.003422
132.5	0.009455	0.004374	0.000232	0.005057
135.0	0.01349	0.005633	0.001126	0.007141
137.5	0.02131	0.006496	0.002319	0.009672
140.0	0.03073	0.006559	0.004364	0.01116
142.5	0.03710	0.005579	0.005972	0.009067
145.0	0.03581	0.004549	0.007018	0.002524
147.5	0.02503	0.006995	0.006141	-0.003009
150.0	0.01447	0.01133	0.004450	-0.003373
152.5	0.01043	0.01377	0.003288	0.000477
155.0	0.01088	0.01356	0.002987	0.002717
157.5	0.01161	0.01267	0.002844	0.002860
160.0	0.01117	0.01294	0.002757	0.002378
162.5	0.01074	0.01324	0.002789	0.002238
164.0	0.01042	0.01393	0.002858	0.002070
166.0	0.01005	0.01498	0.003020	0.001987
168.0	0.01029	0.01641	0.003183	0.002035
170.0	0.01081	0.01863	0.003957	0.002594
172.0	0.01142	0.02128	0.005289	0.002599
174.0	0.01518	0.02772	0.008411	0.003600
175.0	0.01871	0.03480	0.01255	0.004286
176.0	0.02524	0.04374	0.01934	0.004252
177.0	0.03317	0.04672	0.02480	0.001034
178.0	0.03666	0.02947	0.01145	-0.003274
179.0	0.04170	0.02698	-0.02776	-0.005015
180.0	0.05055	0.05055	-0.05055	0

Table T.37

$m = 1.322 - 0.00001i$
 $\lambda = 1.19 \mu$

Model: Water cloud C.I
 $x: 0.20(0.20)70$

$\beta_{\text{ex}} = 17.29 \text{ km}^{-1}$
 $w = 0.9994$

θ	$P_1/4\pi$	$P_2/4\pi$	$P_3/4\pi$	$P_4/4\pi$
0.0	48.23	48.23	48.23	0
2.0	29.38	29.43	29.40	-0.2640
4.0	8.370	8.407	8.372	-0.2729
6.0	2.360	2.350	2.339	-0.1022
8.0	1.174	1.159	1.153	-0.03017
10.0	0.8332	0.8160	0.8161	-0.01374
12.0	0.6612	0.6441	0.6464	-0.008468
14.0	0.5470	0.5373	0.5362	-0.002526
16.0	0.4666	0.4626	0.4592	-0.002022
18.0	0.4036	0.4023	0.3980	-0.001528
20.0	0.3508	0.3512	0.3461	0.000055
30.0	0.1751	0.1847	0.1757	0.002212
40.0	0.08760	0.09810	0.08879	0.002808
50.0	0.04376	0.05248	0.04439	0.002501
60.0	0.02220	0.02821	0.02191	0.001897
70.0	0.01166	0.01529	0.01058	0.001350
80.0	0.006572	0.008516	0.004931	0.000957
85.0	0.005124	0.006490	0.003293	0.000818
90.0	0.004134	0.005065	0.002160	0.000728
95.0	0.003476	0.004083	0.001387	0.000671
100.0	0.003109	0.003425	0.000907	0.000641
105.0	0.003132	0.003005	0.000678	0.000677
110.0	0.003586	0.002755	0.000591	0.000878
115.0	0.004337	0.002681	0.000480	0.001294
120.0	0.005234	0.002910	0.000284	0.001968

TABLE T.37

θ	$P_1/4\pi$	$P_2/4\pi$	$P_3/4\pi$	$P_4/4\pi$
125.0	0.006546	0.003682	0.000143	0.003115
130.0	0.009453	0.005253	0.000338	0.005298
135.0	0.01585	0.007290	0.001226	0.008797
140.0	0.02569	0.007948	0.002988	0.01143
142.0	0.02907	0.007307	0.003865	0.01088
144.0	0.03087	0.006465	0.004687	0.009036
146.0	0.03039	0.005860	0.005238	0.006082
148.0	0.02744	0.005975	0.005439	0.002576
150.0	0.02262	0.007397	0.005406	-0.000257
152.0	0.01718	0.009925	0.005009	-0.001437
154.0	0.01311	0.01230	0.004440	-0.000765
156.0	0.01090	0.01421	0.004015	0.000696
158.0	0.01058	0.01553	0.004061	0.002248
160.0	0.01039	0.01607	0.004057	0.003399
162.0	0.01127	0.01578	0.004005	0.003910
164.0	0.01183	0.01719	0.004457	0.004054
166.0	0.01230	0.01967	0.005344	0.004323
168.0	0.01316	0.02142	0.005554	0.005056
170.0	0.01621	0.02610	0.007705	0.006312
172.0	0.02009	0.03301	0.01342	0.005630
174.0	0.02707	0.03887	0.02091	0.003614
176.0	0.03397	0.03554	0.01677	-0.001990
178.0	0.03528	0.02326	-0.01825	-0.007242
180.0	0.04556	0.04556	-0.04556	0

Table T.38

$m = 1.318 - 0.00003i$
 $\lambda = 1.45 \mu$

Model: Water cloud C.I
 $x: 0.20(0.20)60$

$\beta_{\text{ex}} = 17.63 \text{ km}^{-1}$
 $\tau = 0.9849$

θ	$P_1/4\pi$	$P_2/4\pi$	$P_3/4\pi$	$P_4/4\pi$
0.0	33.76	33.76	33.76	0
2.0	23.97	24.01	23.99	-0.1682
4.0	9.550	9.615	9.569	-0.2572
6.0	3.121	3.147	3.114	-0.1490
8.0	1.384	1.375	1.362	-0.05675
10.0	0.8866	0.8759	0.8698	-0.01876
12.0	0.6842	0.6750	0.6717	-0.01124
14.0	0.5658	0.5537	0.5526	-0.007050
16.0	0.4726	0.4675	0.4633	-0.001736
18.0	0.4038	0.4039	0.3980	-0.001683
20.0	0.3502	0.3499	0.3443	-0.001266
30.0	0.1723	0.1798	0.1711	0.002358
40.0	0.08681	0.09594	0.08691	0.003129
50.0	0.04482	0.05271	0.04470	0.002872
60.0	0.02363	0.02955	0.02301	0.002328
70.0	0.01281	0.01683	0.01166	0.001760
80.0	0.007276	0.009789	0.005647	0.001283
85.0	0.005662	0.007601	0.003842	0.001102
90.0	0.004561	0.006017	0.002568	0.000974
95.0	0.003835	0.004890	0.001688	0.000893
100.0	0.003459	0.004112	0.001129	0.000871
105.0	0.003483	0.003597	0.000813	0.000962
110.0	0.003917	0.003297	0.000608	0.001223
115.0	0.004650	0.003246	0.000390	0.001688
120.0	0.005614	0.003571	0.000155	0.002428

TABLE T.38

θ	$P_1/4\pi$	$P_2/4\pi$	$P_3/4\pi$	$P_4/4\pi$
125.0	0.007124	0.004472	0.000025	0.003685
130.0	0.01010	0.006089	0.000197	0.005891
135.0	0.01578	0.008036	0.000888	0.009127
140.0	0.02378	0.008767	0.002258	0.01160
142.0	0.02667	0.008449	0.003030	0.01153
144.0	0.02854	0.007777	0.003709	0.01052
146.0	0.02909	0.006963	0.004453	0.008376
148.0	0.02758	0.006760	0.005218	0.005655
150.0	0.02425	0.007262	0.005554	0.003055
152.0	0.02040	0.008660	0.005689	0.000974
154.0	0.01640	0.01091	0.005651	0.000051
156.0	0.01326	0.01324	0.005450	0.000434
158.0	0.01151	0.01579	0.005321	0.001665
160.0	0.01091	0.01695	0.004819	0.003018
162.0	0.01181	0.01805	0.004798	0.004045
164.0	0.01262	0.02065	0.005671	0.004624
166.0	0.01258	0.02186	0.005516	0.005159
168.0	0.01540	0.02620	0.007345	0.006815
170.0	0.01980	0.03454	0.01227	0.008834
172.0	0.02307	0.03932	0.01670	0.006748
174.0	0.02813	0.03919	0.01993	0.001679
176.0	0.03158	0.02817	0.007336	-0.005158
178.0	0.04054	0.03098	-0.03010	-0.005989
180.0	0.05259	0.05259	-0.05259	0

Table T.39

$m = 1.315$
 $\lambda = 1.61 \mu$

Model: Water cloud C.I
 $x: 0.2(0.20)32(0.10)44$

$\beta_{\text{ex}} = 17.58 \text{ km}^{-1}$
 $w = 1.0$

θ	$P_1/4\pi$	$P_2/4\pi$	$P_3/4\pi$	$P_4/4\pi$
0.0	26.45	26.45	26.45	0
1.25	23.86	23.87	23.86	-0.05492
2.50	17.60	17.64	17.62	-0.1632
3.75	10.85	10.91	10.87	-0.2255
5.00	5.913	5.964	5.920	-0.2072
6.25	3.158	3.192	3.152	-0.1473
7.50	1.849	1.863	1.834	-0.09046
8.75	1.242	1.239	1.222	-0.05132
10.0	0.9417	0.9312	0.9226	-0.02726
11.25	0.7765	0.7658	0.7606	-0.01449
12.50	0.6681	0.6604	0.6554	-0.009393
13.75	0.5884	0.5818	0.5768	-0.007814
15.00	0.5270	0.5193	0.5152	-0.006385
16.25	0.4751	0.4676	0.4637	-0.003753
17.50	0.4282	0.4241	0.4189	-0.000989
18.75	0.3868	0.3868	0.3801	0.000047
20.0	0.3516	0.3535	0.3464	-0.000557
30.0	0.1729	0.1794	0.1707	0.002877
40.0	0.08770	0.09675	0.08743	0.003655
50.0	0.04592	0.05401	0.04565	0.003299
60.0	0.02452	0.03079	0.02384	0.002637
70.0	0.01354	0.01788	0.01231	0.002033
80.0	0.007891	0.01069	0.006173	0.001557
85.0	0.006206	0.008417	0.004297	0.001373
90.0	0.005004	0.006766	0.002953	0.001233
95.0	0.004227	0.005582	0.002030	0.001137

TABLE T.39

θ	$P_1/4\pi$	$P_2/4\pi$	$P_3/4\pi$	$P_4/4\pi$
100.0	0.003885	0.004749	0.001441	0.001126
105.0	0.003964	0.004187	0.001078	0.001266
110.0	0.004395	0.003873	0.000799	0.001581
115.0	0.005117	0.003864	0.000511	0.002097
120.0	0.006151	0.004291	0.000243	0.002935
125.0	0.007806	0.005328	0.000115	0.004357
130.0	0.01090	0.007044	0.000286	0.006692
135.0	0.01649	0.008965	0.000904	0.009899
140.0	0.02392	0.009747	0.002112	0.01242
142.5	0.02728	0.009283	0.003117	0.01230
145.0	0.02889	0.008371	0.003964	0.01089
147.5	0.02909	0.007574	0.005030	0.008100
150.0	0.02601	0.007729	0.005775	0.004844
152.5	0.02186	0.008841	0.006198	0.002075
155.0	0.01744	0.01212	0.006489	0.000517
157.5	0.01338	0.01509	0.006036	0.001236
160.0	0.01271	0.01776	0.005847	0.002920
162.5	0.01258	0.02171	0.006135	0.004353
165.0	0.01390	0.02300	0.005433	0.005537
167.5	0.01877	0.02925	0.009394	0.008660
170.0	0.02311	0.03886	0.01421	0.01095
172.5	0.02822	0.04528	0.02122	0.005700
175.0	0.03133	0.03457	0.01557	-0.006307
177.5	0.04100	0.03203	-0.02800	-0.008685
180.0	0.06043	0.06043	-0.06043	0

Table T.40

$m = 1.308 - 0.0018i$
 $\lambda = 1.94 \mu$

Model: Water cloud C.I
 $x: 0.10(0.10)45$

$\beta_{\text{ex}} = 18.05 \text{ km}^{-1}$
 $\varpi = 0.9395$

θ	$P_1/4\pi$	$P_2/4\pi$	$P_3/4\pi$	$P_4/4\pi$
0.0	20.37	20.37	20.37	0
2.0	16.77	16.79	16.78	-0.08439
4.0	9.679	9.727	9.696	-0.1908
6.0	4.413	4.457	4.420	-0.1773
8.0	1.971	1.992	1.964	-0.1049
10.0	1.067	1.069	1.055	-0.04957
12.0	0.7294	0.7214	0.7165	-0.02260
14.0	0.5680	0.5582	0.5560	-0.01112
16.0	0.4676	0.4588	0.4568	-0.005667
18.0	0.3946	0.3879	0.3854	-0.002565
20.0	0.3374	0.3330	0.3299	-0.000523
30.0	0.1690	0.1743	0.1674	0.003941
40.0	0.08843	0.09749	0.08913	0.004476
50.0	0.04680	0.05534	0.04748	0.003832
60.0	0.02525	0.03182	0.02522	0.003037
70.0	0.01413	0.01869	0.01336	0.002374
80.0	0.008334	0.01139	0.007012	0.001880
90.0	0.005337	0.007401	0.003666	0.001558
100.0	0.004121	0.005347	0.002038	0.001535
105.0	0.004066	0.004806	0.001579	0.001709
110.0	0.004324	0.004562	0.001236	0.002056
115.0	0.004884	0.004668	0.000968	0.002641
120.0	0.005849	0.005218	0.000794	0.003590
125.0	0.007519	0.006295	0.000778	0.005098
130.0	0.01038	0.007813	0.001013	0.007308

TABLE T.40

θ	$P_1/4\pi$	$P_2/4\pi$	$P_3/4\pi$	$P_4/4\pi$
135.0	0.01479	0.009267	0.001611	0.009954
140.0	0.02013	0.009668	0.002679	0.01183
142.0	0.02203	0.009351	0.003260	0.01191
144.0	0.02344	0.008792	0.003903	0.01143
146.0	0.02419	0.008111	0.004595	0.01035
148.0	0.02406	0.007529	0.005306	0.008752
150.0	0.02300	0.007278	0.005957	0.006841
152.0	0.02117	0.007606	0.006501	0.004910
154.0	0.01887	0.008654	0.006885	0.003288
156.0	0.01647	0.01041	0.007067	0.002278
158.0	0.01440	0.01273	0.007078	0.002016
160.0	0.01299	0.01534	0.006968	0.002462
162.0	0.01248	0.01804	0.006926	0.003472
164.0	0.01319	0.02109	0.007457	0.005067
166.0	0.01561	0.02557	0.009336	0.007585
168.0	0.02003	0.03267	0.01316	0.01079
170.0	0.02487	0.04036	0.01827	0.01179
172.0	0.02662	0.04063	0.02119	0.005943
174.0	0.02489	0.02893	0.01476	-0.005385
176.0	0.02653	0.01973	-0.006295	-0.01152
178.0	0.03682	0.03157	-0.03251	-0.005815
180.0	0.04427	0.04427	-0.04427	0

Table T.4I

$m = 1.29 - 0.00035i$
 $\lambda = 2.25 \mu$

Model: Water cloud C.I
 $x: 0.10(0.10)37.5$

$\beta_{ex} = 18.36 \text{ km}^{-1}$
 $\varpi = 0.9894$

θ	$P_1/4\pi$	$P_2/4\pi$	$P_3/4\pi$	$P_4/4\pi$
0.0	14.66	14.66	14.66	0
2.5	11.71	11.73	11.72	-0.07423
5.0	6.251	6.297	6.265	-0.1515
7.5	2.658	2.692	2.659	-0.1202
10.0	1.209	1.220	1.203	-0.05967
12.5	0.7243	0.7221	0.7152	-0.02334
15.0	0.5383	0.5326	0.5289	-0.007395
17.5	0.4359	0.4318	0.4282	-0.000389
20.0	0.3639	0.3631	0.3585	0.002859
30.0	0.1853	0.1960	0.1868	0.006144
40.0	0.09392	0.1064	0.09659	0.005399
50.0	0.04809	0.05796	0.04972	0.004232
60.0	0.02554	0.03241	0.02594	0.003294
70.0	0.01435	0.01890	0.01383	0.002624
80.0	0.008647	0.01169	0.007536	0.002185
90.0	0.005731	0.007904	0.004261	0.001955
100.0	0.004574	0.006145	0.002723	0.002063
105.0	0.004599	0.005808	0.002367	0.002355
110.0	0.005048	0.005810	0.002185	0.002897
115.0	0.005981	0.006186	0.002137	0.003786
120.0	0.007546	0.006972	0.002222	0.005138
125.0	0.009987	0.008119	0.002481	0.007035
130.0	0.01356	0.009330	0.002977	0.009353
135.0	0.01814	0.009958	0.003770	0.01146
140.0	0.02260	0.009293	0.004870	0.01206
145.0	0.02470	0.007582	0.006140	0.009866
147.5	0.02417	0.006943	0.006716	0.007796
150.0	0.02256	0.006968	0.007169	0.005499
152.5	0.02017	0.007943	0.007407	0.003484
155.0	0.01753	0.009954	0.007428	0.002249
157.5	0.01529	0.01273	0.007274	0.002072
160.0	0.01402	0.01583	0.007126	0.002937
162.5	0.01425	0.01904	0.007418	0.004636
165.0	0.01681	0.02346	0.009312	0.007369
167.5	0.02232	0.03137	0.01411	0.01134
170.0	0.02790	0.03993	0.02004	0.01220
172.5	0.02662	0.03564	0.01951	0.001788
175.0	0.02249	0.02057	0.002426	-0.01176
177.5	0.03331	0.02890	-0.02848	-0.008170
180.0	0.04544	0.04544	-0.04544	0

Table T.42

$m = 1.364 - 0.3060i$ Model: Water cloud C.1 $\beta_{\text{ex}} = 17.98 \text{ km}^{-1}$
 $\lambda = 3.00 \mu$ $x: 1.25(0.25)26$ $w = 0.4923$

θ	$P_1/4\pi$	$P_2/4\pi$	$P_3/4\pi$	$P_4/4\pi$
0.0	15.74	15.74	15.74	0
2.5	13.86	13.80	13.83	-0.08243
5.0	9.554	9.378	9.463	-0.2271
7.5	5.334	5.110	5.211	-0.2796
10.0	2.594	2.401	2.481	-0.2251
12.5	1.225	1.085	1.137	-0.1409
15.0	0.6217	0.5236	0.5565	-0.07689
17.5	0.3605	0.2879	0.3106	-0.03944
20.0	0.2379	0.1798	0.1976	-0.02051
22.5	0.1706	0.1213	0.1363	-0.01129
25.0	0.1290	0.08581	0.09886	-0.006511
27.5	0.1009	0.06235	0.07382	-0.003953
30.0	0.08076	0.04605	0.05612	-0.002377
40.0	0.03975	0.01546	0.02135	0.000165
50.0	0.02365	0.005708	0.008829	0.000758
60.0	0.01582	0.002207	0.003332	0.000834
70.0	0.01141	0.000987	0.000589	0.000747
80.0	0.008690	0.000706	-0.000889	0.000618
90.0	0.006892	0.000829	-0.001721	0.000487
100.0	0.005650	0.001117	-0.002199	0.000369
110.0	0.004766	0.001456	-0.002474	0.000269
120.0	0.004125	0.001790	-0.002629	0.000188
130.0	0.003658	0.002091	-0.002713	0.000124
140.0	0.003319	0.002345	-0.002755	0.000075
150.0	0.003080	0.002547	-0.002773	0.000039
160.0	0.002923	0.002691	-0.002779	0.000015
170.0	0.002833	0.002764	-0.002791	0.000003
180.0	0.002803	0.002803	-0.002803	0

Table T.43

$m = 1.353 - 0.0059i$ Model: Water cloud C.I $\beta_{\text{ex}} = 20.64 \text{ km}^{-1}$
 $\lambda = 3.90 \mu$ $x: 0.10(0.10)18$ $w = 0.9140$

θ	$P_1/4\pi$	$P_2/4\pi$	$P_3/4\pi$	$P_4/4\pi$
0.0	5.316	5.316	5.316	0
2.5	4.943	4.949	4.946	-0.01735
5.0	3.988	4.009	3.997	-0.05526
7.5	2.830	2.864	2.844	-0.08507
10.0	1.824	1.864	1.837	-0.08912
12.5	1.132	1.170	1.143	-0.07123
15.0	0.7315	0.7635	0.7390	-0.04635
17.5	0.5182	0.5446	0.5239	-0.02569
20.0	0.4000	0.4230	0.4050	-0.01213
25.0	0.2734	0.2943	0.2788	0.000522
30.0	0.1998	0.2199	0.2056	0.003723
40.0	0.1060	0.1233	0.1111	0.003956
50.0	0.05693	0.06994	0.06025	0.003424
60.0	0.03192	0.04106	0.03353	0.002992
70.0	0.01904	0.02536	0.01940	0.002682
80.0	0.01233	0.01668	0.01175	0.002505
90.0	0.008831	0.01181	0.007481	0.002481
100.0	0.007026	0.009192	0.005016	0.002658
110.0	0.006252	0.008093	0.003616	0.003161
120.0	0.006447	0.008240	0.002934	0.004253
130.0	0.008127	0.009515	0.002785	0.006366
135.0	0.009815	0.01043	0.002881	0.007898
140.0	0.01229	0.01135	0.003067	0.009718
145.0	0.01549	0.01185	0.003489	0.01146
150.0	0.01943	0.01178	0.004315	0.01281
152.5	0.02164	0.01153	0.005137	0.01316
155.0	0.02415	0.01158	0.006507	0.01345
157.5	0.02700	0.01234	0.008583	0.01383
160.0	0.02990	0.01421	0.01143	0.01424
162.5	0.03212	0.01729	0.01473	0.01432
165.0	0.03216	0.02018	0.01729	0.01287
167.5	0.02824	0.01999	0.01694	0.008206
170.0	0.02073	0.01569	0.01194	0.000669
172.5	0.01397	0.01103	0.002726	-0.005689
175.0	0.01275	0.01123	-0.007773	-0.006433
177.5	0.01638	0.01593	-0.01583	-0.002514
180.0	0.01881	0.01881	-0.01881	0

Table T.44

$m = 1.315 - 0.0143i$ Model: Water cloud C.I $\beta_{\text{ex}} = 23.87 \text{ km}^{-1}$
 $\lambda = 5.30 \mu$ $x: 0.10(0.10)14$ $\tau = 0.8848$

0	$P_1/4\pi$	$P_2/4\pi$	$P_3/4\pi$	$P_4/4\pi$
0.0	3.786	3.786	3.786	0
2.5	3.646	3.649	3.648	-0.006352
5.0	3.260	3.272	3.266	-0.02250
7.5	2.717	2.741	2.728	-0.04134
10.0	2.126	2.162	2.143	-0.05543
12.5	1.583	1.626	1.602	-0.06049
15.0	1.141	1.187	1.161	-0.05669
17.5	0.8129	0.8583	0.8317	-0.04729
20.0	0.5835	0.6257	0.6004	-0.03623
22.5	0.4270	0.4648	0.4418	-0.02622
25.0	0.3197	0.3529	0.3325	-0.01828
27.5	0.2450	0.2737	0.2558	-0.01235
30.0	0.1921	0.2164	0.2010	-0.008087
40.0	0.08475	0.09683	0.08856	-0.001421
50.0	0.04224	0.04828	0.04346	0.000327
60.0	0.02297	0.02615	0.02295	0.000907
70.0	0.01380	0.01541	0.01310	0.001128
80.0	0.009113	0.009861	0.008013	0.001300
90.0	0.006599	0.006913	0.005238	0.001435
100.0	0.005341	0.005327	0.003718	0.001611
110.0	0.004859	0.004496	0.002855	0.001929
120.0	0.004961	0.004095	0.002347	0.002370
130.0	0.005674	0.003827	0.002046	0.002915
140.0	0.007049	0.003534	0.001863	0.003433
150.0	0.009291	0.003370	0.002201	0.003735
152.5	0.009861	0.003501	0.002459	0.003752
155.0	0.01040	0.003853	0.002831	0.003803
157.5	0.01084	0.004463	0.003284	0.003886
160.0	0.01090	0.005185	0.003636	0.003856
162.5	0.01022	0.005709	0.003578	0.003477
165.0	0.008642	0.005759	0.002849	0.002616
167.5	0.006499	0.005314	0.001436	0.001418
170.0	0.004538	0.004658	-0.000358	0.000292
172.5	0.003472	0.004175	-0.002070	-0.000353
175.0	0.003458	0.004057	-0.003338	-0.000408
177.5	0.003976	0.004180	-0.004048	-0.000151
180.0	0.004267	0.004267	-0.004267	0

Table T.45

$m = 1.315 - 0.1370i$ Model: Water cloud C.1 $\beta_{\text{ex}} = 19.86 \text{ km}^{-1}$
 $\lambda = 6.05 \mu$ $x: 0.10(0.10)14$ $w = 0.5433$

θ	$P_1/4\pi$	$P_2/4\pi$	$P_3/4\pi$	$P_4/4\pi$
0.0	4.135	4.135	4.135	0
2.5	4.000	3.996	3.998	-0.008093
5.0	3.624	3.612	3.618	-0.02927
7.5	3.084	3.060	3.072	-0.05576
10.0	2.476	2.443	2.458	-0.07883
12.5	1.888	1.850	1.886	-0.09237
15.0	1.380	1.343	1.357	-0.09464
17.5	0.9789	0.9464	0.9567	-0.08765
20.0	0.6825	0.6558	0.6623	-0.07517
22.5	0.4741	0.4533	0.4564	-0.06087
25.0	0.3321	0.3164	0.3170	-0.04729
27.5	0.2372	0.2251	0.2242	-0.03572
30.0	0.1739	0.1643	0.1626	-0.02653
40.0	0.06599	0.05954	0.05826	-0.008409
50.0	0.03295	0.02692	0.02644	-0.003432
60.0	0.01872	0.01339	0.01299	-0.001670
70.0	0.01162	0.007152	0.006535	-0.000858
80.0	0.007776	0.004136	0.003220	-0.000438
90.0	0.005550	0.002644	0.001429	-0.000209
100.0	0.004191	0.001907	0.000418	-0.000082
110.0	0.003328	0.001554	-0.000172	-0.000012
120.0	0.002769	0.001399	-0.000524	0.000025
130.0	0.002407	0.001351	-0.000736	0.000044
140.0	0.002183	0.001380	-0.000850	0.000058
145.0	0.002105	0.001425	-0.000881	0.000073
150.0	0.002032	0.001488	-0.000911	0.000096
155.0	0.001941	0.001546	-0.000970	0.000124
160.0	0.001814	0.001559	-0.001089	0.000138
165.0	0.001669	0.001517	-0.001259	0.000118
170.0	0.001559	0.001477	-0.001415	0.000067
175.0	0.001516	0.001490	-0.001495	0.000019
180.0	0.001512	0.001512	-0.001512	0

Table T.46

$m = 1.29 - 0.0472i$
 $\lambda = 8.15 \mu$

Model: Water cloud C.I
 $x: 0.10(0.10)10$

$\beta_{ex} = 18.75 \text{ km}^{-1}$
 $\varpi = 0.7465$

θ	$P_1/4\pi$	$P_2/4\pi$	$P_3/4\pi$	$P_4/4\pi$
0.0	2.404	2.404	2.404	0
5.0	2.233	2.230	2.231	-0.009236
10.0	1.798	1.786	1.792	-0.02949
15.0	1.270	1.254	1.261	-0.04592
20.0	0.8082	0.7922	0.7979	-0.04965
25.0	0.4804	0.4679	0.4710	-0.04248
30.0	0.2785	0.2699	0.2706	-0.03115
35.0	0.1634	0.1577	0.1571	-0.02072
40.0	0.09969	0.09555	0.09452	-0.01295
45.0	0.06435	0.06074	0.05985	-0.007803
50.0	0.04400	0.04042	0.03986	-0.004653
55.0	0.03151	0.02788	0.02761	-0.002780
60.0	0.02340	0.01978	0.01968	-0.001622
65.0	0.01797	0.01438	0.01437	-0.000888
70.0	0.01416	0.01067	0.01069	-0.000427
75.0	0.01140	0.008062	0.008051	-0.000122
80.0	0.009375	0.006208	0.006128	0.000102
85.0	0.007875	0.004871	0.004714	0.000266
90.0	0.006743	0.003895	0.003652	0.000381
95.0	0.005873	0.003178	0.002838	0.000470
100.0	0.005211	0.002648	0.002210	0.000546
105.0	0.004713	0.002249	0.001719	0.000610
110.0	0.004338	0.001947	0.001327	0.000660
115.0	0.004060	0.001723	0.001010	0.000705
120.0	0.003865	0.001560	0.000750	0.000748
125.0	0.003741	0.001443	0.000533	0.000789
130.0	0.003677	0.001373	0.000352	0.000831
135.0	0.003653	0.001361	0.000203	0.000876
140.0	0.003638	0.001416	0.000067	0.000929
145.0	0.003586	0.001549	-0.000084	0.000992
150.0	0.003447	0.001762	-0.000299	0.001051
155.0	0.003171	0.002019	-0.000649	0.001057
160.0	0.002792	0.002256	-0.001177	0.000949
165.0	0.002490	0.002443	-0.001802	0.000703
170.0	0.002458	0.002594	-0.002344	0.000380
175.0	0.002646	0.002715	-0.002667	0.000107
180.0	0.002766	0.002766	-0.002766	0

Table T.47

$m = 1.29 = 0.0236i$ Model: Water cloud C.I $\beta_{\text{ex}} = 19.30 \text{ km}^{-1}$
 $\lambda = 8.15 \mu$ $x: 0.05(0.05)10$ $\varpi = 0.8537$

θ	$P_1/4\pi$	$P_2/4\pi$	$P_3/4\pi$	$P_4/4\pi$
0.0	2.353	2.353	2.353	0
5.0	2.186	2.184	2.185	-0.008387
10.0	1.761	1.755	1.758	-0.02675
15.0	1.247	1.239	1.242	-0.04154
20.0	0.7956	0.7891	0.7904	-0.04473
25.0	0.4752	0.4711	0.4705	-0.03803
30.0	0.2771	0.2752	0.2732	-0.02765
35.0	0.1637	0.1628	0.1603	-0.01816
40.0	0.1004	0.09975	0.09748	-0.01112
45.0	0.06509	0.06399	0.06227	-0.006464
50.0	0.04461	0.04292	0.04179	-0.003637
55.0	0.03198	0.02983	0.02914	-0.001972
60.0	0.02376	0.02133	0.02093	-0.000949
65.0	0.01826	0.01564	0.01542	-0.000304
70.0	0.01442	0.01172	0.01160	0.000095
75.0	0.01165	0.008957	0.008853	0.000357
80.0	0.009621	0.006984	0.006852	0.000553
85.0	0.008137	0.005553	0.005382	0.000701
90.0	0.007027	0.004501	0.004275	0.000806
95.0	0.006188	0.003723	0.003424	0.000894
100.0	0.005567	0.003143	0.002765	0.000979
105.0	0.005119	0.002702	0.002247	0.001056
110.0	0.004802	0.002363	0.001828	0.001125
115.0	0.004596	0.002108	0.001486	0.001195
120.0	0.004487	0.001919	0.001198	0.001268
125.0	0.004462	0.001779	0.000949	0.001342
130.0	0.004518	0.001691	0.000737	0.001420
135.0	0.004637	0.001675	0.000560	0.001504
140.0	0.004766	0.001748	0.000399	0.001594
145.0	0.004840	0.001939	0.000222	0.001693
150.0	0.004774	0.002269	-0.000031	0.001781
155.0	0.004444	0.002694	-0.000487	0.001778
160.0	0.003850	0.003105	-0.001252	0.001575
165.0	0.003318	0.003421	-0.002236	0.001143
170.0	0.003266	0.003650	-0.003140	0.000604
175.0	0.003641	0.003816	-0.003704	0.000166
180.0	0.003882	0.003882	-0.003882	0

Table T.48

$m = 1.212 - 0.0601i$
 $\lambda = 10.0 \mu$

Model: Water cloud C.I
 $x: 0.10(0.10)10$

$\beta_{ex} = 11.18 \text{ km}^{-1}$
 $\varpi = 0.6014$

θ	$P_1/4\pi$	$P_2/4\pi$	$P_3/4\pi$	$P_4/4\pi$
0.0	1.852	1.852	1.852	0
5.0	1.759	1.751	1.755	-0.004651
10.0	1.510	1.483	1.496	-0.01587
15.0	1.180	1.134	1.156	-0.02756
20.0	0.8491	0.7910	0.8186	-0.03452
25.0	0.5718	0.5123	0.5397	-0.03509
30.0	0.3674	0.3141	0.3376	-0.03081
35.0	0.2300	0.1863	0.2046	-0.02433
40.0	0.1433	0.1094	0.1228	-0.01780
45.0	0.09073	0.06486	0.07434	-0.01234
50.0	0.05930	0.03942	0.04616	-0.008255
55.0	0.04038	0.02473	0.02962	-0.005411
60.0	0.02872	0.01602	0.01965	-0.003506
65.0	0.02128	0.01067	0.01343	-0.002255
70.0	0.01635	0.007265	0.009379	-0.001438
75.0	0.01295	0.005038	0.006636	-0.000902
80.0	0.01052	0.003549	0.004714	-0.000544
85.0	0.008742	0.002543	0.003328	-0.000300
90.0	0.007403	0.001860	0.002307	-0.000132
95.0	0.006377	0.001400	0.001538	-0.000013
100.0	0.005579	0.001095	0.000949	0.000072
105.0	0.004952	0.000901	0.000490	0.000134
110.0	0.004453	0.000786	0.000126	0.000180
115.0	0.004053	0.000732	-0.000168	0.000215
120.0	0.003727	0.000723	-0.000409	0.000243
125.0	0.003457	0.000752	-0.000613	0.000266
130.0	0.003229	0.000813	-0.000791	0.000289
140.0	0.002843	0.001024	-0.001111	0.000333
150.0	0.002510	0.001350	-0.001454	0.000357
160.0	0.002290	0.001767	-0.001857	0.000292
170.0	0.002289	0.002174	-0.002214	0.000113
180.0	0.002355	0.002355	-0.002355	0

Table T.49

$m = 1.111 - 0.1831i$ Model: Water cloud C.1 $\beta_{\text{ex}} = 10.10 \text{ km}^{-1}$
 $\lambda = 11.5 \mu$ $x: 0.05(0.05)8$ $\varpi = 0.2886$

θ	$P_1/4\pi$	$P_2/4\pi$	$P_3/4\pi$	$P_4/4\pi$
0.0	1.469	1.469	1.469	0
5.0	1.415	1.403	1.409	-0.003207
10.0	1.266	1.224	1.245	-0.01139
15.0	1.057	0.9791	1.017	-0.02108
20.0	0.8278	0.7214	0.7721	-0.02869
25.0	0.6137	0.4938	0.5493	-0.03215
30.0	0.4356	0.3173	0.3700	-0.03136
35.0	0.2999	0.1938	0.2388	-0.02761
40.0	0.2030	0.1140	0.1495	-0.02252
45.0	0.1368	0.06546	0.09181	-0.01736
50.0	0.09291	0.03718	0.05589	-0.01285
55.0	0.06423	0.02113	0.03398	-0.009253
60.0	0.04553	0.01214	0.02071	-0.006555
65.0	0.03323	0.007087	0.01262	-0.004615
70.0	0.02500	0.004224	0.007589	-0.003254
75.0	0.01935	0.002588	0.004385	-0.002310
80.0	0.01538	0.001659	0.002287	-0.001655
85.0	0.01251	0.001152	0.000874	-0.001200
90.0	0.01038	0.000902	-0.000100	-0.000882
95.0	0.008766	0.000815	-0.000785	-0.000656
100.0	0.007519	0.000831	-0.001275	-0.000493
105.0	0.006537	0.000913	-0.001627	-0.000373
110.0	0.005753	0.001034	-0.001882	-0.000283
120.0	0.004606	0.001330	-0.002200	-0.000161
130.0	0.003834	0.001639	-0.002366	-0.000083
140.0	0.003308	0.001925	-0.002455	-0.000032
150.0	0.002958	0.002177	-0.002510	0.000000
160.0	0.002742	0.002388	-0.002552	0.000009
170.0	0.002629	0.002538	-0.002583	0.000004
180.0	0.002594	0.002594	-0.002594	0

Table T.50

$m = 1.44 - 0.4000i$
 $\lambda = 16.6 \mu$

Model: Water cloud C.1
 $x: 0.05(0.05)6$

$\beta_{\text{ex}} = 16.97 \text{ km}^{-1}$
 $w = 0.3949$

θ	$P_1/4\pi$	$P_2/4\pi$	$P_3/4\pi$	$P_4/4\pi$
0.0	0.7885	0.7885	0.7885	0
10.0	0.7291	0.7096	0.7192	-0.01019
20.0	0.5803	0.5206	0.5485	-0.03157
30.0	0.4060	0.3176	0.3551	-0.04722
40.0	0.2579	0.1670	0.1996	-0.04906
50.0	0.1550	0.08009	0.09971	-0.04061
60.0	0.09210	0.03797	0.04498	-0.02900
70.0	0.05624	0.01959	0.01798	-0.01889
80.0	0.03629	0.01180	0.005441	-0.01170
90.0	0.02504	0.008354	-0.000294	-0.007098
100.0	0.01846	0.006716	-0.002990	-0.004285
110.0	0.01442	0.005912	-0.004352	-0.002566
120.0	0.01182	0.005542	-0.005141	-0.001484
130.0	0.01008	0.005439	-0.005699	-0.000782
140.0	0.008893	0.005560	-0.006167	-0.000338
150.0	0.008080	0.005911	-0.006574	-0.000093
160.0	0.007553	0.006441	-0.006896	0.000000
170.0	0.007259	0.006950	-0.007097	0.000008
180.0	0.007165	0.007165	-0.007165	0

Table T.51

$m = 1.34$
 $\lambda = 0.45 \mu$

Model: Water cloud C.2
 $x: 5.25(0.25)100$

$\beta_{\text{ex}} = 11.18 \text{ km}^{-1}$
 $\varpi = 1.0$

θ	$P_1/4\pi$	$P_2/4\pi$	$P_3/4\pi$	$P_4/4\pi$
0.0	159.1	159.1	159.1	0
1.0	113.0	113.0	113.0	-0.4632
2.0	38.25	38.32	38.26	-0.7090
3.0	6.076	6.062	6.046	-0.2484
4.0	2.557	2.494	2.514	-0.01042
4.5	2.435	2.377	2.398	-0.01161
5.0	2.066	2.017	2.035	-0.02434
5.5	1.633	1.592	1.606	-0.02623
6.0	1.319	1.281	1.293	-0.01988
6.5	1.134	1.098	1.110	-0.01317
7.0	1.018	0.9856	0.9964	-0.009216
7.5	0.9288	0.9004	0.9096	-0.007261
8.0	0.8536	0.8282	0.8359	-0.006032
8.5	0.7912	0.7670	0.7743	-0.005080
9.0	0.7400	0.7163	0.7237	-0.004454
9.5	0.6974	0.6743	0.6818	-0.004182
10.0	0.6609	0.6391	0.6463	-0.004078
20.0	0.3312	0.3339	0.3297	0.000049
30.0	0.1755	0.1867	0.1775	0.002006
40.0	0.08855	0.1007	0.09098	0.001662
50.0	0.04260	0.05251	0.04426	0.001643
60.0	0.02059	0.02671	0.02073	0.001201
70.0	0.009850	0.01294	0.008886	0.000753
80.0	0.005202	0.005988	0.003325	0.000391
90.0	0.003237	0.003021	0.001043	0.000241
100.0	0.002567	0.002030	0.000093	0.000447
104.0	0.002244	0.001929	-0.000090	0.000316
108.0	0.002404	0.001888	0.000118	0.000141
112.0	0.003507	0.001919	0.000546	0.000422
116.0	0.004758	0.001931	0.000692	0.000979
120.0	0.005330	0.001784	0.000392	0.001429
124.0	0.005291	0.001800	-0.000119	0.001662
128.0	0.004880	0.002010	-0.000478	0.001838

TABLE T.51

θ	$P_1/4\pi$	$P_2/4\pi$	$P_3/4\pi$	$P_4/4\pi$
130.0	0.005266	0.002401	-0.000528	0.002322
132.0	0.005977	0.002808	-0.000482	0.002749
134.0	0.008215	0.003682	-0.000278	0.004092
136.0	0.01236	0.004814	0.000573	0.006247
138.0	0.01907	0.005927	0.001417	0.008867
140.0	0.02693	0.006640	0.003148	0.01115
142.0	0.03679	0.005746	0.005001	0.01102
144.0	0.04247	0.004667	0.006641	0.008266
146.0	0.04043	0.003816	0.007863	0.000997
148.0	0.02971	0.006040	0.006914	-0.005950
150.0	0.01504	0.01174	0.005095	-0.007431
152.0	0.006497	0.01715	0.002791	-0.001963
154.0	0.008503	0.01664	0.002079	0.005451
156.0	0.01488	0.01191	0.003026	0.006720
158.0	0.01625	0.009560	0.003562	0.002160
160.0	0.01217	0.01234	0.003219	-0.000515
162.0	0.009686	0.01498	0.002488	0.001012
164.0	0.01015	0.01491	0.002544	0.002517
166.0	0.01066	0.01487	0.002858	0.002219
168.0	0.01019	0.01595	0.002904	0.001916
170.0	0.01048	0.01802	0.003662	0.002081
171.0	0.01067	0.01935	0.003563	0.002391
172.0	0.01094	0.02080	0.004626	0.002565
173.0	0.01201	0.02286	0.005834	0.002931
174.0	0.01311	0.02604	0.006871	0.003290
175.0	0.01282	0.02568	0.006847	0.002738
176.0	0.01862	0.03992	0.01305	0.005301
177.0	0.03716	0.06846	0.03502	0.007518
178.0	0.04276	0.03786	0.02769	-0.003838
179.0	0.04328	0.02185	-0.02325	-0.007378
180.0	0.05134	0.05134	-0.05134	0

Table T.52

$m = 1.33$
 $\lambda = 0.70 \mu$

Model: Water cloud C.2
 $x: 3.25(0.25)63$

$\beta_{\text{ex}} = 11.43 \text{ km}^{-1}$
 $\varpi = 1.0$

θ	$P_1/4\pi$	$P_2/4\pi$	$P_3/4\pi$	$P_4/4\pi$
0.0	67.49	67.49	67.49	0
1.0	58.51	58.54	58.52	-0.1463
2.0	37.80	37.86	37.82	-0.3977
3.0	17.73	17.79	17.75	-0.4550
4.0	6.009	6.027	5.992	-0.2872
5.0	1.992	1.965	1.958	-0.09380
5.5	1.512	1.473	1.478	-0.03738
6.0	1.399	1.357	1.368	-0.01080
6.5	1.376	1.335	1.349	-0.005145
7.0	1.322	1.286	1.298	-0.009405
7.5	1.219	1.188	1.197	-0.01494
8.0	1.091	1.064	1.071	-0.01738
8.5	0.9697	0.9451	0.9499	-0.01615
9.0	0.8713	0.8477	0.8520	-0.01278
9.5	0.7984	0.7753	0.7798	-0.009116
10.0	0.7451	0.7227	0.7277	-0.006350
10.5	0.7038	0.6827	0.6878	-0.004798
11.0	0.6688	0.6494	0.6542	-0.004194
11.5	0.6371	0.6197	0.6237	-0.004101
12.0	0.6079	0.5924	0.5954	-0.004168
12.5	0.5810	0.5671	0.5693	-0.004202
15.0	0.4767	0.4699	0.4690	-0.001749
25.0	0.2449	0.2522	0.2447	0.001282
35.0	0.1242	0.1348	0.1256	0.002858
45.0	0.06217	0.07228	0.06326	0.002746
55.0	0.03012	0.03829	0.03085	0.001977
65.0	0.01519	0.02009	0.01463	0.001481
75.0	0.007950	0.01050	0.006636	0.000861
85.0	0.004627	0.005635	0.002811	0.000569
95.0	0.003049	0.003312	0.000864	0.000571
105.0	0.002682	0.002512	0.000399	0.000367
115.0	0.004399	0.002213	0.000504	0.001104
120.0	0.005134	0.002271	0.000236	0.001736

TABLE T.52

θ	$P_1/4\pi$	$P_2/4\pi$	$P_3/4\pi$	$P_4/4\pi$
130.0	0.007862	0.004099	-0.000062	0.004163
132.0	0.009666	0.004784	0.000095	0.005439
134.0	0.01247	0.005690	0.000707	0.006821
136.0	0.01604	0.007018	0.001079	0.009017
138.0	0.02123	0.007288	0.001756	0.01045
140.0	0.02651	0.007398	0.003365	0.01164
142.0	0.03128	0.007178	0.004196	0.01177
144.0	0.03533	0.005364	0.005171	0.009369
146.0	0.03551	0.004651	0.006888	0.005388
148.0	0.03078	0.004522	0.006722	0.000543
150.0	0.02387	0.006784	0.006636	-0.004558
152.0	0.01464	0.01132	0.005576	-0.005865
154.0	0.007699	0.01590	0.003870	-0.003392
156.0	0.005872	0.01923	0.002820	0.001462
158.0	0.008636	0.01805	0.002192	0.006369
160.0	0.01282	0.01494	0.003023	0.007635
162.0	0.01493	0.01212	0.003940	0.005276
164.0	0.01402	0.01272	0.004751	0.001865
166.0	0.01174	0.01641	0.004704	0.000882
168.0	0.01063	0.02006	0.004610	0.001912
170.0	0.01241	0.02431	0.006062	0.004319
171.0	0.01312	0.02507	0.006451	0.004825
172.0	0.01266	0.02299	0.006125	0.004074
173.0	0.01335	0.02372	0.006884	0.004166
174.0	0.01998	0.03754	0.01352	0.007289
175.0	0.03195	0.05823	0.02684	0.01023
176.0	0.03951	0.05895	0.03540	0.006012
177.0	0.03741	0.03333	0.02406	-0.004485
178.0	0.03616	0.01767	-0.006515	-0.009769
179.0	0.04426	0.03473	-0.03773	-0.004644
180.0	0.05048	0.05048	-0.05048	0

Table T.53

$m = 1.315$
 $\lambda = 1.61 \mu$

Model: Water cloud C.2
 $x: 1.25(0.25)31$

$\beta_{ex} = 12.56 \text{ km}^{-1}$
 $\varpi = 1.0$

θ	$P_1/4\pi$	$P_2/4\pi$	$P_3/4\pi$	$P_4/4\pi$
0.0	14.62	14.62	14.62	0
2.0	13.11	13.13	13.12	-0.04935
4.0	9.434	9.481	9.452	-0.1445
6.0	5.434	5.497	5.449	-0.1897
8.0	2.565	2.616	2.565	-0.1519
10.0	1.141	1.163	1.128	-0.07764
12.0	0.6626	0.6584	0.6459	-0.02479
14.0	0.5344	0.5180	0.5181	-0.007908
16.0	0.4546	0.4358	0.4379	-0.008341
18.0	0.3690	0.3512	0.3520	-0.008543
20.0	0.2989	0.2826	0.2830	-0.005125
30.0	0.1561	0.1539	0.1495	0.005182
40.0	0.08868	0.09622	0.08758	0.005987
50.0	0.04900	0.05792	0.04898	0.004940
60.0	0.02727	0.03443	0.02669	0.003899
70.0	0.01555	0.02072	0.01429	0.003043
80.0	0.009134	0.01283	0.007445	0.002371
90.0	0.005840	0.008483	0.003939	0.001954
100.0	0.004789	0.006097	0.002161	0.001983
110.0	0.005121	0.005145	0.001002	0.002560
120.0	0.006417	0.006068	0.000238	0.004201
130.0	0.01078	0.009662	0.000224	0.008552
132.5	0.01321	0.01081	0.000375	0.01028

TABLE T.53

211

θ	$P_1/4\pi$	$P_2/4\pi$	$P_3/4\pi$	$P_4/4\pi$
135.0	0.01564	0.01179	0.000856	0.01196
137.5	0.01823	0.01263	0.001304	0.01354
140.0	0.02159	0.01304	0.001826	0.01498
142.5	0.02480	0.01287	0.002692	0.01583
145.0	0.02734	0.01216	0.003743	0.01576
147.5	0.02925	0.01102	0.004920	0.01466
150.0	0.02990	0.009767	0.006247	0.01244
152.5	0.02876	0.008976	0.007585	0.009224
155.0	0.02615	0.009659	0.008949	0.005788
157.5	0.02292	0.01295	0.01028	0.003335
160.0	0.01909	0.01753	0.01046	0.001870
162.5	0.01393	0.02058	0.008473	0.000823
165.0	0.01212	0.02827	0.007830	0.004348
167.5	0.02231	0.05071	0.01550	0.01613
170.0	0.03637	0.06918	0.02894	0.02194
172.5	0.03450	0.05231	0.02926	0.004773
175.0	0.02926	0.02735	0.000973	-0.01554
177.5	0.04668	0.04226	-0.04169	-0.01037
180.0	0.06244	0.06244	-0.06244	0

Table T.54

$$m = 1.364 - 0.3060i$$

$$\lambda = 3.00 \mu$$

Model: Water cloud C.2
 $x: 2.25(0.25)14$

$$\beta_{\text{ex}} = 12.39 \text{ km}^{-1}$$

$$w = 0.4809$$

θ	$P_1/4\pi$	$P_2/4\pi$	$P_3/4\pi$	$P_4/4\pi$
0.0	8.179	8.179	8.179	0
2.5	7.766	7.743	7.754	-0.02738
5.0	6.640	6.561	6.600	-0.09693
7.5	5.094	4.955	5.021	-0.1720
10.0	3.484	3.310	3.388	-0.2173
12.5	2.107	1.934	2.006	-0.2152
15.0	1.119	0.9779	1.029	-0.1720
17.5	0.5286	0.4303	0.4586	-0.1102
20.0	0.2444	0.1818	0.1941	-0.05358
22.5	0.1422	0.1002	0.1062	-0.01641
25.0	0.1188	0.08403	0.09053	-0.00091
27.5	0.1134	0.07891	0.08809	0.002240
30.0	0.1031	0.06797	0.07866	-0.000867
40.0	0.04510	0.02072	0.02578	-0.001959
50.0	0.02623	0.008328	0.01106	0.000130
60.0	0.01700	0.003460	0.004286	0.000409
70.0	0.01200	0.001639	0.001033	0.000484
80.0	0.008987	0.001064	-0.000677	0.000446
90.0	0.007048	0.001036	-0.001617	0.000373
100.0	0.005734	0.001243	-0.002147	0.000294
110.0	0.004813	0.001536	-0.002448	0.000220
120.0	0.004154	0.001844	-0.002616	0.000156
130.0	0.003676	0.002129	-0.002706	0.000103
140.0	0.003331	0.002373	-0.002753	0.000062
150.0	0.003089	0.002569	-0.002773	0.000030
160.0	0.002936	0.002720	-0.002772	0.000009
170.0	0.002849	0.002770	-0.002795	0.000000
180.0	0.002818	0.002818	-0.02818	0

Table T.55

$m = 1.353 - 0.0059i$ Model: Water cloud C.2 $\beta_{ex} = 17.76 \text{ km}^{-1}$
 $\lambda = 3.90 \mu$ x: 0.5(0.5)15 $\varpi = 0.9489$

θ	$P_1/4\pi$	$P_2/4\pi$	$P_3/4\pi$	$P_4/4\pi$
0.0	3.488	3.488	3.488	0
2.5	3.380	3.384	3.382	-0.005512
5.0	3.074	3.090	3.082	-0.02014
7.5	2.623	2.655	2.639	-0.03888
10.0	2.100	2.150	2.124	-0.05553
12.5	1.577	1.644	1.608	-0.06493
15.0	1.116	1.193	1.151	-0.06462
17.5	0.7504	0.8324	0.7864	-0.05530
20.0	0.4917	0.5707	0.5253	-0.04022
22.5	0.3281	0.3984	0.3570	-0.02363
25.0	0.2360	0.2943	0.2593	-0.009301
27.5	0.1894	0.2349	0.2070	0.000551
30.0	0.1657	0.1999	0.1786	0.005502
40.0	0.1001	0.1155	0.1056	0.001544
50.0	0.04800	0.05950	0.05151	0.000913
60.0	0.02644	0.03370	0.02805	0.001767
70.0	0.01632	0.02061	0.01660	0.001859
80.0	0.01063	0.01368	0.01029	0.001802
90.0	0.007773	0.009887	0.006910	0.002030
100.0	0.006384	0.007895	0.004995	0.002245
110.0	0.005720	0.006946	0.003991	0.002708
120.0	0.005925	0.006710	0.003450	0.003560
130.0	0.007522	0.007112	0.003314	0.004904
140.0	0.008602	0.006501	0.002562	0.005596
150.0	0.01658	0.007430	0.004636	0.008785
152.5	0.01954	0.008869	0.006246	0.01020
155.0	0.02146	0.01049	0.007773	0.01126
157.5	0.02148	0.01186	0.008693	0.01152
160.0	0.01925	0.01256	0.008568	0.01069
162.5	0.01515	0.01241	0.007225	0.008832
165.0	0.01028	0.01147	0.004846	0.006322
167.5	0.006050	0.01007	0.001905	0.003762
170.0	0.003584	0.008648	-0.001019	0.001717
172.5	0.003208	0.007521	-0.003451	0.000487
175.0	0.004330	0.006822	-0.005150	0.000010
177.5	0.005771	0.006493	-0.006104	-0.000035
180.0	0.006405	0.006405	-0.006405	0

Table T.56

$m = 1.315 - 0.1370i$
 $\lambda = 6.05 \mu$

Model: Water cloud C.2
 $x: 0.25(0.25)7.5$

$\beta_{\text{ex}} = 13.06 \text{ km}^{-1}$
 $\overline{\omega} = 0.5591$

θ	$P_1/4\pi$	$P_2/4\pi$	$P_3/4\pi$	$P_4/4\pi$
0.0	2.108	2.108	2.108	0
0.5	2.006	1.997	2.001	-0.008368
10.0	1.725	1.696	1.710	-0.02922
15.0	1.337	1.289	1.312	-0.05230
20.0	0.9314	0.8750	0.9000	-0.06711
25.0	0.5797	0.5304	0.5497	-0.06822
30.0	0.3214	0.2888	0.2982	-0.05698
35.0	0.1603	0.1453	0.1454	-0.03940
40.0	0.07615	0.07288	0.06774	-0.02222
50.0	0.02866	0.02803	0.02427	-0.003082
60.0	0.02234	0.01613	0.01650	-0.000721
70.0	0.01516	0.008797	0.009224	-0.001542
80.0	0.009308	0.005002	0.004332	-0.001100
90.0	0.006327	0.003166	0.002034	-0.000453
100.0	0.004799	0.002183	0.000860	-0.000168
110.0	0.003819	0.001668	0.000126	-0.000065
120.0	0.003187	0.001420	-0.000330	-0.000015
130.0	0.002851	0.001379	-0.000535	0.000006
140.0	0.002612	0.001469	-0.000626	0.000073
145.0	0.002444	0.001503	-0.000718	0.000143
150.0	0.002234	0.001510	-0.000874	0.000219
155.0	0.002015	0.001503	-0.001082	0.000273
160.0	0.001838	0.001512	-0.001306	0.000275
165.0	0.001737	0.001559	-0.001502	0.000217
170.0	0.001713	0.001637	-0.001641	0.000122
175.0	0.001730	0.001711	-0.001718	0.000035
180.0	0.001742	0.001742	-0.001742	0

Table T.57

$m = 1.212 - 0.0601i$ Model: Water cloud C.2 $\beta_{\text{ex}} = 4.944 \text{ km}^{-1}$
 $\lambda = 10.0 \mu$ $x: 0.20(0.20)6$ $w = 0.5262$

θ	$P_1/4\pi$	$P_2/4\pi$	$P_3/4\pi$	$P_4/4\pi$
0.0	0.8217	0.8217	0.8217	0
10.0	0.7693	0.7520	0.7606	-0.003395
20.0	0.6313	0.5759	0.6028	-0.01130
30.0	0.4536	0.3683	0.4083	-0.01871
40.0	0.2853	0.1963	0.2355	-0.02156
50.0	0.1571	0.08754	0.1153	-0.01914
60.0	0.07643	0.03372	0.04813	-0.01355
70.0	0.03423	0.01247	0.01774	-0.007639
80.0	0.01604	0.005314	0.006489	-0.003217
90.0	0.009683	0.002757	0.002720	-0.000688
100.0	0.007784	0.001580	0.001055	0.000428
110.0	0.006993	0.001089	-0.000190	0.000802
120.0	0.006278	0.001128	-0.001286	0.000892
130.0	0.005569	0.001561	-0.002224	0.000882
140.0	0.005024	0.002258	-0.003019	0.000785
150.0	0.004738	0.003097	-0.003699	0.000585
160.0	0.004679	0.003920	-0.004253	0.000321
170.0	0.004728	0.004533	-0.004627	0.000091
180.0	0.004761	0.004761	-0.004761	0

Table T.58

$m = 1.440 - 0.4000i$
 $\lambda = 16.60 \mu$

Model: Water cloud C.2
 $x: 0.10(0.10)3$

$\beta_{\text{ex}} = 9.753 \text{ km}^{-1}$
 $\tau = 0.3385$

θ	$P_1/4\pi$	$P_2/4\pi$	$P_3/4\pi$	$P_4/4\pi$
0.0	0.3965	0.3965	0.3965	0
10.0	0.3860	0.3763	0.3811	-0.002468
20.0	0.3565	0.3214	0.3384	-0.009032
30.0	0.3127	0.2466	0.2771	-0.01753
40.0	0.2609	0.1693	0.2085	-0.02537
50.0	0.2079	0.1037	0.1432	-0.03049
60.0	0.1588	0.05675	0.08842	-0.03194
70.0	0.1169	0.02861	0.04748	-0.02992
80.0	0.08366	0.01484	0.02001	-0.02547
90.0	0.05880	0.009773	0.003570	-0.01988
100.0	0.04113	0.008710	-0.005076	-0.01429
110.0	0.02912	0.008806	-0.008899	-0.009450
120.0	0.02124	0.008887	-0.01014	-0.005721
130.0	0.01623	0.008787	-0.01025	-0.003131
140.0	0.01312	0.008706	-0.009998	-0.001515
150.0	0.01125	0.008806	-0.009735	-0.000623
160.0	0.01018	0.009069	-0.009563	-0.000201
170.0	0.009624	0.009341	-0.009479	-0.000038
180.0	0.009455	0.009455	-0.009455	0

Table T.59

$m = 1.34$
 $\lambda = 0.45 \mu$

Model: Water cloud C.3
 $x: 6.125(0.125)56$

$\beta_{\text{ex}} = 2.906 \text{ km}^{-1}$
 $\tau = 1.0$

θ	$P_1/4\pi$	$P_2/4\pi$	$P_3/4\pi$	$P_4/4\pi$
0.0	41.69	41.69	41.69	0
1.0	38.20	38.22	38.21	-0.07391
2.0	29.29	29.36	29.33	-0.2334
3.0	18.63	18.73	18.67	-0.3502
4.0	9.723	9.813	9.750	-0.3442
5.0	4.220	4.265	4.221	-0.2377
6.0	1.780	1.778	1.760	-0.1125
7.0	1.099	1.071	1.072	-0.03178
8.0	1.014	0.9808	0.9879	-0.004492
9.0	0.9604	0.9336	0.9393	-0.005591
10.0	0.8414	0.8205	0.8238	-0.01080
11.0	0.7168	0.6988	0.7012	-0.01135
12.0	0.6265	0.6106	0.6124	-0.008670
13.0	0.5661	0.5532	0.5537	-0.005656
14.0	0.5197	0.5104	0.5092	-0.003512
15.0	0.4793	0.4728	0.4703	-0.002360
20.0	0.3347	0.3337	0.3293	-0.000666
30.0	0.1768	0.1854	0.1767	0.003167
40.0	0.09086	0.1036	0.09291	0.002426
50.0	0.04709	0.05592	0.04763	0.001726
60.0	0.02423	0.03016	0.02386	0.001705
70.0	0.01248	0.01641	0.01156	0.001339
80.0	0.007316	0.009050	0.005508	0.001057
90.0	0.004292	0.005332	0.002221	0.000689
95.0	0.003563	0.004184	0.001451	0.000568
100.0	0.003402	0.003542	0.001092	0.000571
105.0	0.003891	0.003135	0.000972	0.000767
110.0	0.004479	0.002803	0.000718	0.001138
115.0	0.005047	0.002623	0.000268	0.001404
120.0	0.005501	0.002665	-0.000107	0.001711

TABLE T.59, continued

θ	$P_1/4\pi$	$P_2/4\pi$	$P_3/4\pi$	$P_4/4\pi$
124.0	0.005831	0.002970	-0.000128	0.002173
128.0	0.006472	0.003884	-0.000052	0.003230
132.0	0.008987	0.005405	0.000011	0.005143
136.0	0.01393	0.007140	0.000829	0.007997
140.0	0.02202	0.008375	0.002038	0.01124
144.0	0.03133	0.007641	0.003834	0.01223
146.0	0.03466	0.006538	0.004703	0.01072
148.0	0.03603	0.005229	0.005643	0.007467
150.0	0.03360	0.004710	0.006526	0.002931
152.0	0.02863	0.005828	0.006865	-0.001609
154.0	0.02157	0.009007	0.006607	-0.005098
156.0	0.01394	0.01383	0.005945	-0.005502
158.0	0.008594	0.01868	0.005069	-0.002898
160.0	0.007022	0.02221	0.004057	0.001803
162.0	0.009244	0.02276	0.003783	0.006815
164.0	0.01356	0.02022	0.004247	0.008971
166.0	0.01665	0.01808	0.005948	0.007839
168.0	0.01879	0.01918	0.008100	0.005460
170.0	0.01721	0.02035	0.007297	0.002724
171.0	0.01564	0.02290	0.007360	0.002057
172.0	0.01801	0.03194	0.01127	0.003531
173.0	0.02639	0.04761	0.02041	0.007006
174.0	0.03684	0.06078	0.03127	0.009226
175.0	0.04175	0.05890	0.03582	0.006129
176.0	0.03839	0.04103	0.02726	-0.001986
177.0	0.03324	0.02340	0.006140	-0.008974
178.0	0.03476	0.02331	-0.01946	-0.008903
179.0	0.04235	0.03789	-0.03939	-0.003337
180.0	0.04677	0.04677	-0.04677	0

Table T.60

$m = 1.33$ $\lambda = 0.70 \mu$	Model: Water cloud C.3 x: 4.125(0.125)39			$\beta_{\text{ex}} = 3.021 \text{ km}^{-1}$ $\varpi = 1.0$
θ	$P_1/4\pi$	$P_2/4\pi$	$P_3/4\pi$	$P_4/4\pi$
0.0	17.86	17.86	17.86	0
1.0	17.22	17.22	17.22	-0.02023
2.0	15.41	15.43	15.42	-0.07311
3.0	12.79	12.83	12.81	-0.1386
4.0	9.834	9.885	9.850	-0.1931
5.0	6.998	7.057	7.009	-0.2185
6.0	4.622	4.680	4.625	-0.2087
7.0	2.874	2.923	2.866	-0.1704
8.0	1.752	1.785	1.735	-0.1179
9.0	1.137	1.154	1.115	-0.06672
10.0	0.8594	0.8641	0.8374	-0.02806
11.0	0.7625	0.7595	0.7432	-0.005875
12.0	0.7320	0.7265	0.7166	0.002015
13.0	0.7061	0.7018	0.6941	0.001058
14.0	0.6637	0.6624	0.6539	-0.003108
15.0	0.6071	0.6088	0.5983	-0.006731
16.0	0.5462	0.5501	0.5377	-0.008320
17.0	0.4892	0.4941	0.4810	-0.008067
18.0	0.4401	0.4450	0.4322	-0.006862
20.0	0.3638	0.3675	0.3567	-0.004481
30.0	0.1629	0.1640	0.1569	0.000615
40.0	0.08556	0.09061	0.08258	0.003359
50.0	0.04713	0.05426	0.04574	0.003605
60.0	0.02624	0.03291	0.02504	0.003056
70.0	0.01497	0.02005	0.01334	0.002507
80.0	0.008910	0.01235	0.006734	0.001910
90.0	0.005672	0.008088	0.003402	0.001417
95.00	0.004938	0.006572	0.002400	0.001459
100.0	0.004828	0.005410	0.001559	0.001462
105.0	0.004912	0.004533	0.000945	0.001590
110.0	0.005177	0.003946	0.000243	0.001753
115.0	0.005459	0.003669	-0.000400	0.001986

TABLE T60, continued

θ	$P_1/4\pi$	$P_2/4\pi$	$P_3/4\pi$	$P_4/4\pi$
120.0	0.005835	0.003907	-0.000952	0.002424
124.0	0.006496	0.004546	-0.001257	0.003144
128.0	0.007857	0.005759	-0.001474	0.004431
132.0	0.01026	0.007480	-0.001478	0.006477
136.0	0.01420	0.009534	-0.001290	0.009265
140.0	0.01967	0.01124	-0.000753	0.01229
144.0	0.02579	0.01169	0.000363	0.01429
148.0	0.03045	0.01042	0.002270	0.01356
150.0	0.03133	0.009415	0.003517	0.01181
152.0	0.03083	0.008605	0.004872	0.009182
154.0	0.02881	0.008451	0.006218	0.005975
156.0	0.02546	0.009494	0.007405	0.002758
158.0	0.02141	0.01235	0.008332	0.000353
160.0	0.01755	0.01727	0.008887	-0.000621
162.0	0.01422	0.02283	0.008619	-0.000375
164.0	0.01105	0.02644	0.007010	0.000804
165.0	0.009936	0.02798	0.006020	0.002205
166.0	0.01000	0.03081	0.005557	0.004672
167.0	0.01211	0.03630	0.006374	0.008443
168.0	0.01675	0.04504	0.009155	0.01323
169.0	0.02353	0.05590	0.01413	0.01802
170.0	0.03090	0.06578	0.02071	0.02116
171.0	0.03668	0.07057	0.02732	0.02099
172.0	0.03905	0.06723	0.03163	0.01665
173.0	0.03774	0.05590	0.03118	0.008754
174.0	0.03458	0.04075	0.02423	-0.000501
175.0	0.03286	0.02853	0.01048	-0.008144
176.0	0.03554	0.02531	-0.008552	-0.01174
177.0	0.04342	0.03295	-0.02973	-0.01064
178.0	0.05425	0.04766	-0.04903	-0.006369
179.0	0.06365	0.06165	-0.06252	-0.001880
180.0	0.06736	0.06736	-0.06736	0

Table T.61

$m = 1.315$
 $\lambda = 1.61 \mu$

Model: Water cloud C.3
 $x: 2.125(0.125)17$

$\beta_{\text{ex}} = 4.126 \text{ km}^{-1}$
 $\varpi = 1.0$

θ	$P_1/4\pi$	$P_2/4\pi$	$P_3/4\pi$	$P_4/4\pi$
0.0	4.479	4.479	4.479	0
2.5	4.277	4.284	4.281	-0.008258
5.0	3.722	3.751	3.736	-0.02883
7.5	2.952	3.007	2.979	-0.05144
10.0	2.137	2.215	2.174	-0.06529
12.5	1.421	1.514	1.464	-0.06446
15.0	0.8901	0.9849	0.9324	-0.05015
17.5	0.5560	0.6412	0.5927	-0.02898
20.0	0.3798	0.4488	0.4085	-0.008895
22.5	0.3013	0.3528	0.3220	0.004612
25.0	0.2663	0.3035	0.2810	0.01016
27.5	0.2407	0.2687	0.2517	0.009702
30.0	0.2110	0.2344	0.2204	0.006536
40.0	0.09390	0.1123	0.1008	0.001505
50.0	0.04662	0.05732	0.05002	0.002413
60.0	0.02515	0.03174	0.02669	0.002173
70.0	0.01487	0.01908	0.01531	0.002115
80.0	0.009794	0.01257	0.009514	0.002102
90.0	0.007282	0.009168	0.006448	0.002215
100.0	0.006193	0.007476	0.004816	0.002541
110.0	0.006095	0.006816	0.004001	0.003194
120.0	0.006979	0.006792	0.003674	0.004297
130.0	0.009079	0.006903	0.003558	0.005811
140.0	0.01288	0.006985	0.003793	0.007592
142.5	0.01350	0.006684	0.003630	0.007676
145.0	0.01384	0.006028	0.003250	0.007417
147.5	0.01426	0.005102	0.002831	0.006923
150.0	0.01551	0.004249	0.002788	0.006509
152.5	0.01825	0.003969	0.003620	0.006552
155.0	0.02246	0.004626	0.005572	0.007187
157.5	0.02699	0.006125	0.008311	0.008071
160.0	0.02979	0.007841	0.01089	0.008427
162.5	0.02893	0.008906	0.01210	0.007485
165.0	0.02395	0.008761	0.01114	0.005064
167.5	0.01641	0.007554	0.008071	0.001867
170.0	0.009225	0.006055	0.003825	-0.000840
172.5	0.004904	0.005113	-0.000322	-0.002027
175.0	0.004018	0.005044	-0.003422	-0.001620
177.5	0.005034	0.005468	-0.005174	-0.000542
180.0	0.005717	0.005717	-0.005717	0

Table T.62

$m = 1.29 - 0.00035i$
 $\lambda = 2.25 \mu$

Model: Water cloud C.3
 $x: 1.125(0.125)13$

$\beta_{ex} = 4.549 \text{ km}^{-1}$
 $\tau = 0.9975$

0	$P_1/4\pi$	$P_2/4\pi$	$P_3/4\pi$	$P_4/4\pi$
0.0	3.078	3.078	3.078	0
2.5	3.011	3.012	3.012	-0.003065
5.0	2.820	2.823	2.822	-0.01154
7.5	2.528	2.533	2.530	-0.02343
10.0	2.167	2.177	2.172	-0.03604
12.5	1.776	1.792	1.783	-0.04661
15.0	1.390	1.413	1.401	-0.05305
17.5	1.040	1.070	1.053	-0.05430
20.0	0.7451	0.7803	0.7602	-0.05050
22.5	0.5132	0.5518	0.5296	-0.04278
25.0	0.3437	0.3828	0.3601	-0.03286
27.5	0.2286	0.2654	0.2438	-0.02257
30.0	0.1560	0.1883	0.1691	-0.01340
40.0	0.06720	0.07665	0.07043	0.001880
50.0	0.03825	0.04036	0.03830	0.000178
60.0	0.01916	0.02076	0.01891	0.000542
70.0	0.01159	0.01201	0.01079	0.001168
80.0	0.007930	0.007679	0.006792	0.001289
90.0	0.005967	0.005376	0.004584	0.001421
100.0	0.005028	0.004092	0.003331	0.001605
110.0	0.004763	0.003335	0.002575	0.001857
120.0	0.005019	0.002906	0.002114	0.002184
130.0	0.005311	0.002451	0.001445	0.002412
140.0	0.007067	0.001793	0.000894	0.002607
145.0	0.008974	0.001823	0.001291	0.002900
150.0	0.01033	0.002292	0.001944	0.003291
155.0	0.009686	0.003014	0.002092	0.003516
160.0	0.006960	0.003655	0.001131	0.003265
165.0	0.004029	0.004030	-0.000738	0.002450
170.0	0.002951	0.004202	-0.002664	0.001329
175.0	0.003693	0.004295	-0.003924	0.000373
180.0	0.004332	0.004332	-0.004332	0

Table T.63

$m = 1.364 = 0.3060i$
 $\lambda = 3.00 \mu$

Model: Water cloud C.3
 $x: 1.25(0.25)11$

$\beta_{ex} = 3.245 \text{ km}^{-1}$
 $\tau = 0.4653$

θ	$P_1/4\pi$	$P_2/4\pi$	$P_3/4\pi$	$P_4/4\pi$
0.0	2.262	2.262	2.262	0
2.5	2.232	2.228	2.230	-0.003310
5.0	2.145	2.130	2.138	-0.01277
7.5	2.008	1.976	1.992	-0.02704
10.0	1.830	1.778	1.803	-0.04415
12.5	1.622	1.551	1.585	-0.06180
15.0	1.399	1.311	1.352	-0.07770
17.5	1.172	1.073	1.118	-0.08996
20.0	0.9544	0.8497	0.8948	-0.09727
22.5	0.7541	0.6509	0.6928	-0.09907
25.0	0.5779	0.4822	0.5180	-0.09554
27.5	0.4295	0.3456	0.3735	-0.08747
30.0	0.3098	0.2402	0.2595	-0.07612
40.0	0.07063	0.05050	0.04607	-0.02510
50.0	0.03136	0.02150	0.01789	-0.001882
60.0	0.02581	0.01257	0.01316	-0.000943
70.0	0.01775	0.006491	0.005859	-0.002084
80.0	0.01160	0.003926	0.001418	-0.001278
90.0	0.008434	0.002819	-0.000420	-0.000524
100.0	0.006645	0.002321	-0.001353	-0.000272
110.0	0.005431	0.002208	-0.001935	-0.000189
120.0	0.004580	0.002280	-0.002282	-0.000140
130.0	0.004003	0.002453	-0.002452	-0.000120
140.0	0.003619	0.002651	-0.002520	-0.000096
150.0	0.003337	0.002723	-0.002605	-0.000039
160.0	0.003112	0.002717	-0.002754	0.000014
170.0	0.002967	0.002822	-0.002880	0.000015
180.0	0.002920	0.002920	-0.002920	0

Table T.64

$m = 1.353 - 0.0059i$
 $\lambda = 3.90 \mu$

Model: Water cloud C.3
 $x: 0.625(0.125)8$

$\beta_{\text{ex}} = 3.241 \text{ km}^{-1}$
 $\varpi = 0.9660$

θ	$P_1/4\pi$	$P_2/4\pi$	$P_3/4\pi$	$P_4/4\pi$
0.0	1.206	1.206	1.206	0
5.0	1.171	1.169	1.170	-0.002612
10.0	1.073	1.063	1.068	-0.009650
15.0	0.9258	0.9069	0.9161	-0.01901
20.0	0.7523	0.7269	0.7389	-0.02799
25.0	0.5750	0.5478	0.5600	-0.03422
30.0	0.4129	0.3892	0.3989	-0.03629
35.0	0.2785	0.2621	0.2674	-0.03408
40.0	0.1770	0.1692	0.1697	-0.02856
50.0	0.06311	0.06766	0.06198	-0.01385
60.0	0.02578	0.03107	0.02577	-0.002857
70.0	0.01733	0.01774	0.01551	0.001433
80.0	0.01415	0.01113	0.01083	0.001814
90.0	0.01091	0.007291	0.007203	0.001425
100.0	0.008451	0.005131	0.004680	0.001448
110.0	0.007518	0.004085	0.003427	0.001803
120.0	0.007448	0.003927	0.003055	0.002296
130.0	0.006843	0.004471	0.002615	0.002930
140.0	0.005232	0.005418	0.001054	0.003524
145.0	0.004448	0.005967	-0.000285	0.003626
150.0	0.004051	0.006548	-0.001918	0.003484
155.0	0.004253	0.007153	-0.003701	0.003057
160.0	0.005093	0.007762	-0.005457	0.002379
165.0	0.006390	0.008335	-0.007012	0.001560
170.0	0.007784	0.008814	-0.008223	0.000775
175.0	0.008650	0.009135	-0.008987	0.000207
180.0	0.009248	0.009248	-0.009248	0

Table T.65

$m = 1.315 - 0.0143i$ Model: Water cloud C.3 $\beta_{\text{ex}} = 1.619 \text{ km}^{-1}$
 $\lambda = 5.30 \mu$ $x: 0.60(0.10)5.5$ $\varpi = 0.8927$

θ	$P_1/4\pi$	$P_2/4\pi$	$P_3/4\pi$	$P_4/4\pi$
0.0	0.7260	0.7260	0.7260	0
10.0	0.6832	0.6714	0.6773	-0.003196
20.0	0.5691	0.5311	0.5497	-0.01083
30.0	0.4195	0.3598	0.3879	-0.01842
40.0	0.2734	0.2096	0.2381	-0.02205
50.0	0.1577	0.1068	0.1275	-0.02047
60.0	0.08135	0.04965	0.06054	-0.01523
70.0	0.03905	0.02317	0.02679	-0.008945
80.0	0.01956	0.01220	0.01241	-0.003694
90.0	0.01220	0.007497	0.006813	-0.000257
100.0	0.009760	0.005100	0.004236	0.001617
110.0	0.008619	0.003801	0.002332	0.002547
120.0	0.007601	0.003320	0.000423	0.002998
130.0	0.006748	0.003572	-0.001597	0.003108
140.0	0.006430	0.004471	-0.003672	0.002817
150.0	0.006817	0.005834	-0.005665	0.002103
160.0	0.007698	0.007323	-0.007364	0.001150
170.0	0.008571	0.008489	-0.008520	0.000326
180.0	0.008931	0.008931	-0.008931	0

Table T.66

$m = 1.315 - 0.1370i$
 $\lambda = 6.05 \mu$

Model: Water cloud C.3
 $x: 0.125(0.125)5$

$\beta_{\text{ex}} = 1.836 \text{ km}^{-1}$
 $\pi = 0.4546$

θ	$P_1/4\pi$	$P_2/4\pi$	$P_3/4\pi$	$P_4/4\pi$
0.0	0.6234	0.6234	0.6234	0
10.0	0.5944	0.5812	0.5878	-0.003276
20.0	0.5154	0.4706	0.4924	-0.01142
30.0	0.4066	0.3306	0.3660	-0.02043
40.0	0.2921	0.2013	0.2409	-0.02634
50.0	0.1916	0.1066	0.1398	-0.02723
60.0	0.1152	0.05002	0.07118	-0.02364
70.0	0.06429	0.02226	0.03162	-0.01759
80.0	0.03420	0.01084	0.01223	-0.01128
90.0	0.01838	0.006503	0.004130	-0.006098
100.0	0.01095	0.004514	0.001073	-0.002523
110.0	0.007786	0.003273	-0.000301	-0.000387
120.0	0.006519	0.002562	-0.001361	0.000701
130.0	0.006013	0.002467	-0.002456	0.001103
140.0	0.005826	0.002970	-0.003555	0.001073
150.0	0.005802	0.003883	-0.004542	0.000791
160.0	0.005865	0.004900	-0.005318	0.000421
170.0	0.005945	0.005686	-0.005811	0.000117
180.0	0.005980	0.005980	-0.005980	0

Table T.67

$m = 1.29 - 0.0472i$ $\lambda = 8.15 \mu$		Model: Water cloud C.3 $x: 0.30(0.05)3.25$		$\beta_{\text{ex}} = 0.7290 \text{ km}^{-1}$ $\varpi = 0.5713$
θ	$P_1/4\pi$	$P_2/4\pi$	$P_3/4\pi$	$P_4/4\pi$
0.0	0.3834	0.3834	0.3834	0
10.0	0.3741	0.3653	0.3697	-0.000615
20.0	0.3475	0.3157	0.3312	-0.002263
30.0	0.3076	0.2470	0.2756	-0.004430
40.0	0.2600	0.1741	0.2126	-0.006477
50.0	0.2104	0.1097	0.1515	-0.007861
60.0	0.1635	0.06095	0.09911	-0.008287
70.0	0.1226	0.02912	0.05853	-0.007751
80.0	0.08921	0.01149	0.02999	-0.006486
90.0	0.06354	0.003645	0.01168	-0.004842
100.0	0.04480	0.001467	0.000937	-0.003169
110.0	0.03175	0.001992	-0.004821	-0.001733
120.0	0.02307	0.003518	-0.007663	-0.000682
130.0	0.01753	0.005255	-0.008994	-0.000049
140.0	0.01416	0.006906	-0.009643	0.000226
150.0	0.01221	0.008351	-0.01002	0.000252
160.0	0.01116	0.009496	-0.01028	0.000155
170.0	0.01065	0.01024	-0.01044	0.000045
180.0	0.01050	0.01050	-0.01050	0

Table T.68

$$m = 1.212 - 0.0601i$$

$$\lambda = 10.0 \mu$$

Model: Water cloud C.3
 $x: 0.10(0.10)3$

$$\beta_{\text{ex}} = 0.4298 \text{ km}^{-1}$$

$$\varpi = 0.3118$$

θ	$P_1/4\pi$	$P_2/4\pi$	$P_3/4\pi$	$P_4/4\pi$
0.0	0.2797	0.2797	0.2797	0
20.0	0.2628	0.2351	0.2486	-0.000677
40.0	0.2192	0.1365	0.1730	-0.002070
60.0	0.1649	0.04909	0.08986	-0.002980
80.0	0.1151	0.006659	0.02726	-0.002837
90.0	0.09456	0.000649	0.006458	-0.002454
100.0	0.07742	0.001035	-0.008074	-0.001973
120.0	0.05271	0.01040	-0.02328	-0.001027
140.0	0.03829	0.02055	-0.02802	-0.000383
160.0	0.03103	0.02683	-0.02885	-0.000080
180.0	0.02885	0.02885	-0.02885	0

Table T.69

$$m = 1.44 - 0.4000i$$

$$\lambda = 16.6 \mu$$

Model: Water cloud C.3
 $x: 0.125(0.025)1.6$

$$\beta_{\text{ex}} = 1.179 \text{ km}^{-1}$$

$$\varpi = 0.1544$$

θ	$P_1/4\pi$	$P_2/4\pi$	$P_3/4\pi$	$P_4/4\pi$
0.0	0.1720	0.1720	0.1720	0
20.0	0.1680	0.1497	0.1586	-0.000771
40.0	0.1569	0.09590	0.1226	-0.002590
60.0	0.1412	0.03964	0.07465	-0.004348
80.0	0.1238	0.005823	0.02622	-0.005103
90.0	0.1154	0.000466	0.004590	-0.004994
100.0	0.1075	0.002207	-0.01446	-0.004595
120.0	0.09395	0.02082	-0.04406	-0.003215
140.0	0.08407	0.04716	-0.06293	-0.001630
160.0	0.07813	0.06826	-0.07303	-0.000437
180.0	0.07616	0.07616	-0.07616	0

Table T.70

$m = 1.34$
 $\lambda = 0.45 \mu$

Model: Water cloud C.4
 $x: 30.125(0.125)55(0.25)85$

$\beta_{\text{ex}} = 10.86 \text{ km}^{-1}$
 $\varpi = 1.0$

θ	$P_1/4\pi$	$P_2/4\pi$	$P_3/4\pi$	$P_4/4\pi$
0.0	140.2	140.2	140.2	0
1.0	105.9	105.9	105.9	-0.3891
2.0	42.33	42.44	42.37	-0.7226
3.0	6.584	6.599	6.564	-0.3379
4.0	1.528	1.457	1.480	0.02993
4.5	2.316	2.244	2.275	0.04225
5.0	2.565	2.510	2.534	-0.004542
5.5	2.101	2.062	2.076	-0.04527
6.0	1.428	1.398	1.405	-0.04994
6.5	0.9868	0.9562	0.9632	-0.02790
7.0	0.8617	0.8291	0.8389	-0.004128
7.5	0.8944	0.8628	0.8741	0.005421
8.0	0.9124	0.8848	0.8949	0.001599
8.5	0.8560	0.8324	0.8401	-0.005769
9.0	0.7615	0.7395	0.7458	-0.009010
9.5	0.6831	0.6607	0.6673	-0.007268
10.0	0.6414	0.6188	0.6261	-0.003964
20.0	0.3291	0.3319	0.3276	0.000018
30.0	0.1768	0.1879	0.1787	0.001860
40.0	0.08853	0.09979	0.09041	0.001844
50.0	0.04288	0.05284	0.04451	0.001917
60.0	0.02086	0.02694	0.02092	0.001197
70.0	0.01007	0.01313	0.009065	0.000771
80.0	0.005326	0.006088	0.003394	0.000414
90.0	0.003340	0.003160	0.001113	0.000171
100.0	0.002492	0.002039	0.000026	0.000518
110.0	0.003056	0.001957	0.000526	0.000220
120.0	0.005392	0.001781	0.000333	0.001538
130.0	0.005282	0.002406	-0.000499	0.002330
132.0	0.006197	0.002868	-0.000571	0.003004
134.0	0.008291	0.003870	-0.000228	0.004323
136.0	0.01276	0.004998	0.000467	0.006540
138.0	0.01840	0.006084	0.001341	0.008939
140.0	0.02666	0.006700	0.003009	0.01118

TABLE T.70, continued

θ	$P_1/4\pi$	$P_2/4\pi$	$P_3/4\pi$	$P_4/4\pi$
142.0	0.03581	0.006083	0.004769	0.01157
144.0	0.04184	0.004789	0.006464	0.008984
146.0	0.04121	0.003708	0.007970	0.002371
148.0	0.03205	0.005140	0.007502	-0.005450
150.0	0.01751	0.01049	0.005836	-0.008879
152.0	0.005460	0.01788	0.003119	-0.004622
153.0	0.003560	0.01943	0.002178	-0.000080
154.0	0.004476	0.01963	0.001523	0.004734
155.0	0.008358	0.01791	0.001573	0.008875
156.0	0.01335	0.01397	0.002237	0.01036
157.0	0.01749	0.009934	0.003146	0.009058
158.0	0.02015	0.007143	0.003985	0.005762
159.0	0.01974	0.006194	0.004379	0.001043
160.0	0.01606	0.008239	0.004379	-0.003006
161.0	0.01148	0.01230	0.003934	-0.004434
162.0	0.007626	0.01640	0.002882	-0.003166
163.0	0.005722	0.01959	0.001993	0.000133
164.0	0.006739	0.01999	0.001651	0.004028
165.0	0.009412	0.01733	0.001758	0.006312
166.0	0.01206	0.01423	0.002696	0.005968
167.0	0.01381	0.01254	0.003675	0.004000
168.0	0.01315	0.01238	0.003650	0.001348
169.0	0.01078	0.01480	0.003796	-0.000760
170.0	0.01011	0.02060	0.004634	0.000030
171.0	0.009350	0.02179	0.003375	0.001874
172.0	0.008223	0.01975	0.002323	0.002833
173.0	0.01405	0.02935	0.007672	0.005897
174.0	0.01634	0.02720	0.008717	0.005483
175.0	0.008903	0.01302	0.001550	0.000911
176.0	0.02078	0.04760	0.01551	0.006335
177.0	0.04284	0.07538	0.04156	0.008163
178.0	0.04184	0.03070	0.02449	-0.006652
179.0	0.04465	0.02510	-0.02787	-0.008124
180.0	0.05457	0.05457	-0.05457	0

Table T.7I

$m = 1.33$
 $\lambda = 0.70 \mu$

Model: Water cloud C.4
 $x: 20.125(0.125)55$

$\beta_{cx} = 11.16 \text{ km}^{-1}$
 $\varpi = 1.0$

θ	$P_1/4\pi$	$P_2/4\pi$	$P_3/4\pi$	$P_4/4\pi$
0.0	59.79	59.79	59.79	0
1.0	53.22	53.24	53.23	-0.1221
2.0	37.13	37.20	37.16	-0.3579
3.0	19.59	19.67	19.61	-0.4644
4.0	7.277	7.328	7.277	-0.3479
5.0	1.888	1.884	1.863	-0.1333
5.5	1.093	1.066	1.062	-0.04765
6.0	0.9704	0.9295	0.9380	0.005040
6.5	1.131	1.084	1.101	0.02428
7.0	1.307	1.262	1.281	0.01830
7.5	1.366	1.326	1.343	-0.000390
8.0	1.286	1.251	1.265	-0.01974
8.5	1.111	1.081	1.090	-0.03164
9.0	0.9086	0.8811	0.8869	-0.03328
9.5	0.7360	0.7086	0.7135	-0.02643
10.0	0.6223	0.5938	0.5998	-0.01542
10.5	0.5689	0.5393	0.5472	-0.004809
11.0	0.5584	0.5286	0.5381	0.002281
11.5	0.5670	0.5385	0.5486	0.004889
12.0	0.5752	0.5493	0.5587	0.003913
12.5	0.5724	0.5499	0.5574	0.001226
15.0	0.4751	0.4685	0.4671	0.001459
25.0	0.2426	0.2490	0.2421	-0.000193
35.0	0.1196	0.1280	0.1200	0.003161
45.0	0.06196	0.07281	0.06367	0.003209
55.0	0.03102	0.03923	0.03168	0.002411
65.0	0.01553	0.02043	0.01496	0.001604
75.0	0.008020	0.01056	0.006684	0.000989
85.0	0.004779	0.005656	0.002937	0.000711
95.0	0.003102	0.003254	0.000864	0.000656
105.0	0.002733	0.002455	0.000480	0.000428
115.0	0.004320	0.002127	0.000505	0.001202
125.0	0.005561	0.002925	-0.000150	0.002689
130.0	0.007758	0.004479	-0.000062	0.004660
132.0	0.009753	0.005297	0.000131	0.006000

TABLE T.7I, continued

θ	$P_1/4\pi$	$P_2/4\pi$	$P_3/4\pi$	$P_4/4\pi$
134.0	0.01237	0.006453	0.000594	0.007674
136.0	0.01620	0.007402	0.001241	0.009615
138.0	0.02088	0.008142	0.002010	0.01140
140.0	0.02605	0.008235	0.003248	0.01262
142.0	0.03110	0.007590	0.004419	0.01265
144.0	0.03471	0.006229	0.005756	0.01075
146.0	0.03555	0.004917	0.006948	0.006964
148.0	0.03248	0.004398	0.007465	0.001697
150.0	0.02573	0.006098	0.007512	-0.003614
152.0	0.01657	0.01031	0.006365	-0.006435
154.0	0.008250	0.01593	0.004714	-0.005415
156.0	0.003945	0.02089	0.003064	-0.000258
158.0	0.005370	0.02142	0.001846	0.006543
160.0	0.01131	0.01830	0.002501	0.01098
161.0	0.01443	0.01531	0.003070	0.01121
162.0	0.01656	0.01156	0.003551	0.009674
163.0	0.01767	0.008820	0.004416	0.006821
164.0	0.01822	0.009003	0.005930	0.003785
165.0	0.01784	0.01139	0.007108	0.001263
166.0	0.01531	0.01303	0.006465	-0.001011
167.0	0.01093	0.01371	0.004453	-0.002868
168.0	0.007989	0.01818	0.003959	-0.002559
169.0	0.009279	0.02850	0.006552	0.001038
170.0	0.01212	0.03609	0.008958	0.005337
171.0	0.01101	0.03039	0.006516	0.006387
172.0	0.007175	0.01799	0.001277	0.005299
173.0	0.01037	0.02050	0.002848	0.008061
174.0	0.02569	0.04408	0.01707	0.01566
175.0	0.04285	0.06311	0.03535	0.01896
176.0	0.04733	0.05152	0.04021	0.009922
177.0	0.04050	0.02275	0.02252	-0.004882
178.0	0.03745	0.01460	-0.009477	-0.01075
179.0	0.04414	0.03475	-0.03811	-0.004872
180.0	0.04927	0.04927	-0.04927	0

Table T.72

$m = 2.4066 - 0.4771i$ Model: Rain L (0°C water) $\beta_{\text{ex}} = 0.5084 \text{ km}^{-1}$
 $\lambda = 0.1 \text{ cm}$ $x: 0.025(0.025)4(0.10)20$ $w = 0.4972$

θ	$P_1/4\pi$	$P_2/4\pi$	$P_3/4\pi$	$P_4/4\pi$
0.0	1.315	1.315	1.315	0
2.5	1.287	1.286	1.286	-0.005346
5.0	1.210	1.204	1.206	-0.01958
7.5	1.098	1.086	1.091	-0.03841
10.0	0.9719	0.9532	0.9600	-0.05734
12.5	0.8449	0.8201	0.8277	-0.07334
15.0	0.7263	0.6965	0.7036	-0.08507
17.5	0.6206	0.5869	0.5926	-0.09239
20.0	0.5288	0.4925	0.4961	-0.09580
30.0	0.2841	0.2457	0.2386	-0.08555
40.0	0.1645	0.1309	0.1152	-0.06355
50.0	0.1040	0.07688	0.05591	-0.04452
60.0	0.07120	0.05003	0.02619	-0.03078
70.0	0.05210	0.03589	0.01055	-0.02137
80.0	0.04024	0.02799	0.001897	-0.01503
90.0	0.03247	0.02327	-0.003160	-0.01074
100.0	0.02716	0.02019	-0.006317	-0.007850
110.0	0.02342	0.01790	-0.008483	-0.005930
120.0	0.02075	0.01603	-0.01017	-0.004681
130.0	0.01888	0.01456	-0.01166	-0.003830
140.0	0.01770	0.01380	-0.01311	-0.003086
150.0	0.01715	0.01406	-0.01455	-0.002220
160.0	0.01709	0.01525	-0.01591	-0.001221
170.0	0.01725	0.01669	-0.01695	-0.000352
180.0	0.01735	0.01735	-0.01735	0

Table T.73

$m = 2.5604 - 0.8947i$
 $\lambda = 0.2 \text{ cm}$

Model: Rain L (0°C water)
 $x: 0.025(0.025)2(0.10)10$

$\beta_{\text{ex}} = 0.4563 \text{ km}^{-1}$
 $\varpi = 0.4579$

θ	$P_1/4\pi$	$P_2/4\pi$	$P_3/4\pi$	$P_4/4\pi$
0.0	0.4805	0.4805	0.4805	0
2.5	0.4778	0.4770	0.4774	-0.000986
5.0	0.4698	0.4668	0.4683	-0.003845
7.5	0.4570	0.4506	0.4537	-0.008295
10.0	0.4403	0.4295	0.4345	-0.01393
12.5	0.4204	0.4046	0.4117	-0.02027
15.0	0.3984	0.3773	0.3863	-0.02686
17.5	0.3752	0.3487	0.3594	-0.03329
20.0	0.3516	0.3199	0.3319	-0.03925
30.0	0.2628	0.2156	0.2275	-0.05540
40.0	0.1934	0.1401	0.1455	-0.05903
50.0	0.1441	0.09162	0.08784	-0.05466
60.0	0.1100	0.06215	0.04915	-0.04689
70.0	0.08650	0.04465	0.02365	-0.03850
80.0	0.07005	0.03432	0.006852	-0.03079
90.0	0.05836	0.02824	-0.004329	-0.02422
100.0	0.04994	0.02471	-0.01193	-0.01883
110.0	0.04382	0.02280	-0.01726	-0.01446
120.0	0.03937	0.02211	-0.02115	-0.01090
130.0	0.03619	0.02248	-0.02413	-0.007949
140.0	0.03401	0.02385	-0.02650	-0.005431
150.0	0.03262	0.02600	-0.02844	-0.003282
160.0	0.03181	0.02848	-0.02995	-0.001556
170.0	0.03142	0.03051	-0.03095	-0.000407
180.0	0.03130	0.03130	-0.03130	0

Table T.74

$m = 2.7589 - 1.2408i$ Model: Rain L (0°C water) $\beta_{\text{ex}} = 0.3821 \text{ km}^{-1}$
 $\lambda = 0.3 \text{ cm}$ $x: 0.025(0.025)2(0.10)8$ $w = 0.4312$

θ	$P_1/4\pi$	$P_2/4\pi$	$P_3/4\pi$	$P_4/4\pi$
0.0	0.2939	0.2939	0.2939	0
5.0	0.2908	0.2889	0.2899	-0.001643
10.0	0.2820	0.2748	0.2783	-0.006238
15.0	0.2686	0.2535	0.2604	-0.01291
20.0	0.2519	0.2276	0.2381	-0.02055
30.0	0.2147	0.1720	0.1871	-0.03480
40.0	0.1788	0.1225	0.1368	-0.04404
50.0	0.1482	0.08463	0.09327	-0.04745
60.0	0.1236	0.05846	0.05814	-0.04632
70.0	0.1045	0.04170	0.03094	-0.04238
80.0	0.08972	0.03180	0.01034	-0.03705
90.0	0.07844	0.02670	-0.005128	-0.03128
100.0	0.06984	0.02489	-0.01674	-0.02563
110.0	0.06332	0.02542	-0.02551	-0.02035
120.0	0.05842	0.02767	-0.03221	-0.01556
130.0	0.05483	0.03120	-0.03741	-0.01128
140.0	0.05227	0.03559	-0.04146	-0.007551
150.0	0.05055	0.04028	-0.04457	-0.004431
160.0	0.04946	0.04456	-0.04684	-0.002040
170.0	0.04888	0.04760	-0.04823	-0.000522
180.0	0.04870	0.04870	-0.04870	0

Table T.75

$m = 3.1918 - 1.7657i$
 $\lambda = 0.5 \text{ cm}$

Model: Rain L (0°C water)
 $x: 0.0125(0.0125)1(0.05)5$

$\beta_{\text{ex}} = 0.2450 \text{ km}^{-1}$
 $\varpi = 0.3901$

θ	$P_1/4\pi$	$P_2/4\pi$	$P_3/4\pi$	$P_4/4\pi$
0.0	0.1832	0.1832	0.1832	0
5.0	0.1824	0.1812	0.1818	-0.000662
10.0	0.1804	0.1756	0.1779	-0.002587
15.0	0.1770	0.1667	0.1716	-0.005596
20.0	0.1727	0.1551	0.1632	-0.009426
30.0	0.1616	0.1267	0.1413	-0.01830
40.0	0.1490	0.09658	0.1152	-0.02683
50.0	0.1364	0.06920	0.08768	-0.03338
60.0	0.1248	0.04731	0.06079	-0.03721
70.0	0.1145	0.03194	0.03590	-0.03830
80.0	0.1057	0.02299	0.01369	-0.03706
90.0	0.09849	0.01973	-0.005603	-0.03403
100.0	0.09263	0.02120	-0.02204	-0.02979
110.0	0.08800	0.02634	-0.03583	-0.02484
120.0	0.08441	0.03412	-0.04725	-0.01961
130.0	0.08172	0.04348	-0.05656	-0.01447
140.0	0.07976	0.05334	-0.06398	-0.009734
150.0	0.07841	0.06259	-0.06966	-0.005697
160.0	0.07754	0.07018	-0.07369	-0.002606
170.0	0.07706	0.07517	-0.07610	-0.000663
180.0	0.07691	0.07691	-0.07691	0

Table T.76

$m = 4.2214 - 2.5259i$
 $\lambda = 1.0 \text{ cm}$

Model: Rain L (0°C water)
 $x: 0.005(0.005)1(0.05)3$

$\beta_{\text{ex}} = 0.07818 \text{ km}^{-1}$
 $w = 0.2746$

θ	$P_1/4\pi$	$P_2/4\pi$	$P_3/4\pi$	$P_4/4\pi$
0.0	0.1273	0.1273	0.1273	0
10.0	0.1268	0.1231	0.1249	-0.001186
20.0	0.1254	0.1111	0.1180	-0.004528
30.0	0.1233	0.09338	0.1068	-0.009438
40.0	0.1208	0.07251	0.09199	-0.01509
50.0	0.1182	0.05149	0.07435	-0.02062
60.0	0.1156	0.03306	0.05471	-0.02524
70.0	0.1134	0.01936	0.03393	-0.02839
80.0	0.1117	0.01172	0.01280	-0.02978
90.0	0.1104	0.01059	-0.007956	-0.02935
100.0	0.1096	0.01569	-0.02774	-0.02727
110.0	0.1092	0.02605	-0.04605	-0.02386
120.0	0.1092	0.04026	-0.06253	-0.01956
130.0	0.1094	0.05658	-0.07688	-0.01484
140.0	0.1097	0.07319	-0.08888	-0.01018
150.0	0.1101	0.08830	-0.09838	-0.006035
160.0	0.1105	0.1003	-0.1052	-0.002783
170.0	0.1107	0.1081	-0.1094	-0.000711
180.0	0.1108	0.1108	-0.1108	0

Table T.77

$m = 5.8368 - 3.0046i$ Model: Rain L (0°C water) $\beta_{\text{ex}} = 0.01754 \text{ km}^{-1}$
 $\lambda = 2.0 \text{ cm}$ $x: 0.005(0.005)1.6$ $\varpi = 0.1089$

θ	$P_1/4\pi$	$P_2/4\pi$	$P_3/4\pi$	$P_4/4\pi$
0.0	0.1129	0.1129	0.1129	0
10.0	0.1128	0.1093	0.1110	-0.000898
20.0	0.1124	0.09923	0.1056	-0.003122
30.0	0.1120	0.08391	0.09663	-0.006623
40.0	0.1115	0.06547	0.08452	-0.01084
50.0	0.1111	0.04636	0.06962	-0.01521
60.0	0.1109	0.02908	0.05239	-0.01917
70.0	0.1111	0.01586	0.03339	-0.02223
80.0	0.1116	0.008336	0.01320	-0.02402
90.0	0.1126	0.007420	-0.007523	-0.02437
100.0	0.1139	0.01319	-0.02815	-0.02325
110.0	0.1156	0.02493	-0.04806	-0.02085
120.0	0.1174	0.04124	-0.06664	-0.01745
130.0	0.1192	0.06026	-0.08335	-0.01348
140.0	0.1210	0.07985	-0.09771	-0.009387
150.0	0.1226	0.09783	-0.1093	-0.005630
160.0	0.1238	0.1123	-0.1178	-0.002617
170.0	0.1245	0.1216	-0.1231	-0.000672
180.0	0.1248	0.1248	-0.1248	0

Table T.78

$m = 7.1755 - 2.8642i$ Model: Rain L (0°C water) $\beta_{ex} = 0.005455 \text{ km}^{-1}$
 $\lambda = 3.3 \text{ cm}$ $x: 0.005(0.005)1.2$ $w = 0.04547$

θ	$P_1/4\pi$	$P_2/4\pi$	$P_3/4\pi$	$P_4/4\pi$
0.0	0.1219	0.1219	0.1219	0
10.0	0.1216	0.1183	0.1200	-0.000638
20.0	0.1210	0.1081	0.1143	-0.002470
30.0	0.1199	0.09246	0.1051	-0.005263
40.0	0.1187	0.07340	0.09263	-0.008659
50.0	0.1173	0.05324	0.07737	-0.01223
60.0	0.1159	0.03444	0.05981	-0.01554
70.0	0.1147	0.01928	0.04053	-0.01817
80.0	0.1138	0.009527	0.02016	-0.01981
90.0	0.1132	0.006287	-0.000656	-0.02028
100.0	0.1130	0.009856	-0.02128	-0.01952
110.0	0.1131	0.01971	-0.04109	-0.01765
120.0	0.1135	0.03460	-0.05951	-0.01489
130.0	0.1141	0.05267	-0.07602	-0.01158
140.0	0.1149	0.07176	-0.09016	-0.008112
150.0	0.1156	0.08959	-0.1016	-0.004888
160.0	0.1162	0.1041	-0.1099	-0.002280
170.0	0.1166	0.1135	-0.1150	-0.000587
180.0	0.1167	0.1167	-0.1167	0

Table T.79

$m = 8.1084 - 2.4102i$
 $\lambda = 5.0 \text{ cm}$

Model: Rain L (0°C water)
 $x: 0.0025(0.0025)1.0$

$\beta_{\text{ex}} = 0.001824 \text{ km}^{-1}$
 $w = 0.02424$

θ	$P_1/4\pi$	$P_2/4\pi$	$P_3/4\pi$	$P_4/4\pi$
0.0	0.1319	0.1319	0.1319	0
20.0	0.1307	0.1175	0.1239	-0.001543
40.0	0.1272	0.08087	0.1010	-0.005429
60.0	0.1224	0.03864	0.06684	-0.009794
80.0	0.1174	0.009579	0.02631	-0.01257
100.0	0.1130	0.005805	-0.01514	-0.01247
120.0	0.1100	0.02740	-0.05254	-0.009574
140.0	0.1081	0.06279	-0.08193	-0.005243
160.0	0.1072	0.09441	-0.1006	-0.001479
180.0	0.1070	0.1070	-0.1070	0

Table T.80

$m = 8.7889 - 1.7531i$
 $\lambda = 8.0 \text{ cm}$

Model: Rain L (0°C water)
 $x: 0.001(0.001)0.6$

$\beta_{\text{ex}} = 0.0005175 \text{ km}^{-1}$
 $w = 0.01234$

θ	$P_1/4\pi$	$P_2/4\pi$	$P_3/4\pi$	$P_4/4\pi$
0.0	0.1309	0.1309	0.1309	0
20.0	0.1300	0.1163	0.1230	-0.000479
40.0	0.1276	0.07920	0.1004	-0.001687
60.0	0.1241	0.03633	0.06661	-0.003054
80.0	0.1200	0.006764	0.02631	-0.003934
100.0	0.1160	0.003003	-0.01515	-0.003918
120.0	0.1126	0.02536	-0.05277	-0.003019
140.0	0.1100	0.06204	-0.08249	-0.001658
160.0	0.1085	0.09488	-0.1014	-0.000468
180.0	0.1079	0.1079	-0.1079	0

Table T.81

$m = 2.4806 - 0.7050i$ Model: Rain L (10°C water) $\beta_{ex} = 0.5047 \text{ km}^{-1}$
 $\lambda = 0.1 \text{ cm}$ $x: 0.025(0.025)4(0.10)20$ $w = 0.4923$

θ	$P_1/4\pi$	$P_2/4\pi$	$P_3/4\pi$	$P_4/4\pi$
0.0	1.325	1.325	1.325	0
2.5	1.297	1.294	1.295	-0.005732
5.0	1.219	1.210	1.214	-0.02098
7.5	1.107	1.089	1.097	-0.04113
10.0	0.9801	0.9522	0.9632	-0.06134
12.5	0.8525	0.8160	0.8286	-0.07837
15.0	0.7334	0.6899	0.7026	-0.09080
17.5	0.6272	0.5784	0.5899	-0.09850
20.0	0.5350	0.4829	0.4921	-0.1020
30.0	0.2887	0.2355	0.2318	-0.09064
40.0	0.1680	0.1226	0.1079	-0.06701
50.0	0.1069	0.07055	0.04899	-0.04673
60.0	0.07370	0.04533	0.01990	-0.03217
70.0	0.05436	0.03241	0.004899	-0.02226
80.0	0.04235	0.02542	-0.003199	-0.01560
90.0	0.03449	0.02142	-0.007783	-0.01112
100.0	0.02913	0.01896	-0.01053	-0.008069
110.0	0.02537	0.01730	-0.01231	-0.005989
120.0	0.02270	0.01613	-0.01360	-0.004542
130.0	0.02085	0.01541	-0.01467	-0.003471
140.0	0.01964	0.01526	-0.01567	-0.002567
150.0	0.01895	0.01578	-0.01665	-0.001703
160.0	0.01866	0.01687	-0.01759	-0.000881
170.0	0.01861	0.01807	-0.01832	-0.000245
180.0	0.01861	0.01861	-0.01861	0

Table T.82

$m = 3.1060 - 1.6626i$ Model: Rain L (10°C water) $\beta_{\text{ex}} = 0.3923 \text{ km}^{-1}$
 $\lambda = 0.3 \text{ cm}$ $x: 0.025(0.025)2(0.10)8$ $\varpi = 0.4581$

θ	$P_1/4\pi$	$P_2/4\pi$	$P_3/4\pi$	$P_4/4\pi$
0.0	0.2674	0.2674	0.2674	0
5.0	0.2647	0.2628	0.2638	-0.001685
10.0	0.2571	0.2498	0.2533	-0.006402
15.0	0.2455	0.2301	0.2371	-0.01326
20.0	0.2312	0.2063	0.2168	-0.02114
30.0	0.1991	0.1555	0.1702	-0.03594
40.0	0.1682	0.1108	0.1237	-0.04572
50.0	0.1420	0.07709	0.08293	-0.04956
60.0	0.1208	0.05427	0.04967	-0.04871
70.0	0.1044	0.04013	0.02360	-0.04488
80.0	0.09168	0.03226	0.003612	-0.03952
90.0	0.08198	0.02875	-0.01159	-0.03358
100.0	0.07460	0.02825	-0.02317	-0.02765
110.0	0.06905	0.02990	-0.03208	-0.02203
120.0	0.06493	0.03311	-0.03904	-0.01686
130.0	0.06197	0.03750	-0.04456	-0.01221
140.0	0.05992	0.04262	-0.04898	-0.008147
150.0	0.05857	0.04793	-0.05247	-0.004762
160.0	0.05776	0.05267	-0.05505	-0.002183
170.0	0.05734	0.05600	-0.05666	-0.000557
180.0	0.05721	0.05721	-0.05721	0

Table T.83

$m = 5.1553 - 2.8341i$ Model: Rain L (10°C water) $\beta_{\text{ex}} = 0.07781 \text{ km}^{-1}$
 $\lambda = 1.0 \text{ cm}$ $x: 0.005(0.005)1(0.05)3$ $w = 0.2836$

θ	$P_1/4\pi$	$P_2/4\pi$	$P_3/4\pi$	$P_4/4\pi$
0.0	0.1158	0.1158	0.1158	0
10.0	0.1155	0.1119	0.1137	-0.001269
20.0	0.1146	0.1008	0.1073	-0.004849
30.0	0.1133	0.08433	0.09708	-0.01011
40.0	0.1118	0.06509	0.08336	-0.01619
50.0	0.1104	0.04594	0.06682	-0.02213
60.0	0.1094	0.02950	0.04815	-0.02710
70.0	0.1088	0.01779	0.02810	-0.03051
80.0	0.1088	0.01205	0.007432	-0.03201
90.0	0.1094	0.01270	-0.01317	-0.03155
100.0	0.1104	0.01939	-0.03309	-0.02931
110.0	0.1117	0.03114	-0.05179	-0.02564
120.0	0.1133	0.04651	-0.06883	-0.02101
130.0	0.1150	0.06379	-0.08384	-0.01592
140.0	0.1166	0.08114	-0.09651	-0.01092
150.0	0.1180	0.09680	-0.1066	-0.006470
160.0	0.1190	0.1092	-0.1140	-0.002982
170.0	0.1197	0.1172	-0.1184	-0.000762
180.0	0.1199	0.1199	-0.1199	0

Table T.84

$m = 8.0253 - 2.2727i$ Model: Rain L (10°C water) $\beta_{\text{ex}} = 0.005071 \text{ km}^{-1}$
 $\lambda = 3.3 \text{ cm}$ $x: 0.005(0.005)1.2$ $w = 0.05084$

θ	$P_1/4\pi$	$P_2/4\pi$	$P_3/4\pi$	$P_4/4\pi$
0.0	0.1236	0.1236	0.1236	0
10.0	0.1232	0.1202	0.1217	-0.000758
20.0	0.1221	0.1102	0.1160	-0.002936
30.0	0.1204	0.09507	0.1066	-0.006255
40.0	0.1182	0.07652	0.09404	-0.01029
50.0	0.1159	0.05688	0.07863	-0.01454
60.0	0.1136	0.03852	0.06093	-0.01847
70.0	0.1116	0.02362	0.04154	-0.02161
80.0	0.1100	0.01391	0.02110	-0.02356
90.0	0.1090	0.01047	0.000256	-0.02412
100.0	0.1086	0.01358	-0.02034	-0.02322
110.0	0.1088	0.02276	-0.04008	-0.02100
120.0	0.1095	0.03681	-0.05839	-0.01772
130.0	0.1106	0.05395	-0.07476	-0.01378
140.0	0.1118	0.07211	-0.08876	-0.009654
150.0	0.1131	0.08909	-0.1000	-0.005818
160.0	0.1141	0.1029	-0.1083	-0.002714
170.0	0.1148	0.1119	-0.1133	-0.000698
180.0	0.1150	0.1150	-0.1150	0

Table T.85

$m = 8.9218 - 1.1423i$ Model: Rain L (10°C water) $\beta_{ex} = 0.0003432 \text{ km}^{-1}$
 $\lambda = 8.0 \text{ cm}$ $x: 0.001(0.001)0.6$ $\varpi = 0.01866$

θ	$P_1/4\pi$	$P_2/4\pi$	$P_3/4\pi$	$P_4/4\pi$
0.0	0.1326	0.1326	0.1326	0
20.0	0.1316	0.1180	0.1246	-0.000394
40.0	0.1287	0.08079	0.1018	-0.001388
60.0	0.1245	0.03765	0.06770	-0.002511
80.0	0.1197	0.007644	0.02721	-0.003234
100.0	0.1152	0.003278	-0.01425	-0.003220
120.0	0.1113	0.02494	-0.05168	-0.002479
140.0	0.1085	0.06096	-0.08112	-0.001361
160.0	0.1068	0.09333	-0.09981	-0.000385
180.0	0.1062	0.1062	-0.1062	0

Table T.86

$m = 1.7800 - 0.0024i$
 $\lambda = 0.20 \text{ cm}$

Model: Rain L (ice)
 $x: 0.025(0.025)2(0.10)10$

$\beta_{\text{ex}} = 0.3225 \text{ km}^{-1}$
 $w = 0.9890$

θ	$P_1/4\pi$	$P_2/4\pi$	$P_3/4\pi$	$P_4/4\pi$
0.0	0.5131	0.5131	0.5131	0
2.5	0.5102	0.5102	0.5102	-0.000451
5.0	0.5016	0.5016	0.5016	-0.001757
7.5	0.4878	0.4879	0.4877	-0.003785
10.0	0.4696	0.4697	0.4694	-0.006340
12.5	0.4480	0.4481	0.4476	-0.009197
15.0	0.4239	0.4239	0.4231	-0.01214
17.5	0.3983	0.3981	0.3970	-0.01496
20.0	0.3721	0.3716	0.3700	-0.01753
30.0	0.2714	0.2688	0.2657	-0.02378
40.0	0.1906	0.1857	0.1816	-0.02384
50.0	0.1326	0.1264	0.1213	-0.02040
60.0	0.09302	0.08657	0.08040	-0.01580
70.0	0.06652	0.06078	0.05328	-0.01128
80.0	0.04880	0.04446	0.03545	-0.007357
90.0	0.03688	0.03446	0.02368	-0.004182
100.0	0.02868	0.02869	0.01576	-0.001753
110.0	0.02292	0.02582	0.01020	-0.000051
120.0	0.01867	0.02484	0.005876	0.000774
130.0	0.01542	0.02480	0.001807	0.000389
140.0	0.01328	0.02470	-0.003041	-0.001578
150.0	0.01373	0.02445	-0.009899	-0.004476
160.0	0.01978	0.02664	-0.02005	-0.005448
165.0	0.02527	0.02965	-0.02620	-0.004347
170.0	0.03137	0.03350	-0.03214	-0.002484
175.0	0.03630	0.03686	-0.03656	-0.000723
180.0	0.03821	0.03821	-0.03821	0

Table T.87

$m = 1.7800 - 0.0024i$		Model: Rain L (ice)		$\beta_{\text{ex}} = 0.005072 \text{ km}^{-1}$
$\lambda = 1.0 \text{ cm}$		$x: 0.005(0.005)1(0.05)3$		$w = 0.9493$
θ	$P_1/4\pi$	$P_2/4\pi$	$P_3/4\pi$	$P_4/4\pi$
0.0	0.1873	0.1873	0.1873	0
10.0	0.1855	0.1813	0.1834	-0.000104
20.0	0.1802	0.1643	0.1720	-0.000376
30.0	0.1720	0.1389	0.1545	-0.000708
40.0	0.1618	0.1090	0.1324	-0.000972
50.0	0.1504	0.07834	0.1077	-0.001065
60.0	0.1386	0.05063	0.08206	-0.000946
70.0	0.1271	0.02843	0.05696	-0.000634
80.0	0.1164	0.01321	0.03340	-0.000202
90.0	0.1067	0.005392	0.01204	0.000258
100.0	0.09818	0.004485	-0.006774	0.000653
110.0	0.09096	0.009347	-0.02294	0.000916
120.0	0.08499	0.01843	-0.03649	0.001013
130.0	0.08024	0.02999	-0.04754	0.000947
140.0	0.07661	0.04230	-0.05627	0.000756
150.0	0.07399	0.05373	-0.06283	0.000500
160.0	0.07225	0.06294	-0.06739	0.000248
170.0	0.07126	0.06889	-0.07006	0.000066
180.0	0.07095	0.07095	-0.07095	0

Table T.88

$m = 1.7800 - 0.0024i$
 $\lambda = 3.3 \text{ cm}$

Model: Rain L (ice)
 $x: 0.005(0.005)1.2$

$\beta_{\text{ex}} = 0.0001070 \text{ km}^{-1}$
 $\varpi = 0.3855$

θ	$P_1/4\pi$	$P_2/4\pi$	$P_3/4\pi$	$P_4/4\pi$
0.0	0.1258	0.1258	0.1258	0
10.0	0.1257	0.1220	0.1238	0.000000
20.0	0.1254	0.1110	0.1180	0.000003
30.0	0.1249	0.09414	0.1084	0.000007
40.0	0.1242	0.07358	0.09560	0.000012
50.0	0.1234	0.05179	0.07994	0.000017
60.0	0.1225	0.03141	0.06201	0.000022
70.0	0.1214	0.01484	0.04244	0.000025
80.0	0.1203	0.003990	0.02188	0.000028
90.0	0.1192	0.000020	0.001003	0.000028
100.0	0.1181	0.003248	-0.01956	0.000027
110.0	0.1171	0.01312	-0.03919	0.000025
120.0	0.1161	0.02832	-0.05735	0.000021
130.0	0.1153	0.04692	-0.07355	0.000016
140.0	0.1146	0.06663	-0.08737	0.000011
150.0	0.1140	0.08508	-0.09847	0.000007
160.0	0.1135	0.1001	-0.1066	0.000003
170.0	0.1133	0.1098	-0.1115	0.000000
180.0	0.1132	0.1132	-0.1132	0

Table T.89

$m = 1.78 - 0.0024i$
 $\lambda = 0.2 \text{ cm}$

Model: Hail H (ice)
 $x: 0.10(0.10)4(0.20)44$

$\beta_{\text{ex}} = 0.2441 \text{ km}^{-1}$
 $\varpi = 0.9563$

θ	$P_1/4\pi$	$P_2/4\pi$	$P_3/4\pi$	$P_4/4\pi$
0.0	3.705	3.705	3.705	0
2.5	3.450	3.453	3.451	-0.02059
5.0	2.815	2.825	2.818	-0.06528
7.5	2.072	2.087	2.073	-0.1025
10.0	1.431	1.447	1.426	-0.1159
12.5	0.9657	0.9788	0.9535	-0.1086
15.0	0.6604	0.6687	0.6411	-0.09110
17.5	0.4692	0.4726	0.4448	-0.07174
20.0	0.3507	0.3499	0.3234	-0.05451
30.0	0.1662	0.1597	0.1413	-0.01709
40.0	0.1063	0.1043	0.08850	-0.005639
50.0	0.07485	0.07878	0.06277	-0.001908
60.0	0.05092	0.06135	0.04322	0.000528
70.0	0.03744	0.04883	0.03136	0.001422
80.0	0.02588	0.03933	0.02098	0.002233
90.0	0.01983	0.03182	0.01481	0.003149
100.0	0.01440	0.02700	0.009753	0.002570
110.0	0.01194	0.02328	0.006396	0.003171
120.0	0.01098	0.02068	0.004365	0.003033
130.0	0.01133	0.02020	0.004188	0.003290
140.0	0.01396	0.02090	0.003013	0.003081
150.0	0.01965	0.02127	0.004329	-0.001455
160.0	0.03634	0.03835	-0.006898	-0.01235
162.5	0.04501	0.05143	-0.01806	-0.01647
165.0	0.05816	0.06994	-0.03663	-0.02166
167.5	0.07961	0.09634	-0.06612	-0.02671
170.0	0.1143	0.1336	-0.1097	-0.02897
172.5	0.1649	0.1825	-0.1670	-0.02553
175.0	0.2259	0.2371	-0.2297	-0.01599
177.5	0.2790	0.2826	-0.2807	-0.004963
180.0	0.3006	0.3006	-0.3006	0

Table T.90

$m = 1.78 - 0.0024i$
 $\lambda = 0.5 \text{ cm}$

Model: Hail H (ice)
 $x: 0.05(0.05)2(0.10)18$

$\beta_{\text{ex}} = 0.3044 \text{ km}^{-1}$
 $w = 0.9843$

θ	$P_1/4\pi$	$P_2/4\pi$	$P_3/4\pi$	$P_4/4\pi$
0.0	0.8141	0.8141	0.8141	0
5.0	0.7780	0.7796	0.7787	-0.005145
10.0	0.6832	0.6888	0.6851	-0.01741
15.0	0.5605	0.5710	0.5621	-0.03005
20.0	0.4393	0.4538	0.4389	-0.03778
30.0	0.2557	0.2742	0.2510	-0.03585
40.0	0.1513	0.1703	0.1461	-0.02395
50.0	0.09455	0.1130	0.09036	-0.01381
60.0	0.06247	0.07976	0.05885	-0.007341
70.0	0.04319	0.05906	0.03974	-0.003429
80.0	0.03112	0.04556	0.02763	-0.000948
90.0	0.02369	0.03681	0.01993	0.000609
100.0	0.01886	0.03141	0.01495	0.001608
110.0	0.01621	0.02876	0.01197	0.002399
120.0	0.01488	0.02865	0.01037	0.002805
130.0	0.01431	0.03064	0.009437	0.002191
140.0	0.01396	0.03263	0.007287	-0.001900
150.0	0.01570	0.03278	-0.000888	-0.01121
160.0	0.03080	0.04083	-0.02556	-0.01770
162.5	0.03851	0.04648	-0.03536	-0.01707
165.0	0.04781	0.05382	-0.04632	-0.01532
167.5	0.05827	0.06252	-0.05792	-0.01260
170.0	0.06914	0.07189	-0.06937	-0.009266
172.5	0.07937	0.08093	-0.07975	-0.005809
175.0	0.08781	0.08850	-0.08807	-0.002790
177.5	0.09339	0.09356	-0.09347	-0.000731
180.0	0.09534	0.09534	-0.09534	0

Table T.9I

$m = 1.78 - 0.0024i$
 $\lambda = 1.0 \text{ cm}$

Model: Hail H (ice)
 $x: 0.025(0.025)1(0.05)9$

$\beta_{\text{ex}} = 0.2002 \text{ km}^{-1}$
 $\varpi = 0.9905$

θ	$P_1/4\pi$	$P_2/4\pi$	$P_3/4\pi$	$P_4/4\pi$
0.0	0.4539	0.4539	0.4539	0
5.0	0.4472	0.4468	0.4470	-0.001078
10.0	0.4279	0.4266	0.4272	-0.004085
15.0	0.3983	0.3955	0.3967	-0.008413
20.0	0.3614	0.3569	0.3585	-0.01325
25.0	0.3207	0.3143	0.3162	-0.01779
30.0	0.2791	0.2711	0.2729	-0.02142
40.0	0.2024	0.1924	0.1929	-0.02483
50.0	0.1419	0.1318	0.1301	-0.02350
60.0	0.09859	0.08981	0.08566	-0.01940
70.0	0.06922	0.06265	0.05614	-0.01444
80.0	0.04977	0.04575	0.03711	-0.009774
90.0	0.03686	0.03555	0.02489	-0.005879
100.0	0.02808	0.02964	0.01684	-0.002890
110.0	0.02177	0.02640	0.01108	-0.000862
120.0	0.01689	0.02464	0.006264	0.000078
130.0	0.01302	0.02341	0.001391	-0.000194
140.0	0.01066	0.02220	-0.004155	-0.001427
150.0	0.01111	0.02132	-0.01045	-0.002598
160.0	0.01523	0.02161	-0.01685	-0.002410
170.0	0.02105	0.02303	-0.02192	-0.000918
180.0	0.02389	0.02389	-0.02389	0

Table T.92

$m = 1.78 - 0.0024i$
 $\lambda = 2.0 \text{ cm}$

Model: Hail H (ice)
 $x: 0.025(0.025)1(0.05)5$

$\beta_{ex} = 0.03943 \text{ km}^{-1}$
 $\varpi = 0.9860$

θ	$P_1/4\pi$	$P_2/4\pi$	$P_3/4\pi$	$P_4/4\pi$
0.0	0.2576	0.2576	0.2576	0
20.0	0.2394	0.2245	0.2318	-0.002011
40.0	0.1945	0.1488	0.1693	-0.005546
60.0	0.1431	0.07501	0.1001	-0.006624
80.0	0.09954	0.02931	0.04460	-0.004430
100.0	0.06867	0.01246	0.007318	-0.001062
120.0	0.04964	0.01406	-0.01535	0.001153
140.0	0.04000	0.02340	-0.02811	0.001396
160.0	0.03668	0.03250	-0.03435	0.000521
180.0	0.03616	0.03616	-0.03616	0

Table T.93

$m = 1.78 - 0.0024i$
 $\lambda = 3.3 \text{ cm}$

Model: Hail H (ice)
 $x: 0.01(0.01)3$

$\beta_{\text{ex}} = 0.006448 \text{ km}^{-1}$
 $\varpi = 0.9656$

θ	$P_1/4\pi$	$P_2/4\pi$	$P_3/4\pi$	$P_4/4\pi$
0.0	0.1763	0.1763	0.1763	0
20.0	0.1713	0.1549	0.1629	0.000044
40.0	0.1580	0.1027	0.1272	0.000229
60.0	0.1397	0.04640	0.07979	0.000604
80.0	0.1206	0.009887	0.03186	0.001045
100.0	0.1037	0.002335	-0.008939	0.001292
120.0	0.09059	0.01820	-0.03949	0.001157
140.0	0.08157	0.04414	-0.05979	0.000701
160.0	0.07642	0.06624	-0.07114	0.000209
180.0	0.07476	0.07476	-0.07476	0

Table T.94

$m = 1.78 - 0.0024i$
 $\lambda = 8.0 \text{ cm}$

Model: Hail H (ice)
 $x: 0.005(0.005)1.25$

$\beta_{\text{ex}} = 0.0002578 \text{ km}^{-1}$
 $\varpi = 0.7090$

θ	$P_1/4\pi$	$P_2/4\pi$	$P_3/4\pi$	$P_4/4\pi$
0.0	0.1283	0.1283	0.1283	0
20.0	0.1277	0.1131	0.1202	0.000004
40.0	0.1261	0.07492	0.09719	0.000014
60.0	0.1236	0.03200	0.06290	0.000026
80.0	0.1207	0.004135	0.02232	0.000033
100.0	0.1177	0.003112	-0.01911	0.000033
120.0	0.1149	0.02774	-0.05646	0.000025
140.0	0.1127	0.06533	-0.08581	0.000014
160.0	0.1113	0.09801	-0.1045	0.000004
180.0	0.1108	0.1108	-0.1108	0

Table T.95

$m = 4.2214 - 2.5259i$ Model: Hail H (0°C water) $\beta_{\text{ex}} = 0.2594 \text{ km}^{-1}$
 $\lambda = 1.0 \text{ cm}$ $x: 0.025(0.025)1(0.05)9$ $w = 0.05872$

θ	$P_1/4\pi$	$P_2/4\pi$	$P_3/4\pi$	$P_4/4\pi$
0.0	0.3016	0.3016	0.3016	0
10.0	0.2881	0.2786	0.2831	-0.01070
20.0	0.2536	0.2226	0.2342	-0.03545
30.0	0.2103	0.1598	0.1705	-0.05930
40.0	0.1693	0.1100	0.1080	-0.07199
50.0	0.1358	0.07847	0.05665	-0.07231
60.0	0.1106	0.06122	0.01949	-0.06446
70.0	0.09222	0.05241	-0.005023	-0.05330
80.0	0.07893	0.04770	-0.02017	-0.04210
90.0	0.06930	0.04473	-0.02913	-0.03236
100.0	0.06232	0.04253	-0.03437	-0.02447
110.0	0.05731	0.04086	-0.03758	-0.01824
120.0	0.05381	0.03986	-0.03981	-0.01333
130.0	0.05147	0.03978	-0.04170	-0.009396
140.0	0.05001	0.04083	-0.04354	-0.006199
150.0	0.04921	0.04294	-0.04539	-0.003620
160.0	0.04884	0.04557	-0.04706	-0.001667
170.0	0.04871	0.04781	-0.04825	-0.000428
180.0	0.04869	0.04869	-0.04869	0

Table T.96

$m = 7.1755 - 2.8642i$ Model: Hail H (0°C water) $\beta_{\text{ex}} = 0.09053 \text{ km}^{-1}$
 $\lambda = 3.3 \text{ cm}$ $x: 0.01(0.01)3$ $\varpi = 0.3503$

θ	$P_1/4\pi$	$P_2/4\pi$	$P_3/4\pi$	$P_4/4\pi$
0.0	0.09493	0.09493	0.09493	0
20.0	0.09484	0.08199	0.08803	-0.004993
40.0	0.09538	0.05160	0.06790	-0.01684
60.0	0.09809	0.02274	0.03658	-0.02853
80.0	0.1038	0.01224	-0.002062	-0.03397
100.0	0.1120	0.02595	-0.04285	-0.03120
120.0	0.1211	0.05805	-0.08049	-0.02232
140.0	0.1291	0.09580	-0.1105	-0.01156
160.0	0.1345	0.1254	-0.1298	-0.003144
180.0	0.1364	0.1364	-0.1364	0

Table T.97

$m = 8.7889 - 1.7531i$ Model: Hail H (0°C water) $\beta_{\text{ex}} = 0.01847 \text{ km}^{-1}$
 $\lambda = 8.0 \text{ cm}$ $x: 0.005(0.005)1.25$ $\varpi = 0.07287$

θ	$P_1/4\pi$	$P_2/4\pi$	$P_3/4\pi$	$P_4/4\pi$
0.0	0.1079	0.1079	0.1079	0
20.0	0.1058	0.09688	0.1011	-0.004334
40.0	0.1008	0.06960	0.08140	-0.01519
60.0	0.09606	0.04011	0.05081	-0.02723
80.0	0.09479	0.02363	0.01262	-0.03469
100.0	0.09889	0.02897	-0.02881	-0.03415
120.0	0.1077	0.05457	-0.06847	-0.02602
140.0	0.1185	0.08959	-0.1013	-0.01416
160.0	0.1272	0.1191	-0.1230	-0.003979
180.0	0.1305	0.1305	-0.1305	0

Table T.98

$m = 1.55$
 $\lambda = 0.589 \mu$

Model: Silicate haze M
 $x: 0.10(0.10)12.0(0.20)56$

$\beta_{\text{ex}} = 0.1085 \text{ km}^{-1}$
 $\varpi = 1.0$

θ	$P_1/4\pi$	$P_2/4\pi$	$P_3/4\pi$	$P_4/4\pi$
0.0	6.022	6.022	6.022	0
2.5	4.850	4.857	4.853	-0.03756
5.0	3.070	3.084	3.073	-0.07453
7.5	1.911	1.926	1.909	-0.08072
10.0	1.248	1.261	1.242	-0.07312
12.5	0.8676	0.8779	0.8575	-0.06140
15.0	0.6395	0.6476	0.6272	-0.04928
17.5	0.4945	0.5013	0.4819	-0.03820
20.0	0.3963	0.4022	0.3846	-0.02938
30.0	0.2032	0.2111	0.1970	-0.01021
40.0	0.1201	0.1310	0.1168	-0.002534
50.0	0.07530	0.08666	0.07272	0.000745
60.0	0.04882	0.05922	0.04595	0.002077
70.0	0.03239	0.04119	0.02877	0.002592
80.0	0.02198.	0.02951	0.01781	0.002502
90.0	0.01527	0.02191	0.01108	0.002356
100.0	0.01111	0.01716	0.007086	0.002352
110.0	0.008818	0.01446	0.007422	0.002425
120.0	0.007938	0.01330	0.003399	0.002813
130.0	0.007956	0.01397	0.002795	0.003817
135.0	0.008502	0.01522	0.002767	0.004562
140.0	0.009607	0.01791	0.002784	0.005716
145.0	0.01150	0.02230	0.003082	0.007826
150.0	0.01498	0.02961	0.003075	0.01092
155.0	0.01982	0.04061	0.002312	0.01450
160.0	0.02703	0.05352	-0.001146	0.01664
165.0	0.03852	0.06394	-0.007299	0.01390
170.0	0.05647	0.08033	-0.02457	0.008314
175.0	0.08133	0.1008	-0.07119	-0.003157
180.0	0.1154	0.1154	-0.1154	0

Table T.99

$m = 1.55 - 0.0155i$ Model: Silicate haze M $\beta_{\text{ex}} = 0.1079 \text{ km}^{-1}$
 $\lambda = 0.589 \mu$ $x: 0.10(0.10)12.0(0.20)56$ $\varpi = 0.8090$

θ	$P_1/4\pi$	$P_2/4\pi$	$P_3/4\pi$	$P_4/4\pi$
0.0	7.345	7.345	7.345	0
2.5	5.894	5.901	5.898	-0.04848
5.0	3.691	3.705	3.696	-0.09716
7.5	2.259	2.272	2.260	-0.1049
10.0	1.442	1.452	1.439	-0.09328
12.5	0.9744	0.9817	0.9686	-0.07695
15.0	0.6957	0.7009	0.6877	-0.06148
17.5	0.5212	0.5250	0.5122	-0.04843
20.0	0.4062	0.4092	0.3971	-0.03796
30.0	0.1929	0.1968	0.1865	-0.01447
40.0	0.1108	0.1173	0.1068	-0.005275
50.0	0.06828	0.07387	0.06534	-0.001265
60.0	0.04371	0.05113	0.04091	0.000552
70.0	0.02882	0.03560	0.02581	0.001355
80.0	0.01961	0.02564	0.01635	0.001703
90.0	0.01384	0.01923	0.01041	0.001878
100.0	0.01025	0.01517	0.006682	0.002004
110.0	0.008094	0.01277	0.004379	0.002187
120.0	0.006947	0.01174	0.003034	0.002525
130.0	0.006677	0.01218	0.002400	0.003214
135.0	0.006915	0.01317	0.002314	0.003787
140.0	0.007467	0.01499	0.002378	0.004621
145.0	0.008431	0.01802	0.002562	0.005810
150.0	0.009833	0.02269	0.002708	0.007281
155.0	0.01138	0.02881	0.002349	0.008242
160.0	0.01244	0.03393	0.000478	0.006419
165.0	0.01445	0.03592	-0.004686	0.000634
170.0	0.02337	0.04145	-0.01873	-0.004401
175.0	0.04317	0.05258	-0.04473	-0.004767
180.0	0.06098	0.06098	-0.06098	0

Table T.100

$m = 1.55 - 0.1550i$
 $\lambda = 0.589 \mu$

Model: Silicate haze M
 $x: 0.10(0.10)12.0(0.20)56$

$\beta_{\text{ex}} = 0.1032 \text{ km}^{-1}$
 $\varpi = 0.5231$

θ	$P_1/4\pi$	$P_2/4\pi$	$P_3/4\pi$	$P_4/4\pi$
0.0	11.37	11.37	11.37	0
2.5	9.071	9.057	9.064	-0.07841
5.0	5.586	5.556	5.567	-0.1565
7.5	3.324	3.287	3.299	-0.1682
10.0	2.041	2.002	2.011	-0.1489
12.5	1.310	1.273	1.280	-0.1226
15.0	0.8804	0.8466	0.8502	-0.09809
17.5	0.6162	0.5827	0.5870	-0.07781
20.0	0.4472	0.4161	0.4193	-0.06174
30.0	0.1629	0.1401	0.1408	-0.02598
40.0	0.07872	0.06196	0.06112	-0.01222
50.0	0.04475	0.03211	0.03020	-0.006264
60.0	0.02820	0.01850	0.01575	-0.003392
70.0	0.01913	0.01164	0.008191	-0.001884
80.0	0.01376	0.008002	0.003945	-0.001041
90.0	0.01040	0.006038	0.001452	-0.000546
100.0	0.008204	0.005001	-0.000052	-0.000242
110.0	0.006733	0.004500	-0.000973	-0.000042
120.0	0.005729	0.004331	-0.001535	0.000100
130.0	0.005042	0.004388	-0.001870	0.000217
140.0	0.004564	0.004613	-0.002074	0.000306
150.0	0.004179	0.004808	-0.002282	0.000280
160.0	0.003805	0.004358	-0.002745	-0.000070
170.0	0.003786	0.003732	-0.003557	-0.000284
180.0	0.004066	0.004066	-0.004066	0

Table T.101

$m = 1.55$	Model: Silicate haze L			$\beta_{\text{ex}} = 0.05134 \text{ km}^{-1}$
$\lambda = 0.589 \mu$	$x: 0.1(0.1)10(0.2)34$			$\varpi = 1.0$
θ	$P_1/4\pi$	$P_2/4\pi$	$P_3/4\pi$	$P_4/4\pi$
0.0	2.042	2.042	2.042	0
2.5	1.939	1.941	1.940	-0.006291
5.0	1.688	1.693	1.690	-0.02026
7.5	1.393	1.402	1.395	-0.03364
10.0	1.124	1.136	1.125	-0.04222
12.5	0.9020	0.9161	0.9018	-0.04551
15.0	0.7280	0.7434	0.7266	-0.04471
17.5	0.5934	0.6093	0.5911	-0.04141
20.0	0.4889	0.5049	0.4864	-0.03697
30.0	0.2480	0.2632	0.2467	-0.01990
40.0	0.1396	0.1539	0.1387	-0.009576
50.0	0.08343	0.09559	0.08196	-0.003854
60.0	0.05266	0.06246	0.05034	-0.000974
70.0	0.03454	0.04248	0.03159	0.000678
80.0	0.02351	0.03017	0.02016	0.001509
90.0	0.01682	0.02270	0.01340	0.002050
100.0	0.01287	0.01819	0.009223	0.002547
110.0	0.01046	0.01580	0.006671	0.003090
120.0	0.009423	0.01527	0.005266	0.003797
130.0	0.009384	0.01678	0.004685	0.005094
140.0	0.01068	0.02192	0.004620	0.007124
150.0	0.01312	0.03322	0.004331	0.009927
160.0	0.01459	0.04676	-0.001769	0.005313
165.0	0.01732	0.05036	-0.01143	-0.002369
170.0	0.03041	0.05694	-0.03200	-0.007460
175.0	0.05908	0.07024	-0.06281	-0.004882
180.0	0.07964	0.07964	-0.07964	0

Table T.102

$m = 1.56$
 $\lambda = 0.45 \mu$

Model: Silicate haze H
 $x: 0.05(0.05)2(0.10)18$

$\beta_{\text{ex}} = 0.02913 \text{ km}^{-1}$
 $w = 1.0$

θ	$P_1/4\pi$	$P_2/4\pi$	$P_3/4\pi$	$P_4/4\pi$
0.0	1.146	1.146	1.146	0
5.0	1.086	1.088	1.087	-0.005779
10.0	0.9305	0.9385	0.9337	-0.01881
15.0	0.7360	0.7501	0.7405	-0.03061
20.0	0.5515	0.5698	0.5561	-0.03591
30.0	0.2897	0.3100	0.2930	-0.02988
40.0	0.1541	0.1719	0.1558	-0.01805
50.0	0.08722	0.1011	0.08737	-0.009362
60.0	0.05280	0.06317	0.05177	-0.004229
70.0	0.03404	0.04183	0.03222	-0.001341
80.0	0.02330	0.02938	0.02097	0.000339
90.0	0.01695	0.02201	0.01429	0.001413
100.0	0.01315	0.01777	0.01027	0.002224
110.0	0.01099	0.01573	0.007910	0.003005
120.0	0.009990	0.01563	0.006677	0.003970
130.0	0.009857	0.01790	0.006260	0.005297
140.0	0.009959	0.02328	0.006037	0.006657
150.0	0.008596	0.03031	0.003611	0.005290
160.0	0.007619	0.03308	-0.006426	-0.002364
165.0	0.01239	0.03352	-0.01596	-0.005602
170.0	0.02330	0.03595	-0.02765	-0.005199
175.0	0.03628	0.04010	-0.03803	-0.001940
180.0	0.04229	0.04229	-0.04229	0

Table T.103

$m = 1.54$
 $\lambda = 0.70 \mu$

Model: Silicate haze H
 $x: 0.05(0.05)2(0.10)14$

$\beta_{\text{ex}} = 0.02065 \text{ km}^{-1}$
 $w = 1.0$

θ	$P_1/4\pi$	$P_2/4\pi$	$P_3/4\pi$	$P_4/4\pi$
0.0	0.7824	0.7824	0.7824	0
5.0	0.7613	0.7609	0.7611	-0.002188
10.0	0.7022	0.7007	0.7014	-0.007934
15.0	0.6168	0.6137	0.6149	-0.01523
20.0	0.5192	0.5145	0.5158	-0.02187
30.0	0.3345	0.3274	0.3281	-0.02812
40.0	0.2006	0.1930	0.1923	-0.02519
50.0	0.1186	0.1118	0.1097	-0.01836
60.0	0.07201	0.06626	0.06330	-0.01170
70.0	0.04586	0.04125	0.03773	-0.006627
80.0	0.03097	0.02740	0.02346	-0.003112
90.0	0.02224	0.01969	0.01527	-0.000709
100.0	0.01697	0.01555	0.01041	0.001010
110.0	0.01368	0.01372	0.007380	0.002355
120.0	0.01150	0.01359	0.005266	0.003481
130.0	0.009772	0.01480	0.003272	0.004289
140.0	0.008055	0.01673	0.000454	0.004270
150.0	0.006841	0.01814	-0.004105	0.002786
160.0	0.008541	0.01830	-0.01029	0.000524
165.0	0.01117	0.01821	-0.01342	-0.000157
170.0	0.01449	0.01825	-0.01606	-0.000302
175.0	0.01734	0.01839	-0.01784	-0.000123
180.0	0.01847	0.01847	-0.01847	0

Table T.104

$m = 1.56$
 $\lambda = 0.45 \mu$

Model: Silicate cloud C.3
 $x: 7.125(0.125)27(0.25)47$

$\beta_{\text{ex}} = 2.896 \text{ km}^{-1}$
 $\varpi = 1.0$

θ	$P_1/4\pi$	$P_2/4\pi$	$P_3/4\pi$	$P_4/4\pi$
0.0	41.38	41.38	41.38	0
1.0	37.90	37.92	37.91	-0.1031
2.0	29.04	29.08	29.06	-0.3276
3.0	18.41	18.47	18.42	-0.4968
4.0	9.510	9.556	9.500	-0.4959
5.0	4.000	4.013	3.965	-0.3501
6.0	1.552	1.532	1.505	-0.1721
7.0	0.8704	0.8263	0.8232	-0.05429
8.0	0.7925	0.7338	0.7482	-0.01333
9.0	0.7538	0.6885	0.7096	-0.01380
10.0	0.6513	0.5873	0.6067	-0.01887
11.0	0.5397	0.4836	0.4983	-0.01560
12.0	0.4575	0.4123	0.4229	-0.008619
13.0	0.4032	0.3686	0.3757	-0.004534
14.0	0.3640	0.3387	0.3419	-0.004391
15.0	0.3331	0.3152	0.3143	-0.005253
20.0	0.2458	0.2320	0.2307	-0.007837
30.0	0.1617	0.1623	0.1548	0.003045
40.0	0.1001	0.1119	0.09947	0.000958
50.0	0.06229	0.07506	0.06290	0.002111
60.0	0.03860	0.05113	0.03930	0.001699
70.0	0.02734	0.03381	0.02319	0.003437
80.0	0.01706	0.02173	0.01126	0.002221
90.0	0.009683	0.01348	0.005059	0.000823
100.0	0.006575	0.008615	0.001615	0.000755
110.0	0.003973	0.005814	0.000126	-0.000092
120.0	0.004408	0.004517	-0.001122	0.000143

TABLE T.104

θ	$P_1/4\pi$	$P_2/4\pi$	$P_3/4\pi$	$P_4/4\pi$
130.0	0.003560	0.004086	-0.001123	0.000024
140.0	0.004317	0.005242	-0.001404	0.000622
142.0	0.004378	0.005280	-0.001238	0.000738
144.0	0.004186	0.006007	-0.000789	0.000891
146.0	0.004783	0.006074	-0.000644	0.001177
148.0	0.005085	0.006626	-0.000666	0.001956
150.0	0.005825	0.008506	-0.000425	0.002299
152.0	0.007986	0.009473	-0.000670	0.003832
154.0	0.009863	0.01265	-0.001478	0.005992
156.0	0.01482	0.01620	-0.002098	0.008898
158.0	0.02374	0.02161	-0.004382	0.01569
160.0	0.03632	0.03072	-0.008288	0.02348
162.0	0.05850	0.03729	-0.01460	0.03348
164.0	0.08790	0.04480	-0.02016	0.04516
166.0	0.1238	0.04858	-0.02295	0.05592
168.0	0.1558	0.04856	-0.02360	0.06054
170.0	0.1576	0.03456	-0.01800	0.03797
171.0	0.1637	0.02627	-0.003969	0.02198
172.0	0.1928	0.03215	0.02677	0.01596
173.0	0.2372	0.05774	0.07224	0.02187
174.0	0.2604	0.08977	0.1144	0.02612
175.0	0.2271	0.1052	0.1270	0.01170
176.0	0.1457	0.09579	0.09584	-0.01973
177.0	0.07159	0.07917	0.03177	-0.04385
178.0	0.05403	0.07839	-0.03726	-0.03917
179.0	0.08297	0.09361	-0.08611	-0.01415
180.0	0.1032	0.1032	-0.1032	0

Table T.105

 $m = 1.54$
 $\lambda = 0.70 \mu$

 Model: Silicate cloud C.3
 $x: 4.125(0.125)34$
 $\beta_{\text{ex}} = 2.995 \text{ km}^{-1}$
 $w = 1.0$

θ	$P_1/4\pi$	$P_2/4\pi$	$P_3/4\pi$	$P_4/4\pi$
0.0	17.81	17.81	17.81	0
1.0	17.16	17.16	17.16	-0.02628
2.0	15.34	15.35	15.34	-0.09518
3.0	12.71	12.73	12.71	-0.1812
4.0	9.729	9.754	9.730	-0.2538
5.0	6.865	6.894	6.858	-0.2897
6.0	4.457	4.485	4.439	-0.2805
7.0	2.677	2.697	2.648	-0.2338
8.0	1.526	1.533	1.489	-0.1673
9.0	0.8899	0.8804	0.8483	-0.1010
10.0	0.6014	0.5761	0.5591	-0.04941
11.0	0.5029	0.4662	0.4629	-0.01818
12.0	0.4797	0.4378	0.4433	-0.005165
13.0	0.4679	0.4272	0.4354	-0.003780
14.0	0.4444	0.4091	0.4154	-0.006965
15.0	0.4094	0.3809	0.3833	-0.009835
16.0	0.3712	0.3484	0.3473	-0.01043
17.0	0.3367	0.3174	0.3144	-0.009032
18.0	0.3087	0.2910	0.2877	-0.006854
20.0	0.2687	0.2527	0.2502	-0.003853
30.0	0.1632	0.1621	0.1547	0.000368
40.0	0.1033	0.1100	0.09986	0.002767
50.0	0.06309	0.07558	0.06331	0.002751
60.0	0.03940	0.05209	0.03963	0.003447
70.0	0.02676	0.03477	0.02341	0.003551
80.0	0.01813	0.02259	0.01235	0.002599

TABLE T.105

θ	$P_1/4\pi$	$P_2/4\pi$	$P_3/4\pi$	$P_4/4\pi$
90.0	0.01170	0.01582	0.006127	0.001702
100.0	0.007241	0.01041	0.002616	0.001082
110.0	0.005141	0.007464	0.000619	0.000520
120.0	0.004550	0.005953	-0.000535	0.000512
130.0	0.004013	0.005417	-0.000833	0.000636
140.0	0.004974	0.006422	-0.000899	0.001375
145.0	0.006295	0.008541	-0.000815	0.002807
150.0	0.009502	0.01257	-0.001033	0.005834
155.0	0.01989	0.02136	-0.003855	0.01400
160.0	0.04580	0.04000	-0.008127	0.03337
162.0	0.05687	0.04736	-0.01320	0.04034
164.0	0.06713	0.04808	-0.01830	0.04108
166.0	0.09236	0.04212	-0.01609	0.04391
168.0	0.1459	0.04769	0.000551	0.06433
170.0	0.1989	0.07537	0.02875	0.09469
171.0	0.2048	0.08908	0.04166	0.1016
172.0	0.1889	0.09498	0.04946	0.09645
173.0	0.1534	0.09005	0.04954	0.07881
174.0	0.1075	0.07616	0.04083	0.05279
175.0	0.06495	0.05942	0.02432	0.02586
176.0	0.03768	0.04703	0.002884	0.005451
177.0	0.03040	0.04328	-0.01956	-0.004509
178.0	0.03851	0.04722	-0.03896	-0.005252
179.0	0.05093	0.05362	-0.05201	-0.001901
180.0	0.05660	0.05660	-0.05660	0

Table T.106

$m = 2.20$
 $\lambda = 0.589 \mu$

Model: Limonite haze M
 $x: 0.10(0.10)12.0(0.20)56$

$\beta_{\text{ex}} = 0.1049 \text{ km}^{-1}$
 $\varpi = 1.0$

θ	$P_1/4\pi$	$P_2/4\pi$	$P_3/4\pi$	$P_4/4\pi$
0.0	5.916	5.916	5.916	0
2.5	4.721	4.739	4.728	-0.06663
5.0	2.917	2.950	2.921	-0.1316
7.5	1.757	1.786	1.747	-0.1404
10.0	1.107	1.123	1.081	-0.1259
12.5	0.7388	0.7446	0.7029	-0.1073
15.0	0.5211	0.5207	0.4802	-0.08970
17.5	0.3856	0.3830	0.3438	-0.07397
20.0	0.2978	0.2945	0.2572	-0.06026
30.0	0.1492	0.1429	0.1169	-0.02653
40.0	0.09559	0.09593	0.07412	-0.01303
50.0	0.06855	0.07419	0.05227	-0.006123
60.0	0.05184	0.06054	0.03972	-0.002003
70.0	0.03980	0.05167	0.03011	-0.000525
80.0	0.03143	0.04632	0.02325	0.001117
90.0	0.02546	0.03960	0.01647	0.002132
100.0	0.02140	0.03556	0.01161	0.002001
110.0	0.02019	0.03285	0.007488	0.003132
120.0	0.01952	0.02845	0.004489	0.002309
130.0	0.02191	0.02732	0.000441	0.000330
132.5	0.02296	0.02707	-0.000472	0.000028
135.0	0.02430	0.02682	-0.001417	-0.000276
137.5	0.02591	0.02658	-0.002438	-0.000531
140.0	0.02782	0.02647	-0.003544	-0.000848
142.5	0.02934	0.02675	-0.004961	-0.001576
145.0	0.03049	0.02783	-0.007096	-0.002601
147.5	0.03394	0.02938	-0.01006	-0.003257
150.0	0.03914	0.03142	-0.01354	-0.004026
152.5	0.04388	0.03420	-0.01743	-0.005298
155.0	0.04864	0.03794	-0.02224	-0.006734
157.5	0.05473	0.04300	-0.02866	-0.008047
160.0	0.06295	0.04965	-0.03724	-0.009102
162.5	0.07370	0.05846	-0.04857	-0.009859
165.0	0.08728	0.07046	-0.06348	-0.01010
167.5	0.1043	0.08682	-0.08286	-0.009753
170.0	0.1251	0.1088	-0.1074	-0.008775
172.5	0.1495	0.1363	-0.1368	-0.006898
175.0	0.1760	0.1672	-0.1689	-0.004170
177.5	0.2000	0.1965	-0.1979	-0.001334
180.0	0.2108	0.2108	-0.2108	0

Table T.107

$m = 2.20 - 0.0220i$ Model: Limonite haze M $\beta_{ex} = 0.1047 \text{ km}^{-1}$
 $\lambda = 0.589 \mu$ $x: 0.10(0.10)12.0(0.20)56$ $\varpi = 0.7478$

θ	$P_1/4\pi$	$P_2/4\pi$	$P_3/4\pi$	$P_4/4\pi$
0.0	7.816	7.816	7.816	0
2.5	6.228	6.239	6.233	-0.08535
5.0	3.827	3.847	3.831	-0.1709
7.5	2.279	2.294	2.273	-0.1849
10.0	1.406	1.412	1.390	-0.1652
12.5	0.9133	0.9106	0.8895	-0.1374
15.0	0.6252	0.6159	0.5957	-0.1114
17.5	0.4493	0.4355	0.4165	-0.08956
20.0	0.3374	0.3209	0.3028	-0.07210
30.0	0.1492	0.1319	0.1163	-0.03226
40.0	0.09084	0.07909	0.06340	-0.01618
50.0	0.06360	0.05770	0.04123	-0.008426
60.0	0.04731	0.04616	0.02906	-0.004156
70.0	0.03628	0.03921	0.02092	-0.001719
80.0	0.02853	0.03451	0.01490	-0.000329
90.0	0.02302	0.03098	0.01017	0.000473
100.0	0.01921	0.02831	0.006482	0.000891
110.0	0.01680	0.02626	0.003662	0.001018
120.0	0.01566	0.02460	0.001303	0.000656
130.0	0.01592	0.02333	-0.001030	-0.000310
135.0	0.01670	0.02292	-0.002405	-0.001034
140.0	0.01806	0.02289	-0.004193	-0.001852
145.0	0.02021	0.02357	-0.006727	-0.002734
150.0	0.02347	0.02521	-0.01042	-0.003704
155.0	0.02833	0.02812	-0.01585	-0.004755
160.0	0.03556	0.03287	-0.02398	-0.005680
165.0	0.04604	0.04051	-0.03610	-0.005956
170.0	0.05987	0.05260	-0.05282	-0.004809
175.0	0.07396	0.06950	-0.07123	-0.001989
180.0	0.08050	0.08050	-0.08050	0

Table T.108

$m = 2.20 - 0.2200i$
 $\lambda = 0.589 \mu$

Model: Limonite haze M
 $x: 0.10(0.10)12.0(0.20)56$

$\beta_{\text{ex}} = 0.1040 \text{ km}^{-1}$
 $\varpi = 0.5317$

θ	$P_1/4\pi$	$P_2/4\pi$	$P_3/4\pi$	$P_4/4\pi$
0.0	10.99	10.99	10.99	0
2.5	8.749	8.742	8.745	-0.1230
5.0	5.358	5.339	5.340	-0.2457
7.5	3.168	3.137	3.135	-0.2649
10.0	1.933	1.893	1.888	-0.2357
12.5	1.234	1.189	1.182	-0.1952
15.0	0.8255	0.7770	0.7700	-0.1573
17.5	0.5763	0.5266	0.5196	-0.1258
20.0	0.4180	0.3685	0.3616	-0.1008
30.0	0.1563	0.1133	0.1067	-0.04431
40.0	0.08128	0.04668	0.03932	-0.02197
50.0	0.05135	0.02413	0.01537	-0.01199
60.0	0.03648	0.01532	0.004982	-0.007007
70.0	0.02790	0.01166	-0.000222	-0.004291
80.0	0.02243	0.01021	-0.003112	-0.002717
90.0	0.01872	0.009772	-0.004830	-0.001764
100.0	0.01608	0.009814	-0.005901	-0.001174
110.0	0.01417	0.01005	-0.006597	-0.000823
120.0	0.01278	0.01025	-0.007096	-0.000664
130.0	0.01179	0.01021	-0.007559	-0.000695
140.0	0.01117	0.009895	-0.008156	-0.000881
150.0	0.01098	0.009730	-0.009038	-0.001018
160.0	0.01130	0.01019	-0.01027	-0.000842
170.0	0.01190	0.01140	-0.01160	-0.000331
180.0	0.01223	0.01223	-0.01223	0

Table T.109

$m = 2.20$
 $\lambda = 0.589 \mu$

Model: Limonite haze L
 $x: 0.0(0.1)10(0.2)34$

$\beta_{\text{ex}} = 0.05071 \text{ km}^{-1}$
 $\tau = 1.0$

θ	$P_1/4\pi$	$P_2/4\pi$	$P_3/4\pi$	$P_4/4\pi$
0.0	1.770	1.770	1.770	0
2.5	1.700	1.673	1.672	-0.01040
5.0	1.427	1.438	1.431	-0.03325
7.5	1.146	1.163	1.149	-0.05489
10.0	0.8956	0.9160	0.8947	-0.06900
12.5	0.6949	0.7163	0.6883	-0.07531
15.0	0.5423	0.5635	0.5300	-0.07554
17.5	0.4289	0.4489	0.4116	-0.07165
20.0	0.3456	0.3632	0.3239	-0.06536
30.0	0.1781	0.1844	0.1488	-0.03869
40.0	0.1102	0.1190	0.08636	-0.02285
50.0	0.07671	0.08758	0.05737	-0.01257
60.0	0.05749	0.06802	0.04224	-0.005435
70.0	0.04471	0.05686	0.03243	-0.002721
80.0	0.03556	0.05031	0.02529	-0.000990
90.0	0.02964	0.04373	0.01870	-0.001313
100.0	0.02509	0.04002	0.01360	-0.001312
110.0	0.02390	0.03817	0.009988	-0.002338
120.0	0.02279	0.03434	0.007061	-0.000789
130.0	0.02612	0.03349	0.002037	-0.002219
140.0	0.03333	0.03355	-0.003678	-0.004801
142.5	0.03519	0.03412	-0.005938	-0.005840
145.0	0.03747	0.03534	-0.008976	-0.007014
147.5	0.04092	0.03730	-0.01291	-0.008150
150.0	0.04567	0.04000	-0.01772	-0.009229
152.5	0.05123	0.04344	-0.02341	-0.01032
155.0	0.05725	0.04773	-0.03017	-0.01139
157.5	0.06385	0.05306	-0.03832	-0.01223
160.0	0.07146	0.05970	-0.04818	-0.01258
162.5	0.08054	0.06802	-0.06005	-0.01225
165.0	0.09137	0.07846	-0.07410	-0.01113
167.5	0.1039	0.09140	-0.09027	-0.009310
170.0	0.1179	0.1068	-0.1080	-0.007000
172.5	0.1323	0.1240	-0.1262	-0.004515
175.0	0.1455	0.1409	-0.1427	-0.002238
177.5	0.1553	0.1540	-0.1546	-0.000602
180.0	0.1590	0.1590	-0.1590	0

Table T.110

$m = 2.20$
 $\lambda = 0.45 \mu$

Model: Limonite cloud C.3
 $x: 7.125(0.125)27(0.25)47$

$\beta_{ex} = 2.876 \text{ km}^{-1}$
 $w = 1.0$

θ	$P_1/4\pi$	$P_2/4\pi$	$P_3/4\pi$	$P_4/4\pi$
0.0	40.98	40.98	40.98	0
1.0	37.54	37.57	37.56	-0.1631
2.0	28.76	28.85	28.80	-0.5164
3.0	18.24	18.36	18.25	-0.7786
4.0	9.413	9.503	9.366	-0.7692
5.0	3.941	3.952	3.826	-0.5327
6.0	1.498	1.428	1.347	-0.2494
7.0	0.8011	0.6871	0.6595	-0.06411
8.0	0.7053	0.5842	0.5915	-0.001619
9.0	0.6536	0.5434	0.5614	-0.006411
10.0	0.5463	0.4456	0.4611	-0.02102
11.0	0.4384	0.3397	0.3519	-0.02351
12.0	0.3660	0.2654	0.2783	-0.01787
13.0	0.3238	0.2224	0.2376	-0.01259
14.0	0.2953	0.1963	0.2126	-0.01092
15.0	0.2712	0.1770	0.1928	-0.01192
20.0	0.1848	0.1223	0.1295	-0.01439
30.0	0.1064	0.08798	0.08529	-0.003796
40.0	0.08064	0.07508	0.06779	-0.000976
50.0	0.06139	0.06631	0.05265	-0.000619
60.0	0.04728	0.05558	0.03936	0.000019
70.0	0.03387	0.04964	0.02938	0.001081
80.0	0.02538	0.04232	0.02002	0.001114
90.0	0.01869	0.03545	0.01236	0.001331
100.0	0.01532	0.02928	0.007521	0.001353
110.0	0.01342	0.02463	0.003011	0.001711
120.0	0.01412	0.01990	0.000154	0.001548
130.0	0.01390	0.01511	-0.002533	0.002231
140.0	0.01620	0.01122	-0.003913	0.002210
145.0	0.02012	0.01174	-0.006308	0.002396
150.0	0.02607	0.01165	-0.009242	0.002032
155.0	0.03433	0.01401	-0.01489	0.002216
160.0	0.04608	0.02138	-0.02528	0.001009
165.0	0.06929	0.03750	-0.04505	-0.002189
170.0	0.1186	0.08652	-0.09441	-0.008687
175.0	0.2453	0.2190	-0.2130	-0.01365
180.0	0.3874	0.3874	-0.3874	0

Table T.III

$m = 2.20$
 $\lambda = 0.70 \mu$

Model: Limonite cloud C.3
 $x: 4.125(0.125)34$

$\beta_{\text{ex}} = 2.963 \text{ km}^{-1}$
 $\varpi = 1.0$

θ	$P_1/4\pi$	$P_2/4\pi$	$P_3/4\pi$	$P_4/4\pi$
0.0	17.52	17.52	17.52	0
1.0	16.87	16.88	16.88	-0.04533
2.0	15.08	15.11	15.09	-0.1641
3.0	12.48	12.53	12.50	-0.3119
4.0	9.541	9.608	9.547	-0.4362
5.0	6.718	6.781	6.698	-0.4969
6.0	4.347	4.387	4.289	-0.4801
7.0	2.595	2.597	2.497	-0.3993
8.0	1.461	1.421	1.333	-0.2859
9.0	0.8309	0.7523	0.6886	-0.1738
10.0	0.5412	0.4359	0.4003	-0.08739
11.0	0.4375	0.3194	0.3093	-0.03599
12.0	0.4081	0.2895	0.2973	-0.01550
13.0	0.3910	0.2804	0.2966	-0.01466
14.0	0.3639	0.2654	0.2818	-0.02159
15.0	0.3270	0.2410	0.2530	-0.02808
16.0	0.2882	0.2130	0.2192	-0.03064
17.0	0.2545	0.1871	0.1890	-0.02935
18.0	0.2287	0.1664	0.1661	-0.02593
20.0	0.1954	0.1398	0.1395	-0.01900
30.0	0.1140	0.09235	0.08802	-0.006090
40.0	0.08154	0.07467	0.06644	-0.001533
50.0	0.06155	0.06574	0.05207	0.000148
60.0	0.04648	0.05715	0.03955	0.000764
70.0	0.03480	0.04957	0.02894	0.001249
80.0	0.02605	0.04256	0.02013	0.001636
90.0	0.01999	0.03626	0.01356	0.001803
100.0	0.01668	0.03115	0.009096	0.001888
110.0	0.01456	0.02555	0.004537	0.002038
120.0	0.01475	0.02089	0.001061	0.002040
130.0	0.01549	0.01729	-0.001658	0.001991
140.0	0.01783	0.01430	-0.004173	0.002435
145.0	0.02075	0.01448	-0.006168	0.002342
150.0	0.02610	0.01538	-0.01010	0.002064
155.0	0.03580	0.01778	-0.01590	0.000764
160.0	0.04809	0.02568	-0.02657	-0.000965
165.0	0.07205	0.04234	-0.04669	-0.005060
170.0	0.1247	0.1071	-0.09873	-0.009606
175.0	0.2301	0.2083	-0.2085	-0.008571
180.0	0.3286	0.3286	-0.3286	0

Table T.112

$m = 1.28 - 1.37i$
 $\lambda = 0.441 \mu$

Model: Iron haze M
 $x: 0.10(0.10)12(0.20)72$

$\beta_{\text{ex}} = 0.1034 \text{ km}^{-1}$
 $\varpi = 0.5946$

θ	$P_1/4\pi$	$P_2/4\pi$	$P_3/4\pi$	$P_4/4\pi$
0.0	17.75	17.75	17.75	0
2.5	12.39	12.00	12.19	-0.1735
5.0	6.385	5.785	6.065	-0.2647
7.5	3.372	2.822	3.062	-0.2309
10.0	1.922	1.477	1.656	-0.1718
12.5	1.181	0.8300	0.9593	-0.1206
15.0	0.7744	0.4967	0.5891	-0.08224
17.5	0.5367	0.3134	0.3796	-0.05491
20.0	0.3897	0.2068	0.2545	-0.03566
22.5	0.2943	0.1417	0.1761	-0.02212
25.0	0.2298	0.1003	0.1249	-0.01255
27.5	0.1847	0.07298	0.09031	-0.005752
30.0	0.1521	0.05447	0.06619	-0.000903
32.5	0.1279	0.04160	0.04891	0.002565
35.0	0.1095	0.03247	0.03623	0.005041
37.5	0.09520	0.02588	0.02672	0.006795
40.0	0.08394	0.02105	0.01944	0.008019
45.0	0.06750	0.01481	0.009275	0.009396
50.0	0.05628	0.01133	0.002726	0.009888
55.0	0.04827	0.009410	-0.001716	0.009863
60.0	0.04232	0.008408	-0.004869	0.009539
65.0	0.03775	0.007975	-0.007179	0.009046
70.0	0.03414	0.007898	-0.008918	0.008451
75.0	0.03123	0.008054	-0.01026	0.007805
80.0	0.02883	0.008360	-0.01131	0.007140
85.0	0.02682	0.008759	-0.01213	0.006473
90.0	0.02512	0.009218	-0.01279	0.005817
95.0	0.02366	0.009710	-0.01331	0.005185
100.0	0.02240	0.01022	-0.01372	0.004580
105.0	0.02130	0.01072	-0.01404	0.004008
110.0	0.02033	0.01122	-0.01430	0.003472
120.0	0.01875	0.01217	-0.01465	0.002514
130.0	0.01752	0.01301	-0.01484	0.001715
140.0	0.01660	0.01371	-0.01495	0.001073
150.0	0.01592	0.01428	-0.01501	0.000587
160.0	0.01547	0.01471	-0.01506	0.000251
170.0	0.01523	0.01501	-0.01512	0.000060
180.0	0.01515	0.01515	-0.01515	0

Table T.113

$m = 1.51 - 1.63i$
 $\lambda = 0.589 \mu$

Model: Iron haze M
 $x: 0.10(0.10)12(0.20)56$

$\beta_{\text{ex}} = 0.1083 \text{ km}^{-1}$
 $\tau = 0.5971$

θ	$P_1/4\pi$	$P_2/4\pi$	$P_3/4\pi$	$P_4/4\pi$
0.0	10.18	10.18	10.18	0
2.5	8.184	7.978	8.079	-0.1168
5.0	5.125	4.714	4.904	-0.2343
7.5	3.108	2.662	2.854	-0.2503
10.0	1.945	1.541	1.699	-0.2181
12.5	1.273	0.9303	1.050	-0.1750
15.0	0.8718	0.5859	0.6733	-0.1353
17.5	0.6221	0.3839	0.4462	-0.1029
20.0	0.4604	0.2606	0.3040	-0.07746
22.5	0.3519	0.1826	0.2119	-0.05796
25.0	0.2766	0.1316	0.1504	-0.04309
27.5	0.2229	0.09729	0.1081	-0.03175
30.0	0.1835	0.07364	0.07832	-0.02308
32.5	0.1540	0.05698	0.05691	-0.01643
35.0	0.1314	0.04504	0.04120	-0.01131
37.5	0.1138	0.03633	0.02946	-0.007358
40.0	0.09983	0.02990	0.02054	-0.004301
45.0	0.07944	0.02149	0.008281	-0.000099
50.0	0.06556	0.01670	0.000621	0.002411
55.0	0.05570	0.01394	-0.004387	0.003862
60.0	0.04843	0.01241	-0.007794	0.004643
65.0	0.04290	0.01162	-0.01018	0.004996
70.0	0.03859	0.01129	-0.01191	0.005065
75.0	0.03515	0.01127	-0.01318	0.004950
80.0	0.03235	0.01144	-0.01413	0.004719
85.0	0.03003	0.01173	-0.01485	0.004409
90.0	0.02810	0.01210	-0.01541	0.004055
95.0	0.02646	0.01252	-0.01583	0.003678
100.0	0.02505	0.01295	-0.01616	0.003292
105.0	0.02384	0.01340	-0.01641	0.002908
110.0	0.02280	0.01383	-0.01660	0.002536
120.0	0.02110	0.01466	-0.01685	0.001843
130.0	0.01982	0.01539	-0.01699	0.001244
140.0	0.01887	0.01601	-0.01708	0.000756
150.0	0.01822	0.01651	-0.01717	0.000389
160.0	0.01781	0.01693	-0.01729	0.000148
170.0	0.01762	0.01734	-0.01747	0.000029
180.0	0.01758	0.01758	-0.01758	0

Table T.114

$m = 1.70 - 1.84i$
 $\lambda = 0.668 \mu$

Model: Iron haze M
 $x: 0.10(0.10)12(0.20)52$

$\beta_{\text{ex}} = 0.1103 \text{ km}^{-1}$
 $\varpi = 0.6070$

θ	$P_1/4\pi$	$P_2/4\pi$	$P_3/4\pi$	$P_4/4\pi$
0.0	7.904	7.904	7.904	0
2.5	6.628	6.479	6.552	-0.09935
5.0	4.458	4.133	4.282	-0.2198
7.5	2.862	2.485	2.644	-0.2542
10.0	1.868	1.509	1.644	-0.2358
12.5	1.260	0.9449	1.048	-0.1994
15.0	0.8825	0.6127	0.6873	-0.1615
17.5	0.6402	0.4111	0.4626	-0.1281
20.0	0.4796	0.2848	0.3184	-0.1007
22.5	0.3699	0.2031	0.2233	-0.07873
25.0	0.2927	0.1488	0.1588	-0.06142
27.5	0.2370	0.1117	0.1140	-0.04783
30.0	0.1958	0.08579	0.08226	-0.03715
32.5	0.1647	0.06734	0.05929	-0.02874
35.0	0.1407	0.05397	0.04238	-0.02211
37.5	0.1220	0.04413	0.02973	-0.01685
40.0	0.1071	0.03679	0.02014	-0.01268
45.0	0.08519	0.02705	0.006999	-0.006702
50.0	0.07026	0.02137	-0.001130	-0.002871
55.0	0.05963	0.01800	-0.006367	-0.000425
60.0	0.05180	0.01602	-0.009867	0.001120
65.0	0.04586	0.01489	-0.01227	0.002069
70.0	0.04123	0.01432	-0.01396	0.002610
75.0	0.03756	0.01409	-0.01518	0.002876
80.0	0.03457	0.01410	-0.01607	0.002956
85.0	0.03212	0.01425	-0.01673	0.002906
90.0	0.03008	0.01451	-0.01722	0.002768
95.0	0.02835	0.01482	-0.01759	0.002575
100.0	0.02688	0.01516	-0.01786	0.002345
105.0	0.02562	0.01552	-0.01807	0.002095
110.0	0.02454	0.01589	-0.01823	0.001839
120.0	0.02280	0.01658	-0.01843	0.001334
130.0	0.02150	0.01720	-0.01855	0.000879
140.0	0.02056	0.01772	-0.01864	0.000503
150.0	0.01994	0.01817	-0.01877	0.000226
160.0	0.01958	0.01860	-0.01897	0.000060
170.0	0.01946	0.01911	-0.01927	0.000002
180.0	0.01945	0.01945	-0.01945	0

Table T.115

$m = 1.28 - 1.37i$
 $\lambda = 0.441 \mu$

Model: Iron haze L
 $x: 0.1(0.1)12(0.2)24$

$\beta_{\text{ex}} = 0.04835 \text{ km}^{-1}$
 $\varpi = 0.5604$

θ	$P_1/4\pi$	$P_2/4\pi$	$P_3/4\pi$	$P_4/4\pi$
0.0	5.194	5.194	5.194	0
2.5	4.807	4.737	4.771	-0.93363
5.0	3.873	3.659	3.762	-0.1014
7.5	2.844	2.526	2.673	-0.1486
10.0	2.019	1.668	1.821	-0.1593
12.5	1.440	1.099	1.238	-0.1484
15.0	1.043	0.7313	0.8485	-0.1290
17.5	0.7695	0.4940	0.5884	-0.1071
20.0	0.5807	0.3406	0.4146	-0.08649
22.5	0.4478	0.2394	0.2962	-0.06868
25.0	0.3524	0.1717	0.2143	-0.05368
27.5	0.2829	0.1256	0.1569	-0.04145
30.0	0.2312	0.09362	0.1158	-0.03162
32.5	0.1921	0.07111	0.08596	-0.02372
35.0	0.1620	0.05501	0.06401	-0.01744
37.5	0.1386	0.04329	0.04756	-0.01247
40.0	0.1200	0.03470	0.03509	-0.008517
45.0	0.09304	0.02350	0.01807	-0.002942
50.0	0.07485	0.01714	0.007557	0.000519
55.0	0.06208	0.01346	0.000783	0.002610
60.0	0.05278	0.01135	-0.003742	0.003816
65.0	0.04581	0.01019	-0.006858	0.004453
70.0	0.04044	0.009623	-0.009067	0.004710
75.0	0.03621	0.009439	-0.01067	0.004718
80.0	0.03281	0.009505	-0.01184	0.004567
90.0	0.02774	0.01006	-0.01339	0.003991
100.0	0.02418	0.01088	-0.01427	0.003265
110.0	0.02159	0.01178	-0.01478	0.002525
120.0	0.01967	0.01265	-0.01506	0.001840
130.0	0.01825	0.01342	-0.01521	0.001248
140.0	0.01720	0.01409	-0.01530	0.000766
150.0	0.01647	0.01463	-0.01538	0.000403
160.0	0.01600	0.01509	-0.01549	0.000162
170.0	0.01577	0.01549	-0.01562	0.000036
180.0	0.01570	0.01570	-0.01570	0

Table T.116

$m = 1.70 - 1.84i$
 $\lambda = 0.668 \mu$

Model: Iron haze L
 $x: 0.05(0.05)6(0.1)18$

$\beta_{\text{ex}} = 0.05190 \text{ km}^{-1}$
 $\omega = 0.5736$

θ	$P_1/4\pi$	$P_2/4\pi$	$P_3/4\pi$	$P_4/4\pi$
0.0	2.395	2.395	2.395	0
2.5	2.306	2.284	2.295	-0.01571
5.0	2.069	1.992	2.029	-0.05415
7.5	1.753	1.616	1.679	-0.09639
10.0	1.431	1.248	1.327	-0.1271
12.5	1.147	0.9415	1.022	-0.1417
15.0	0.9167	0.7047	0.7796	-0.1438
17.5	0.7353	0.5276	0.5924	-0.1379
20.0	0.5937	0.3968	0.4494	-0.1276
22.5	0.4836	0.3009	0.3411	-0.1150
25.0	0.3979	0.2308	0.2593	-0.1018
27.5	0.3311	0.1792	0.1974	-0.08908
30.0	0.2784	0.1409	0.1552	-0.07735
32.5	0.2365	0.1124	0.1140	-0.06674
35.0	0.2030	0.09104	0.08625	-0.05734
37.5	0.1759	0.07482	0.06473	-0.04916
40.0	0.1538	0.06242	0.04794	-0.04206
50.0	0.09751	0.03514	0.009559	-0.02228
60.0	0.06861	0.02457	-0.006252	-0.01166
70.0	0.05216	0.02022	-0.01326	-0.005998
80.0	0.04203	0.01847	-0.01654	-0.002999
90.0	0.03539	0.01790	-0.01812	-0.001449
100.0	0.03083	0.01787	-0.01889	-0.000691
110.0	0.02761	0.01808	-0.01927	-0.000368
120.0	0.02531	0.01838	-0.01947	-0.000270
130.0	0.02368	0.01870	-0.01962	-0.000269
140.0	0.02258	0.01902	-0.01982	-0.000284
150.0	0.02190	0.01944	-0.02015	-0.000263
160.0	0.02159	0.02009	-0.02065	-0.000181
170.0	0.02152	0.02100	-0.02124	-0.000062
180.0	0.02153	0.02153	-0.02153	0

Table T.II7

$m = 2.660 - 2.840i$
 $\lambda = 0.441 \mu$

Model: Iron haze L
 $x: 0.10(0.10)12(0.20)36$

$\beta_{\text{ex}} = 0.04782 \text{ km}^{-1}$
 $w = 0.7401$

θ	$P_1/4\pi$	$P_2/4\pi$	$P_3/4\pi$	$P_4/4\pi$
0.0	4.089	4.089	4.089	0
2.5	3.715	3.662	3.687	-0.07410
5.0	2.894	2.751	2.810	-0.2057
7.5	2.092	1.899	1.960	-0.2848
10.0	1.484	1.282	1.322	-0.3019
12.5	1.060	0.8719	0.8842	-0.2818
15.0	0.7719	0.6055	0.5923	-0.2463
20.0	0.4405	0.3168	0.2694	-0.1719
25.0	0.2772	0.1854	0.1224	-0.1150
30.0	0.1900	0.1200	0.05177	-0.07652
35.0	0.1396	0.08467	0.01603	-0.05124
40.0	0.1085	0.06421	-0.002878	-0.03463
45.0	0.08822	0.05168	-0.01328	-0.02361
50.0	0.07427	0.04367	-0.01916	-0.01618
60.0	0.05698	0.03479	-0.02454	-0.007609
70.0	0.04709	0.03060	-0.02640	-0.003444
80.0	0.04091	0.02856	-0.02699	-0.001401
90.0	0.03680	0.02758	-0.02712	-0.000435
100.0	0.03393	0.02715	-0.02707	-0.000035
120.0	0.03042	0.02696	-0.02686	0.000006
140.0	0.02874	0.02702	-0.02684	-0.000222
160.0	0.02849	0.02736	-0.02757	-0.000245
180.0	0.02908	0.02908	-0.02908	0

Table T.118

$m = 3.460 - 3.880i$
 $\lambda = 0.589 \mu$

Model: Iron haze L
 $x: 0.05(0.05)8(0.10)32$

$\beta_{\text{ex}} = 0.04788 \text{ km}^{-1}$
 $\varpi = 0.7205$

θ	$P_1/4\pi$	$P_2/4\pi$	$P_3/4\pi$	$P_4/4\pi$
0.0	2.390	2.390	2.390	0
2.5	2.257	2.239	2.248	-0.03316
5.0	1.931	1.877	1.900	-0.1051
7.5	1.553	1.466	1.494	-0.1702
10.0	1.214	1.107	1.129	-0.2084
12.5	0.9402	0.8266	0.8357	-0.2206
15.0	0.7311	0.6192	0.6122	-0.2149
20.0	0.4577	0.3599	0.3245	-0.1791
25.0	0.3043	0.2236	0.1696	-0.1377
30.0	0.2150	0.1491	0.08527	-0.1027
35.0	0.1604	0.1063	0.03823	-0.07599
40.0	0.1254	0.08055	0.01132	-0.05634
45.0	0.1018	0.06429	-0.004437	-0.04204
50.0	0.08541	0.05363	-0.01384	-0.03163
60.0	0.06468	0.04140	-0.02302	-0.01839
70.0	0.05265	0.03529	-0.02646	-0.01108
80.0	0.04509	0.03205	-0.02768	-0.006906
90.0	0.04006	0.03027	-0.02804	-0.004470
100.0	0.03657	0.02928	-0.02806	-0.003021
120.0	0.03238	0.02838	-0.02789	-0.001615
140.0	0.03049	0.02810	-0.02806	-0.000998
160.0	0.03026	0.02876	-0.02920	-0.000447
180.0	0.03074	0.03074	-0.03074	0

Table T.119

$m = 3.57 - 4.03i$
 $\lambda = 0.668 \mu$

Model: Iron haze L
 $x: 0.05(0.05)6(0.10)26$

$\beta_{\text{ex}} = 0.04810 \text{ km}^{-1}$
 $\varpi = 0.7227$

θ	$P_1/4\pi$	$P_2/4\pi$	$P_3/4\pi$	$P_4/4\pi$
0.0	1.871	1.871	1.871	0
2.5	1.790	1.778	1.784	-0.02294
5.0	1.582	1.543	1.560	-0.07644
7.5	1.323	1.257	1.279	-0.1313
10.0	1.074	0.9879	1.008	-0.1696
12.5	0.8610	0.7652	0.7761	-0.1886
15.0	0.6897	0.5914	0.5894	-0.1920
20.0	0.4520	0.3608	0.3326	-0.1721
25.0	0.3099	0.2316	0.1837	-0.1401
30.0	0.2234	0.1580	0.09775	-0.1094
35.0	0.1688	0.1144	0.04756	-0.08405
40.0	0.1329	0.08753	0.01776	-0.06433
45.0	0.1084	0.07029	-0.000249	-0.04935
50.0	0.09103	0.05883	-0.01129	-0.03807
60.0	0.06889	0.04542	-0.02242	-0.02315
70.0	0.05591	0.03850	-0.02677	-0.01453
80.0	0.04770	0.03467	-0.02840	-0.009423
90.0	0.04223	0.03246	-0.02893	-0.006326
100.0	0.03846	0.03112	-0.02902	-0.004401
120.0	0.03396	0.02975	-0.02891	-0.002383
140.0	0.03201	0.02927	-0.02923	-0.001380
160.0	0.03185	0.03012	-0.03067	-0.000556
180.0	0.03236	0.03236	-0.03236	0

Table T.120

$m = 1.28 - 1.37i$
 $\lambda = 0.441 \mu$

Model: Iron haze H
 $x: 0.05(0.05)2(0.10)18$

$\beta_{\text{ex}} = 0.02684 \text{ km}^{-1}$
 $\varpi = 0.5195$

θ	$P_1/4\pi$	$P_2/4\pi$	$P_3/4\pi$	$P_4/4\pi$
0.0	1.572	1.572	1.572	0
5.0	1.483	1.447	1.465	-0.01679
10.0	1.257	1.139	1.195	-0.05407
15.0	0.9758	0.7856	0.8691	-0.08662
20.0	0.7138	0.4907	0.5780	-0.09953
30.0	0.3571	0.1665	0.2153	-0.07772
40.0	0.1865	0.06012	0.06978	-0.04266
50.0	0.1091	0.02814	0.01747	-0.01972
60.0	0.07160	0.01762	-0.001886	-0.007894
70.0	0.05160	0.01381	-0.009677	-0.002346
80.0	0.03988	0.01254	-0.01311	0.000076
100.0	0.02751	0.01275	-0.01552	0.001191
120.0	0.02158	0.01396	-0.01605	0.000807
140.0	0.01859	0.01505	-0.01619	0.000284
160.0	0.01729	0.01606	-0.01658	0.000023
180.0	0.01700	0.01700	-0.01700	0

Table T.121

$m = 1.70 - 1.84i$
 $\lambda = 0.668 \mu$

Model: Iron haze H
 $x: 0.05(0.05)2(0.10)14$

$\beta_{\text{ex}} = 0.02871 \text{ km}^{-1}$
 $w = 0.5336$

θ	$P_1/4\pi$	$P_2/4\pi$	$P_3/4\pi$	$P_4/4\pi$
0.0	0.7189	0.7189	0.7189	0
5.0	0.7008	0.6895	0.6951	-0.006892
10.0	0.6502	0.6094	0.6288	-0.02487
15.0	0.5771	0.4997	0.5342	-0.04740
20.0	0.4938	0.3842	0.4282	-0.06745
30.0	0.3356	0.1987	0.2360	-0.08506
40.0	0.2194	0.09810	0.1077	-0.07527
50.0	0.1457	0.05478	0.03801	-0.05533
60.0	0.1012	0.03766	0.004203	-0.03706
70.0	0.07422	0.03057	-0.01118	-0.02388
80.0	0.05742	0.02718	-0.01788	-0.01529
100.0	0.03935	0.02406	-0.02173	-0.006620
120.0	0.03106	0.02253	-0.02226	-0.003259
140.0	0.02736	0.02195	-0.02298	-0.001678
160.0	0.02617	0.02377	-0.02478	-0.000550
180.0	0.02604	0.02604	-0.02604	0

Table T.122

$m = 2.66 - 3.84i$
 $\lambda = 0.441 \mu$

Model: Iron haze H
 $x: 0.05(0.05)2(0.10)18$

$\beta_{ex} = 0.02633 \text{ km}^{-1}$
 $\varpi = 0.7243$

θ	$P_1/4\pi$	$P_2/4\pi$	$P_3/4\pi$	$P_4/4\pi$
0.0	1.088	1.088	1.088	0
5.0	1.028	1.006	1.016	-0.02685
10.0	0.8746	0.8032	0.8324	-0.08694
15.0	0.6851	0.5734	0.6054	-0.1407
20.0	0.5094	0.3842	0.3974	-0.1641
30.0	0.2708	0.1751	0.1300	-0.1351
40.0	0.1548	0.09813	0.02187	-0.08169
50.0	0.1001	0.06663	-0.01440	-0.04483
60.0	0.07219	0.05084	-0.02544	-0.02444
70.0	0.05656	0.04195	-0.02836	-0.01373
80.0	0.04707	0.03671	-0.02876	-0.008075
100.0	0.03683	0.03159	-0.02796	-0.003343
120.0	0.03207	0.02942	-0.02717	-0.001893
140.0	0.03023	0.02804	-0.02715	-0.001334
160.0	0.03056	0.02838	-0.02906	-0.000633
180.0	0.03140	0.03140	-0.03140	0

Table T.123

$m = 3.57 - 4.03i$
 $\lambda = 0.668 \mu$

Model: Iron haze H
 $x: 0.05(0.05)2(0.10)14$

$\beta_{\text{ex}} = 0.02626 \text{ km}^{-1}$
 $\varpi = 0.7005$

θ	$P_1/4\pi$	$P_2/4\pi$	$P_3/4\pi$	$P_4/4\pi$
0.0	0.5136	0.5136	0.5136	0
5.0	0.5011	0.4943	0.4976	-0.008189
10.0	0.4664	0.4420	0.4528	-0.02968
15.0	0.4165	0.3705	0.3876	-0.05695
20.0	0.3600	0.2956	0.3126	-0.08181
30.0	0.2537	0.1758	0.1705	-0.1058
40.0	0.1759	0.1100	0.07022	-0.09687
50.0	0.1259	0.07908	0.01343	-0.07418
60.0	0.09472	0.06377	-0.01438	-0.05214
70.0	0.07495	0.05473	-0.02657	-0.03549
80.0	0.06204	0.04853	-0.03130	-0.02414
100.0	0.04744	0.04043	-0.03290	-0.01182
120.0	0.04070	0.03549	-0.03256	-0.006349
140.0	0.03821	0.03315	-0.03352	-0.003326
160.0	0.03820	0.03535	-0.03652	-0.001061
180.0	0.03863	0.03863	-0.03863	0

Table T.124

$m = 1.28 - 1.37i$
 $\lambda = 0.441 \mu$

Model: Iron cloud C.3
 x: 7.20(0.20)51

$\beta_{\text{ex}} = 2.940 \text{ km}^{-1}$
 $\varpi = 0.6441$

θ	$P_1/4\pi$	$P_2/4\pi$	$P_3/4\pi$	$P_4/4\pi$
0.0	67.56	67.56	67.56	0
2.0	47.17	45.70	46.42	-0.6459
4.0	15.12	12.99	13.98	-0.8800
6.0	2.232	1.495	1.775	-0.1877
8.0	0.9861	0.8139	0.8601	0.06902
10.0	0.7122	0.5091	0.5822	0.02756
12.0	0.4043	0.2522	0.2990	0.03252
16.0	0.2120	0.1123	0.1388	0.03465
20.0	0.1350	0.05844	0.07534	0.03120
30.0	0.06943	0.01912	0.02383	0.02420
40.0	0.04843	0.01004	0.007614	0.01982
50.0	0.03851	0.007435	-0.000362	0.01666
60.0	0.03265	0.006959	-0.005251	0.01405
70.0	0.02866	0.007371	-0.008553	0.01172
80.0	0.02567	0.008196	-0.01086	0.009606
90.0	0.02330	0.009205	-0.01246	0.007693
100.0	0.02138	0.01027	-0.01355	0.005993
110.0	0.01980	0.01132	-0.01427	0.004516
120.0	0.01851	0.01229	-0.01472	0.003263
130.0	0.01746	0.01315	-0.01499	0.002229
140.0	0.01664	0.01388	-0.01513	0.001406
150.0	0.01601	0.01447	-0.01520	0.000781
160.0	0.01558	0.01489	-0.01522	0.000344
170.0	0.01532	0.01515	-0.01523	0.000085
180.0	0.01523	0.01523	-0.01523	0

Table T.125

$m = 1.70 - 1.84i$
 $\lambda = 0.668 \mu$

Model: Iron cloud C.3
 $x: 4.125(0.125)34$

$\beta_{\text{ex}} = 3.079 \text{ km}^{-1}$
 $\varpi = 0.6586$

θ	$P_1/4\pi$	$P_2/4\pi$	$P_3/4\pi$	$P_4/4\pi$
0.0	30.02	30.02	30.02	0
2.0	25.62	25.09	25.35	-0.3504
4.0	15.74	14.39	15.02	-0.8883
6.0	6.739	5.343	5.923	-0.8864
8.0	2.002	1.222	1.462	-0.4234
10.0	0.6407	0.3655	0.3920	-0.04427
12.0	0.4860	0.3372	0.3508	0.04789
14.0	0.4144	0.2479	0.2869	0.01878
16.0	0.2961	0.1412	0.1719	0.007758
18.0	0.2133	0.09009	0.1055	0.01749
20.0	0.1701	0.06675	0.07661	0.02306
30.0	0.08267	0.01822	0.01623	0.02068
40.0	0.05535	0.009143	-0.000454	0.01733
50.0	0.04308	0.007684	-0.007539	0.01450
60.0	0.03624	0.008301	-0.01146	0.01212
70.0	0.03184	0.009555	-0.01394	0.01005
80.0	0.02872	0.01097	-0.01562	0.008215
90.0	0.02635	0.01237	-0.01677	0.006583
100.0	0.02449	0.01368	-0.01754	0.005142
110.0	0.02299	0.01485	-0.01805	0.003891
120.0	0.02177	0.01587	-0.01837	0.002825
130.0	0.02079	0.01674	-0.01855	0.001939
140.0	0.02001	0.01744	-0.01864	0.001229
150.0	0.01943	0.01799	-0.01868	0.000685
160.0	0.01902	0.01839	-0.01870	0.000302
170.0	0.01878	0.01862	-0.01870	0.000075
180.0	0.01870	0.01870	-0.01870	0

Subject Index

- Absorbing particles, 33–35, 47–51, 108, 114, 119, 133, 136
 - blackbody definition, 35
 - van de Hulst's parameter for, 29
- Albedo of single scattering, 35, 95, 115, 118, 125, 134, 135
- Angular coefficients, 15
- Anisotropic scattering, 8, 114
 - asymmetry factor, 36, 92
 - backward asymmetry, 45, 47, 51, 123
 - forward asymmetry, 45, 46, 51
- Asymptotic behavior
 - of absorption efficiency, 36–37
 - of back scattering efficiency, 39–41
 - of extinction efficiency, 36, 41
 - of Mie coefficients, 21
 - of scattering efficiency, 36, 40, 41
- Attenuation, *see* Extinction and Polydisperse scattering
- Aureole, 5, 53, 98, 100–102, 109–110, 113, 135
 - silver lining, 161
- Bessel functions, 16–17
 - spherical, 16
 - with complex argument, 16, 18–24
 - with real argument, 17, 23
- Bishop's ring, 53, 82, 107
 - see also* Volcanic dust
- Chemical composition, 7, 141
- Clouds, 4
 - corona producing, 82–83, 109
 - cumulus, 82
 - ice crystal, 131
 - iridescent, 109, 111
 - liquid water content, 115
 - mother-of-pearl, 82, 108–109
 - noctilucent, 106, 133
 - stratiform, 113
 - water droplet, 108–119
- Colloidal suspension, 4, 71
- Complex amplitude, *see* Mie theory
- Complex angle of refraction, 36
- Complex index of refraction, 12, 36, 83–88
 - ice, 84
 - iron, 85, 88
 - limonite, 88
 - liquid water, 83, 84–85, 118
 - silicates, 88
- Coronas, 51, 53, 82, 108–111
- Creeping wave, 46
- Cross-section theorem, 14, 41

- Differential cross section, 13, 40, 59
- Diffraction theory, 10, 51, 53, 102, 108
- Double precision, 21, 39, 89
- Electric field, 12
 - phase angles and difference, 61
 - scalar amplitude, 12, 13, 61
 - vector amplitude, 13, 61
- Extinction cross-section and efficiency, 14
 - for absorbing spheres, 28, 35
 - for metallic spheres, 19, 35
 - for non-absorbing spheres, 28, 32
 - for reflecting spheres, 35, 36
 - series expansion, 33
 - van de Hulst approximation, 10, 29
 - with empirical correction, 29–33
- Filtered-sun effect, 113–114
- Forest fire smoke, 107, 108
 - blue sun, 107
- Geometrical optics, 10, 35, 41, 46, 55
- Glory phenomena, 51, 53–55, 108, 111–113, 116, 118, 119, 131
- Halo, 10, 131
- Haze and aerosol particles, 98
 - see also* Aureole, Mixing ratio, Polarization, Polydisperse scattering, Radiative transfer, Scattering layers, Size distribution function
- Incident flux, 13, 14, 72, 74
- Incoherent or independent scattering, 56, 60, 105, 127
- Incoherent radiation, 56, 127
- Intensity function, *see* Mie theory
- Interstellar dust and grains, 136, 139–142
 - differential extinction, 139–142
 - iron particles, 140–141
 - mass, 141
 - polarization, 141
 - starlight polarization, 139, 142
- Inverse problems, 7, 8, 102, 119, 140
- Isotropic scattering, 8, 38
- Laser light and scattering, 57, 71, 105, 124–126
 - bistatic system, 125
 - communications and propagation, 125–127
- Legendre polynomials, 15
- Machine computation, 14, 15, 23
 - convergence of integrals, 90
 - integration scheme, 89–92
 - printout, 89, 91
 - significant figures, 93
 - time, 89
- Martian atmosphere, 132–134
- Microwave scattering, 119–123, 130
 - bistatic system, 123
 - extinction coefficient, 123
 - radar cross-section, 10, 37, 119, 121
- Mie theory, 4, 11–12
 - complex amplitude, 13, 61, 71
 - coefficients, 14, 16–27
 - convergence circle, 26–27
 - functions, 12
 - intensity functions, 72
 - particles, 11, 68, 70
 - scattering parameters, 14
 - series, 13, 14
 - Stokes matrix elements, 68–71
- Mixing ratio for scattering, 99
 - as a turbidity coefficient, 100
- Monodispersed suspension, 3, 51, 53, 72–74, 109
- Natural (unpolarized) light, 13, 67, 72
- Non-spherical particles, 108
- Non-polar molecules, 9, 98
- Normalization, 72–73
 - of incident flux, 72, 74
 - of scattering matrix elements, 73, 100
- Optical thickness, 95, 99
- Phase function, 73
- Polarization, 46
 - depolarization, 71, 105, 126–127
 - elliptical, 60, 65, 71, 104, 138

- Polarization, (*Contd.*)
 - full, 60, 64, 70, 71
 - handedness, 65
 - linear, 54, 71, 118, 138
 - observations of, 104, 112
 - of cloudbows and glories, 112–113
 - partial, 56, 67, 70
- Polydispersed suspension, 3, 4, 71, 115
- Polydisperse scattering, 4, 74–75, 98
 - mass-absorption coefficient, 115
 - scattering matrix, 75, 99
 - volume absorption coefficient, 89, 115
 - volume back-scattering coefficient, 119–123
 - volume extinction coefficient, 89, 116–118, 123
 - volume scattering coefficient, 75, 89, 117
- Poynting's vector, 13
- Precipitation, 119
 - hail, 81, 121, 123
 - rain, 81, 121
- Propagation constant, 12
- Radar cross section, 119, 130
 - see* Microwave scattering
- Radiation
 - balance, 114
 - field, 13
 - pressure, 36
- Radiative transfer, 6, 72
 - equation of, 94–97
 - for primary scattering, 96
 - in mixed media, 98–100
 - in optically thin media, 97
- Rainbow and cloudbow phenomena, 10, 51, 54, 108, 111–113, 116
- Rayleigh scattering and approximation, 9, 45, 46, 47, 98, 100–102
- Rayleigh-Gans approximation, 10
- Recursion formula, 15
 - for angular functions, 15
 - for Bessel functions, 17, 18
- Reflection
 - Fresnel, 35, 39, 46
 - Lambert, 105
- Refractive index, 83
 - see* Complex index of refraction
- Ricatti-Bessel functions, 16, 18
- Saturn's rings, 54, 134–136, 138
- Scattering layers
 - of arbitrary optical thickness, 96
 - optically thin, 47, 51, 74, 97, 108, 125
- Scattering plane and angle, 13, 60, 68, 69
- Single particle scattering, 3, 24
 - absorption efficiency, 28, 34
 - back scattering (radar) efficiency, 37–41
 - complex amplitude components, 41–46
 - extinction efficiency, 28–37
 - intensity parameters, 46–55
 - matrix elements, 94, 72–74
 - scattering efficiency, 14, 28, 33
 - volume scattering coefficient, 74
- Size-distribution models, 6, 75
 - composite, 83
 - continuous, 74
 - gamma distribution, 75
 - integration of, 74, 76
 - mode radius, 76
 - properties of function, 75–77
 - specific functions, 77–83
 - volume and mass of particles, 76, 77
- Size parameter, 9
 - for Mie particles, 12, 75
 - for van de Hulst's approximation, 29
- Skylight, 3
 - blue color of, 5
 - brightness, 114
 - polarization, 104, 105, 108
- Snell's law, 36
- Source function, 95
- Space platforms, 98, 124, 131, 133, 136, 138
- Spheres
 - hard, 11
 - large absorbing, 24
 - metallic, 27, 35, 38, 108, 139

- Spheres, (*Contd.*)
 totally reflecting, 11, 29, 38, 45
 transparent, 29–33
Stokes vector, matrix and parameters,
 56, 57, 64–72
 for incident flux, 72
 modified, 70
Sunlit planetary atmosphere, 7, 95

Turbidity coefficient, 100
 see Mixing ratio
Twilight phenomena, 82, 106

van de Hulst's approximation, 10
 see Extinction

Venus, 54, 128–132
 clouds, 118, 129–131
 greenhouse effect, 128, 130
 microwave emission, 129, 131
 polarization, 130, 131, 132
 radar cross-section, 123, 130
 temperature, 128, 129
Volcanic dust, 53, 102, 107
 green sun, 108

Water-vapor bands, 8, 130

Zodiacal light, 137–139
 gegenschein, 139
 polarization, 138, 139.

Selected RAND Books

- Arrow, Kenneth J., and Marvin Hoffenberg. *A Time Series Analysis of Inter-industry Demands*. Amsterdam, Holland: North-Holland Publishing Company, 1959.
- Bellman, Richard. *Dynamic Programming*. Princeton, N.J.: Princeton University Press, 1957.
- Bellman, Richard. *Introduction to Matrix Analysis*. New York: McGraw-Hill Book Company, Inc., 1960.
- Bellman, Richard E., and Kenneth L. Cooke. *Differential-Difference Equations*. New York: Academic Press Inc., 1963.
- Bellman, Richard E., and Stuart E. Dreyfus. *Applied Dynamic Programming*. Princeton, N.J.: Princeton University Press, 1962.
- Bellman, R. E., H. H. Kagiwada, R. E. Kalaba, and M. C. Prestrud. *Invariant Imbedding and Time-Dependent Transport Processes*. New York: American Elsevier Publishing Company, Inc., 1964.
- Bellman, R. E., R. E. Kalaba, and M. C. Prestrud. *Invariant Imbedding and Radiative Transfer in Slabs of Finite Thickness*. New York: American Elsevier Publishing Company, Inc., 1963.
- Bellman, R. E., R. E. Kalaba, and Jo Ann Lockett. *Numerical Inversion of the Laplace Transform*. New York: American Elsevier Publishing Company, Inc., 1966.
- Bellman, Richard E., and Robert E. Kalaba. *Quasilinearization and Nonlinear Boundary-Value Problems*. New York: American Elsevier Publishing Company, Inc., 1965.
- Dantzig, George B. *Linear Programming and Extensions*. Princeton, N.J.: Princeton University Press, 1963.
- Dresher, Melvin. *Games of Strategy: Theory and Applications*. Englewood Cliffs, N.J.: Prentice-Hall Inc., 1961.
- Dreyfus, Stuart. *Dynamic Programming and the Calculus of Variations*. New York: Academic Press Inc., 1965.

- Edelen, Dominic G. B. *The Structure of Field Space: An Axiomatic Formulation of Field Physics*. Los Angeles, California: University of California Press, 1962.
- Ford, L. R., Jr. and D. R. Fulkerson. *Flows in Networks*. Princeton, N.J.: Princeton University Press, 1962.
- Gale, David. *The Theory of Linear Economic Models*. New York: McGraw-Hill Book Company, Inc., 1960.
- Gazley, C., Jr., J. P. Hartnett, and E. R. G. Eckert. *Proceedings of the Second All-Soviet Union Conference on Heat and Mass Transfer*, Volumes 1-7. Ann Arbor, Michigan: University Microfilms, 1968.
- Gruenberger, Fred, and George Jaffray. *Problems for Computer Solution*. New York: John Wiley & Sons, Inc., 1965.
- Gruenberger, Fred J., and Daniel D. McCracken. *Introduction to Electronic Computers: Problem Solving with the IBM 1620*. New York: John Wiley & Sons, Inc., 1963.
- Harris, Theodore E. *The Theory of Branching Processes*. Berlin, Germany: Springer-Verlag, 1963; Englewood Cliffs, N.J.: Prentice-Hall, Inc., 1964.
- Hastings, Cecil, Jr. *Approximations for Digital Computers*. Princeton, N.J.: Princeton University Press, 1955.
- Hirshleifer, Jack, James C. DeHaven, and Jerome W. Milliman. *Water Supply: Economics, Technology, and Policy*. Chicago, Illinois: The University of Chicago, 1960.
- Hitch, Charles J., and Roland McKean. *The Economics of Defense in the Nuclear Age*. Cambridge, Massachusetts: Harvard University Press, 1960.
- Judd, William R. (ed.). *State of Stress in the Earth's Crust*. New York: American Elsevier Publishing Company, Inc., 1964.
- McKinsey, J. C. C. *Introduction to the Theory of Games*. New York: McGraw-Hill Book Company, Inc., 1952.
- Meyer, John R., Martin Wohl, and John F. Kain. *The Urban Transportation Problem*. Cambridge, Massachusetts: Harvard University Press, 1965.
- Novick, David (ed.). *Program Budgeting: Program Analysis and the Federal Budget*. Cambridge, Massachusetts: Harvard University Press, 1965.
- Quade, E. S., and Wayne I. Boucher (eds.). *Systems Analysis and Policy Planning: Applications in Defense*. New York: American Elsevier Publishing Company, Inc., 1968.
- The RAND Corporation. *A Million Random Digits with 100,000 Normal Deviates*. Glencoe, Illinois: The Free Press, 1955.
- Selin, Ivan. *Detection Theory*. Princeton, N.J.: Princeton University Press, 1965.
- Sheppard, J. J. *Human Color Perception*. New York: American Elsevier Publishing Company, 1968.
- Williams, J. D. *The Compleat Strategyst: Being a Primer on the Theory of Games of Strategy*. New York: McGraw-Hill Book Company, Inc., 1954.

